



The  
University  
Of  
Sheffield.

# Structural and functional studies on the cytochrome $b_6f$ complex from higher plants and cyanobacteria.

Lorna Alexandra Malone

Faculty of Science  
School of Biosciences

A thesis submitted for the degree of Doctor of Philosophy

October 2021

FOR E.M.D.,

WHO'S BEEN WITH ME EVERY STEP.

ALL MY LOVE ALWAYS AND A BIG HUG X



## Abstract

Oxygenic photosynthesis plays a pivotal role at the very heart of global ecosystems, providing the food, fuel and oxygen that sustains virtually all life on Earth (**Hohmann-Marriott and Blankenship, 2011**). Despite the essential and highly intricate role that photosynthesis plays on Earth, the actual process of photosynthesis appears to be remarkably inefficient with only ~ 9 - 12 % of useable solar energy (wavelengths between 400 – 700 nm) being converted to biomass (**Zhu et al., 2010**). Given the rising demands on the global food chain associated with climate change and a rising population, it is widely recognised that improvements in the efficiency of this vital process will be required to ensure food security for an ever-increasing population over the coming decades (**Long et al., 2015; Zhu et al., 2010**).

Among the multiple targets which have been identified for potential improvement is cytochrome *b<sub>6</sub>f* (*cytb<sub>6</sub>f*), an integral membrane complex found at the heart of oxygenic photosynthesis. As well as facilitating the rate-limiting step in light dependent electron and proton transfer, the *cytb<sub>6</sub>f* complex also plays a key role as a redox-sensing hub in higher plants involved in the regulation of light-harvesting, electron transfer, photosynthetic gene expression and adaptation to environmental stress. Together, these characteristics make *cytb<sub>6</sub>f* a judicious target for genetic manipulation to enhance photosynthetic yield and promote stress tolerance in crop plants. While a number of studies show great promise in this regard (**Simkin et al., 2017**), further progress is hindered by the lack of a detailed understanding of the structure and function of the *cytb<sub>6</sub>f* complex from higher plants.

Here we present the first structures of the *cytb<sub>6</sub>f* complex from a higher plant (*Spinacia oleracea*), shedding light on the internal mechanics of the Q-cycle and providing new clues as to how this extraordinary complex fulfils its various roles in photosynthetic regulation. We offer further opportunities to explore these insights by presenting a second structure, from the model cyanobacterium *Synechocystis* sp. 6803. Together these structures provide a number of key mechanistic insights into the *cytb<sub>6</sub>f* complex, many of which may now be further explored through structure-based mutagenesis of the *Synechocystis* complex and molecular dynamics simulations.

## Acknowledgements

First and foremost, I would like to thank my supervisors Matt Johnson and Neil Hunter for giving me the opportunity to undertake this project and for their ongoing support over the last four years. It's been a privilege working with you and learning from you both; I am extremely grateful for the opportunities you've given me. I would also like to say a special thanks to Neil for his extreme patience, unwavering support and encouragement over the years. Thank you for having faith in me when I haven't believed in myself and for encouraging me to do the things that I might be scared of – your guidance and support has been absolutely invaluable to me.

Next I would like to express my gratitude towards members of the Hunter/Johnson lab, both past and present, for welcoming me into the lab and generally being a pretty nice bunch. Particular thanks to Pu Qian for his help with the cryo-EM, Dave Farmer for help with processing in RELION and Guy Mayneord for showing me the ropes, for being a good friend and for all of his help with the first spinach purifications. A big thanks also to Craig Mcgregor-Chatwin for all of the late night sucrose gradient help and for making sure I didn't blow up the centrifuge.

For their efforts with the *Synechocystis cytb<sub>6f</sub>*, a big shout out to Matt Proctor, Andy Hitchcock and Dave Swainsbury (aka. Team *b<sub>6f</sub>*). Particular thanks to Dave Swainsbury for teaching me valuable lessons in the lab, for his incredible patience, for being the fountain of \*most\* knowledge and for always being on call for emergency bubble-related AKTA queries. Also thanks to Andrew Hitchcock for the insightful conversations, for watering my plants, all of those early morning antibody incubations and for just generally being a really lovely person.

A huge thank you to Svet Tzokov, Julien Bergeron, Jason Wilson, Daniel Mann, Rebecca Thompson (and the wider EM community too numerous to specify) for their helpful advice and assistance with EM, data processing and all of those times 'computer says no'. I'd also like to say a special thanks to Becky (and Charlie Scarff) for welcoming me into the Astbury team during my PIPs placement, trusting me not to break things and for all of the tea and cryoEM training. Thank you also to Ben Engel and Wojciech Wiertrynski for hosting me in their lab for an extended visit, showing me good beer, good food and for teaching me the dark arts of tomography.

Last but by no means least, I would like to take the time to thank my wonderful friends and family. To my friends (H.S., O.T. and J.E.), I doubt you'll ever read this but I appreciate you all very much. To my ~~partner~~ fiancé R.M., thank you for being my rock, through all of the good times and the bad. For the many hours listening to me practice talks (I swear you know them all off by heart by now!), for indulging me in my nerdiness (we can have 3D printed *b6fs* on the Christmas tree right?!), for all of the late night pick-ups from the lab, for the endless cups of tea during the long days of thesis writing and for just being you. I love you my darling, thank you for all of your love and support.

To my hilarious, grumpy, cuddly cat (H.R.H. A.), (we can't forget you!), although you can't read this, you deserve a mention for being a great companion, through everything, and for being the best alarm clock I could ask for.

To my parents (all of you), I thank you for the ever present love, support and encouragement. For giving me opportunities and for helping me stick with it when things get tough.

Finally, to my grandparents, who have been instrumental in my achievements thus far - for their unwavering support over the years, for all of the opportunities, for inspiring me to fulfil my potential and for never failing to make me feel special. I miss you both more than words can say but in my heart I know you're cheering me on and you'd be so very proud of me for getting this far.

## Declaration

I, the author, confirm that this Thesis is my own work. I am aware of the University's Guidance on the Use of Unfair Means ([www.sheffield.ac.uk/ssid/unfair-means](http://www.sheffield.ac.uk/ssid/unfair-means)). This work has not previously been presented for an award at this, or any other, university.

The work described in this Thesis contributed to the following research publication:

- 1) Mayneord, G.E., Vasilev, C., Malone, L.A., Swainsbury, D.J.K., Hunter, C.N., and Johnson, M.P. (2019). Single-molecule study of redox control involved in establishing the spinach plastocyanin-cytochrome *b<sub>6</sub>f* electron transfer complex. *Biochim. Biophys. Acta - Bioenerg.* *1860*, 591–599.
- 2) Malone, L.A., Qian, P., Mayneord, G.E., Hitchcock, A., Farmer, D.A., Thompson, R.F., Swainsbury, D.J.K., Ranson, N.A., Hunter, C.N., and Johnson, M.P. (2019). Cryo-EM structure of the spinach cytochrome *b<sub>6</sub>f* complex at 3.6 Å resolution. *Nature* *575*, 535–539.
- 3) Malone, L.A., Proctor, M.S., Hitchcock, A., Hunter, C.N., and Johnson, M.P. (2021). Cytochrome *b<sub>6</sub>f* – Orchestrator of photosynthetic electron transfer. *BBA - Bioenerg.* *1862*, 148380.

# Contents

<b>Abstract</b> .....	<b><i>i</i></b>
<b>Acknowledgements</b> .....	<b><i>ii</i></b>
<b>Declaration</b> .....	<b><i>iv</i></b>
<b>Figures</b> .....	<b><i>x</i></b>
<b>Tables</b> .....	<b><i>xiv</i></b>
<b>Equations</b> .....	<b><i>xvi</i></b>
<b>List of abbreviations</b> .....	<b><i>xvii</i></b>
<b>1 Introduction</b> .....	<b><i>1</i></b>
<b>1.1 An overview of oxygenic photosynthesis</b> .....	<b><i>1</i></b>
<b>1.2 Light-dependent electron transfer in the chloroplast thylakoid</b> .....	<b><i>4</i></b>
1.2.1 Principles of biological electron transfer reactions.....	<i>4</i>
1.2.2 Linear electron transfer (LET) in the chloroplast thylakoid membrane .....	<i>7</i>
1.2.3 Cyclic electron transfer (CET) provides a means to fine tune photosynthetic output .....	<i>7</i>
<b>1.3 The <i>cytb<sub>6</sub>f</i> complex: orchestrator of electron transfer</b> .....	<b><i>10</i></b>
1.3.1 The structure of the <i>cytb<sub>6</sub>f</i> complex .....	<i>10</i>
1.3.2 Structural similarities between the <i>cytb<sub>6</sub>f</i> and <i>bc<sub>1</sub></i> complexes.....	<i>14</i>
1.3.3 The modified Q-cycle and electron transfer mechanics .....	<i>18</i>
1.3.4 Architecture and dynamics at the Q <sub>p</sub> site .....	<i>22</i>
1.3.5 Avoiding side-reactions and Q-cycle short-circuits at the Q <sub>p</sub> site. ....	<i>29</i>
1.3.6 Architecture and dynamics at the Q <sub>n</sub> site .....	<i>30</i>
1.3.7 Outstanding questions .....	<i>36</i>
<b>1.4 Using structural biology to study photosynthesis</b> .....	<b><i>37</i></b>
1.4.1 Principles of electron microscopy .....	<i>38</i>
1.4.2 Point Spread Functions (PSF) and the Contrast Transfer Function (CTF) .....	<i>43</i>
1.4.3 Single particle cryo-EM image analysis .....	<i>44</i>
<b>2 Materials and Methods</b> .....	<b><i>48</i></b>
<b>2.1 Materials, buffers and reagents</b> .....	<b><i>48</i></b>
<b>2.2 The preparation of plant material</b> .....	<b><i>48</i></b>
2.2.1 <i>Spinacia oleracea</i> material .....	<i>48</i>

2.2.2	Thylakoid preparation with NaBr wash for the purification of <i>cytb<sub>6</sub>f</i> from <i>S. oleracea</i> .....	48
2.2.3	Thylakoid preparation without NaBr wash for the purification of plastocyanin from <i>S. oleracea</i> 49	
2.2.4	Chlorophyll quantification assay .....	50
<b>2.3</b>	<b>The preparation of <i>Synechocystis</i> material.....</b>	<b>51</b>
2.3.1	Strains and plasmids .....	51
2.3.2	Growth media .....	52
2.3.3	<i>Synechocystis</i> thylakoid preparation.....	54
<b>2.4</b>	<b>Protein purification techniques.....</b>	<b>54</b>
2.4.1	Solubilisation .....	55
2.4.2	Sucrose gradients.....	55
2.4.3	Sonication .....	57
2.4.4	Ceramic Hydroxyapatite (CHT) chromatography .....	57
2.4.5	StrepTactin affinity chromatography .....	58
2.4.6	Gel filtration .....	59
2.4.7	Anionic exchange chromatography (AEC).....	60
<b>2.5</b>	<b>Biochemical analysis of proteins .....</b>	<b>61</b>
2.5.1	Sodium dodecyl sulphate polyacrylamide gel electrophoresis (SDS-PAGE).....	61
2.5.2	Blue-native polyacrylamide gel electrophoresis (BN-PAGE) .....	62
2.5.3	Ultraviolet - visible (UV/Vis) absorbance spectroscopy .....	63
2.5.4	Stopped-flow absorbance spectroscopy .....	64
2.5.5	Western blotting .....	64
<b>2.6</b>	<b>Negative stain transmission electron microscopy (TEM) .....</b>	<b>65</b>
2.6.1	Grid preparation and negative staining .....	65
2.6.2	Imaging.....	65
<b>2.7</b>	<b>Single particle cryo-TEM .....</b>	<b>66</b>
2.7.1	Cryo-TEM materials.....	66
2.7.2	Grid preparation, plunge freezing and vitrification .....	66
2.7.3	Screening.....	66
2.7.4	Data collection and imaging.....	67
<b>2.8</b>	<b>Image Processing .....</b>	<b>67</b>
2.8.1	Single particle reconstruction using RELION .....	67
2.8.2	Conformational flexibility analysis .....	68
<b>2.9</b>	<b>Structural modelling and validation .....</b>	<b>69</b>
2.9.1	Homology-based modelling, rigid body fitting and manual model building .....	69

2.9.2	Comprehensive validation .....	69
<b>3</b>	<b><i>Results: The purification of dimeric cytb<sub>6</sub>f from the chloroplasts of Spinacia oleracea</i></b>	
	<b>71</b>	
<b>3.1</b>	<b>Selective solubilisation of dimeric cytb<sub>6</sub>f from <i>S. oleracea</i>.....</b>	<b>73</b>
3.1.1	Initial small-scale optimisation of solubilisation conditions .....	73
3.1.2	Scaled up selective solubilisation using HECAMEG.....	76
<b>3.2</b>	<b>Differential Sedimentation using Sucrose Gradient Ultracentrifugation .....</b>	<b>76</b>
<b>3.3</b>	<b>Hydroxyapatite Column Purification .....</b>	<b>76</b>
<b>3.4</b>	<b>Detergent Exchange using Sucrose Gradient Ultracentrifugation .....</b>	<b>78</b>
<b>3.5</b>	<b>Further improvements to the yield .....</b>	<b>81</b>
<b>3.6</b>	<b>Quantification of purified dimeric cytb<sub>6</sub>f in tPCC-<math>\alpha</math>-M using redox difference spectra ..</b>	<b>83</b>
<b>3.7</b>	<b>Activity assays .....</b>	<b>85</b>
3.7.1	Purification of plastocyanin .....	85
3.7.2	Activity assays .....	86
<b>3.8</b>	<b>Discussion.....</b>	<b>87</b>
<b>4</b>	<b><i>Results: Structural determination of cytb<sub>6</sub>f from S. oleracea.....</i></b>	<b>89</b>
<b>4.1</b>	<b>Negative stain TEM analysis.....</b>	<b>89</b>
<b>4.2</b>	<b>Cryo-TEM analysis .....</b>	<b>91</b>
4.2.1	Sample preparation and screening .....	91
4.2.2	Data acquisition .....	91
4.2.3	Beam-induced motion correction and CTF estimation .....	91
4.2.4	Particle picking and 2D classification .....	91
4.2.5	<i>De novo</i> 3D model generation .....	93
4.2.6	3D reconstruction to 3.58 Å.....	93
<b>4.3</b>	<b>Structural modelling .....</b>	<b>96</b>
4.3.1	Multiple sequence alignment of the <i>S. oleracea</i> cytb <sub>6</sub> f with cyanobacterial and algal complexes	96
4.3.2	Model Building .....	99
4.3.3	Model Validation.....	99
<b>4.4</b>	<b>Structural analysis .....</b>	<b>105</b>
4.4.1	Overall architecture and comparison with the cyanobacterial and algal complexes .....	105
4.4.2	The intermonomer cavity and native PQ molecules.....	112

4.4.3	The Q <sub>p</sub> portal and the luminal (p-) side plastoquinol oxidation (Q <sub>p</sub> ) site .....	117
4.4.4	The stromal (n-) side plastoquinone reduction (Q <sub>n</sub> ) site.....	119
<b>4.5</b>	<b>The role of Chl <i>a</i> .....</b>	<b>125</b>
<b>4.6</b>	<b>Conclusions .....</b>	<b>126</b>
<b>5</b>	<b><i>Results: The purification and structural determination of cytb<sub>6</sub>f from Synechocystis sp. PCC 6803 .....</i></b>	<b>128</b>
<b>5.1</b>	<b>Initial trials to isolate dimeric cytb<sub>6</sub>f from <i>Synechocystis</i> sp. PCC 6803 using glyco- diosgenin (GDN).....</b>	<b>129</b>
5.1.1	Thylakoid preparation .....	129
5.1.2	Solubilisation trials .....	129
5.1.3	Purification by Strep-Tactin Chromatography .....	130
5.1.4	Purification by Gel Filtration .....	132
<b>5.2</b>	<b>Quantification of purified dimeric cytb<sub>6</sub>f using redox difference spectra .....</b>	<b>133</b>
<b>5.3</b>	<b>Activity assays .....</b>	<b>133</b>
<b>5.4</b>	<b>Negative stain TEM analysis.....</b>	<b>134</b>
<b>5.5</b>	<b>Single particle cryo-EM .....</b>	<b>135</b>
5.5.1	Sample preparation and screening .....	135
5.5.2	Sample preparation and screening .....	135
5.5.3	Beam-induced motion correction, particle picking, CTF estimation and 2D classification .....	136
5.5.4	Particle picking and 2D classification .....	136
5.5.5	<i>De novo</i> 3D model generation .....	138
5.5.6	3D reconstruction to 2.98 Å .....	139
<b>5.6</b>	<b>Structural modelling .....</b>	<b>142</b>
5.6.1	Multiple sequence alignment of the <i>Synechosystis</i> sp. PCC 6803 cytb <sub>6</sub> f complex with cyanobacterial, algal and plant complexes .....	142
5.6.2	Model building .....	145
5.6.3	Model Validation.....	147
<b>5.7</b>	<b>Structural analysis .....</b>	<b>153</b>
5.7.1	Overall architecture and comparison with the <i>S. oleracea</i> complex .....	153
5.7.2	The intermonomer cavity and clues regarding substrate movement in plants .....	161
5.7.3	The plastoquinol oxidation (Q <sub>p</sub> ) site and the high-potential electron transfer pathway .....	164
<b>5.8</b>	<b>Conclusion.....</b>	<b>167</b>



<b>6</b>	<b><i>Results: Rieske head domain dynamics</i></b> .....	<b>168</b>
6.1	Introduction .....	168
6.2	Indications of motion in the <i>S. oleracea</i> and <i>Synechocystis</i> datasets .....	175
6.3	<b>3D variability analysis of the <i>Synechocystis</i> <i>cytb<sub>6</sub>f</i> dataset</b> .....	<b>178</b>
6.3.1	3DVA using a full mask.....	179
6.3.2	3DVA using a mask focussed on the extrinsic luminal portion of the map.....	181
6.4	<b>3DVA using a ‘lumen-only’ mask</b> .....	<b>183</b>
6.4.1	Analysis of the two ‘extremes’ revealed by the lumen-only 3DVA.....	183
6.4.2	The 70 : 30 model- bridging the gap through the movement of <i>cyt<sub>f</sub></i> .....	184
6.4.3	Alternatives: a third conformational state? .....	186
6.5	<b>Conclusions</b> .....	<b>187</b>
<b>7</b>	<b><i>Concluding remarks and further work</i></b> .....	<b>188</b>
7.1	<b>Insights into the photosynthetic Q-cycle</b> .....	<b>189</b>
7.1.1	The role of the enigmatic Chl <i>a</i> molecule in the <i>cytb<sub>6</sub>f</i> complex .....	189
7.1.2	Bridging cofactor distances in the high-potential ET pathway.....	190
7.1.3	The role of haem <i>c<sub>n</sub></i> in the <i>cytb<sub>6</sub>f</i> complex .....	191
7.1.4	Native substrate.....	191
7.2	<b>Concluding remarks</b> .....	<b>192</b>
<b>8</b>	<b><i>Bibliography</i></b> .....	<b>193</b>

## Figures

<b>Figure 1.1</b>   The site of photosynthesis in plants.....	2
<b>Figure 1.2</b>   The linear electron transfer chain of photosynthesis.....	3
<b>Figure 1.3</b>   The photosynthetic cyclic electron transfer chain .....	9
<b>Figure 1.4</b>   The similarities and differences between the cytochrome <i>b<sub>6</sub>f</i> and <i>bc<sub>1</sub></i> complexes .....	11
<b>Figure 1.5</b>   Haems of the <i>cytb<sub>6</sub>f</i> complex.....	17
<b>Figure 1.6</b>   The proton motive Q-cycle of cytochrome <i>b<sub>6</sub>f</i> .....	21
<b>Figure 1.7</b>   Architecture of the Q <sub>p</sub> site and proton movements linked to catalysis in <i>cytbc<sub>1</sub></i>	23
<b>Figure 1.8</b>   Large scale conformational changes occurring within the extrinsic domain of the ISP underlie catalysis in the cytochrome <i>bc<sub>1</sub></i> complex .....	24
<b>Figure 1.9</b>   Architecture of the Q <sub>p</sub> site and proton movements linked to catalysis in <i>cytb<sub>6</sub>f</i>	26
<b>Figure 1.10</b>   The Q <sub>p</sub> sites of <i>cytbc<sub>1</sub></i> and <i>cytb<sub>6</sub>f</i> .....	28
<b>Figure 1.11</b>   The Q <sub>n</sub> site of <i>cytbc<sub>1</sub></i> and the proposed reaction mechanics.....	31
<b>Figure 1.12</b>   The Q <sub>n</sub> site of <i>cytb<sub>6</sub>f</i> compared to <i>cytbc<sub>1</sub></i> .....	33
<b>Figure 1.13</b>   Putative proton transfer pathways on the n-side of <i>cytb<sub>6</sub>f</i> .....	35
<b>Figure 1.14</b>   Comparison of a typical light microscope to a typical transmission electron microscope (TEM).....	39
<b>Figure 1.15</b>   Interactions between the electron beam and the sample .....	40
<b>Figure 1.16</b>   Schematic demonstrating projection theorem .....	45
<b>Figure 3.1</b>   Optimising the concentration of HECAMEG for selective solubilisation of <i>cytb<sub>6</sub>f</i> from spinach thylakoids .....	74
<b>Figure 3.2</b>   Optimising the length of HECAMEG solubilisation for selective solubilization of <i>cytb<sub>6</sub>f</i> from spinach thylakoids .....	75
<b>Figure 3.3</b>   The purification of <i>cytb<sub>6</sub>f</i> from spinach thylakoids.....	77
<b>Figure 3.4</b>   Stability of <i>cytb<sub>6</sub>f</i> dimer in changing concentrations of HECAMEG .....	79
<b>Figure 3.5</b>   Detergent exchange into tPCCαM.....	80
<b>Figure 3.6</b>   A modified purification of <i>cytb<sub>6</sub>f</i> from spinach to optimise yield.....	82
<b>Figure 3.7</b>   Purification of <i>cytb<sub>6</sub>f</i> from spinach.....	84
<b>Figure 3.8</b>   Purification of plastocyanin from spinach.....	85

<b>Figure 3.9 </b> The catalytic rate of PC reduction by the purified dimeric <i>cytb<sub>6</sub>f</i> complex as determined by stopped-flow absorbance spectroscopy .....	87
<b>Figure 4.1 </b> Negative stain analysis of the <i>cytb<sub>6</sub>f</i> complex purified from <i>S. oleracea</i> .....	90
<b>Figure 4.2 </b> Cryo-EM micrographs of the spinach <i>cytb<sub>6</sub>f</i> complex and calculation of the cryo-EM map resolution .....	92
<b>Figure 4.3 </b> A flowchart for processing of the <i>S. oleracea cytb<sub>6</sub>f</i> cryo-EM map outlining the steps for data processing in RELION.....	95
<b>Figure 4.4 </b> Calculation of the <i>S. oleracea cytb<sub>6</sub>f</i> cryo-EM map global and local resolution .....	96
<b>Figure 4.5 </b> Multiple sequence alignment of <i>cytb<sub>6</sub>f</i> subunits <i>cytf</i> and <i>cytb<sub>6</sub></i> .....	97
<b>Figure 4.6 </b> Multiple sequence alignment of <i>cytb<sub>6</sub>f</i> subunits Rieske ISP, subunit IV, PetG, PetL, PetM and PetN .....	98
<b>Figure 4.7 </b> Ramachandran analysis of the <i>S. oleracea cytb<sub>6</sub>f</i> model.....	101
<b>Figure 4.8 </b> An assessment of the quality of modelled data fit in the cryo-EM map of <i>S. oleracea cytb<sub>6</sub>f</i> .....	103
<b>Figure 4.9 </b> Cryo-EM structure of the <i>S. oleracea cytb<sub>6</sub>f</i> complex.....	107
<b>Figure 4.10 </b> Cryo-EM densities and structural models of polypeptides in the <i>cytb<sub>6</sub>f</i> complex .....	108
<b>Figure 4.11 </b> Cryo-EM densities and structural models of prosthetic groups, lipids and plastoquinone molecules in the <i>cytb<sub>6</sub>f</i> complex .....	110
<b>Figure 4.12 </b> The intermonomer cavity of the <i>S. oleracea cytb<sub>6</sub>f</i> complex .....	113
<b>Figure 4.13 </b> Three native plastoquinone molecules can be modelled in the <i>S. oleracea cytb<sub>6</sub>f</i> complex .....	116
<b>Figure 4.14 </b> The Q <sub>p</sub> sites of <i>cytb<sub>6</sub>c<sub>1</sub></i> and <i>cytb<sub>6</sub>f</i> .....	118
<b>Figure 4.15 </b> The Q <sub>n</sub> sites of <i>cytb<sub>6</sub>c<sub>1</sub></i> and <i>cytb<sub>6</sub>f</i> .....	119
<b>Figure 4.16 </b> Conformational changes in the Q <sub>n</sub> site of the <i>cytb<sub>6</sub>f</i> complex may promote catalysis .....	121
<b>Figure 4.17 </b> An electronic bus-bar lies within the core of the <i>cytb<sub>6</sub>f</i> complex allowing electrons to move both within and between monomers via a bridge formed between the two haem <i>b<sub>p</sub></i> molecules.....	124
<b>Figure 4.18 </b> Conformational alterations in the Chl <i>α</i> phytol chain at the plastoquinol oxidation (Q <sub>p</sub> ) site may gate access to and from the Q <sub>p</sub> site.....	125

<b>Figure 5.1</b>   Comparing the efficacy of HECAMEG and GDN for the selective solubilisation of <i>cytb<sub>6</sub>f</i> from <i>S. oleracea</i> .....	129
<b>Figure 5.2</b>   The purification of <i>cytb<sub>6</sub>f</i> ( <i>petA-strep</i> ) from <i>Synechocystis</i> sp. PCC 6803 thylakoids using Strep-Tactin affinity chromatography .....	131
<b>Figure 5.3</b>   The purification of <i>cytb<sub>6</sub>f</i> ( <i>petA-strep</i> ) from <i>Synechocystis</i> sp. PCC 6803 thylakoids using gel filtration .....	133
<b>Figure 5.4</b>   The catalytic rate of PC reduction by the purified dimeric <i>cytb<sub>6</sub>f</i> complex as determined by stopped-flow absorbance spectroscopy .....	134
<b>Figure 5.5</b>   Negative stain analysis of the <i>cytb<sub>6</sub>f</i> complex purified from <i>Synechocystis</i> sp. PCC 6803 ( <i>petA-strep</i> ) .....	135
<b>Figure 5.6</b>   Initial assessment of cryo-EM micrographs of the <i>Synechocystis</i> sp. PCC 6803 ( <i>petA-strep</i> ) <i>cytb<sub>6</sub>f</i> complex.....	137
<b>Figure 5.7</b>   Automated picking of particles from cryo-EM micrographs of the <i>Synechocystis</i> sp. PCC 6803 ( <i>petA-strep</i> ) <i>cytb<sub>6</sub>f</i> complex.....	138
<b>Figure 5.8</b>   A flowchart for processing of the <i>Synechocystis</i> sp. PCC 6803 ( <i>petA-strep</i> ) <i>cytb<sub>6</sub>f</i> cryo-EM map outlining the steps for data processing in RELION .....	140
<b>Figure 5.9</b>   Cryo-EM micrographs of the <i>Synechocystis</i> sp. PCC 6803 ( <i>petA-strep</i> ) <i>cytb<sub>6</sub>f</i> complex and calculation of the cryo-EM map global and local resolution.....	141
Figure 5.10   Multiple sequence alignment of <i>cytb<sub>6</sub>f</i> subunits <i>cytf</i> , <i>cytb<sub>6</sub></i> , Rieske ISP, subunit IV, PetG, PetL, PetM and PetN .....	145
<b>Figure 5.11</b>   The modelling of Echinenone in the cryo-EM map of <i>Synechocystis</i> sp. PCC 6803 ( <i>petA-strep</i> ) <i>cytb<sub>6</sub>f</i> .....	146
<b>Figure 5.12</b>   Ramachandran analysis of the <i>Synechocystis</i> sp. PCC 6803 ( <i>petA-strep</i> ) <i>cytb<sub>6</sub>f</i> model .....	148
<b>Figure 5.13</b>   An assessment of the quality of modelled data fit in the cryo-EM map of <i>Synechocystis</i> sp. PCC 6803 ( <i>petA-strep</i> ) <i>cytb<sub>6</sub>f</i> .....	152
<b>Figure 5.14</b>   The root-mean-square-deviation (RMSD) of $\alpha$ atoms in the <i>S. oleracea</i> and <i>Synechocystis</i> sp. PCC 6803 ( <i>petA-strep</i> ) <i>cytb<sub>6</sub>f</i> structures .....	154
<b>Figure 5.15</b>   Cryo-EM structure of the <i>Synechocystis</i> sp. PCC 6803 ( <i>petA-strep</i> ) <i>cytb<sub>6</sub>f</i> complex .....	155
<b>Figure 5.16</b>   Cryo-EM densities and structural models of polypeptides in the <i>Synechocystis</i> sp. PCC 6803 ( <i>petA-strep</i> ) <i>cytb<sub>6</sub>f</i> complex .....	156

<b>Figure 5.17</b>   Prosthetic groups, substrate, lipids and hydrocarbons modelled into the <i>Synechocystis</i> sp. PCC 6803 ( <i>petA-strep</i> ) <i>cyt<sub>b6f</sub></i> complex .....	158
<b>Figure 5.18</b>   Cryo-EM densities and structural models of prosthetic groups, lipids and plastoquinone molecules in the <i>cyt<sub>b6f</sub></i> complex .....	159
<b>Figure 5.19</b>   The intermonomer cavity of the <i>Synechocystis</i> sp. PCC 6803 ( <i>petA-strep</i> ) <i>cyt<sub>b6f</sub></i> complex .....	162
<b>Figure 5.20</b>   A native plastoquinone molecule is copurified in the <i>Synechocystis</i> sp. PCC 6803 ( <i>petA-strep</i> ) <i>cyt<sub>b6f</sub></i> complex.....	163
<b>Figure 5.21</b>   Conformations of the Chl <i>a</i> molecule at the plastoquinol oxidation (Q <sub>p</sub> ) site .....	165
<b>Figure 5.22</b>   Conformational differences within the extrinsic domains of the ISP and <i>cyt<sub>f</sub></i> . .....	166
<b>Figure 6.1</b>   The Q <sub>p</sub> sites of <i>cyt<sub>b6f</sub></i> and <i>cyt<sub>b6f</sub></i> .....	169
<b>Figure 6.2</b>   Conformational changes occurring within the extrinsic domains of the ISP in <i>cyt<sub>b6f</sub></i> .....	170
<b>Figure 6.3</b>   Evidence for conformational changes occurring within the extrinsic domains of the ISP in <i>cyt<sub>b6f</sub></i> .....	174
<b>Figure 6.4</b>   Videos showing the 3D-variability analysis (3DVA) of the <i>Synechocystis</i> sp. PCC 6803 ( <i>petA-strep</i> ) <i>cyt<sub>b6f</sub></i> using a full mask.....	180
<b>Figure 6.5</b>   3DVA of the <i>Synechocystis</i> sp. PCC 6803 ( <i>petA-strep</i> ) <i>cyt<sub>b6f</sub></i> using a mask focused around the p-side extrinsic domains .....	182
<b>Figure 6.6</b>   3D-variability analysis (3DVA) of the <i>Synechocystis</i> sp. PCC 6803 ( <i>petA-strep</i> ) <i>cyt<sub>b6f</sub></i> using a mask focused only on the extrinsic luminal domains .....	183
<b>Figure 6.7</b>   Conformational changes occurring within the extrinsic domains of the ISP and <i>cyt<sub>f</sub></i> .....	186

## Tables

<b>Table 1.1</b>   Standard midpoint potentials of redox couples involved in photosynthesis .....	6
<b>Table 1.2</b>   The subunit composition of the <i>cytb<sub>6</sub>f</i> complex.....	12
<b>Table 1.3</b>   A comparison of edge-to-edge cofactor distances (Å) in each half of <i>bc<sub>1</sub></i> from <i>G. gallus</i> .....	25
<b>Table 1.4</b>   A comparison of edge-to-edge cofactor distances (Å) in each half of the <i>b<sub>6</sub>f</i> dimer from different species .....	27
<b>Table 2.1</b>   An outline of the buffers used to prepare <i>S. oleracea</i> thylakoids in section 3.1.1. ....	49
<b>Table 2.2</b>   An outline of the buffers used for the preparation of <i>S. oleracea</i> thylakoids in section 3.7.1. ....	50
<b>Table 2.3</b>   Strains of <i>Synechocystis</i> sp. PCC6803 used in this study. ....	51
<b>Table 2.4</b>   An outline of plasmids used in this study. ....	51
<b>Table 2.5</b>   An outline of stock solutions for media preparation.....	52
<b>Table 2.6</b>   An outline of media used in this study. ....	53
<b>Table 2.7</b>   An outline of buffers used for the preparation of <i>Synechocystis</i> thylakoids in section 5.1. ....	54
<b>Table 2.8</b>   An outline of the detergents used in this study. ....	55
<b>Table 2.9</b>   An outline of sucrose gradient solutions used in section 3.2. ....	56
<b>Table 2.10</b>   An outline of sucrose gradient solutions used in sections 3.4 and 3.5.....	57
<b>Table 2.11</b>   An outline of buffers used for CHT chromatography in sections 3.3 and 3.5. ....	58
<b>Table 2.12</b>   <b>An outline of buffers used for StrepTactin affinity chromatography in section 5.1.2.</b> ....	59
<b>Table 2.13</b>   An outline of buffers used for gel filtration in sections 3.4 and 3.5. ....	60
<b>Table 2.14</b>   An outline of buffers used for gel filtration in section 5.1.3.....	60
<b>Table 2.15</b>   An outline of buffers used for anionic exchange chromatography in sections 3.7.1.....	61
<b>Table 2.16</b>   Buffers used for SDS-PAGE. ....	62
<b>Table 2.17</b>   Buffers used for BN-PAGE.....	63
<b>Table 2.18</b>   Buffers used for western blots. ....	65

<b>Table 2.19</b>   Microscopes used for cryo-EM in this study.....	66
<b>Table 4.1</b>   Cryo-EM data collection, refinement and validation statistics.....	104
<b>Table 4.2</b>   A comparison of edge-to-edge cofactor distances (Å) in each half of the $b_6f$ dimer from different species .....	111
<b>Table 5.1</b>   Cryo-EM data collection, processing, refinement and validation statistics.....	149
<b>Table 5.2</b>   A comparison of edge-to-edge cofactor distances (Å) in each half of the $b_6f$ dimer from different species .....	160
<b>Table 6.1</b>   A comparison of edge-to-edge cofactor distances (Å) in each half of $bc_1$ from various species with and without $Q_p$ inhibitors.....	171
<b>Table 6.2</b>   A comparison of edge-to-edge cofactor distances (Å) in each half of the $b_6f$ dimer from different species with and without $Q_p$ inhibitors .....	173
<b>Table 6.3</b>   A comparison of edge-to-edge cofactor distances (Å) in each half of the $b_6f$ dimer from <i>S. oleracea</i> , <i>Synechocystis</i> sp. PCC 6803 in relation <i>M. laminosus</i> with and without $Q_p$ inhibitors .....	177
<b>Table 6.4</b>   A comparison of edge-to-edge cofactor distances (Å) in the two ‘extreme’ conformations revealed by 3DVA on the <i>Synechocystis</i> sp. PCC 6803 $cytb_6f$ cryo-EM map. ....	184

## Equations

<b>Equation 1</b>   An equation to describe the core process of oxygenic photosynthesis.....	1
<b>Equation 2</b>   An equation to describe the light dependent reactions .....	1
<b>Equation 3</b>   An equation to describe the light independent reactions .....	1
<b>Equation 4</b>   An equation to describe the various factor which determine the rate of electron transfer .....	4
<b>Equation 5</b>   An equation to describe the Q-cycle (full equation).....	20
<b>Equation 6</b>   An equation to describe the Q-cycle (simplified equation) .....	20
<b>Equation 7</b>   An equation to describe the various factors that affect phase contrast in EM images	
<b>Equation 8</b>   Equations to calculate the total Chlorophyll content in in a sample and the ratio of Chl <i>a</i> : Chl <i>b</i> .....	51
<b>Equation 9</b>   An equation to describe the standard cryo-EM image formation model .....	178



## List of abbreviations

AA	antimycin A
AFM	atomic force microscopy
AMY	antimycin (PDB notation)
ATP	adenosine triphosphate
CBB	Calvin-Benson-Bassham
CET	cyclic electron transfer
Chl	Chlorophyll
cryo-EM	cryogenic electron microscopy
CTF	contrast transfer function
Cyt	cytochrome
e <sup>-</sup>	electron
EDTA	ethylenediaminetetraacetic acid disodium salt
$E_m$	redox midpoint potential
EM	electron microscope
EPR	electron paramagnetic resonance
Fd	ferredoxin
FNR	ferredoxin NADP <sup>+</sup> reductase
GDN	glyco-diosgenin
H <sup>+</sup>	proton
HECAMEG	6-O-(n-Heptylcarbamoyl)-Methyl- $\alpha$ -D-Glucopyranoside
ISP	iron-sulphur protein
LET	linear electron transfer
LHC	light harvesting complex
MOAS	methoxyacrylatestilbene

MGDG	monogalactosyldiacalglyceride
NADPH	Nicotinamide adenine dinucleotide phosphate
NDH	NADH dehydrogenase
NMR	nuclear magnetic resonance
NPQ	non-photochemical quenching
NQNO	2-Nonyl-4-hydroxyquinoline N-oxide
PC	plastocyanin
PG	phosphatidylglycerol
PGR	proton gradient regulation
<i>pmf</i>	proton motive force
PQ/PQH <sub>2</sub>	plastoquinone/plastoquinol
PQH <sup>•</sup>	semiplastoquinone
PS	photosystem
QH <sup>•</sup>	semiquinone
Q <sub>n</sub>	plastoquinone reduction site
Q <sub>p</sub>	plastoquinol oxidation site
ROS	reactive oxygen species
STG	stigmatellin
SQDG	sulfoquinovosyl diacylglycerol
tPCC- $\alpha$ -M	4-trans-(4-trans-Propylcyclohexyl)-cyclohexyl $\alpha$ -maltoside
TDS	tridecylstigmatellin
TEM	transmission electron microscope
TMH	transmembrane helix
UQ/UQH <sub>2</sub>	ubiquinone/ubiquinol

“CONGRATULATIONS!  
TODAY IS YOUR DAY.  
YOU'RE OFF TO GREAT PLACES!  
YOU'RE OFF AND AWAY!

YOU HAVE BRAINS IN YOUR HEAD.  
YOU HAVE FEET IN YOUR SHOES  
YOU CAN STEER YOURSELF  
ANY DIRECTION YOU CHOOSE.

YOU'RE ON YOUR OWN. AND YOU KNOW WHAT YOU KNOW.  
AND YOU ARE THE GUY WHO'LL DECIDE WHERE TO GO.”

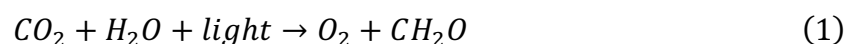
- DR. SUESS, OH THE PLACES YOU'LL GO!

# 1 Introduction

## 1.1 An overview of oxygenic photosynthesis

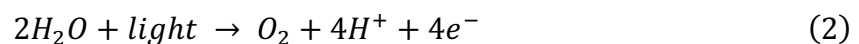
Oxygenic photosynthesis is a fundamental biochemical process which forms the foundation of virtually all life on Earth, providing a primary source of energy within the biosphere as well as supplying atmospheric oxygen crucial for the evolution and sustained existence of complex multicellular life (**Hohmann-Marriott and Blankenship, 2011**). This vital mechanism is carried out by a range of photoautotrophic organisms, including cyanobacteria, algae and plants, all of whom possess highly organised networks of membrane-associated pigment-protein complexes with which they capture solar energy and convert it into biochemical energy (**Johnson, 2016**).

Although the specific details of oxygenic photosynthesis vary in different organisms, the core process can be described by the equation below:

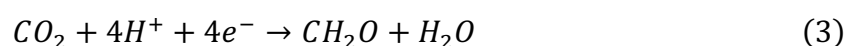


This equation can be subdivided into two sets of reactions: the light-dependent ('light') reactions encompassing the light-induced oxidation of water to electrons ( $e^-$ ), protons ( $H^+$ ) and molecular oxygen ( $O_2$ ); and the light-independent ('dark') reactions, where products from the light-dependent stage are utilised to reduce carbon dioxide ( $CO_2$ ) to carbohydrate ( $CH_2O$ ) via the Calvin-Benson-Bassham (CBB) cycle (**Bassham et al., 1950**). These two sub-reactions can be summarised by the equations shown below (**Johnson, 2016**).

*Light-dependent reactions:*



*Light-independent reactions:*



In plants, the light-dependent and light-independent reactions are localised to specific regions within a specialised photosynthetic organelle known as the chloroplast (**Figure 1.1**).

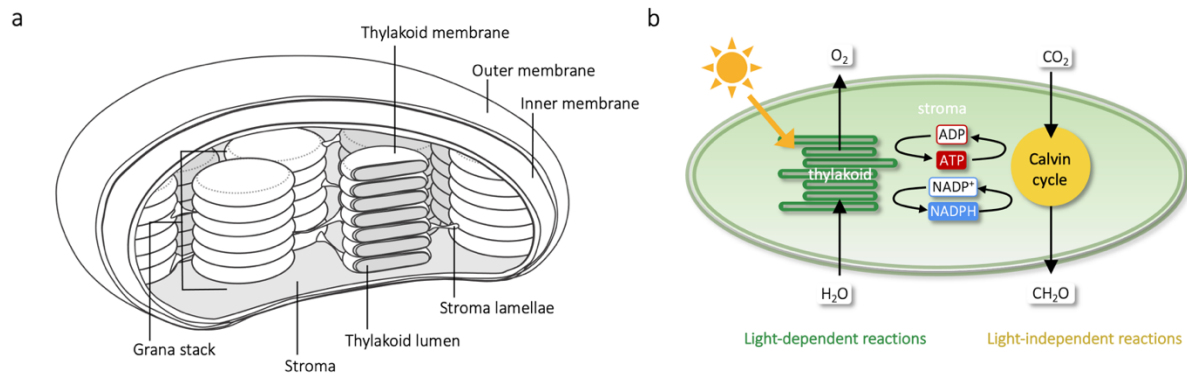


**Figure 1.1 | The site of photosynthesis in plants. a,** A cross sectional view of a chloroplast showing the double membrane envelope which surrounds a complex internal membrane system termed the thylakoid. The thylakoid membrane is subdivided into grana disks, these are connected by intergranal stroma lamellae. Surrounding the thylakoid system is an aqueous solution termed the stroma. **b,** A schematic view of the chloroplast showing how the light-dependent (dark green) and light-independent stages (yellow) of photosynthesis are intimately linked by their respective products. Adapted from **Johnson, 2016**.

The chloroplast comprises a double membrane envelope surrounding a continuous internal membrane structure termed the thylakoid membrane, this sits within an aqueous environment called the stroma. The stroma contains the enzymes that catalyse the light-independent reactions whereas the thylakoid membrane is the site of the light-dependent reactions and contains all of the photosynthetic machinery necessary to capture, convert and store light energy in a stable, usable form (e.g. energy storage molecules such as adenosine triphosphate (ATP) and nicotinamide adenine dinucleotide phosphate (NADPH)) (**Figure 1.2**) (**Johnson, 2016**).

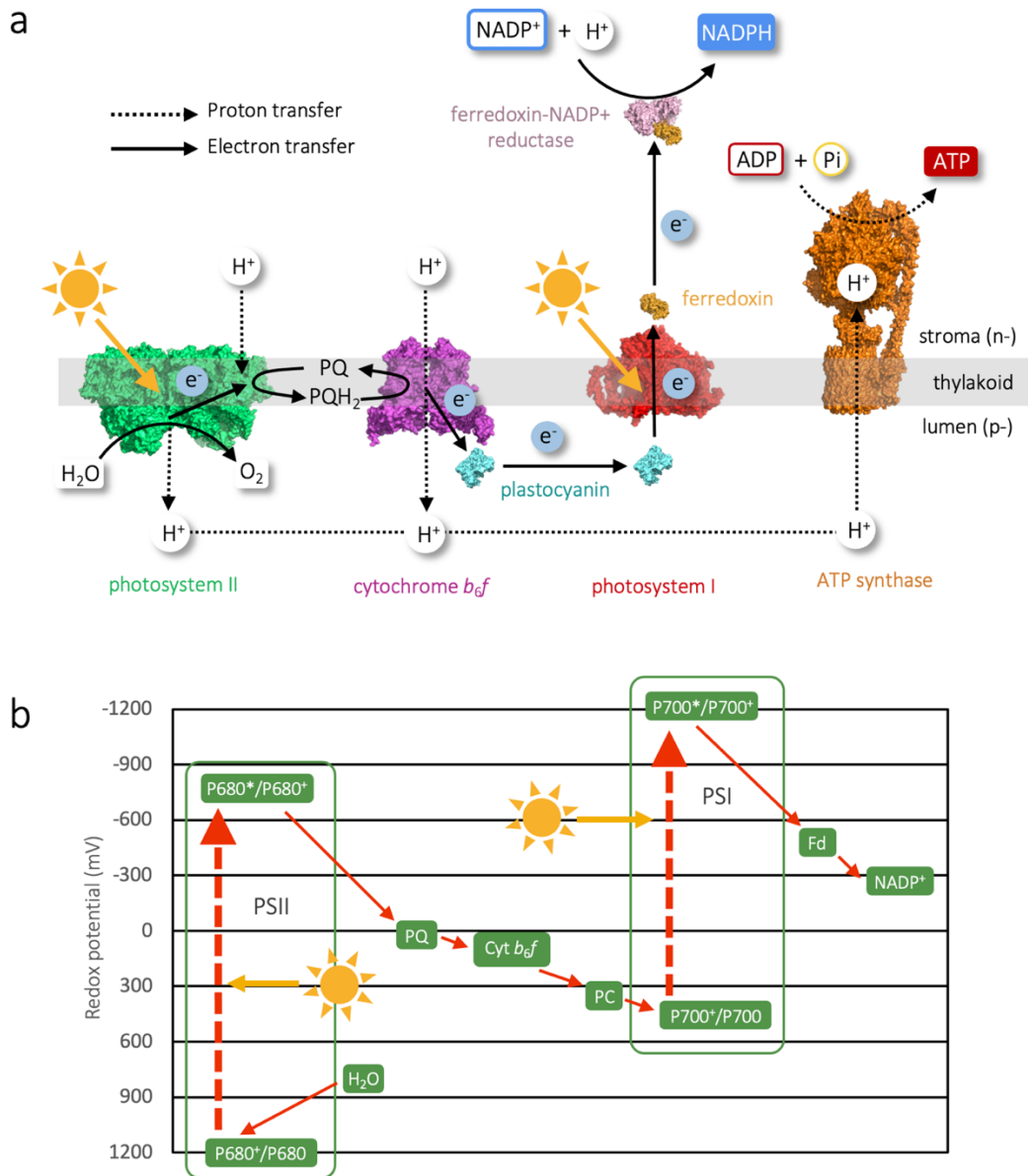


**Figure 1.2 | The linear electron transfer chain of photosynthesis. a**, A schematic representation of the linear electron transfer chain (solid black line) showing the electron flow from water to  $\text{NADP}^+$  to form NADPH. Components involved in electron transfer are coloured as follows: photosystem II (PSII, green), cytochrome  $b_6/f$  ( $\text{cyt}_{b_6/f}$ , purple), plastocyanin (Pc, cyan), photosystem I (PSI, red), ferredoxin (Fd, light orange), the ferredoxin- $\text{NADP}^+$  reductase complex (FNR, pink). The proton gradient formed as part of the LET reactions is used by ATP synthase (orange) to make ATP. **b**, the Z-scheme of photosynthetic electron transfer shows how two inputs of light energy facilitate electron transfer from water to  $\text{NADP}^+$ . Adapted from **Johnson, 2016**.

## 1.2 Light-dependent electron transfer in the chloroplast thylakoid

### 1.2.1 Principles of biological electron transfer reactions

In all organisms, biological energy conservation relies on ‘pushing’ electrons between various electron donors and electron acceptors. In nature, these primarily take the form of redox-active cofactors including organic molecules (such as nicotinamide adenine dinucleotide phosphate (NADPH), quinones etc.) and inorganic metallocofactors containing transition metals (e.g. Fe, Cu, Mn etc.).

The rate of electron transfer ( $k_{et}$ ) is reliant on three principal components including the edge-to-edge distance between the donor and acceptor species ( $R$ , the strength of coupling between electron donor/acceptor pairs decreases exponentially with distance), the driver ( $\Delta G$ , this is proportional to the difference in redox midpoint potential between the donor and acceptor species) and the reorganisation energy ( $\lambda$ ) required to reorganise the geometry of the pre-electron-transfer system to resemble the post-electron-transfer product.

The relationship between these components can be described by the following equation:

$$\log_{10}k_{et} = 13 - 0.6(R - 3.6) - \frac{3.1(\Delta G + \lambda)^2}{\lambda} \quad (4)$$

In biological systems, the dominant factor that affects electron transfer rate is distance between redox active cofactors (**Marcus and Sutin, 1985; Moser et al., 1992, 2000; Page et al., 1999**). For physiologically relevant electron rates (i.e. milliseconds or less), the edge-to-edge distance between cofactors generally does not exceed 14 Å (**Page et al., 1999**).

In biological systems, electron transfer potentials are generally discussed in terms of redox midpoint potential ( $E_m$ ) where a high redox midpoint potential ( $E_m$  is positive) indicates a greater affinity for electrons (i.e. the species is a strong oxidant, it has a greater tendency to gain electrons from donor species and become reduced). Conversely, a species with a low redox midpoint potential ( $E_m$  is negative) has a lower affinity for electrons with a greater tendency to lose electrons to acceptor species and become oxidised. Redox potential also varies with concentration ratio of [ox]/[red] forms and with pH (e.g. for PQ/PQH<sub>2</sub> the  $E_m$  varies by around – 60 mV per pH unit).

While in respiration electrons are commonly transferred from NADH ( $E_m = -320$  mV; a strong reductant) to  $O_2$  ( $E_m = +820$  mV); a strong oxidising agent), the opposite is true in the case of photosynthesis where an input of light energy is required to drive electron flow from water ( $E_m = +820$  mV) to  $NADP^+$  ( $E_m = -320$  mV).

In photosynthesis, redox active cofactors involved in the light-dependent electron transfer reactions are primarily bound to large integral membrane proteins (e.g. light harvesting complexes (LHC) I and II; photosystems (PS) I and II; cytochrome (cyt) *b<sub>6</sub>f* etc.). Since these large stationary proteins are often relatively far apart, smaller mobile electron carriers (such as plastoquinone/ol (PQ/PQH<sub>2</sub>); plastocyanin (PC) and ferredoxin (Fd)) are also present to facilitate electron transfer across large distances.

The redox midpoint potentials of many biological important redox couples involved in photosynthesis are shown in **Table 1.1**.



**Table 1.1| Standard midpoint potentials of redox couples involved in photosynthesis.** <sup>a</sup> Some cofactors are omitted for simplicity. <sup>b</sup> *n* is the number of electrons transferred. <sup>c</sup> Midpoint potentials ( $E_m$ ) shown for cofactors are from *S. oleracea* measured at pH 7 (Corrado et al., 1996; Hope, 1993; Kirchhoff et al., 2004). Midpoint potentials for other molecules are standard midpoint potentials measured at pH 7 as referenced in (Berg et al., 2015). <sup>d</sup> Midpoint redox potential by the addition of axial ligands (e.g. CO and quinone analogues) due to high-spin, pentacoordinate character (Alric et al., 2005a). <sup>e</sup> Redox potential changes when bound to PSI.

Redox couple	<i>n</i> <sup>b</sup>	$E_m$ (mV) <sup>c</sup>
½ O <sub>2</sub> /H <sub>2</sub> O	2	+ 820
NADP <sup>+</sup> /NADPH	1	- 320
O <sub>2</sub> /O <sub>2</sub> <sup>-</sup>	1	- 160
<b>PSII</b>		
P680 <sup>+</sup> /P680*	1	+ 1200
P680 <sup>+</sup> /P680	1	- 850
<b>Plastoquinone</b>		
PQ/PQH <sub>2</sub>	2	+ 100
PQH <sup>+</sup> /PQH <sub>2</sub>	1	+ 480
PQ/PQ <sup>-</sup>	1	- 280
<b>Cytb<sub>6</sub>f</b>		
2Fe-2S <sub>(ox)}/2Fe-2S<sub>(red)}</sub></sub>	1	+ 310
Haem <i>f</i> <sub>(ox)}/haem <i>f</i><sub>(red)}</sub></sub>	1	+ 355
Haem <i>b<sub>p</sub></i> <sub>(ox)}/haem <i>b<sub>p</sub></i><sub>(red)}</sub></sub>	1	- 150
Haem <i>b<sub>n</sub></i> <sub>(ox)}/haem <i>b<sub>n</sub></i><sub>(red)}</sub></sub>	1	- 85
Haem <i>c<sub>n</sub></i> <sub>(ox)}/haem <i>c<sub>n</sub></i><sub>(red)}</sub></sub>	?	+ 100/- 150 <sup>d</sup>
<b>Plastocyanin</b>		
Cu <sup>+</sup> /Cu <sup>2+</sup>	1	+ 370/+ 420 <sup>e</sup>
<b>PSI</b>		
P700 <sup>+</sup> /P700	1	+ 480
P700 <sup>+</sup> /P700*	1	- 1200
<b>Ferredoxin</b>		
2Fe-2S <sub>(ox)}/2Fe-2S<sub>(red)}</sub></sub>	1	- 450
<b>Ferredoxin-NADP<sup>+</sup> reductase</b>		
FAD/FADH <sub>2</sub>		- 342

### 1.2.2 Linear electron transfer (LET) in the chloroplast thylakoid membrane

The primary route for electron transfer from water ( $E_m = + 820$  mV) to  $\text{NADP}^+$  ( $E_m = - 320$  mV) in the chloroplast thylakoid (**Figure 1.2a**) begins with the absorption of solar energy by a series of protein-bound pigment molecules (e.g. chlorophyll *a* (Chl *a*), chlorophyll *b* (Chl *b*) and carotenoids) contained within a large photosystem known as photosystem II (PSII). Within the reaction centre of PSII, absorbed energy is used to power the extremely endergonic oxidation of water; this results in the generation of molecular oxygen ( $\text{O}_2$ ), electrons ( $e^-$ ) and protons ( $\text{H}^+$ ).

While the oxygen is released into the atmosphere and liberated protons are released to the lumenal (electrochemically positive, p-) side of the membrane where they contribute towards a proton motive force (*pmf*), resultant electrons are used to reduce the mobile electron carrier molecule, plastoquinone. Reduced plastoquinol shuttles the acquired electrons to the next thylakoid-embedded membrane protein, *cytb<sub>6</sub>f* (**Figure 1.2**).

*Cytb<sub>6</sub>f* catalyses the oxidation of  $\text{PQH}_2$  to PQ and reduces the  $\text{Cu}^{2+}$  centre of a small soluble electron carrier protein, plastocyanin (PC); this process is coupled to a proton translocation mechanism which further contributes to the *pmf* required for ATP synthesis by the fourth membrane complex, ATP synthase. Following reduction by *cytb<sub>6</sub>f*, reduced PC diffuses to the photosystem I complex taking the acquired electron with it.

At PSI, a second input of light energy promotes the oxidation of PC and reduction of the iron-sulphur centre of a soluble electron carrier, ferredoxin (Fd). Fd is then utilised by the enzyme ferredoxin- $\text{NADP}^+$  reductase (FNR) to reduce  $\text{NADP}^+$  ( $E_m = - 320$  mV) to NADPH providing a reducing equivalent for downstream photosynthetic reactions (**Johnson, 2016**). This pathway of electron transfer from PSII to PSI via *cytb<sub>6</sub>f* is known as the linear electron transfer chain (LET).

### 1.2.3 Cyclic electron transfer (CET) provides a means to fine tune photosynthetic output

As mentioned in **section 1.1**, the light-dependent and light independent reactions are intimately linked both by their respective products (e.g. NADPH/  $\text{NADP}^+$  and ATP/ADP) and in terms of their regulation (**Foyer et al., 1990; Horton, 1985; Kramer and Evans, 2011; Kramer**

**et al., 2004**). In principle, the light-independent reactions in plants consume ATP/NADPH in a ratio of 1.5:1, with 9 ATP and 6 NADPH required for the complete reduction of CO<sub>2</sub>. Despite this demand, biochemical and structural studies of the ATP synthase complex from *S. oleracea* suggest that the linear electron transfer (LET) pathway only produces ATP and NADPH in a ratio of 1.28 : 1 (**Hahn et al., 2018; Ort and Izawa, 1974; Seelert et al., 2000**). Given the rapid turnover of ATP and NADPH, it is essential that any imbalance in the ratio of ATP/NADPH be rapidly rectified for the correct functioning of photosynthesis. In plants, the primary mechanism to supplement ATP and correct the ratio between these energy storage molecules appears to be an alternate electron transfer pathway known as cyclic electron transfer (CET) (**Munekage et al., 2004**).

While LET involves the four membrane protein complexes (PSII, *cytb<sub>6</sub>f*, PSI, ATP synthase) acting in series alongside various electron carrier molecules (PQ, PC, Fd, FNR etc.) to produce NADPH and ATP, the so-called cyclic electron transfer (CET) pathway takes a different route. During CET, electrons are reinjected back into the PQ/PQH<sub>2</sub> pool from reduced Fd forming a cyclic flow of electrons around *cytb<sub>6</sub>f* and PSI. This alternative electron transfer route allows proton movements and subsequent ATP synthesis without any net NADPH formation (**Figure 1.3**) (**Johnson, 2011; Yamori and Shikanai, 2016**).

By controlling the balance between LET and CET, plants can fine tune their production of energy storage molecules to meet the needs of both the light-independent reactions and additional metabolic processes in the cell requiring varying levels of ATP and NADPH (**Horton, 1985; Kramer and Evans, 2011; Kramer et al., 2004**).

In addition to playing an essential role in supplementing ATP production, it has also been demonstrated that the pH gradient ( $\Delta$ pH) generated by CET plays a key role in regulating photoprotective mechanisms such as non-photochemical quenching (NPQ) and photosynthetic control. These mechanisms are essential to the ability of higher plants to adapt to environmental stresses such as drought, extreme temperatures and high light.

In plants, two major routes of Fd-dependent CET exist, the PGRL1/PGR5-dependent pathway (CET1) and the NDH-dependent pathway (involving photosynthetic Complex I) (CET2) (**Johnson, 2011; Yamori and Shikanai, 2016**). Despite numerous studies, the exact

mechanism involved in CET1 remains unclear. It has been suggested that CET1 may involve transfer of electrons from an Fd–FNR complex directly to the n-side PQ binding reduction site ( $Q_n$ ) of *cytb<sub>6</sub>f* (Buchert et al., 2020; Joliot and Johnson, 2011; Nandha et al., 2007) via an unusual high-spin c-type haem (haem  $c_n$ ) located near the stromal (p-) side of the *b<sub>6</sub>f* complex (Figure 1.3) (Kurusu et al., 2003; Stroebel et al., 2003).

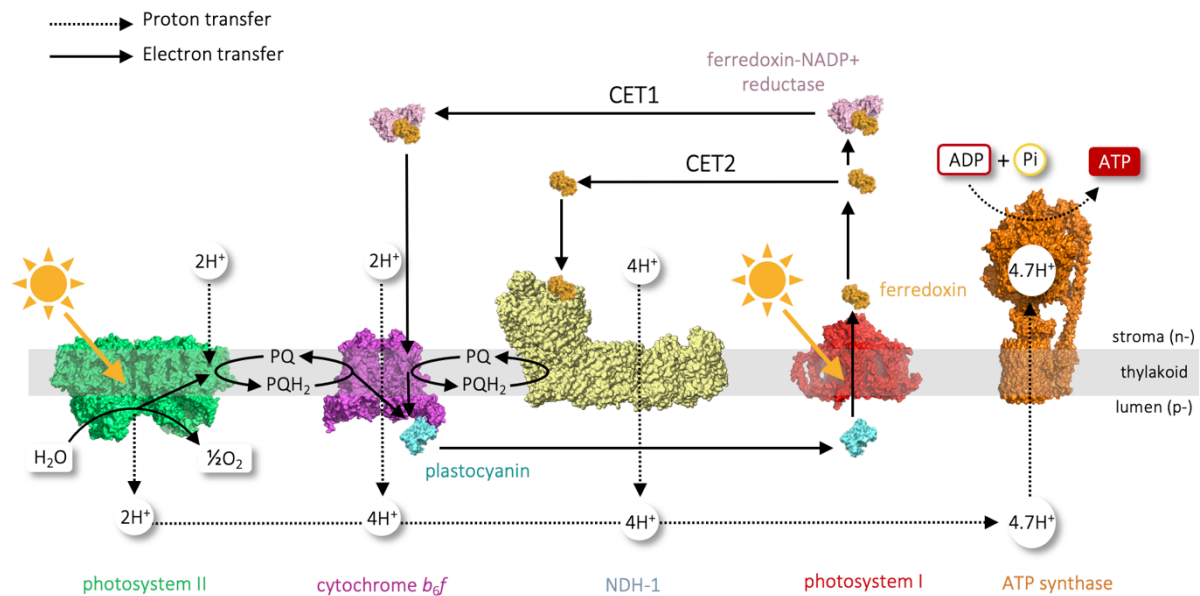


**Figure 1.3| The photosynthetic cyclic electron transfer chain.** A schematic representation of the photosynthetic electron transfer chain the two proposed cyclic routes (solid black line) routes to reinject electrons from Fd back into the electron transfer chain. The CET1 pathway comprises the Fd-FNR complex, *cytb<sub>6</sub>f*, Pc, PSI and ATP synthase; the CET2 pathway comprises the NADH dehydrogenase-like complex 1 (NDH-1, yellow), *cytb<sub>6</sub>f*, Pc, PSI and ATP synthase. The position of the lipid bilayer that separates the stromal (n-) and luminal (p-) sides of the membrane is indicated by a grey stripe and components are coloured as in Figure 1.2. Black dotted arrows indicate proton transfers while electron transfer is indicated by a solid black line.  $4.7 H^+$  are required per ATP synthesized by the ATP synthase.

### 1.3 The *cyt<sub>b</sub><sub>6</sub>f* complex: orchestrator of electron transfer

Central to both the linear and cyclic electron transfer mechanisms is the *cyt<sub>b</sub><sub>6</sub>f* complex, a multi-subunit heterooligomeric complex which connects elements of the electron transfer chain through the oxidation of lipophilic PQH<sub>2</sub> and reduction of soluble PC (**Figure 1.2** and **Figure 1.3**) (**Cramer and Kallas, 2016**). Electron transfers within the complex are coupled to proton translocating mechanism from the stromal (electrochemically negative, n-) side of the thylakoid to lumenal (electrochemically positive, p-) side in a mechanism similar to mitochondrial (complex III) and bacterial (*cyt<sub>b</sub><sub>c</sub><sub>1</sub>*) respiratory complexes (**Berry et al., 2000; Cramer and Kallas, 2016**). This mechanism, termed the modified Q-cycle, contributes to the generation of the *pmf* necessary for ATP synthesis (**Crofts and Meinhardt, 1982; Crofts et al., 1983a; Mitchell, 1975a**).

#### 1.3.1 The structure of the *cyt<sub>b</sub><sub>6</sub>f* complex

A number of structural studies have been carried out on the *cyt<sub>b</sub><sub>6</sub>f* complex from various species including the prokaryotic filamentous cyanobacteria *Mastigocladus laminosus* (**Hasan et al., 2013b, 2013a, 2014; Kurisu et al., 2003; Yamashita et al., 2007; Yan et al., 2006**) and *Nostoc sp.* PCC 7120 (hereafter *Nostoc*) (**Baniulis et al., 2009; Hasan and Cramer, 2014a; Hasan et al., 2013a**) and the eukaryotic unicellular green alga *Chlamydomonas reinhardtii* (**Stroebel et al., 2003**). These structures show that *cyt<sub>b</sub><sub>6</sub>f* is a functional dimer of ~ 220 kDa with each multi-subunit monomeric unit encompassing four large core polypeptide subunits: cytochrome *f* (*cyt<sub>f</sub>*; PetA), cytochrome *b<sub>6</sub>* (*cyt<sub>b</sub><sub>6</sub>*; PetB), the Rieske iron-sulphur protein (ISP, PetC) and subunit IV (subIV, PetD), these are surrounded by four small, peripheral subunits (PetG, L, M and N) (**Figure 1.4**). Further details for each subunit including molecular weight, their respective cofactors etc. are provided in **Table 1.2**.

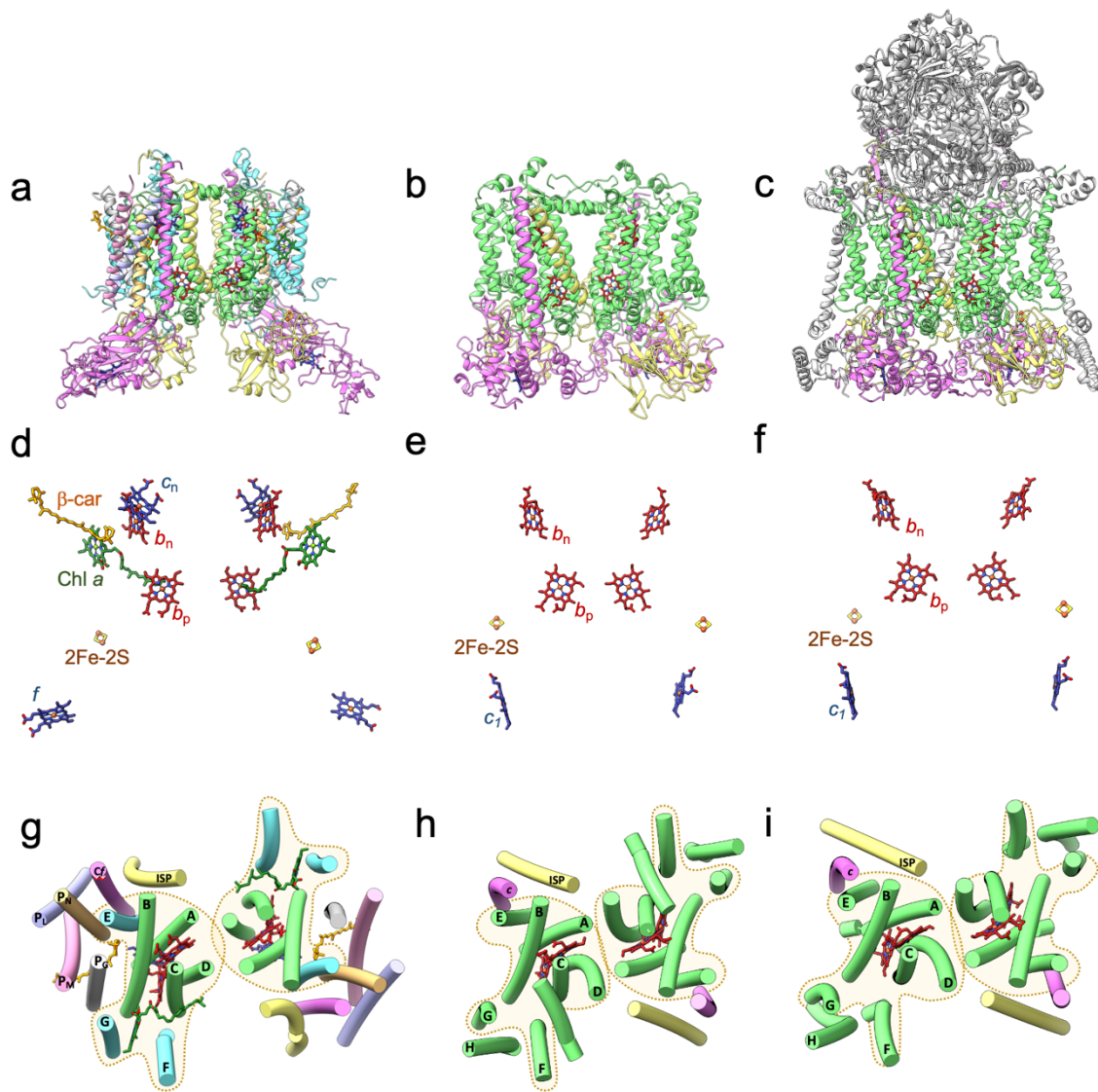


**Figure 1.4 | The similarities and differences between the cytochrome  $b_6f$  and  $b_1$  complexes.** a-c, the polypeptide composition of: **a**, the  $cytb_6f$  complex (*Nostoc* sp. PCC 7120, 4H44 (Hasan et al., 2013a)) coloured with  $cytb_6$  (green),  $cytf$  (magenta), the ISP (yellow), subIV (cyan), PetG (grey), PetM (pink), PetN (pale orange) and PetL (pale purple); **b**, the bacterial  $cytb_1$  complex (*Rhodobacter sphaeroides*, 2QJP (Esser et al., 2008)) coloured with the ISP (yellow),  $cytb$  (green) and  $cytc_1$  (magenta); **c**, the mitochondrial  $cytb_1$  complex (*M. musculus*, 3CX5 (Solmaz and Hunte, 2008)) coloured with the ISP (yellow),  $cytb$  (green),  $cytc_1$  (magenta) and additional peripheral subunits (grey). **d-f**, the global arrangements of prosthetic groups within complexes shown in panels a-c with  $c$ -type haems ( $f$ ,  $c_n$  and  $c_1$ ; dark blue),  $b$ -type haems ( $b_p$  and  $b_n$ , red), Chl  $a$  (dark green),  $\beta$ -carotene ( $\beta$ -car - orange) and the 2Fe-2S cluster (S coloured yellow and Fe coloured red-orange). **g-i**, the arrangement of TM helices within complexes shown in panels a-c viewed perpendicular to the membrane plane from the p-side

of the membrane (extrinsic domains, loops and additional non-conserved subunits in the  $bc_1$  complexes are not shown for clarity).

**Table 1.2 | The subunit composition of the *cyt<sub>b</sub>f* complex.** <sup>a</sup> Based on sequence minus signal peptides, Uniprot IDs are shown in brackets below each value. <sup>b</sup> Residues numbered according to the *Nostoc sp.* PCC 7120 structure (PDB ID: 4H44) (Hasan et al., 2013a).

Subunit	Gene	Molecular Weight (kDa) <sup>a</sup>				Associated Cofactor(s)
		<i>S. oleracea</i>	<i>C. reinhardtii</i>	<i>M. lamosus</i>	<i>Nostoc</i>	
<b>Cyt <i>f</i></b>	<i>petA</i>	31.32 (P16013)	31.25 (P23577)	32.30 (P83793)	31.15 (Q93SW9)	<i>c</i> -type haem ( <i>f</i> )
<b>Cyt <i>b<sub>6</sub></i></b>	<i>petB</i>	24.17 (P00165)	24.17 (Q00471)	24.23 (P83791)	24.27 (P0A384)	<i>b</i> -type haems ( <i>b<sub>p</sub></i> and <i>b<sub>n</sub></i> )
<b>ISP</b>	<i>petC</i>	18.94 (P08980)	18.40 (P49728)	19.40 (P83794)	19.20 (Q93SX0)	2Fe-2S cluster
<b>SubIV</b>	<i>petD</i>	17.45 (P00166)	17.44 (P23230)	17.67 (P83792)	17.54 (Q93SX1)	-
<b>PetL</b>	<i>petL</i>	3.45 (Q9M3L0)	4.88 (P50369)	3.50 (P83795)	3.25 (Q8YVQ2)	-
<b>PetM</b>	<i>petM</i>	3.77 (P80883)	4.04 (Q42496)	3.84 (P83796)	3.55 (P0A3Y1)	-
<b>PetG</b>	<i>petG</i>	4.17 (P69461)	3.98 (Q08362)	4.02 (P83797)	4.00 (P58246)	-
<b>PetN</b>	<i>petN</i>	3.17 (P61045)	3.73 (P0C1D4)	3.28 (P83798)	3.23 (P61048)	-

Cofactor	Ligation <sup>b</sup>	Covalent bonds
<b><i>c</i>-type haems</b>		
haem <i>f</i>	Y1/H26 (cyt <i>f</i> )	C22/C25 (cyt <i>f</i> )
haem <i>c<sub>n</sub></i>	H <sub>2</sub> O	C35 (cyt <i>b<sub>6</sub></i> )
<b><i>b</i>-type haems</b>		
haem <i>b<sub>p</sub></i>	H86/H187 (cyt <i>b<sub>6</sub></i> )	-
haem <i>b<sub>n</sub></i>	H100/H202 (cyt <i>b<sub>6</sub></i> )	-
<b>2Fe-2S</b>	C108/H110/C126/H120 (ISP)	-
<b>β-carotene</b>	-	-
<b>chlorophyll <i>a</i></b>	-	-

At its core, the *cytb<sub>6</sub>f* displays a strong similarity to the respiratory *cytbc<sub>1</sub>* complex (complex III, coenzyme Q : cytc oxidoreductase, *cytbc<sub>1</sub>*), a quinol-cytc oxidoreductase found in mitochondria and anoxygenic photosynthetic bacteria (**Cramer et al., 2011; Esser et al., 2008; Malkin, 1992; Xia et al., 1997; Zhang et al., 1998**). Both *cytbc* complexes form a central four helix bundle (A-D) to house their core redox components (**Figure 1.4**). In *cytb<sub>6</sub>f*, this four-helix bundle forms a part of the *cytb<sub>6</sub>* subunit which binds the two highly conserved *b*-type haems common to both cytochrome complexes (haems *b<sub>n</sub>* and *b<sub>p</sub>*) as well as a single *c'* (high spin)-type haem unique to *cytb<sub>6</sub>f* (haem *c<sub>n</sub>*) (**Figure 1.4**). Surrounding this central helical structure are several additional transmembrane helices (TMH); in *cytb<sub>6</sub>f* these include three helices from subIV (E-G), four from each of the small peripheral subunits (PetG, L, M and N) and two single helices which serve as a tether for the two membrane extrinsic subunits (*cytf* and the ISP) (**Figure 1.4**). On the p-side of the complex, the soluble portions of these latter two subunits protrude into the thylakoid lumen with the long  $\beta$ -sheet rich element of *cytf* extending like an arm around the smaller, globular head of the ISP (**Figure 1.4**). Encompassed within these two soluble domains are the final two core components of the redox-active cofactors: the 2Fe-2S cluster (ISP) and the *c*-type haem *f* (*'frons'* which is latin for 'leaf'; *cytf*).

In both *cytb<sub>6</sub>f* and *cytbc<sub>1</sub>*, the overall structure comprises two monomeric units interlocked by domain swapping of their p-side extrinsic ISP domains (**Baniulis et al., 2009; Hasan and Cramer, 2014a; Hasan et al., 2013b, 2013a, 2014; Kurisu et al., 2003; Stroebel et al., 2003; Yamashita et al., 2007; Yan et al., 2006**). This provides stability through the interlocked domain swapped regions as well as stabilising interactions between the core membrane embedded subunits at the monomer-monomer interface (*subIV* and *cytb<sub>6</sub>* in *b<sub>6</sub>f*). In *cytb<sub>6</sub>f*, additional stabilisation of the dimeric structure is also provided by protein-lipid interactions, as evidenced through various biochemical and structural studies (**Breyton et al., 1997; Cramer and Zhang, 2006; Hasan and Cramer, 2014b; Hasan et al., 2011, 2013c; Pierre et al., 1995; Zhang et al., 2003**).

At the heart of both *cytb<sub>6</sub>f* and *cytbc<sub>1</sub>* lies a large, protein-free intermonomer cavity formed between the interface of the two monomeric units. In *cytb<sub>6</sub>f*, this cavity is considered to provide a space where an internal pool of PQH<sub>2</sub>/PQ molecules may be sequestered (**Baniulis**



et al., 2009; Kurisu et al., 2003; Stroebel et al., 2003). The presence of this internal source of substrate may be beneficial to the complex and provide a means of enhancing catalysis by increasing the rate of substrate exchange between the p-side PQH<sub>2</sub> oxidation site (Q<sub>p</sub>) and the n-side PQ reduction (Q<sub>n</sub>) sites in neighbouring monomers (Baniulis et al., 2008; Cramer et al., 2006, 2011; Kurisu et al., 2003).

### 1.3.2 Structural similarities between the *cytb<sub>6</sub>f* and *bc<sub>1</sub>* complexes

Whilst there is similarity both structurally and functionally between the *cytbc<sub>1</sub>* and *b<sub>6</sub>f* complexes, these similarities decrease significantly away from the core of the complexes.

Both *cytb<sub>6</sub>f* and *bc<sub>1</sub>* have a variety of additional subunits within their polytopic and exterior domains which have no reciprocal counterparts (Figure 1.4). In *cytb<sub>6</sub>f*, an additional four unique subunits (PetG, L, M and N) are present, each comprising a single TMH; together these form a hydrophobic 'picket fence' around the core of the structure (Cramer et al., 2006; Stroebel et al., 2003). While these four additional *cytb<sub>6</sub>f* subunits appear to be conserved across all species, it is observed that several species-specific subunits may also be present such as PetP in the cyanobacterial *cytb<sub>6</sub>f* (Volkmer et al., 2007) and PetO (Hamel et al., 2000) in *Chlamydomonas reinhardtii*. The exact function of additional species-specific subunits is currently unclear however it is possible they may have a role in regulation of cyclic electron flow in cyanobacteria and green algae respectively.

Another significant difference between the two complexes is found in the extrinsic domain of the *c*-type haem containing subunit on the p-side of each complex. While in *cytb<sub>6</sub>f* this position is occupied by a large membrane tethered  $\beta$ -sheet rich protein (*cytf*) the counterpart in *cytbc<sub>1</sub>* is a sequentially unrelated  $\alpha$ -helical protein (*cytc<sub>1</sub>*). Both subunits are similarly anchored to the core of their respective complexes by a single TMH (Hasan and Cramer, 2012; Martinez et al., 1994). Despite the dissimilarity of these two subunits in terms of their sequence and overall architecture, both proteins fulfil the same role in their respective complexes by providing a covalently bound *c*-type haem to function as an electron acceptor to the 2Fe-2S cluster of the ISP. In this interesting example of convergent evolution (Martinez et al., 1994), the only point of similarity between these two proteins is the conserved Cys-X-X-Cys-His motif which coordinates the *c*-type haem in each complex. Additionally, both

complexes also reduce a transiently bound soluble electron carrier protein (cytc or cytc<sub>2</sub> in cytb<sub>c1</sub> and PC in cytb<sub>6f</sub>) on the p-side of their respective membranes.

In addition to these substantial differences in the polypeptide architecture of the two complexes, further disparity can also be found in their respective prosthetic groups. While the functionally essential redox prosthetic groups are highly conserved in both structures, cytb<sub>6f</sub> has 2 additional pigment molecules not present in cytb<sub>c1</sub>, these comprise a Chl *a* and a carotenoid molecule ( $\beta$ -carotene or echinenone depending on species) (Cramer et al., 2011; Huang et al., 1994; Pierre et al., 1997; Zhang et al., 1999). The potential role for these two pigment molecules in the cytb<sub>6f</sub> complex has been a topic of much debate with various roles in photoprotection, super complex formation, signalling and redox-gating having been suggested over the years (Hasan et al., 2014; Iwai et al., 2010; Kurisu et al., 2003; Rebeiz et al., 2010; Stroebel et al., 2003; Zhang et al., 1999).

The final and perhaps most surprising feature that sets cytb<sub>6f</sub> apart from the cytb<sub>c1</sub> complexes is the addition of a second *c*-type haem identified through a combination of structural (Kurisu et al., 2003; Stroebel et al., 2003) and biochemical studies (Berry and Trumpower, 1987; Hurt and Hauska, 1981; Joliot and Joliot, 1988; Lavalette et al., 2008; Lavergne, 1983; Whitelegge et al., 2002).

Prior to structural study, this additional component (characterised by its peak at  $\sim 425$  nm), initially assigned as carrier 'G' was found to have several interesting properties which added further intrigue:

- i) The spectral characteristics of 'G' were comparable to those of a *c'*-type (high-spin) haem found in some species of photosynthetic bacteria (Joliot and Joliot, 1988; Lavergne, 1983).
- ii) The spectral features characteristic of 'G' appeared concomitantly with haem *b* oxidation and with the decay in membrane potential.
- iii) Rapid electron transfer (100  $\mu$ s) between 'G' and haem *b<sub>n</sub>* indicates the new component must be tightly bound to the cytb<sub>6f</sub> complex within close proximity to haem *b<sub>n</sub>* on the stromal side of the membrane.
- iv) The redox potential of 'G' was  $\sim 30$  mV higher than that of haem *b<sub>n</sub>*.

- v) The equilibrium constant between 'G' and haem  $b_n$  depends on membrane potential (**Lavergne, 1983**).
- vi) The redox potential of 'G' could be modulated by the addition of axial ligands of haems (e.g. CO) (**Cramer and Kallas, 2016; Joliot and Joliot, 1988**).

The first two structural studies of the *cytb<sub>6f</sub>* complex (in *M. lamosus* (**Kurisu et al., 2003**) and *C. reinhardtii* (**Stroebel et al., 2003**) revealed an unexpected large flat region of density with two lateral extensions positioned between the haem  $b_n$  molecule and the intermonomer cavity in a location corresponding the Q<sub>n</sub> site in *cytb<sub>c1</sub>* (**Kurisu et al., 2003; Stroebel et al., 2003**). Given the shape, size, strong central density and other porphyrin-like characteristics, it was determined that the additional density likely corresponded to a haem molecule. These observations coupled with previous biochemical evidence for an additional *c'*-type haem led to the assignment of this density as haem  $c_n$  (**Kurisu et al., 2003; Stroebel et al., 2003**).

Further analyses of haem  $c_n$  revealed it to have a variety of highly unusual characteristics. Firstly, the C2 vinyl group of haem  $c_n$  is covalently bonded to the *cytb<sub>6</sub>* subunit of *b<sub>6f</sub>* through a single thioether linkage to the sulphur atom of a nearby cysteine residue (Cys35) (**Figure 1.5**). This observation is noteworthy in two ways:

- i) Cys35 is not part of a highly conserved Cys-X-X-Cys-His binding motif characteristic of *c*-type haems.
- ii) *c*-type haems are usually covalently bonded to polypeptides through two thioether linkages as opposed to just one.

A second point of difference lies in the ligation of the central Fe<sup>2+</sup> atom of the haem  $c_n$  porphyrin ring. While the central Fe<sup>2+</sup> of the other haems in *cytb<sub>6f</sub>* are found in a hexa-coordinated state with the two axial ligands provided by amino acid residues, the Fe<sup>2+</sup> in haem  $c_n$  has only a single axial ligand making it only penta-coordinated. Accordingly, haem  $c_n$  can be classed as a *c'*-type (high-spin) haem; this observation is further supported by electron paramagnetic resonance (EPR) studies which suggest haem  $c_n$  has high-spin characteristics (**Schünemann et al., 1999**). Further, unlike other haems, the axial ligand to haem  $c_n$  is not provided by an amino acid residue but by a small molecule attributed as a H<sub>2</sub>O (**Figure 1.5**). The assigned H<sub>2</sub>O molecule which coordinates the central Fe<sup>2+</sup> of haem  $c_n$  also functions as a

bridge to the nearby haem  $b_n$  molecule (Figure 1.5). Such a close proximity ( $\sim 4.7 \text{ \AA}$ ) and physical bridging of these two haems indicates the potential for efficient electron transfer between the two cofactors (Joliot and Joliot, 1988; Kurisu et al., 2003; Lavergne, 1983; Stroebel et al., 2003).

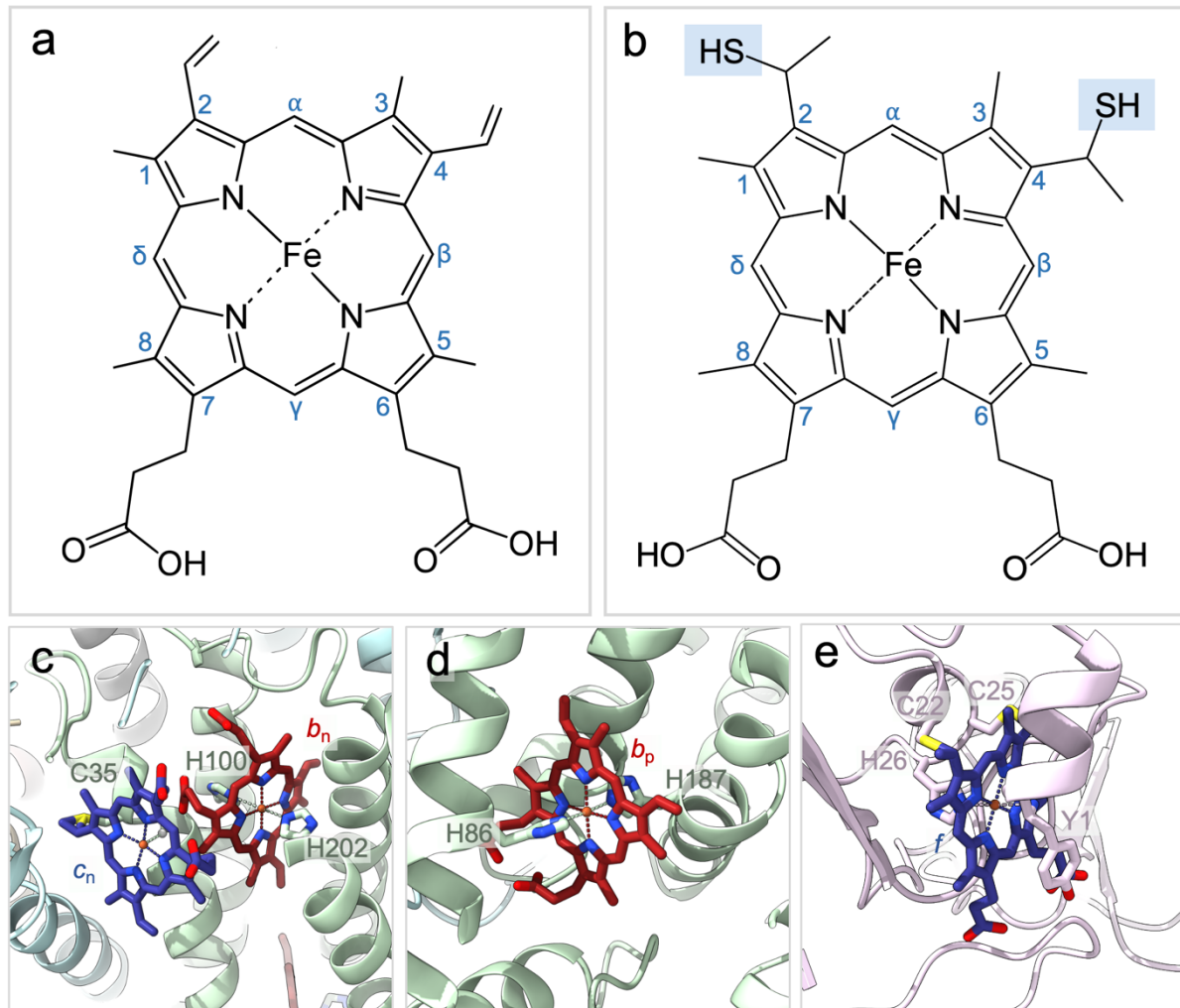


**Figure 1.5 | Haems of the *cytb<sub>6</sub>f* complex.** Each monomeric unit of *cytb<sub>6</sub>f* contains four haems including two *b*-type haems ( $b_n$  and  $b_p$ ) and two *c*-type haems ( $c_n$  and  $f$ ). **a-b**, Schematics showing the molecular structure of a *b*-type haem (a) and a *c*-type haem (b). In both cases the haem molecules are numbered according to the Fischer numeration for tetrapyrroles (Moss, 1988). While in *b*-type haems a vinyl group is present at position C2 and C4, in *c*-type haems a thioether linkage (blue box) is also present at C2 and C4 (in haem  $c_n$  this is only present at position C2), these are typically formed with nearby cysteine residues of a polypeptide chain. **c-e**, a zoomed in perspective of each of the four haem molecules in the *cytb<sub>6</sub>f* complex (PDB: 4OGQ (Hasan and Cramer, 2014a)) together with their coordinating axial ligands. Subunits and prosthetic groups are coloured as in Figure 1.4.

### 1.3.3 The modified Q-cycle and electron transfer mechanics

In the *cytbc<sub>1</sub>* complex, the process of ubiquinol : cytc oxidoreduction has been extensively studied and is generally accepted to occur via a modified 'Q-cycle' mechanism (**Brandt and Trumpower, 1994; Crofts and Meinhardt, 1982; Crofts et al., 1983a, 1999a, 2004; Mitchell, 1975a, 1975b, 1976**).

Given the overall similarities between *cytbc<sub>1</sub>* and *cytb<sub>6f</sub>*, a similar overall mechanism is thought to occur in *cytb<sub>6f</sub>*, however, due to structural differences, the exact mechanism differs in its detail.

In both complexes, the modified Q-cycle can be split into two half cycles, each half cycle resulting in the net movement of two protons across the membrane and the transfer of electrons from a two-electron quinol carrier to a high-potential, soluble single electron carrier (**Figure 1.6**).

#### *1st half cycle*

In the first half of the modified Q-cycle (**Figure 1.6a**), one molecule of PQH<sub>2</sub> from the PQ/PQH<sub>2</sub> pool diffuses to the complex, binding with high affinity to the Q<sub>p</sub> site on the electrochemically positive (p-) side of the intermonomer cavity. Here, the *b<sub>6f</sub>* complex catalyses the two-step deprotonation and oxidation of PQH<sub>2</sub>, first to a semiplastoquinone radical species (PQH<sup>•</sup>), then to fully oxidised plastoquinone (PQ). Each deprotonation and oxidation step results in the release of one proton and one electron. The protons are released to the p-side of the membrane where they contribute to the generation of a proton motive force (*pmf*) while electrons are transferred to either the 'high' or 'low' potential electron transfer pathways via an electron bifurcation mechanism.

The high potential chain involves the transfer of one electron from the PQH<sup>•</sup>/PQH<sub>2</sub> redox couple ( $E_m = + 480$  mV) to a one-electron carrier bound on the p-side of the membrane (PC;  $E_m = + 370$  mV) via the 2Fe-2S cluster of the ISP ( $E_m = + 310$  mV) and the c-type haem *f* located in the soluble domain of the *cytf* subunit ( $E_m = + 355$  mV).

While initial electron transfer from PQH<sub>2</sub> ( $E_m = + 480$  mV) to the 2Fe-2S cluster ( $E_m = + 310$  mV) is endergonic (**Figure 1.6c**), it is made possible by the close proximity between the 2Fe-2S cluster and the PQH<sub>2</sub> binding site (Q<sub>p</sub>) ( $\sim 7$  Å in PDB 4H13 (**Hasan et al., 2013a**)) as well as close coupling with the second (exergonic) electron transfer from the PQ/PQH<sup>\*</sup> couple ( $E_m = - 280$  mV) to the low-potential chain (haem  $b_p$ ;  $E_m = - 150$  mV and haem  $b_n$ ;  $E_m = - 85$  mV). This second oxidation step is also accompanied by the release of a second proton to the p-side of the membrane.

Following electron bifurcation between the high and low potential chains in *cytbc*<sub>1</sub>, a large movement of the ISP head domain is required to facilitate the subsequent electron transfer from the 2Fe-2S cluster to the *c*-type haem of *cytc*<sub>1</sub> (**Zhang et al., 1998**). Given the large (27 Å) distance between the 2Fe-2S cluster and the *c*-type haem of *cytf*, it is expected that a similar movement would be necessary to facilitate the transfer of an electron to the *c*-type haem of *cytf* in *cytb*<sub>6f</sub> however this has not yet been directly observed.

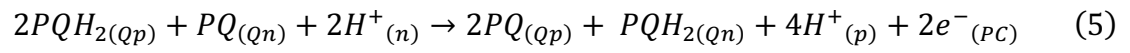
While in *cytbc*<sub>1</sub>, the electron residing on haem  $b_n$  is transferred to a bound quinone molecule at the Q<sub>n</sub> site to form a semiquinone (QH<sup>\*</sup>) radical species (Berry et al., 2000; Crofts, 2004; Crofts et al., 1983a; Gray and Winkler, 1996; Mitchell, 1975a, 1975b; Moser et al., 1992; Solmaz and Hunte, 2008b; Trumpower, 1990; Zhang et al., 1998), in *cytb*<sub>6f</sub> there is no evidence of such a species at the Q<sub>n</sub> site and the electron instead appears to be transferred to haem  $c_n$  (**Zito and Alric, 2016**).

#### *2nd half cycle*

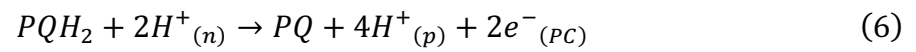
In the second half of the Q-cycle (**Figure 1.6b**), PQ diffuses away from the Q<sub>p</sub> site and is replaced by a PQH<sub>2</sub> molecule from the membrane pool. As in the first half cycle, an electron from this PQH<sub>2</sub> molecule is transferred to a one-electron carrier (PC) bound on the p-side of the membrane via the high potential electron transfer chain and one proton is simultaneously released to the luminal side of the membrane generating a semiplastoquinone (PQH<sup>\*</sup>) radical at the Q<sub>p</sub> site. A second round of deprotonation and oxidation then occurs, with the second electron entering the low potential chain while a second proton is released to the p-side. The electron is transferred along the low potential chain to the Q<sub>n</sub> site where the concerted two electron reduction of PQ takes place via haems  $b_n$  and  $c_n$ . Together with two protons taken

up from the aqueous phase of the stroma (n-side), these events result in the full reduction of PQ at the Q<sub>n</sub> site and the release of PQH<sub>2</sub> to the membrane pool.

*Complete Equation*



*Simplified Equation*



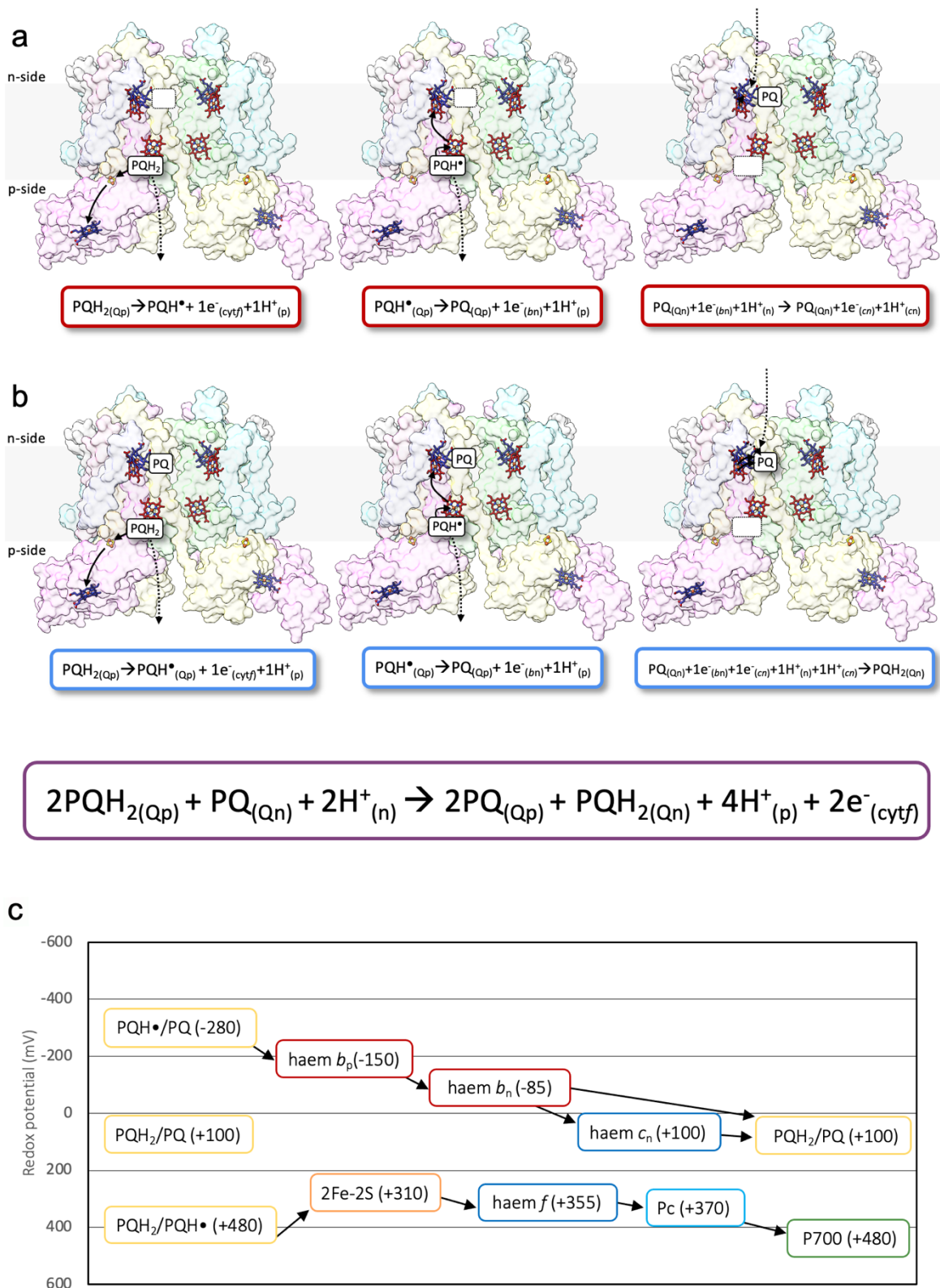


**Figure 1.6 | The proton motive Q-cycle of cytochrome  $b_6f$ .** A schematic representation of the Q-cycle model for electron and proton transfer through the  $cytb_6f$  complex (*Nostoc sp.* PCC 7120, 4H44 (Hasan et al., 2013a) based on the original cycle proposed by Mitchell (Mitchell, 1975b) with modifications



proposed by Crofts (**Crofts et al., 1983b**). The cycle in *cytb<sub>6</sub>f* is split into two half-cycles with **a**, showing each reaction step of the first half-cycle overlaid on the structure and summarised below in a red box and **b**, showing each reaction step of the second half-cycle overlaid on the structure and summarised below in a blue box. The complete reaction is outlined below in the purple box. The position of the lipid bilayer that separates the stromal (n-) and lumenal (p-) sides of the membrane is indicated by a grey stripe. The Q<sub>p</sub> and Q<sub>n</sub> sites are denoted by a white box overlaid on the structure with a solid outline indicating the site is occupied by substrate while a black dashed outline indicates the site is empty. Black dotted arrows indicate proton transfers while solid black arrows indicate electron transfers. Subunits and prosthetic groups are coloured as in **Figure 1.4. c**, Redox potential diagram of the cofactors involved in the Q-cycle. Midpoint potentials shown are those defined for the higher plants (**Hope, 1993; Kirchhoff et al., 2004**).

#### 1.3.4 Architecture and dynamics at the Q<sub>p</sub> site

In *cytb<sub>6</sub>c<sub>1</sub>*, structural studies have shown that the Q<sub>p</sub> site is bifurcated into two lobes comprising a 2Fe-2S-proximal lobe and a haem *b<sub>p</sub>*-proximal lobe. It is further observed that different quinone species appear to occupy these two lobes with differing affinities such that quinone analogue inhibitors that mimic the structural state of ubiquinone (UQ) (class I inhibitors: stigmatellin and 5-*n*-undecyl-6-hydroxy-4,7-dioxobenzothiaole) appear to preferentially occupy the 2Fe-2S proximal lobe (**Figure 1.7a**) while inhibitors which mimic the structural state of semiquinone (class II inhibitors: myxothiazole and β-methoxyacrylatestilbene (MOAS)-type inhibitors) appear to show a preference for the haem *b<sub>p</sub>* proximal lobe (**Figure 1.7c**).

In addition to these findings, it appears that occupation of either lobe is a mutually exclusive event suggesting that a conformational change in the position of substrate within the Q<sub>p</sub> site accompanies catalysis (**Crofts et al., 1999a; Esser et al., 2004; Zhang et al., 1998**).

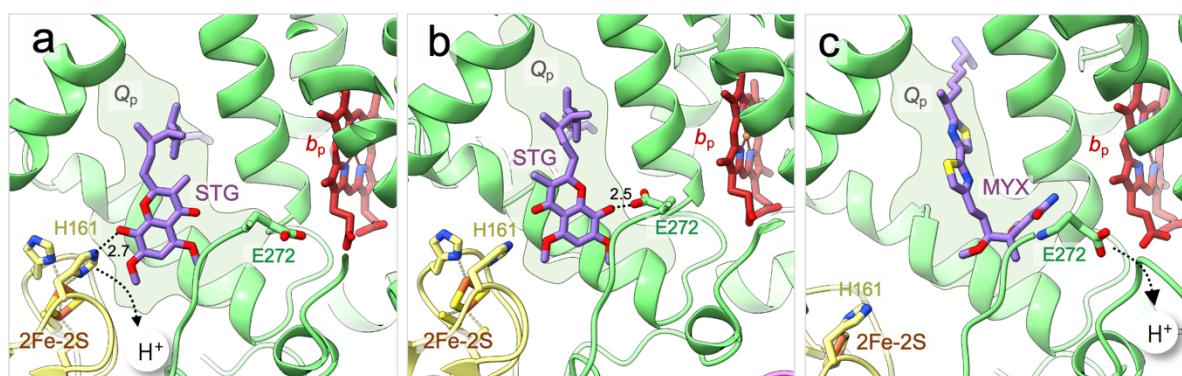


**Figure 1.7 | Architecture of the  $Q_p$  site and proton movements linked to catalysis in  $cytb_1$ .** a-c, The binding of  $UQH_2$  in the  $Q_p$  site of  $cytb_1$  probed using quinone analogue inhibitors stigmatellin (a, 3BCC; b, 2BCC (Zhang et al., 1998)) and myxothiazole (c, 1SQP (Esser et al., 2004)). An outline of the  $Q_p$  site is indicated by semi-transparent green shading while the putative proton channel is highlighted with semi-transparent blue shading. Putative proton exit pathways are indicated by black dotted lines and arrows. H-bond distances are indicated in (Å). Prosthetic groups, key catalytic residues and quinone analogue inhibitors are shown in stick representation with proteins shown as ribbons. Subunits, inhibitors and prosthetic groups are coloured as in Figure 1.4.

It is likely that the first stages of the p-side oxidation reactions may be initiated upon binding of substrate within the 2Fe-2S proximal lobe via an H-bond with one of the highly conserved histidine residues (H161) which ligates the 2Fe-2S cluster (ISP). While an electron may be efficiently transferred over the  $\sim 7$  Å distance to the 2Fe-2S cluster, the surface proximal H161 is expected to provide a short exit route for the first proton to the aqueous p-side of the complex (Figure 1.7a).

To facilitate electron transfer down the high potential chain from the 2Fe-2S cluster to the c-type haem of  $cytc_1$ , it appears that the head domain of the ISP undergoes a large scale conformational change from its  $cytb$  interfacing position ('b' position) to form an interface with  $cytc_1$  ('c' position) (Figure 1.8). Overall, this conformational change results in a reduced distance (from  $\sim 27$  Å to  $\sim 10$  Å) between the 2Fe-2S cluster and the c-type haem of  $cytc_1$  allowing efficient, rapid electron transfer to occur (Table 1.3) (Crofts et al., 1999a, 1999b, 1999c; Zhang et al., 1998).

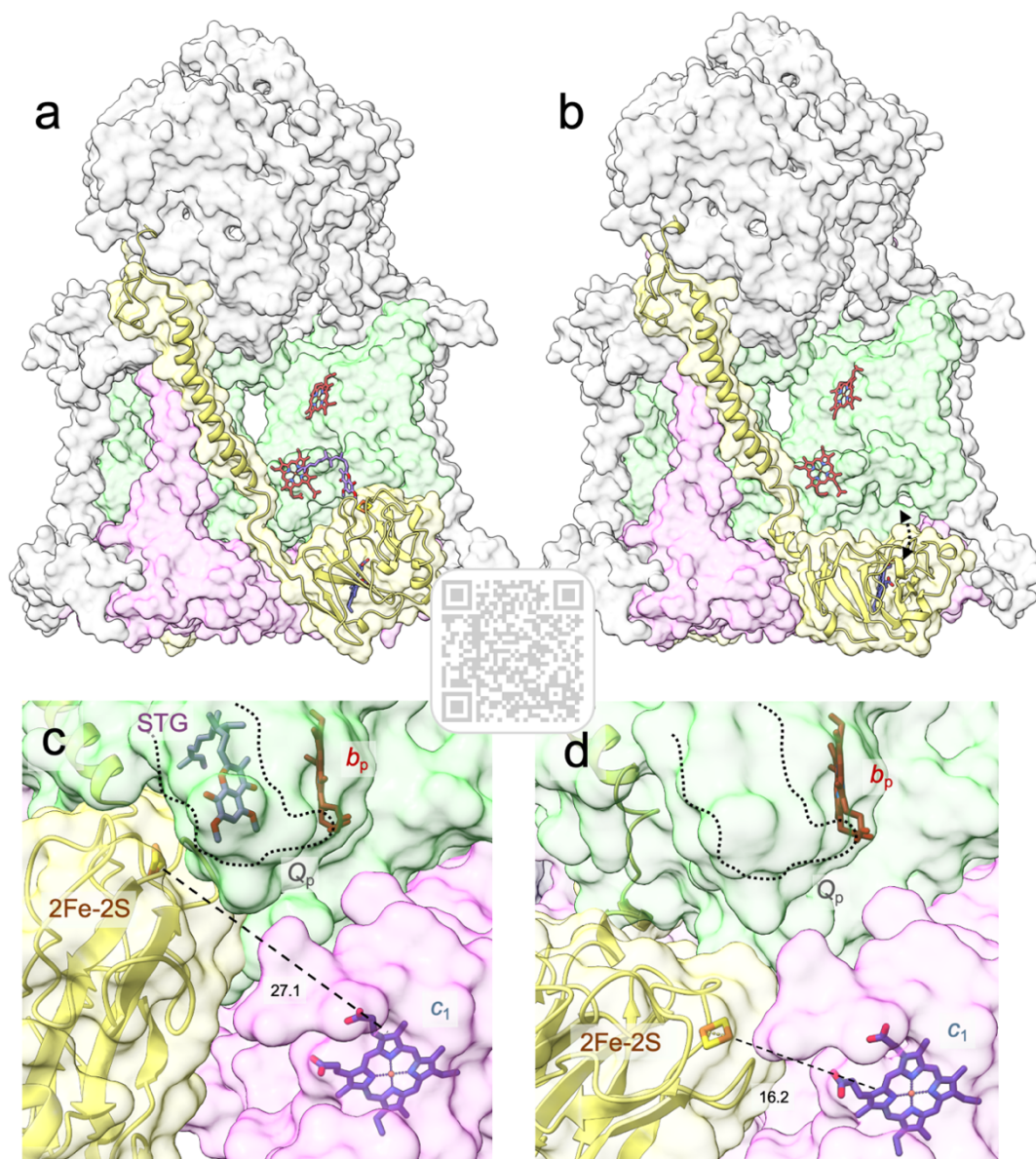


**Figure 1.8| Large scale conformational changes occurring within the extrinsic domain of the ISP underlie catalysis in the cytochrome  $bc_1$  complex.** **a-b**, two conformations of the ISP are observed in the *Gallus gallus* cytochrome  $bc_1$ , the  $Q_p$  proximal position (**a**, 3BCC (**Zhang et al., 1998**)) and the  $Q_p$  distal position (**b**, 1BCC (**Zhang et al., 1998**)) with an arrow indicating the scale of movement undergone. A video of the conformational change undergone by the Rieske subunit depicted in panel **b** can be accessed using the QR code in the centre of this figure. **c-d**, a close-up view of **a-b** showing the relative distances between cofactors in the  $Q_p$  proximal position (**c**, 3BCC) and the  $Q_p$  distal position (**d**, 1BCC). Distances are indicated by a black dashed line with the distance indicated below in (Å). Prosthetic groups are shown in stick representation beneath a transparent protein surface. An outline of the  $Q_p$  site is also indicated by a grey dotted line. Subunits and prosthetic groups are coloured as in **Figure 1.4**.

**Table 1.3| A comparison of edge-to-edge cofactor distances (Å) in each half of  $bc_1$  from *G. gallus*.** Models used include the  $bc_1$  dimer from *G. gallus* with the Rieske ISP in its distal (1BCC) and proximal (3BCC) positions (Zhang et al., 1998). <sup>a</sup> Inhibitors are indicated by the abbreviations STG (stigmatellin) and AMY (antimycin).

PDB ID	1BCC (distal)	3BCC (proximal)
Source	<i>G. gallus</i>	<i>G. gallus</i>
Resolution (Å)	3.2	3.7
Inhibitors <sup>a</sup>	-	STG (Q <sub>p</sub> ), AMY (Q <sub>n</sub> )
Distances:		
$b_n - b_p$ (Å)	12.4, 12.4	12.3, 12.3
$b_p - b_p$ (Å)	14.4	14.5
$b_p - 2Fe-2S$ (Å)	30.3, 30.3	23.0, 23.1
$2Fe-2S - c_1$ (Å)	16.8, 16.8	27.3, 27.5

In addition to bridging the gap between cofactors along the high-potential chain, the conformational change in the ISP head domain also provides a means to insulate the reactive QH<sup>•</sup> species from unfavourable reactions with either the reoxidised 2Fe-2S cluster or molecular oxygen. This insulating effect is further augmented by the migration of the substrate species within the Q<sub>p</sub> site from the 2Fe-2S proximal lobe to the haem  $b_p$  proximal lobe (Crofts et al., 1999a; Esser et al., 2004; Zhang et al., 1998).

Within the haem  $b_p$  proximal lobe, it is anticipated that the QH<sup>•</sup> species forms contacts with a highly conserved glutamate residue (Gln272, PEWY sequence of *cytb*) proximal to haem  $b_p$  (Figure 1.7b). Structural evidence suggests that Glu272 abstracts a proton from the QH<sup>•</sup> species before undergoing a rotation to enable the release of the abstracted proton to the p-side aqueous phase (Figure 1.7c) (Crofts et al., 1999d; Izrailev et al., 1999).

Given the strong conservation of these proposed catalytic residues (His161 and Glu272 in *cytbc*<sub>1</sub>; His129 and Glu78 in *cytb*<sub>6f</sub>) and pronounced bifurcation of the Q<sub>p</sub> site in both complexes, it is expected that similar mechanisms to those assigned in *cytbc*<sub>1</sub> may underlie catalysis in *b*<sub>6f</sub>. Indeed, structural studies on the *cytb*<sub>6f</sub> complex from *M. lamosus* (Hasan et al., 2013a) suggest the presence of two potential proton exit routes extending from either lobe of the Q<sub>p</sub> site.



As in *cytbc<sub>1</sub>*, catalysis may be initiated upon the formation of an H-bond between the substrate and one of the residues ligating the 2Fe-2S cluster (His129 in *cytb<sub>6f</sub>*) within the 2Fe-2S proximal lobe of the Q<sub>p</sub> site (**Figure 1.9a**). Following the first deprotonation and oxidation event, a second proton transfer event may proceed via a route involving the highly conserved glutamate residue (Glu78 in *b<sub>6f</sub>*; PEWY sequence of subIV) at the base of the haem *b<sub>p</sub>* proximal lobe of the Q<sub>p</sub> site (**Figure 1.9b**) (**Hasan et al., 2013a**).

While the vital role of both His161 and Gln272 in catalysis is further supported by evidence from mutagenesis studies in *C. reinhardtii* and from kinetics studies (**Zito et al., 1998**), a number of potential differences between the *bc<sub>1</sub>* and *b<sub>6f</sub>* complexes mean the exact details of the molecular mechanisms underlying catalysis in *cytb<sub>6f</sub>* may differ in their detail.

Indeed, while a large-scale conformational change in the ISP head domain facilitates electron transfer between the 2Fe-2S cluster and haem *c<sub>1</sub>* in *cytbc<sub>1</sub>*, no equivalent conformational change to bridge the high-potential chain has been observed so far in any high-resolution structures of the *cytb<sub>6f</sub>* complex (**Table 1.4**) (**Baniulis et al., 2008; Brugna et al., 1999, 2000; Crofts et al., 1999b; Hasan, 2013; Iwata et al., 1998; Kurisu et al., 2003; Stroebel et al., 2003; Xia et al., 1997; Yamashita et al., 2007; Yan et al., 2006; Zhang et al., 1998**).

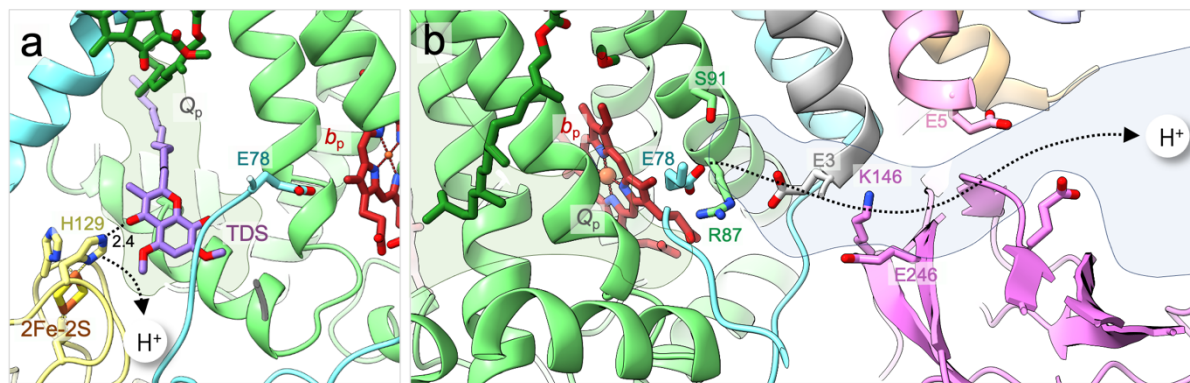


**Figure 1.9 | Architecture of the Q<sub>p</sub> site and proton movements linked to catalysis in *cytb<sub>6f</sub>*.** **a**, Binding of PQH<sub>2</sub> within the Q<sub>p</sub> site of *cytb<sub>6f</sub>* probed using tridecylstigmatellin (PDB ID: 4H13 (**Hasan et al., 2013a**)). **b**, The putative exit pathway for the second proton from the Q<sub>p</sub> site (PDB ID: 4H13 (**Hasan et al., 2013a**)). An outline of the Q<sub>p</sub> site is indicated by semi-transparent green shading while the putative proton channel is highlighted with semi-transparent blue shading. Putative proton exit pathways are indicated by black dotted lines and arrows. H-bond distances are indicated in (Å). Prosthetic groups,

key catalytic residues and quinone analogue inhibitors are shown in stick representation with proteins shown as ribbons. Subunits, inhibitors and prosthetic groups are coloured as in **Figure 1.4**.

**Table 1.4 | A comparison of edge-to-edge cofactor distances (Å) in each half of the  $b_6f$  dimer from different species.** Models used include  $b_6f$  from *C. reinhardtii* (PDB ID: 1Q90 (Stroebel et al., 2003)), *M. lamosus* (PDB ID: 2E74 (Yamashita et al., 2007)) and *Nostoc* sp. PCC 7120 (PDB ID: 4OGQ (Hasan and Cramer, 2014a)). <sup>a</sup> Inhibitor is indicated by the abbreviation TDS (tridecylstigmatellin).

PDB ID	1Q90	2E74	4OGQ
Source	<i>C. reinhardtii</i>	<i>M. lamosus</i>	<i>Nostoc</i> sp. PCC 7120
Resolution (Å)	3.1	3.0	2.5
Inhibitors <sup>a</sup>	TDS (Q <sub>p</sub> )	-	-
Distances:			
$b_n - c_n$ (Å)	4.7, 4.7	4.7, 4.7	4.6, 4.6
$b_n - b_p$ (Å)	12.2, 12.2	12.2, 12.2	12.1, 12.1
$b_p - b_p$ (Å)	15.1	15.2	15.3
$b_p - 2Fe-2S$ (Å)	22.9, 22.9	25.5, 25.5	25.3, 25.3
$2Fe-2S - f$ (Å)	27.8, 27.8	26.2, 26.2	26.2, 26.2

Further areas of potential disparity between the mechanisms underlying catalysis in these two complexes arise in the haem  $b_p$  proximal domain of the Q<sub>p</sub> site. While the surface proximal position of Glu272 in *cytb<sub>c1</sub>* appears to facilitate the relatively short, direct exit of a proton to the aqueous p-side of the membrane, the same route in *cytb<sub>6f</sub>* is obstructed by the presence of PetG and PetM. The presence of these additional single TMH subunits presents a major architectural hurdle to proton transfer; given this observation it is suggested that proton exit in *cytb<sub>6f</sub>* is facilitated by a comparatively longer, hydrophilic channel extending from Glu78 to the aqueous p-side of the complex. Indeed, such a channel appears to incorporate residues from both PetG and PetM as well as the *cytf* subunit, creating a highly hydrated, hydrophilic exit route for protons from the Q<sub>p</sub> site (**Figure 1.9**) (Hasan et al., 2013a).

While in existing structures of the *cytb<sub>6f</sub>* complex, the side chain of Glu78 has been captured in a position facing this highly hydrated p-side exposed channel on the periphery of the Q<sub>p</sub> site (**Figure 1.9**), evidence for rotational changes of Glu78 equivalent to those observed for Glu272 in the *bc<sub>1</sub>* complex is lacking (Baniulis et al., 2009; Crofts et al., 1999d; Hasan and

Cramer, 2014a; Hasan et al., 2013b, 2013a, 2014; Kurisu et al., 2003; Stroebel et al., 2003; Yamashita et al., 2007; Yan et al., 2006).

Another key difference between the two complexes which likely influences catalysis resides within the long ( $\sim 15$  Å), narrow entrance portal which connects the quinol oxidation site ( $Q_p$ ) site to the intermonomer cavity (**Figure 1.10**) (Cramer et al., 2006). While the polypeptide architecture of this portal is mostly conserved between the two complexes, in *cytb<sub>6</sub>f* access to/from the  $Q_p$  site is further restricted by the presence of Chl *a*.

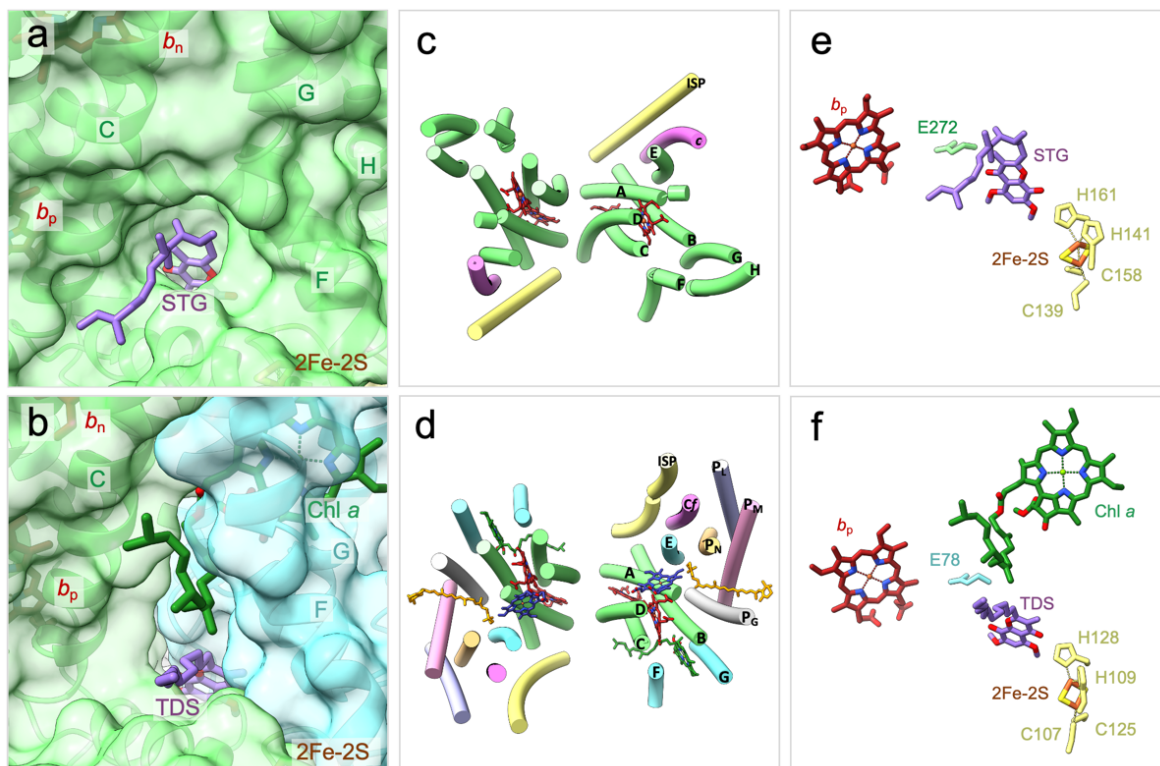


**Figure 1.10** | The  $Q_p$  sites of *cytb<sub>6</sub>c<sub>1</sub>* and *cytb<sub>6</sub>f*. **a–b**, a surface view of the  $Q_p$  site in the *cytb<sub>6</sub>c<sub>1</sub>* complex from *G. gallus* (a, PDB ID: 3BCC (Zhang et al., 1998)) and the *cytb<sub>6</sub>f* complex from *Mastigocladus laminosus* (b, PDB ID: 4H13 (Hasan et al., 2013a)). In both complexes, the  $Q_p$  site is defined by TM helices ‘C’ and ‘G’ (shown as ribbons); additionally, in both complexes the site is occupied by quinone analogue inhibitors (stigmatellin in *cytb<sub>6</sub>c<sub>1</sub>* and tridecylstigmatellin in *cytb<sub>6</sub>f*). **c–d**, the arrangement of TM helices (shown as cylinders) within complexes shown in panels a–b viewed perpendicular to the membrane plane from the n-side of the membrane (extrinsic domains, loops and additional non-conserved subunits in the *bc<sub>1</sub>* complexes are not shown for clarity). **e–f**, A protein-free view of panels a and b showing the position of each quinone analogue in relation to catalytically essential residues and cofactors (shown as sticks).

While the chlorin head group of the Chl *a* is bound between the F and G helices of subIV (**Baniulis et al., 2009; Kurisu et al., 2003; Stroebel et al., 2003**), the long phytyl tail of the molecule protrudes into the portal resulting in further steric hindrance to PQH<sub>2</sub> access (**Figure 1.10**). This additional restriction of the Q<sub>p</sub> portal size compared to *cytbc*<sub>1</sub> is consistent with the observation that the binding of the p-side *bc*<sub>1</sub> inhibitor, stigmatellin, is ~ 20 - 30 fold weaker than the binding of the smaller quinol analogue tridecylstigmatellin (TDS) (**Hope and Valente, 1996; Yamashita et al., 2007**). Despite this additional size constraint, the presence of Chl *a* does not appear to significantly hinder the rate of quinol passage to the Q<sub>p</sub> site in *b*<sub>6</sub>*f*. It does however appear that the Chl *a* molecule may have a role in retaining substrate within the Q<sub>p</sub> site for an extended period of time relative to the *bc*<sub>1</sub> complex (**Hasan et al., 2014; Yu et al., 2009; Zhang et al., 2001, 2003**). This increased residence time of the semiquinone radical species within the Q<sub>p</sub> site may have important consequences for the formation of reactive oxygen species (ROS) (e.g. superoxide, O<sub>2</sub><sup>-</sup>) in *cytb*<sub>6</sub>*f* (**Baniulis et al., 2013**).

#### 1.3.5 Avoiding side-reactions and Q-cycle short-circuits at the Q<sub>p</sub> site.

In both *cytbc*<sub>1</sub> and *cytb*<sub>6</sub>*f*, a key hazard of catalysis is the potential for the semiquinone radical species ( $E_m = - 280$  mV) to reduce molecular oxygen ( $E_m = - 160$  mV) forming the reactive oxygen species superoxide (O<sub>2</sub><sup>-</sup>) (**Baniulis et al., 2013; Petlicki and Van De Ven, 1998**).

Another hazard to both *cytb*<sub>6</sub>*f* and *cytbc*<sub>1</sub> complexes is the potential for short-circuiting of electrons between the low and high potential chains of the complex; this would undermine *pmf* generation through bypass of the Q-cycle. How such short-circuits are avoided and how the production of ROS is largely mitigated has been the subject of intense debate in both *cytb*<sub>6</sub>*f* and *cytbc*<sub>1</sub> fields for many years with a variety of models proposed (Cape et al., 2006; Mulkidjanian, 2005; Osyczka et al., 2005; Rich, 2004; Tikhonov, 2014).

The observation of a spin-coupled state between the semiquinone and the reduced 2Fe-2S cluster is suggestive of a potential mechanism to prevent oxidative damage and potential short circuits (**Sarewicz et al., 2017**). Crucially, such a spin coupled state is only observed when the low potential chain is reduced suggesting that subsequent reactions in the haem *b*<sub>p</sub> proximal lobe may only proceed when haem *b*<sub>p</sub> becomes available as an electron acceptor. In this manner, stabilisation of the semiquinone through spin coupling may increase the



midpoint potential of the semiquinone such that any potential side reaction with  $O_2$  become energetically unfavourable. Once an electron is transferred from the semiquinone to haem  $b_p$ , the loss of the spin-coupled state with the 2Fe-2S cluster may allow the substrate to migrate to the haem  $b_p$  proximal lobe for deprotonation and release the ISP head allowing electron transfer to proceed down the high potential chain.

In addition to reducing the risk of ROS generation, such a spin-coupled mechanism could provide a means to prevent short circuits of the Q-cycle, preventing the accidental escape of the semiquinone from the  $Q_p$  site and the potential for unfavourable back reactions between the semiquinone species and the 2Fe-2S cluster.

In contrast to *cytbc<sub>1</sub>*, the rate of formation of superoxide *in vitro* at the  $Q_p$  site of *cytb<sub>6f</sub>* is some twenty fold higher despite the detection of a similar spin-coupled state (**Baniulis et al., 2013; Sarewicz et al., 2016**). This difference may reflect the obstruction of the  $Q_p$  portal by phytol tail of the Chl *a* molecule (**Baniulis et al., 2009; Kurisu et al., 2003; Stroebel et al., 2003**), (**Figure 1.10**). Indeed, it has been suggested that the increased retention time of semiquinone within the  $Q_p$  site could serve as a redox signalling mechanism in photosynthetic organisms. For instance in algae and higher plants it has been suggested that superoxide may activate the kinase STT7/STN7 that regulates the relative light absorption by the photosystems, a mechanism known as state transitions. (**Bonaventura and Myers, 1969; Murata and Sugahara, 1969; Singh et al., 2016**).

### 1.3.6 Architecture and dynamics at the $Q_n$ site

On the n-side of the complex, the differences between *bc<sub>1</sub>* and *b<sub>6f</sub>* become far more pronounced both structurally (as described in **section 1.3.2**) and functionally. In both complexes, the quinone reduction reactions on the n-side of the complex proceed with the binding of a fully oxidised quinone molecule from the Q/QH<sub>2</sub> pool to the  $Q_n$  site. In *cytbc<sub>1</sub>*, the  $Q_n$  binding pocket is delimited by the haem  $b_n$  molecule (**Figure 1.11**) and surrounding residues from the *cytb* subunit (helices A, D, E and the *de* loop) (**Zhang et al., 1998**).

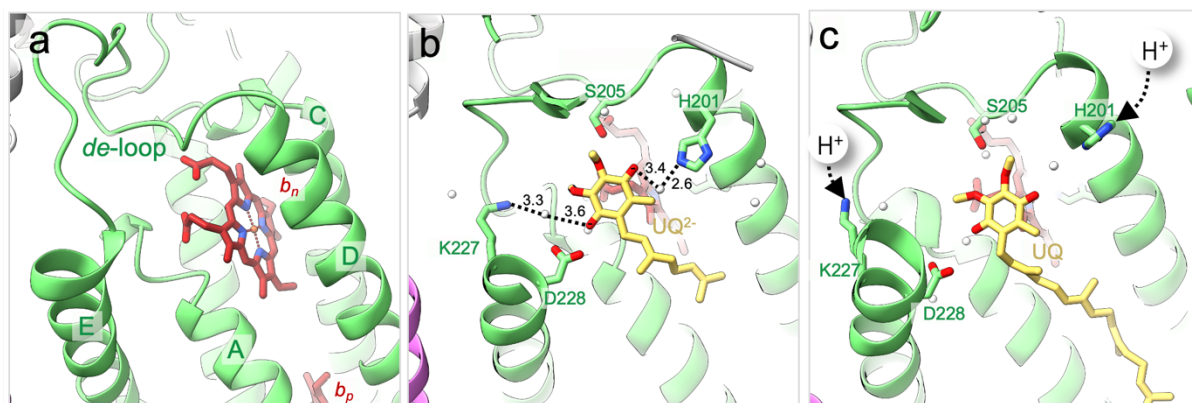


**Figure 1.11 | The  $Q_n$  site of  $cytb_1$  and the proposed reaction mechanics.** **a-b**, a ribbon representation of the unoccupied  $Q_n$  site in  $cytb_1$  from *G. gallus* (**a**, PDB ID: 2BCC (**Zhang et al., 1998**)). **b-c**, a ribbon representation of the occupied  $Q_n$  site in  $cytb_1$  from *B. taurus* (**b**, PDB ID: 1NTZ (**Gao et al., 2003**); **c**, PDB ID: 1EZV (**Hunte et al., 2000**)) showing the two proton transfer pathways proposed by **Gao et al., 2003**. Prosthetic groups, key interacting residues and quinone analogue inhibitors are shown in stick representation with protein shown as ribbons. Distances between residues are shown by black dashed lines with distances indicated in (Å). Subunits, inhibitors and prosthetic groups are coloured as in **Figure 1.4**. Key water molecules are shown as white spheres.

Structural studies of the bovine  $bc_1$  complex in the presence of quinone analogue inhibitors (Antimycin-A, PDB ID: 1NTK; 2-nonyl-4-hydroxyquinoline N-oxide (NQNO), PDB ID: 1NU1) and natively associated UQ (PDB ID: 1EZV and 1NTZ) indicate substrate binding in the  $Q_n$  site is mediated by residues from the  $cytb$  subunit (D228, H201, S205, K227) (**Gao et al., 2003; Hunte et al., 2000**). These highly conserved residues form stabilising interactions with the incoming substrate, both directly via H-bonding and indirectly via bridging water molecules (**Figure 1.11**). In a 4-step mechanism proposed by **Gao et al.**, the reduction of the UQ molecule at the  $Q_n$  site is mediated by the close proximity of the bound UQ with haem  $b_n$  (reduced by electrons transferred one at a time from the  $Q_p$  site via the low potential pathway) (**Gao et al., 2003**). Subsequent protonation is thought to occur via two separate pathways, each involving a conserved protonated residue with access to the n-side aqueous phase (H201 and K227) as well as a bridging water molecule contacting the bound substrate at the  $Q_n$  site. Protons may be donated directly to the ubisemiquinone radical species bound at the  $Q_n$  site by the two conserved water molecules, these may subsequently be reprotonated by nearby H201 and K227 (**Figure 1.11**). The involvement of these two highly conserved residues in such a proton transfer mechanism is further supported by structural identification of

conformational changes in both residues between the bovine (PDB ID: 1NTM) and yeast *bc<sub>1</sub>* complexes (PDB ID: 1EZV) (**Gao et al., 2003; Hunte et al., 2000**). It is apparent that the side chains of H201 and K227 are capable of undergoing  $\sim 90^\circ$  and  $\sim 180^\circ$  rotations, respectively, switching between a Q<sub>n</sub>-site facing position and a position facing the n-side aqueous phase of the mitochondrial matrix (**Figure 1.11**). Such a switch could allow acquisition of protons from the n-side of the complex and subsequent transfer of protons to the conserved water molecules which contact the bound substrate (**Figure 1.11**).

Various alternative mechanisms for the n-side protonation of ubiquinone in mitochondrial *bc<sub>1</sub>* have also been suggested. One such mechanism, known as the CL/K pathway, involves protein transfer from a peripheral cardiolipin molecule to ubiquinone bound at the Q<sub>n</sub> site via a conserved lysine (Lys228, *cytb*) and a series of water molecules. Another putative proton transfer mechanism involves proton conduction from the aqueous n-side to ubiquinone via a pathway including Glu52 (of the mitochondrial-specific Qcr7 subunit), water molecules and Arg218 (*cytb*) (**Hunte et al., 2003; Lange et al., 2001**).

In *cytbc<sub>1</sub>*, ubiquinone reduction is specifically inhibited by antimycin A (AA), which occupies the Q<sub>n</sub> site with high affinity (**Huang et al., 2009; Slater, 1973**). In contrast, the same inhibitor has no effect on plastoquinone reduction in *b<sub>6</sub>f* (**Moss and Bendall, 1984**) indicating the Q<sub>n</sub> site must harbour significant structural differences to its counterpart in *bc<sub>1</sub>*. Amongst these differences is the addition of haem *c<sub>n</sub>* in *cytb<sub>6f</sub>* which is positioned in a location approximately equivalent to the Q<sub>n</sub> site in *bc<sub>1</sub>* with its open axial position facing out towards the quinone exchange cavity (**Figure 1.12**) (**Kurisu et al., 2003; Stroebel et al., 2003; Yamashita et al., 2007**).

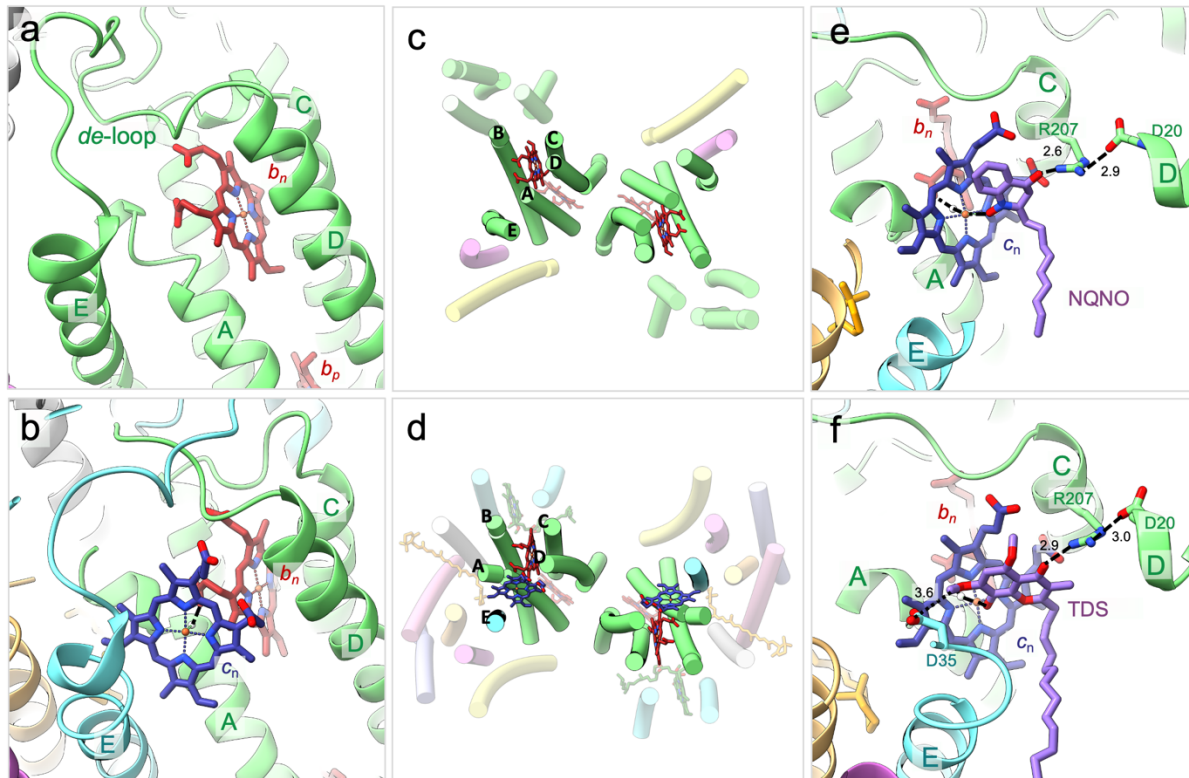


**Figure 1.12 | The  $Q_n$  site of  $cytb_{6f}$  compared to  $cytb_{c1}$ .** **a**, a ribbon representation of the unoccupied  $Q_n$  site in the *G. gallus*  $cytb_{c1}$  complex (**a**, PDB ID: 2BCC (**Zhang et al., 1998**)) and *Nostoc* sp. PCC 7120  $cytb_{6f}$  complex (**b**, PDB ID: 4OGQ (**Hasan and Cramer, 2014a**)). In both complexes, the position of haem  $b_n$  between TM helices 'B', 'C' and 'D' is conserved, however in the  $cytb_{6f}$  (**b**) the additional  $c'$ -type haem ( $c_n$ ) is present, this is connected to haem  $b_n$  via an intervening water molecule and obstructs access to haem  $b_n$ . **c-d**, the arrangement of TM helices (shown as cylinders) within complexes shown in panels a-b viewed perpendicular to the membrane plane from the n-side of the membrane (extrinsic domains, loops and additional non-conserved subunits in the  $cytb_{c1}$  complex are not shown for clarity). **e-f**, ribbon representation of the occupied  $Q_n$  site in: **e**, the  $cytb_{6f}$  complex occupied by NQNO (**e**, PDB ID: 4H0L (**Hasan et al., 2013a**)); **f**, the  $cytb_{6f}$  complex occupied by TDS (**f**, PDB ID: 4H13 (**Hasan et al., 2013a**)). Prosthetic groups, key interacting residues and quinone analogue inhibitors are shown in stick representation with protein shown as ribbons. Distances between residues are shown by black dashed lines with distances indicated in (Å). Subunits, inhibitors and prosthetic groups are coloured as in **Figure 1.4**. Key water molecules are shown as white spheres.

The apparent obstruction of the  $Q_n$  site by haem  $c_n$  explains the differences in affinity for AA, and also indicates that the mechanism of quinone binding, reduction and protonation must differ significantly between  $bc_1$  and  $b_{6f}$ . Given the intermediate position of haem  $c_n$  with regards to haem  $b_n$  and the central quinone exchange cavity, it is likely that haem  $c_n$

participates in the reduction of PQ by transferring electrons from haem  $b_n$  to PQ (**Lavergne, 1983; Zito and Alric, 2016**). Indeed, the close proximity of haems  $c_n$  and  $b_n$  ( $\sim 4 \text{ \AA}$ ) and physical bridging via a conserved  $\text{H}_2\text{O}$  molecule indicates the potential for electron sharing between the two haems. The idea of electronic coupling between the two haems is further corroborated by EPR spectroscopy evidence from Zatsman *et al* (**Zatsman et al., 2006**), who also suggest that structural coupling of these two haem molecules may facilitate a concerted two-electron reduction of PQ at the  $Q_n$  site. Such a mechanism would avoid semiquinone formation at the  $Q_n$  site and make the  $b_6f$  complex more suitable to the oxygen-rich environment of the photosynthetic thylakoid (**Baymann et al., 2007; Cramer and Kallas, 2016; Zatsman et al., 2006**).

Further evidence for this ‘double barrelled shotgun’ concerted mechanism of electron transfer to PQ is provided by the observation that the EPR spectrum of the complex is altered dramatically in the presence of NQNO (**Alric et al., 2005b; Baymann et al., 2007; Zatsman et al., 2006**). Interestingly although the dramatic shift in the EPR spectra indicates NQNO may directly bind to haem  $c_n$ , the high-spin state of the molecule remains unaltered suggesting the binding of NQNO either displaces the axial  $\text{H}_2\text{O}$  ligand or NQNO binds very weakly to haem  $c_n$  (**Baymann et al., 2007**). Structural studies with NQNO (PDB ID: 4H0L) (**Hasan et al., 2013a**) showed that the semiquinone analogue binds in a position adjacent to haem  $c_n$ . This analysis indicates that PQ is indeed a natural ligand of haem  $c_n$  implying a distinct difference in the n-side electron transfer reactions that diverges from the classical Q-cycle mechanism described in the  $bc_1$  complex.

A similar binding site proximal to the haem  $c_n$  molecule was found for the quinone analogue inhibitor TDS (PDB ID: 4H13) (**Hasan et al., 2013a**). Interestingly, in  $bc_1$  TDS is exclusively a p-side inhibitor rather than an n-side inhibitor (**Hope and Valente, 1996**). This distinct difference indicates a reduced specificity for substrate binding between the  $b_6f$  and  $bc_1$  complexes, which can be explained by comparing the surrounding polypeptide environments. While the polypeptide environment surrounding haems  $c_n$  and  $b_n$  does not vary significantly between the two complexes, it appears that the region surrounding haem  $c_n$  provides far fewer polar interactions for incoming substrate. Additionally, the amphipathic TMH A of  $\text{cyt}b_6$  is shifted by  $\sim 6 \text{ \AA}$  towards the n-side relative to that in  $\text{cyt}bc_1$ . Together these two effects

create a  $Q_n$  binding site with both reduced specificity and greater access to the quinone substrate relative to the site in  $bc_1$ , however the efficiency of binding of PQ to the  $Q_n$  site may also be reduced. Consequences for the changes between  $b_{6f}$  and  $bc_1$  at the  $Q_n$  site in terms of kinetics, equilibrium and mechanistic differences in quinone reduction remain to be explored.

The differences discussed in PQ binding and electron transfer at the  $Q_n$  site necessitate the need for alternate proton transfer pathways in  $b_{6f}$  (**Figure 1.13**).

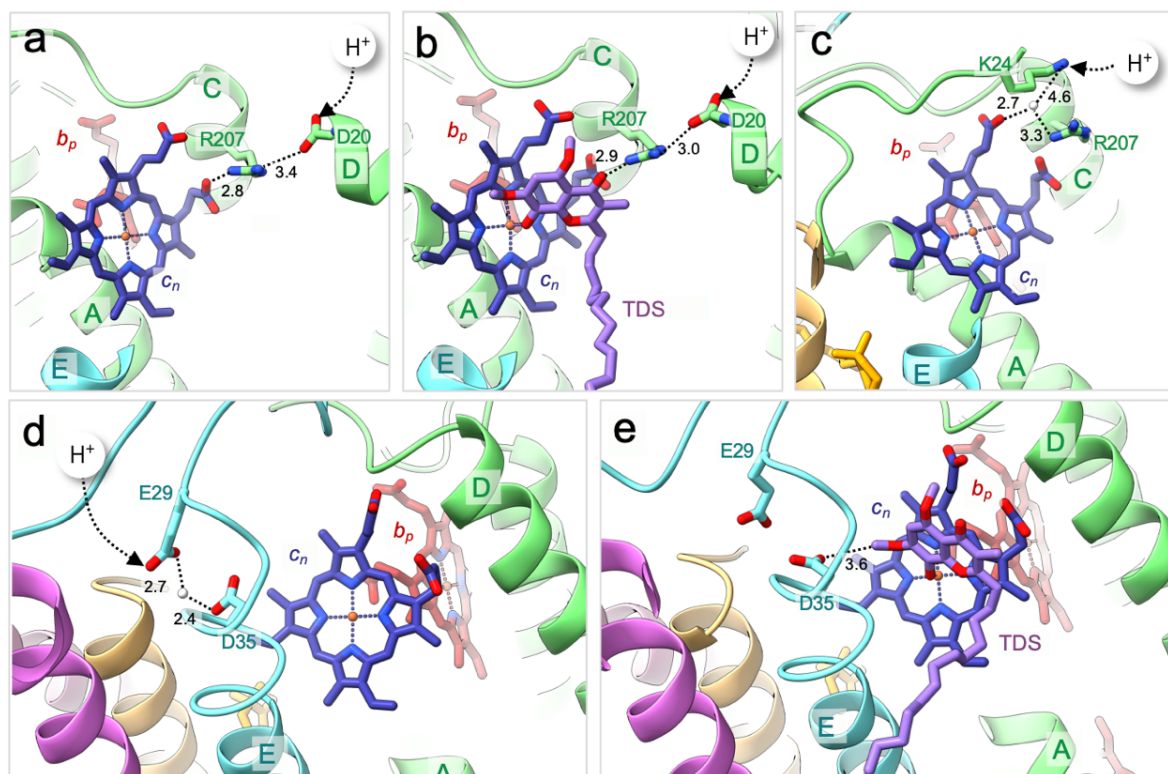


**Figure 1.13| Putative proton transfer pathways on the n-side of  $cytb_{6f}$ .** Ribbon representations representation of putative proton pathways at the  $Q_n$  site. **a-b**, shows the putative D/R pathway in *Nostoc* PCC 7120 (PDB ID: 4H44 (**Hasan et al., 2013a**)) and *M. laminosus* (PDB ID: 4H13 (**Hasan et al., 2013a**)). **c**, shows the Lys24-based pathway in *Nostoc* sp. PCC 7120 (PDB ID: 4H44 (**Hasan et al., 2013a**)). **e-d**, shows the E/D pathway in *M. laminosus* (PDB ID: 4H44 (**Hasan et al., 2013a**)) and *Nostoc* sp. PCC 7120 (e, PDB ID 4H13 (**Hasan et al., 2013a**)). Prosthetic groups, key interacting residues and quinone analogue inhibitors are shown in stick representation with protein shown as ribbons. Distances between residues are shown by black dashed lines with distances indicated in (Å). Subunits, inhibitors and prosthetic groups are coloured as in **Figure 1.4**. Key water molecules are shown as white spheres.

In comparison to the *bc<sub>1</sub>* complex, the Q<sub>n</sub> site in *b<sub>6</sub>f* lies much closer to the aqueous phase of the stroma allowing the potential for a much shorter pathway for proton conduction from the stroma to the PQ bound at the Q<sub>n</sub> site. Various mechanisms for the n-side protonation of PQ in *b<sub>6</sub>f* have been explored following structural analysis of the native complex from *Nostoc* (PDB ID: 4H44) and the complex with bound quinone analogue inhibitors (TDS and NQNO) (PDB IDs: 4H13 and 4H0L) (**Figure 1.13**) (**Hasan et al., 2013a**).

The simplest of these proposed proton transfer pathways extends from the n-side aqueous phase to the Q<sub>n</sub> site via the surface exposed side chain of Asp20 (*cytb<sub>6</sub>*) and the highly conserved Arg207 (*cytb<sub>6</sub>*) proximal to the Q<sub>n</sub> site. This unique anhydrous ‘D/R pathway’ provides a short route to conduct protons directly from the aqueous phase of the stroma to the PQ bound at the Q<sub>n</sub> site of the complex. The role of Arg207 in such a pathway is further supported by evidence from both mutagenesis (**Nelson et al., 2005**) and structural studies (**Hasan et al., 2013a**) whereby Arg207 is implicated in the binding of TDS and NQNO (PDB IDs: 4H13 and 4H0L). A second putative mechanism for protonation on the n-side of the *b<sub>6</sub>f* complex is a pathway involving Lys24 (*cytb<sub>6</sub>*), a water molecule (wat416) adjacent to haem *c<sub>n</sub>* and Arg207 (*cytb<sub>6</sub>*). It is suggested that this ‘Lys24-based pathway’ is mediated by the flexible motion of the surface exposed Lys24 residue, which could bridge the gap between the stroma and wat416 and facilitate proton transfer to wat416 and then to the Q<sub>n</sub> site via Arg207. Additional protons may also be supplied to the Q<sub>n</sub> site via a pathway involving the acidic side chains of highly conserved Glu29 and Asp35 residues (subIV) as well as a water molecule. The putative ‘E/D pathway’ is proposed to proceed from the stroma exposed Glu29 via a water molecule to Asp35. In structural studies with bound TDS, the side chain of Asp35 forms a close contact (~ 3.7 Å) with the analogue inhibitor providing a route for proton transfer to the Q<sub>n</sub> site (**Hasan et al., 2013a**).

### 1.3.7 Outstanding questions

Despite numerous studies on the *b<sub>6</sub>f* complex from various species, a number of questions still remain regarding this complex and its vital role at the heart of the photosynthetic electron



transfer chain. Among the major outstanding questions concerning the mechanism of the *b<sub>6</sub>f* complex are:

- 1) The function of the enigmatic Chl *a* molecule unique to *b<sub>6</sub>f*.
- 2) The role of haem *c<sub>n</sub>* and its role in binding the PQ substrate at the Q<sub>n</sub> site.
- 3) How the *b<sub>6</sub>f* complex overcomes the physical and kinetic restraints imposed on the high potential pathway by the large distance between the 2Fe-2S cluster and the *c*-type haem acceptor of *cyt<sub>f</sub>* (i.e. does the Rieske protein undergo significant conformational change to accommodate this as observed in *cytbc<sub>1</sub>* or is some other mechanism in place?).

#### 1.4 Using structural biology to study photosynthesis

A number of structural techniques exist which can be used to visualise life on a molecular level. The most commonly used and accessible of these techniques include x-ray crystallography, nuclear magnetic resonance (NMR) and electron microscopy (EM), the last of which was utilised in these studies to gain a molecular insight into the structure and function of photosynthetic membrane protein complexes. Whilst x-ray crystallography has largely dominated the field of structural biology since the early 1950s, EM has been gaining popularity in recent years, particularly in light of technological advances in cryogenic-EM (cryo-EM) which have yielded the so-called 'resolution revolution' (**Kuhlbrandt, 2014**).

In comparison to x-ray crystallography, cryo-EM has several key advantages which are invaluable for studying macromolecular complexes. These advantages extend beyond simply enabling structural determination of proteins which cannot be crystallised and now encompass a range of new opportunities from visualising protein dynamics (**Murata and Wolf, 2018**) to *in situ* structural studies (**Pfeffer and Mahamid, 2018**). In many instances, cryo-EM has become the routine technique for visualising a range of macromolecular complexes under near native conditions with over 12,000 entries in the Electron Microscopy Data Bank (EMDB) as of 2021.



### 1.4.1 Principles of electron microscopy

In theory, the basic principles of electron microscopy can largely be understood by drawing comparisons with a conventional light microscope.

In both techniques, a source of illumination is focussed on a specimen using a series of lenses to create a magnified, projected image of the specimen containing areas of light and dark. While in light microscopy, the source of illumination is a beam of photons with a relatively long wavelength ( $\sim 400 - 700 \text{ nm}$ , theoretical resolution of  $\sim 200 - 400 \text{ nm}$ ), electron microscopes utilise a beam of energised electrons with a much shorter wavelength (wavelength dependent on the accelerating voltage applied); this theoretically enables imaging of specimens at an atomic level. While the theoretical resolution of electron microscopy vastly exceeds that of conventional light microscopy, the use of electrons to visualise specimens presents a number of challenges which set the technical details of electron microscopy apart significantly from light microscopy.

In its most basic form, a transmission electron microscope (TEM) comprises an electron gun, a series of lenses and a mechanism to view/record an image of the specimen. These components are all maintained under a high vacuum. While photons may be easily focussed through a series of glass lenses, a beam of energised electrons must be focussed using a series of electromagnetic lenses (**Figure 1.14**).

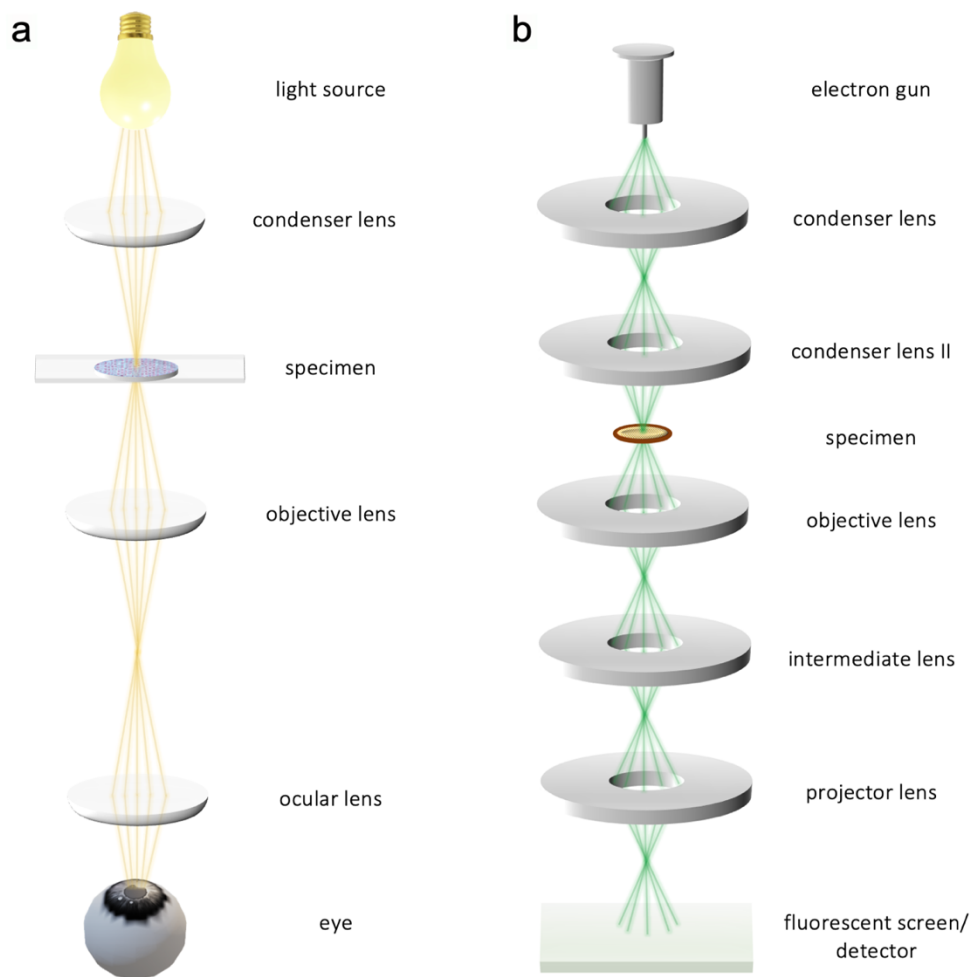


**Figure 1.14 | Comparison of a typical light microscope to a typical transmission electron microscope (TEM).** **a**, In a light microscope, a beam of photons is focused by a glass condenser lens onto the sample. Following interaction with the specimen, the beam is refocused and magnified to produce a magnified image which can be interpreted by the human eye. **b**, In a TEM, the electron beam (green) is focused by a series of electromagnetic lenses onto the specimen. Following interaction with the specimen, the beam is refocused and magnified to produce a magnified image which can be viewed on a fluorescent screen or detector.

As the focussed beam of electrons passes through the specimen, it can interact with atoms in its path and become scattered in two main ways termed ‘elastic’ and ‘inelastic’ scattering (**Figure 1.15**).

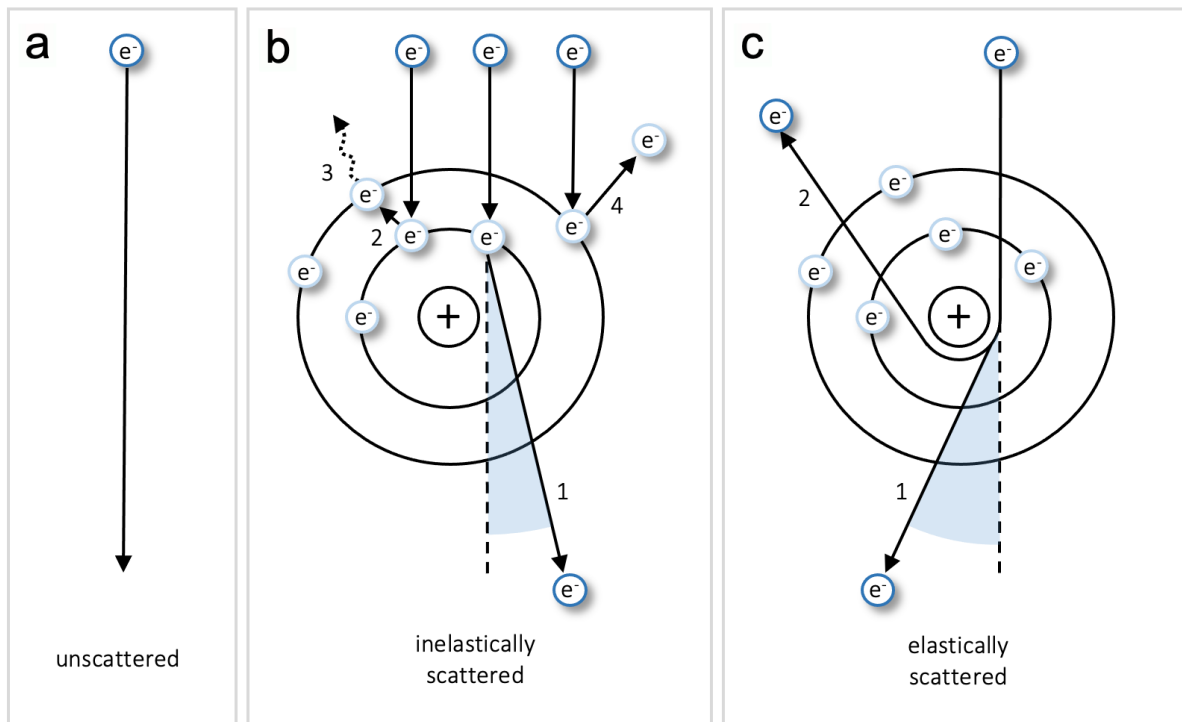


**Figure 1.15 | Interactions between the electron beam and the sample.** **a**, In some cases the electron beam (dark blue circles) may not interact with the sample and passes straight through (unscattered). **b**, In some cases, the electron beam may interact with the specimen and transfer some energy to electrons in the sample (light blue circles). This results in the deflection of the incident electron (now with lower energy) along a path with a different angle relative to the incident path (1) (inelastic scattering). Additionally, the transfer of energy to the sample may result in excitation of an electron in the sample such that it may jump to another orbital (2), emit energy as x-rays (3) or even the ejection of the excited electron from the sample (4). **c**, In some cases the electron beam may interact with the specimen but not lose any energy. This results in the deflection of the incident electron along a path with a different angle relative to the incident path (1) (elastically scattered). Elastically scattered electrons can be deflected at any angle, including the possibility of being scattered back towards the direction of emission (2) (back scattering).

During 'elastic' scattering, electrons within the incident beam are deflected upon interaction with atomic nuclei within the specimen; while there is no transferral of energy during this interaction, the pathlength of the incident electron may be subsequently altered such that it becomes shifted in phase relative to unscattered electrons. Following interaction with the sample, elastically scattered electrons can be refocussed by the electromagnetic lens system and directed towards a detector to reveal information about the structure of the sample.

Conversely, when incident electrons are 'inelastically' scattered, collision with outer shell electrons in the specimen results in the deflection of incident electrons with some concomitant transferral of energy to the specimen. As well as being a source of both radiation damage (e.g. energy transferral can result in x-ray emission, ionisation, free radical formation etc.) and noise (energy transferral can result in the emission of secondary electrons from the sample), inelastically scattered electrons result in blurring of the final image since the loss of differing amounts of energy means emergent electrons will be refocussed to various different focal planes by the electromagnetic lens system. In practice, energy filters are often used to limit the extent to which inelastically scattered electrons contribute to a final image. Filters such as the Gatan Imaging Filter (GIF) provide a means to effectively 'filter' electrons by their respective energy ensuring that only electrons within a set range of wavelengths are directed towards the detector.

Contrast in the resultant image is generated primarily in two ways: amplitude and phase contrast. Amplitude contrast is generated when the number of scattered electrons reaching the detector is fewer than the initial number of incident electrons; this results in areas of high intensity (where large numbers of electrons pass straight through the sample unscattered) and areas of lower intensity (where electrons have lost energy to the sample, been absorbed or been deflected to high scattering angles and subsequently lost within the column or blocked from reaching the detector by the objective aperture). Phase contrast arises from the interference (i.e. constructive or destructive interference) of elastically scattered electron waves with those of unscattered electrons that did not interact with the sample. This interference arises because deflected electrons have a longer pathlength within the microscope relative to the incident path resulting in a shift in their phase at the detector relative to the incident electrons. When the electron waves are recombined at the detector they interfere with each other, this alters their amplitude producing phase contrast. In an electron micrograph, both of these processes contribute to contrast in the image, however the method of preparation defines the extent to which each of these processes will contribute.

Since biological specimens are 'weak' phase objects (i.e. they only cause a very small phase shift in the electron beam) and biological samples are formed primarily of 'light' elements

which scatter electrons very weakly (i.e. C, H, O, N), achieving good contrast in EM micrographs of biological specimens presents a significant challenge. Limitations in contrast are further compounded by the fragility of biological specimens and their susceptibility to radiation damage; this further limits contrast since the dose of electrons used for imaging must be kept low or high-resolution structural information may be lost.

One method to introduce contrast in an image is through heavy metal staining, a process in which the sample is imbued with a heavy metal salt solution (e.g. uranyl acetate) which scatters electrons very strongly. Both positive staining (i.e. staining the specimen itself) and negative staining (i.e. staining the background around the specimen) have historically been employed for EM imaging, however of the two negative staining is the more commonly used technique. As well as introducing additional amplitude and phase contrast to biological specimens (**Brenner and Horne, 1959**), a heavy metal stain is sufficiently resilient so as to allow higher doses of electrons to be used for imaging. While significantly improved contrast can be achieved with negative stain, this comes at the cost of losing high resolution information. As a result, negatively stained specimens are usually unable to achieve resolution past  $\sim 10 - 20 \text{ \AA}$ ; they may also suffer from deformations and artefacts induced by dehydration and staining of the specimen.

While negative stain EM is nevertheless an extremely useful technique to gain a quick insight into a biological specimen where only modest resolutions are required, for high resolution structural studies it is preferable to preserve biological specimens in their native, hydrated state using cryogenic immobilisation (**Adrian et al., 1984**). In cryo-EM, biological specimens can be prepared in several different ways producing filaments, 2D crystalline arrays, monodisperse single particles or even frozen sections of whole cells for tomographic analysis.

For the purposes of this thesis, we will focus primarily on single particle cryo-EM whereby a solution of monodisperse protein 'particles' are preserved in a near-native state within a thin ( $\sim 10-70 \text{ nm}$ ) film of non-crystalline (vitreous) ice via the process of vitrification (**Dubochet et al., 1988**). In an ideal sample, particles would be captured in a range of different orientations within the ice, allowing a number of different views of the protein to be imaged and recombined to form a 3D reconstruction.

While in negative stain, both amplitude and phase contrast are enhanced by introducing a strongly scattering element to the imaging process, in cryo-EM both amplitude and phase contrast are severely limited by a comparative lack of strongly scattering elements in biological samples. Additionally, while imaging under cryogenic conditions affords the sample some protection against radiation damage, electron doses must be kept low to prevent damage to the biological specimen. These various factors result in weak overall contrast (primarily contributed by phase contrast) and a low signal-to-noise ratio in cryo-EM images.

In practice, these limitations can be combatted to an extent through experimental design and image analysis. During an experiment, phase contrast is enhanced by aberrations within the microscope lens system and also by defocussing the microscope; this alters the pathlength of the scattered electrons and induces a larger phase shift relative to the unscattered electrons. By inducing a phase shift, the electron waves can interfere constructively at the image plane, enhancing the phase contrast in the reconstructed image.

#### 1.4.2 Point Spread Functions (PSF) and the Contrast Transfer Function (CTF)

As discussed towards the end of **section 1.4.1**, contrast in the recorded images is greatly influenced by various factors including the defocus of the microscope,  $\Delta f$ , and aberrations within the microscope lens system (the most significant here being the spherical aberration of the objective lens,  $C_s$ ). These various factors, and their effect on the phase of the emergent scattered electron wave, can be cumulatively described using the following equation:

$$\gamma(s) = 2\pi \left( \frac{C_s}{4} \lambda^3 v^4 - \frac{\Delta f}{2} \lambda v^2 \right) \quad (7)$$

where  $\gamma(s)$  is the phase shift,  $C_s$  is the spherical aberration coefficient of the objective lens,  $\Delta f$  is the defocus value,  $v$  stands for spatial frequency and  $\lambda$  is the wavelength of the electrons.

In real space, these various factors result in a blurring of small features in the resultant image such that information from one part of the image is spread into adjacent areas- this is known as the Point Spread Function (PSF). In Fourier space, the effect of these various factors on the observed image can be described by the function  $\sin\gamma(s)$ , known as the Contrast Transfer

Function (CTF). When plotted as a function of as a function of spatial frequency (resolution), the CTF appears as a sinusoidal curve whose amplitude oscillates positively and negatively.

At any given defocus, it is observed at some spatial frequencies that the amplitude of the curve crosses zero resulting in zero contrast (i.e. missing information) in the reconstructed image. In order to fill in this missing information and obtain a reliable 3D reconstruction, images must be collected from a range of defocus values, these can then be combined during processing to 'fill in' missing information at certain spatial frequencies in the recorded images.

### 1.4.3 Single particle cryo-EM image analysis

Image analysis describes a series of processing steps to reconstruct a 3D map of a biological macromolecule from the numerous 2D projections of the molecule recorded within the EM micrographs.

Briefly, an ideal dataset will contain many (potentially millions) of 2D projections of identical protein particles orientated randomly within vitreous ice. In single particle image analysis, 2D projections are selected, aligned, classified according to their orientation and averaged to produce 2D class averages. According to the Projection-slice theorem (**Figure 1.16**), when transformed into Fourier space, these 2D class averages each represent a slice through the 3D Fourier transform of the object. Reconstruction of the 3D structure can be achieved by calculating the angular and phase relationships between each of these slices then reconstructing the 3D structure by reverse Fourier transform.

In practice, the accuracy of these calculations is dependent on the signal-to-noise ratio in the EM micrographs and the presence of 'features' in protein particles which may aid alignment. For these reasons, single-particle analysis has historically been limited to larger, more 'featured' macromolecules however, in recent years, advances in electron microscopes, detectors and image processing programs have made this technique more applicable to a broader range of biological samples at ever increasing resolutions (**Kuhlbrandt, 2014**).

While a number of different programmes exist which can facilitate single particle image analysis, (e.g. RELION (**Scheres, 2012**), Spider (**Shaikh et al., 2008**), EMAN2 (**Tang et al., 2007**),

crYOLO (Wagner et al., 2019), cryoSPARC (Punjani et al., 2017) etc.), we will focus here on methods implemented in RELION 3.1 (Zivanov et al., 2018).

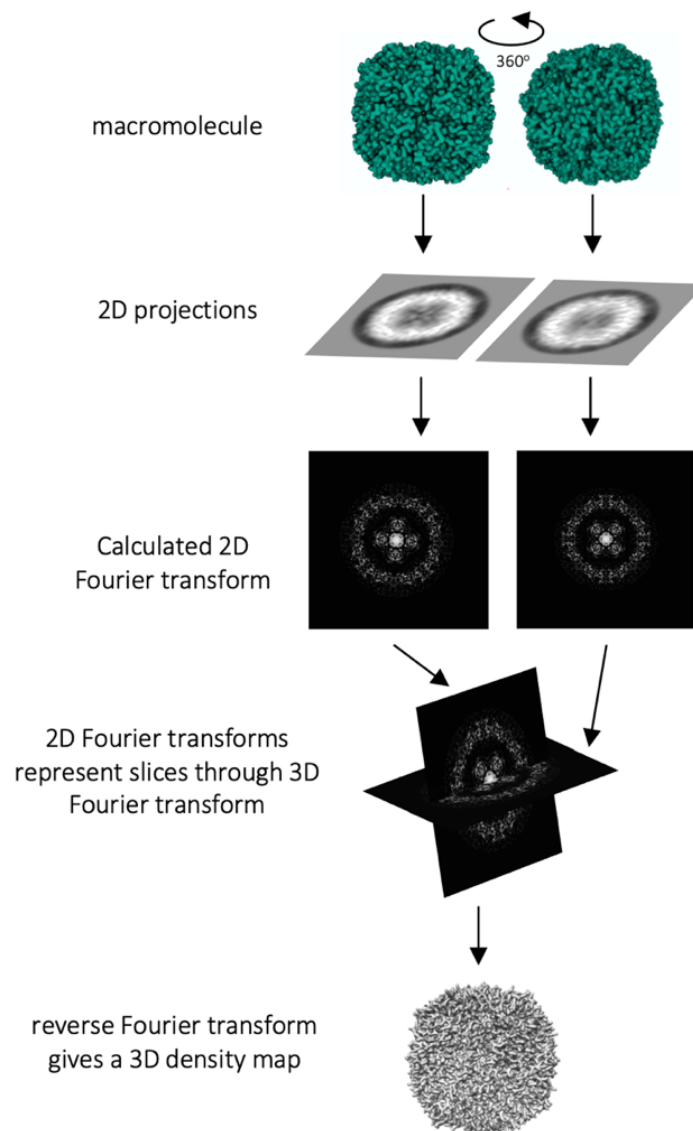


**Figure 1.16 | Schematic demonstrating projection theorem.** A macromolecule adopts an orientation about 360 degrees in real space. When imaged by an electron microscope, a 2D projection of the macromolecule in a particular orientation is observed. A Fourier transform of the 2D projection represents a central slice through the 3D Fourier transform of the object. The angular relationship between Fourier transforms of 2D projections can be calculated to reconstruct the 3D object. Here apoferritin has been used as a model for demonstration purposes (EMDB ID: 6802) (Fan et al., 2017).



### *Initial processing of micrograph movies: motion correction, dose-weighting and CTF estimation*

It is widely acknowledged that exposure of samples to electrons results not only in radiation damage, but also in blurring of the images due to beam-induced motion (**Henderson, 1992**). To a large extent, these two issues can be addressed using direct electron detectors (DEDs) to spread the electron dose across several frames creating a short movie of the exposure. Often the first step of image analysis for many datasets is to align these movie frames (e.g. using MotionCor2 in RELION (**Zheng et al., 2017**)) to correct for beam-induced motion. At the same time, movie frames can also be 'dose weighted' so that frames recorded earlier in the movie with less radiation exposure are given more 'weight' than frames recorded later.

The second step in image analysis is contrast transfer function (CTF) estimation. As discussed in **section 1.4.1**, the recorded image of an object is distorted by various factors (e.g. aberrations in the electromagnetic lens system and the defocus applied during data collection), these can cumulatively be described by a mathematical function known as the CTF. In order to obtain a reliable reconstruction of the specimen, the CTF of micrographs taken at multiple defoci must be estimated. In RELION, motion-corrected images (micrographs) undergo CTF estimation using either CTFFIND (**Rhou and Grigorieff, 2015**) or the GPU accelerated GCTF (**Zhang, 2016**), CTF parameters are then later used for CTF-correction allowing a reliable reconstruction of the object.

### *Selection of 2D projections and classification*

As mentioned earlier, in an ideal sample each EM micrograph will contain many monodisperse 2D projections of identical protein 'particles' randomly orientated within a thin layer of vitreous ice. To further process these 2D projections for 3D reconstruction, each individual projection must be selected, extracted from the micrograph as an individual image and aligned in the same direction. Aligned 2D projections are classified according to their orientation producing homogenous subsets of particles. Averaging of all particles in these subsets produces relatively detailed projection views with significantly enhanced signal-to-noise. Generally, the more particles are averaged, the higher the signal-to-noise ratio and the higher the resolution which can be achieved in the final reconstruction. In practice, 2D classification is often used to quickly assess the quality of a dataset, it is also an extremely

useful step to remove poor quality particles which do not average well and coordinates which may have been selected during particle picking which fail to conform to the molecule of interest (i.e. 'junk'). Since many programs implement an automated particle picking approach (e.g. auto-pick in RELION), it is likely that a significant amount of 'junk' may also be selected initially including ice contamination, carbon edges, areas of aggregation etc.

#### *Reconstruction and 3D classification*

To reconstruct a 3D map from the 2D class averages, the angular relationships between 2D class averages must be determined. Here, 'common lines' of correlation in the Fourier transforms of 2D class averages provide information about the relative positioning of each class in 3D space. In practice, an added complexity in 3D reconstruction is structural heterogeneity and conformational flexibility in the sample, this can be addressed by further classification of the dataset into discrete 3D structures at low resolution. Once a subset of sufficiently homogenous particles has been obtained, the resultant 3D reconstruction can be refined to a higher resolution, producing a map that reveals fine structural features within which an atomic model of the macromolecule can be constructed.

## 2 Materials and Methods

### 2.1 Materials, buffers and reagents

All chemicals and reagents were of standard lab grade or higher supplied by Sigma-Aldrich Company Ltd. (Dorset, UK) or Thermo Fisher Scientific UK Ltd (Loughborough, UK) unless otherwise stated. In all cases, Milli-Q® Integral ultrapure (Milli-Q) water was the standard water source used unless otherwise stated; this was prepared using a Milli-Q® Integral Water Purification System (Millipore UK Ltd., Watford, UK) to a purity of 18.2 mΩ cm at 25 °C.

All buffers were adjusted to the required pH using appropriate concentrations of HCl or NaOH/KOH. Buffers used in chromatography were vacuum sterilised using a 0.2 µM filter and degassed. Buffers containing detergent and/or phospholipids were filtered and degassed prior to the addition of these components.

### 2.2 The preparation of plant material

#### 2.2.1 *Spinacia oleracea* material

All *S. oleracea* material used in this study was purchased from a local supermarket the day before use and stored at 4 °C until required.

#### 2.2.2 Thylakoid preparation with NaBr wash for the purification of *cytb<sub>6</sub>f* from *S. oleracea*

The following is a protocol adapted from **Dietrich and Kuhlbrandt, 1999**. All buffers are outlined in **Table 2.1**.

Briefly, leaves were homogenised in Buffer 1A using a kitchen blender; homogenate was then filtered through two layers of muslin and cotton wool sandwiched between muslin before the filtrate was centrifuged for 15 min at 4540 x g (max), 4°C. Following centrifugation, the supernatant containing cell debris was discarded and the pellet resuspended in Buffer 2A before centrifugation again for 15 min, 4540 x g (max), 4°C. The resultant pellet was resuspended in Buffer 3A and incubated on ice for 15 min before diluting 2-fold with ice cold milliQ and centrifuging for 15 min, 4540 x g (max), 4°C. The resultant pellet was resuspended again in Buffer 3A and incubated on ice for 15 min before diluting 2-fold with ice cold milliQ and centrifuging again for 15 min 4540 x g (max), 4°C. The pellet was resuspended in Buffer

2A and centrifuged for 15 min 4540 x g (max), 4°C. The final pellet was then resuspended in a small volume of Buffer 4A.

**Table 2.1 | An outline of the buffers used to prepare *S. oleracea* thylakoids in section 3.1.1.**

Buffers	Components
<b>Thylakoid Buffer 1A</b>	50 mM tris pH 7.5 200 mM sucrose 100 mM sodium chloride
<b>Thylakoid Buffer 2A</b>	150 mM sodium chloride 10 mM tricine pH 8
<b>Thylakoid Buffer 3A</b>	2 M sodium bromide 10 mM tricine pH 8 300 mM sucrose
<b>Thylakoid Buffer 4A</b>	40 mM tricine pH 8.0 10 mM magnesium chloride 10 mM potassium chloride

### 2.2.3 Thylakoid preparation without NaBr wash for the purification of plastocyanin from *S. oleracea*

All buffers are outlined in **Table 2.2**.

Briefly, spinach leaves were homogenised in Buffer 1B; homogenate was then filtered and centrifuged for 15 min at 4000 x g (max). Following centrifugation, the supernatant containing cell debris was discarded and the pellet resuspended in Buffer 2B. The solution was incubated on ice for 1 min before diluting 2-fold with Buffer 3B and centrifuging for 15 mins at 4000 x g (max). Following centrifugation, the pellet was resuspended to a chlorophyll concentration of 2 mg ml<sup>-1</sup> in Buffer 4B.

Table 2.2| An outline of the buffers used for the preparation of *S. oleracea* thylakoids in **section 3.7.1**.

Buffers	Components
<b>Thylakoid Buffer 1B</b>	50 mM sodium phosphate pH 7.4 5 mM magnesium chloride 300 mM sucrose
<b>Thylakoid Buffer 2B</b>	10 mM tricine pH 7.4 5 mM magnesium chloride
<b>Thylakoid Buffer 3B</b>	10 mM tricine pH 7.4 5 mM magnesium chloride 400 mM sucrose
<b>Thylakoid Buffer 4B</b>	10 mM HEPES pH 7.6 5 mM sodium chloride 5 mM EDTA disodium salt

#### 2.2.4 Chlorophyll quantification assay

Total chlorophyll concentration [Chl] and Chl *a*/Chl *b* ratios of isolated thylakoids were calculated using the following method established by **Porra et al., 1989**:

Pigment was extracted by adding 4  $\mu$ l of thylakoid suspension to 2 ml of 80 % (v/v) acetone. This solution was then mixed by vortex and centrifuged at 14,000 rpm in a bench top centrifuge for 3 mins to remove precipitates prior to spectrophotometric analysis on a Cary 60 UV-Vis Spectrophotometer (Agilent Technologies, Santa Clara, CA, USA).

Total Chlorophyll content in  $\text{mg ml}^{-1}$  ([Chl *a*] + [Chl *b*]) and the ratio of [Chl *a*]/[Chl *b*] were calculated using the following equations:

$$[Chl a] = \frac{12.25A_{663*} - 2.55A_{646*}}{2}$$

$$[Chl b] = \frac{20.31A_{646*} - 4.91A_{663*}}{2}$$

$$A_{646*} = A_{646} - A_{750}$$

$$A_{663*} = A_{663} - A_{750} \quad (8)$$

## 2.3 The preparation of *Synechocystis* material

The preparation of *Synechocystis* material (including all molecular cloning as well as the growth and harvest of selected strains) was carried out by Dr A. Hitchcock and Dr M. Proctor at the University of Sheffield.

### 2.3.1 Strains and plasmids

All strains used in this study are outlined in **Table 2.3**, these were engineered using plasmids outlined in **Table 2.4**.

**Table 2.3| Strains of *Synechocystis* sp. PCC6803 used in this study.**

Strain name	Description	Source
<b>petA-Strep</b>	<i>Synechocystis</i> sp. PCC6803 expressing a strep-tag on the C-terminus of <i>cyt f</i> in place of the native <i>cyt f</i> ( <i>puC19::petA-SII</i> ). Chloramphenicol resistant.	Dr M. Proctor, University of Sheffield

**Table 2.4| An outline of plasmids used in this study.**

Plasmid name	Description	Source
<b>puC19::petA-SII</b>	pUC19 containing <i>petA</i> with a C-terminal StrepII-tag and a chloramphenicol resistance cassette.	Dr M. Proctor, University of Sheffield

<b>puC19::petA-SII</b>	pUC19 containing <i>petA</i> with a C-terminal StrepII-tag and a chloramphenicol resistance cassette.	Dr M. Proctor, University of Sheffield
------------------------	---	--

### 2.3.2 Growth media

All stock solutions and media used in this study are listed in **Table 2.5** and **Table 2.6** respectively. In all cases, media were sterilised by autoclave prior to use. Any heat-labile antibiotics and supplements were sterilised by filtration through a 0.2 µm filter before addition to autoclaved media.

**Table 2.5 | An outline of stock solutions for media preparation.**

Stock solution	Reagents	Amount for 1 litre
<b>10X Trace minerals</b>	Boric acid	2.86 g
	Manganese chloride	1.81 g
	Zinc sulphate	0.22 g
	Sodium molybdate	0.39 g
	Copper sulphate	0.079 g
	Cobaltous nitrate	0.049 g
<b>1 M TES pH 8.2</b>	TES	229.2 g
<b>1000X Iron</b>	Ferric ammonium citrate	6.0 g
<b>1000X Phosphate</b>	Dipotassium hydrophosphate	30.5 g
<b>1000X Carbonate</b>	Sodium carbonate	20.0 g
<b>0.5 M EDTA</b>	Ethylenediaminetetraacetic acid disodium salt	0.5 M
<b>100X BG11</b>	Sodium nitrate	149.6 g
	Magnesium Sulphate	7.5 g
	Calcium chloride	3.6 g

	Citric acid	0.60 g
	Trace minerals mix	100 ml of 10X stock

**Table 2.6| An outline of media used in this study.**

Stock solution	Reagents	Amount for 1 litre
<b>BG11 liquid medium (1X)</b>	100X BG11	10.0 ml
	1000X Iron	1.0 ml
	1000X Phosphate	1.0 ml
	1000X Carbonate	1.0 ml
	1 M TES (add after autoclave)	10.0 ml
<b>BG11 agar (1X)</b>	100X BG11	10.0 ml
	1000X Iron	1.0 ml
	1000X Phosphate	1.0 ml
	1000X Carbonate	1.0 ml
	Bacto-agar (w/v)	15.0 g
	Sodium thiosulphate	3.0 g
	1 M TES (add after melting)	10.0 ml

*Synechocystis* strains were grown photoautotrophically on BG11 agar supplemented with 34  $\mu\text{g ml}^{-1}$  chloramphenicol at 30 °C with 40  $\mu\text{mol photons m}^{-2} \text{s}^{-1}$ . For liquid cultures, a scraping of cells was aseptically inoculated into 50 ml BG11 and incubated at 30 °C in a rotary shaker (150 rpm) at a constant illumination of 40  $\mu\text{mol photons m}^{-2} \text{s}^{-1}$ . *Synechocystis* stocks were prepared from 50 ml cultures by re-suspending in 400  $\mu\text{l}$  liquid BG11 media plus 10 % (v/v) DMSO, flash freezing in liquid nitrogen for storage at - 80 °C.



For purification of *cytb<sub>6</sub>f*, cultures were grown photoautotrophically with 100  $\mu\text{mol photons m}^{-2} \text{ s}^{-1}$  illumination in 8000 ml vessels bubbled with sterile air at 30 °C with constant mixing by magnetic stirrer until an optical density (OD) of 1.0 (measured at 600 nm) was reached. Cells were harvested by centrifugation (10 mins, 4 °C) in a Beckman Coulter FiberLite F10BCI rotor then resuspended in ~ 30 ml *Synechocystis* Thylakoid Buffer 1 (**Table 2.7**) prior to flash freezing in liquid nitrogen and storage at - 20 °C.

### 2.3.3 *Synechocystis* thylakoid preparation

Briefly, *Synechocystis* cell pellets were thawed on ice, protease inhibitors (Roche) were added (1 tablet/10 ml) and the cells were broken by bead beating using 0.1 mm glass beads (Thistle Scientific) in a mini bead beater (Bio Spec). Cells underwent 8 cycles of bead beating, each lasting 55 sec with a 3 min interval of cooling on ice in between each cycle. The beads were separated from the cell lysate by washing with *Synechocystis* Thylakoid Buffer 1 (**Table 2.7**); the cell lysate was then centrifuged at 4696 x *g* (max) for 10 min at 4 °C to remove any unbroken cells. Following centrifugation, the pellet was removed before the supernatant was centrifuged at 48,400 x *g* for 30 min at 4 °C to pellet the *Synechocystis* thylakoid membranes. Pelleted membranes were resuspended in *Synechocystis* Thylakoid Buffer 2 (**Table 2.7**) as specified in the relevant results section.

**Table 2.7** | An outline of buffers used for the preparation of *Synechocystis* thylakoids in section 5.1.

Buffers	Components
<b><i>Synechocystis</i> Thylakoid Buffer 1</b>	25 mM sodium phosphate pH 7.6 10 mM magnesium chloride 50 mM sodium chloride 10 % (w/v) glycerol
<b><i>Synechocystis</i> Thylakoid Buffer 2</b>	25 mM sodium phosphate pH 7.6 10 mM magnesium chloride 300 mM sodium chloride

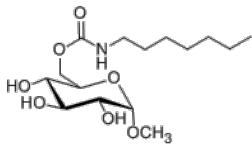
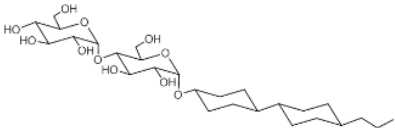
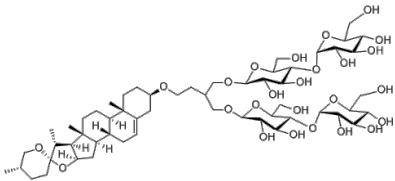
## 2.4 Protein purification techniques

A range of techniques were used to purify the target complexes examined in this study. Descriptions of each of the purification methods utilised are outlined below, with specific details given for each unique protocol in the relevant results section.

### 2.4.1 Solubilisation

Details of detergents used to solubilise membranes in this study are outlined in **Table 2.8** with specific details regarding their use provided in the relevant results section. In all cases, solubilisation was carried out on freshly prepared thylakoid samples on ice; samples were mixed thoroughly following addition of detergent and incubated for a set time (specific details given in relevant results section). Following incubation, samples were diluted to near their critical micelle concentration (CMC) then ultracentrifuged ( $\sim 244,000 \times g$  for 30 min at  $4^\circ\text{C}$  in a Beckman TLA 100.2 rotor for *S. oleracea* preparations;  $48,500 \times g$  (max) for 30 min for *Synechocystis* preparations) to remove any unsolubilised material.

**Table 2.8| An outline of the detergents used in this study.**

Detergent	Synonyms	CMC (mM)	MW (g/mol)	Supplier	Molecular structure
<b>6-O-(n-Heptylcarbamoyl)-Methyl-<math>\alpha</math>-D-Glucopyranoside</b>	HECAM EG	19.5	335.40	Anatrace	
<b>4-trans-(4-trans-Propylcyclohexyl)-cyclohexyl <math>\alpha</math>-maltoside</b>	tPCC- $\alpha$ -M	0.036	547.70	Glycon	
<b>Glyco-diosgenin</b>	GDN	0.018	1165.31	Anatrace	

### 2.4.2 Sucrose gradients

Continuous sucrose gradients were used for density gradient ultracentrifugation here; these were poured on ice using a Hoefer SG 100 Gradient Maker and a Gilson Minipuls 3 peristaltic pump. In all cases, sucrose solutions (**Table 2.9** and **Table 2.10**) were prepared immediately prior to use by dissolving the required amount of sucrose (w/v) into an appropriate base buffer.

The sample was concentrated down to a 0.5 – 3 ml volume depending on the gradient size then carefully layered on top of the density gradients before ultracentrifugation. Specific details for each sucrose gradient ultracentrifugation step used and the samples loaded onto each gradient are provided in the relevant results section. In all cases, low concentrations of appropriate detergent and lipids were added to sucrose solutions prior to pouring as specified in the appropriate results section. Bands were harvested from gradients using a Hoefer SG 100 Gradient Maker and a Gilson Minipuls 3 peristaltic pump.

**Table 2.9 | An outline of sucrose gradient solutions used in section 3.2.**

Solution	Components
<b>10 % sucrose solution</b>	10 % (w/v) sucrose 40 mM Tricine pH 8 10 mM magnesium chloride 10 mM potassium chloride 0.7 % (w/v) HECAMEG 0.1 mg ml <sup>-1</sup> egg yolk L- $\alpha$ -phosphatidylcholine (Sigma)

**Table 2.10** | An outline of sucrose gradient solutions used in sections 3.4 and 3.5.

<b>Solution</b>	<b>Components</b>
<b>10 % sucrose solution</b>	10 % (w/v) sucrose 50 mM HEPES pH 8 20 mM NaCl 0.3 mM tPCC $\alpha$ M
<b>35 % sucrose solution</b>	40 % (w/v) sucrose 50 mM HEPES pH 8 20 mM NaCl 0.3 mM tPCC $\alpha$ M

#### 2.4.3 Sonication

Thylakoid preparations were sonicated for a total of 12 mins in 30 bursts with 30 sec rests using a VCX Vibra-Cell™ Ultrasonic Liquid Processor; separation of soluble and insoluble fractions was achieved by ultracentrifugation (1 hour, 200,000 x g (max), 4 °C in a Ti50.2 rotor to pellet).

#### 2.4.4 Ceramic Hydroxyapatite (CHT) chromatography

A 5 ml Bio-scale Mini Type I CHT (40  $\mu$ m) column (Bio-Rad) was pre-equilibrated with CHT Equilibration Buffer (**Table 2.11**) at a flow rate of 2 ml min<sup>-1</sup>. The sample was loaded on to the column at a flow rate of 2 ml min<sup>-1</sup> then the column was washed with 5 column volumes (CV) of CHT Wash Buffer (**Table 2.11**). The sample was eluted with 5 CV of CHT Elution Buffer (**Table 2.11**) at a flow rate of 2 ml min<sup>-1</sup>.

**Table 2.11 | An outline of buffers used for CHT chromatography in sections 3.3 and 3.5.**

<b>Buffers</b>	<b>Components</b>
<b>CHT Equilibration Buffer</b>	0.7 % (w/v) HECAMEG 0.1 mg ml <sup>-1</sup> egg yolk L- $\alpha$ -phosphatidylcholine (Sigma) 20 mM tricine pH 8
<b>CHT Wash Buffer</b>	0.7 % (w/v) HECAMEG 0.1 mg ml <sup>-1</sup> egg yolk L- $\alpha$ -phosphatidylcholine (Sigma) 100 mM ammonium phosphate pH 8
<b>CHT Elution Buffer</b>	0.7 % (w/v) HECAMEG 0.1 mg ml <sup>-1</sup> egg yolk L- $\alpha$ -phosphatidylcholine (Sigma) 400 mM ammonium phosphate pH 8

#### 2.4.5 StrepTactin affinity chromatography

A 5 ml StrepTrap™ High Performance column (GE Healthcare Life Sciences) connected to a peristaltic pump was used; this was pre-equilibrated in buffer as specified in the appropriate results section. Solubilised thylakoid membranes were applied to the column at a flow rate of 2 ml min<sup>-1</sup>; the column was washed with the same buffer used for equilibration and eluted with buffer containing 2.5 mM *d*-Desthiobiotin as specified in the appropriate results section (**Table 2.12**).

**Table 2.12 | An outline of buffers used for StrepTactin affinity chromatography in section 5.1.2.**

Buffers	Components
<b>StrepTrap Equilibration Buffer</b>	25 mM sodium phosphate pH 7.6 10 mM magnesium chloride 50 mM sodium chloride 0.02 % (w/v) GDN
<b>StrepTrap Elution Buffer</b>	25 mM sodium phosphate pH 7.6 10 mM magnesium chloride 150 mM sodium chloride 0.02 % (w/v) GDN 2.5 mM <i>d</i> -desthiobiotin (Merck)

#### 2.4.6 Gel filtration

A HiLoad 16/600 Superdex 200 pg Gel-filtration column (GE Healthcare Life Sciences) connected to an ÄKTA purification system (GE Healthcare Life Sciences) was for size exclusion chromatography. The column was pre-equilibrated in Gel Filtration Buffer (**Table 2.13 and Table 2.14**) before ~ 1 – 2 ml of concentrated sample was loaded at a flow rate of 0.2 ml min<sup>-1</sup>. In all cases, a low concentration of the appropriate detergent was added to all wash and elution buffers as specified in the appropriate results section.

**Table 2.13 | An outline of buffers used for gel filtration in sections 3.4 and 3.5.**

Buffers	Components
<b><i>S. oleracea</i> Gel Filtration Buffer</b>	50 mM HEPES pH 8 20 mM NaCl 0.3 mM tPCC- $\alpha$ -M

**Table 2.14 | An outline of buffers used for gel filtration in section 5.1.3.**

Buffers	Components
<b><i>Synechocystis</i> Gel Filtration Buffer</b>	25 mM sodium phosphate pH 7.6 10 mM magnesium chloride 150 mM sodium chloride 0.02 % (w/v) GDN

#### 2.4.7 Anionic exchange chromatography (AEC)

4 x 5 ml HiTrap® Q FF, Q Sepharose® Fast Flow (GE Healthcare Life Sciences) were connected to an AKTA purification system (GE Healthcare Life Sciences) for AEC. Columns were pre-equilibrated in Anionic Exchange Buffer A (**Table 2.15**) at a flow rate of 5 ml min<sup>-1</sup> before the sample was loaded at a flow rate of 5 ml min<sup>-1</sup>. Sample was eluted over a 150 ml gradient of 5-500 mM Sodium chloride using Anionic Exchange Buffers A (**Table 2.15**) and B (**Table 2.15**).

**Table 2.15 | An outline of buffers used for anionic exchange chromatography in sections 3.7.1.**

<b>Buffers</b>	<b>Components</b>
Anionic Exchange Buffer A	20 mM HEPES pH 8 5 mM sodium chloride
Anionic Exchange Buffer B	20 mM HEPES pH 8 500 mM sodium chloride

## 2.5 Biochemical analysis of proteins

### 2.5.1 Sodium dodecyl sulphate polyacrylamide gel electrophoresis (SDS-PAGE)

Precast NuPAGE™ 12 % polyacrylamide Bis-Tris gels (Novex Life Technologies, Carlsbad, CA, USA) were used for SDS-PAGE. Samples were diluted two-fold with 2X Laemmli buffer (BioRad, Hemel Hempstead, UK ) and heated to 100 °C for 5 mins before loading onto the gel. 10 µl Precision Plus Protein Unstained Standard (Bio-rad) was also loaded into the first well of every gel as a reference. Gels were run at 160 V for 60 mins with 1X NuPAGE™ MES SDS Running Buffer in the outer and inner chambers of the gel tank (Novex Life Technologies) (**Table 2.16**) then stained for 5 mins in Coomassie brilliant blue G250 (**Table 2.16**) before destaining in milliQ water overnight. Gels were imaged on an Amersham Imager 600 (GE Healthcare).



**Table 2.16 | Buffers used for SDS-PAGE.**

<b>Buffers</b>	<b>Component</b>
<b>NuPAGE™ MES SDS Running Buffer</b>	1X NuPAGE™ MES SDS Running Buffer (20X stock)
<b>Coomassie Brilliant Blue G-250</b>	For 500 ml:  0.6 g Coomassie Brilliant Blue G-250 250 g trichloroacetic acid  0.1 g SDS  0.15 g glycine  0.25 g tris

### 2.5.2 Blue-native polyacrylamide gel electrophoresis (BN-PAGE)

Precast NativePAGE™ 3 – 12 % polyacrylamide Bis-Tris gels (Novex Life Technologies) were used for BN-PAGE. Gels were loaded with 20 µl samples mixed with 2 µl BN-PAGE Loading Dye (**Table 2.17**). Gels were run at 160 V for 120 mins with 1 L of NativePAGE™ Anode Buffer in the outer chamber (Novex Life Technologies) (**Table 2.17**) and ~ 200 ml NativePAGE™ Cathode Buffer (Novex Life Technologies) (**Table 2.17**) in the inner chamber. Gels were further stained with Coomassie Brilliant Blue G250 (**Table 2.17**) before destaining in milliQ water overnight. Gels were imaged on an Amersham Imager 600 (GE Healthcare).

**Table 2.17 | Buffers used for BN-PAGE.**

<b>Buffers</b>	<b>Component</b>
<b>BN-PAGE Loading Dye</b>	125 mM tris pH 6.8 30 % (v/v) glycerol 0.01 % (w/v) bromophenol blue
<b>NativePAGE Cathode Buffer</b>	1X NativePAGE™ Running Buffer (20X stock) ~ 2 ml Coomassie Brilliant Blue G-250
<b>NativePAGE Anode Buffer</b>	1X NativePAGE™ Running Buffer (20X stock)
<b>Coomassie Brilliant Blue G-250</b>	For 500 ml: 0.6 g Coomassie Brilliant Blue G-250 250 g trichloroacetic acid 0.1 g SDS 0.15 g glycine 0.25 g tris

### 2.5.3 Ultraviolet - visible (UV/Vis) absorbance spectroscopy

UV/Vis absorbance spectra were recorded at room temperature on a Cary60 spectrophotometer (Agilent) using a sample cuvette with a 1 cm path length. Prior to the collection of absorbance spectra, the machine was blanked using a sample of an appropriate base buffer. Specific details are provided in the relevant results sections.

For redox-difference spectra, redox active groups were first fully oxidised with a few grains of an appropriate oxidation agent (e.g. potassium ferricyanide) followed by reduction with a few grains of an appropriate reducing agent (e.g. sodium ascorbate (*c*-type haem *f*), sodium dithionite (*c*-type haem *f* and *b*-type haems  $b_n$  and  $b_p$ ). At each stage the sample was mixed thoroughly and incubated for ~ 1 min before recording spectra.

Redox difference spectra (reduced minus oxidised) were calculated accordingly and used to determine the concentrations of redox-active components in the sample using extinction coefficients as outlined in the relevant results section.

#### 2.5.4 Stopped-flow absorbance spectroscopy

An Olis RSM 1000 UV/Vis rapid-scanning spectrophotometer (Olis, Athens, GA, USA) equipped with a U.S.A stopped flow cell (Olis) was used for stopped-flow absorbance spectroscopy. Reaction components were split into two solutions which could be rapidly mixed, the first contained the enzymes required for reaction and the second contained the substrate. Reactions were monitored by recording the change in absorbance occurring at a specific wavelength at 20 °C. Further details are provided in the relevant results section.

#### 2.5.5 Western blotting

SDS-PAGE was carried out as described in **section 2.5.1** however, Precision Plus Protein Dual Color Standards (BioRad) were used and gels were not subjected to staining with Coomassie Brilliant Blue G250. Instead, unstained gels underwent overnight transfer to polyvinylidene fluoride (PVDF) membranes (Novex Life technologies), which were activated in methanol for ~ 1 min prior to use. Transfer was carried out in Transfer Buffer (**Table 2.18**) at 4 °C.

Following protein transfer, PVDF membranes were washed in Tris-buffered saline (**Table 2.18**) and blocked in Blocking Buffer (**Table 2.18**) for 1 hour at room temperature with gentle rocking applied. Membranes were then washed in Antibody Buffer (**Table 2.18**) and incubated in primary (1°) antibody for 4 hours at room temperature with gentle rocking applied. Membranes were washed in Antibody Buffer three times for 5 min before incubation with secondary (2°) antibody conjugated with Horseradish Peroxidase for 1 hour at room temperature with gentle rocking applied. Membranes were washed a further 3 times for 5 min in Antibody Buffer before chemiluminescence imaging. Chemiluminescence was initiated using application of 1 ml of WESTAR SUN chemiluminescence reagents (Cyanagen, Bologna, Italy) then membranes were imaged using the Amersham Imager 600 (GE Healthcare) in chemiluminescence mode. Further details are provided in the relevant results section.

**Table 2.18| Buffers used for western blots.**

<b>Buffers</b>	<b>Component</b>
<b>Transfer Buffer</b>	10 mM sodium bicarbonate (NaHCO <sub>3</sub> ) 3 mM sodium carbonate (Na <sub>2</sub> CO <sub>3</sub> ) 10 % (v/v) methanol
<b>Tris Buffered Saline</b>	50 mM tris pH 7.6 150 mM sodium chloride
<b>Blocking Buffer</b>	50 mM tris pH 7.6 150 mM sodium chloride 5 % (w/v) skimmed milk powder 0.2 % (w/v) tween 20
<b>Antibody Buffer</b>	50 mM tris pH 7.6 150 mM sodium chloride 0.05 % (w/v) tween 20

## 2.6 Negative stain transmission electron microscopy (TEM)

### 2.6.1 Grid preparation and negative staining

Carbon-coated 400 mesh Cu grids (Agar Scientific, Stansted, UK) were rendered hydrophilic by glow discharging for 30 secs using a Cressington Carbon Coater. Purified protein samples (5 µl) were diluted to a suitable concentration with appropriate buffer and adhered to the freshly glow discharged grids by incubating for 1 min. Grids were blotted with filter paper (Whatman No. 1) to remove excess protein sample then washed and blotted twice with 10 µl milliQ then once with 10 µl 0.75 % (w/v) uranyl formate stain. Grids were then incubated for 45 secs in the same stain before blotting for a final time and storing in the dark.

### 2.6.2 Imaging

All grids containing negative stained samples were imaged at room temperature using a Philips CM100 Transmission Electron Microscope (TEM) operating at 100 kV. Images were

recorded at between 25,800 and 73,000 X nominal magnification and defocus value between 500 - 1,200 nm on a Gatan Multiscan 794 1K x 1K CCD.

## 2.7 Single particle cryo-TEM

### 2.7.1 Cryo-TEM materials

**Table 2.19| Microscopes used for cryo-EM in this study.**

Microscope	Location	Detector	Voltage (kV)	Electron source
<b>Technai Arctica</b>	University of Sheffield	Falcon III	200	Field emission gun (FEG)
<b>Titan Krios</b>	University of Leeds	Falcon III	300	Extreme FEG (X-FEG)
<b>Titan Krios</b>	University of Leeds	K2 summit	300	X-FEG
<b>Titan Krios</b>	eBIC, Oxford	BioQuantum K3	300	X-FEG

### 2.7.2 Grid preparation, plunge freezing and vitrification

For single particle experiments, grids were rendered hydrophilic by glow discharging for 30 secs using a Cressington Carbon Coater. Purified protein samples were then adhered to the freshly glow discharged grids under controlled conditions. Grids were incubated with sample before excess liquid was blotted off; samples were then plunge frozen in liquid ethane (-180°C) using a Leica EM GP. Grids were transferred from liquid ethane to liquid nitrogen under vapour then stored under liquid nitrogen conditions until use.

Specific details of grid preparation for each experiment are provided in the relevant results section.

### 2.7.3 Screening

Vitrified protein samples were screened either at The University of Leeds using the EPU software (Thermo Fisher) on a Titan Krios microscope (Thermo Fisher) operated at 300 kV and equipped with a Falcon III direct electron detector (FEI) or at The University of Sheffield using the EPU software on a Technai Arctica (FEI) operated at 200 kV equipped with a Falcon III

direct electron detector (FEI) (**Table 2.19**). Specific parameters used for screening are provided in the relevant results section.

#### 2.7.4 Data collection and imaging

Data acquisition was carried out using the EPU software (Thermo Fisher) on a Titan Krios microscope (Thermo Fisher), this was operated at 300 kV and equipped with either an energy filtered (slit width 20 eV) K2 summit direct electron detector (Gatan) (**Table 2.19**) or a Bioquantum K3 detector (Ametek-Gatan) (**Table 2.19**). Specific details of data acquisition parameters are shown in the relevant results section.

## 2.8 Image Processing

### 2.8.1 Single particle reconstruction using RELION

Single particle processing and reconstruction was performed in RELION 2.1 (**Fernandez-Leiro and Scheres, 2017**), 3.0 (**Zivanov et al., 2018**) or 3.1 (**Zivanov et al., 2019, 2020**). Further details of specific parameters used for each experiment are provided in the relevant results section.

Movies were motion corrected and dose-fractionated using MotionCor2 (**Zheng et al., 2017**) before the GCTF subroutine (**Zhang, 2016**) was employed to estimate Contrast Transfer Function (CTF) parameters of the dose-weighted motion corrected images.

A subset of particles was manually picked from the micrographs, these were extracted and subjected to reference-free 2D classification to iteratively generate 2D class averages. Well averaged 2D classes revealing several different views of the sample were selected for use as templates for autopicking (**Scheres, 2015**). In cases where autopicking was unsuccessful, particles were manually picked.

Particle sorting and reference-free 2D classification were performed iteratively to obtain well averaged and homogenous stacks of particles (**Scheres, 2015**). Particles that categorised into poorly defined classes were rejected, while the remaining particles which averaged well into defined 2D classes were retained for high resolution reconstruction.

A small subset of extracted particles representing as many views of the sample as possible was used to generate a low-resolution 3D model using the 'Initial Model' subroutine in RELION.

To obtain a suitably homogenous set of particles, unsupervised 3D classification ('3D classification') was performed iteratively to generate 3D classes using the initial model low pass filtered to 20 Å as a reference map. Low resolution 3D classes were analysed in UCSF Chimera (v 1.13.1) or Chimera X (v 1.1.1) before stable classes of 3D classes of sufficient homogeneity were selected for further refinement.

The selected subset of homogenous particles underwent re-extraction and re-centring (and rescaling to the original pixel size if data was binned) before 3D auto refinement was carried out. The selected subset of particles was further refined iteratively using the '3D auto-refine' procedure in RELION to produce a higher resolution model. Per-particle CTF-refinement was then carried out and a soft mask was created to exclude solvent around the complex (the detergent micelle was retained within the mask) before another round of 3D refinement. The resultant density map was corrected for the modulation transfer function (MTF) of the detector used (**Table 2.19**) before the map was further sharpened using the post-processing procedure in RELION. For datasets processed in RELION 3.1, the CTF-refined particles were then subjected to 'Bayesian Polishing' (**Zivanov et al., 2019**) followed by a further round of postprocessing and CTF-refinement of polished particles; this was repeated until there was no further improvement in resolution.

The final global resolution was calculated using the gold-standard Fourier shell correlation (FSC= 0.143) criterion (**Scheres and Chen, 2012**). Local resolution was determined using one of the two unfiltered half-maps from the final round of 3D refinement as an input, a calibrated pixel size for the microscope used and a B-factor determined by RELION.

### 2.8.2 Conformational flexibility analysis

Conformational flexibility analysis (**Punjani and Fleet, 2021**) was carried out in cryoSPARC (v 2.15.0) (**Punjani et al., 2017**) using the 3D-variability analysis (3DVA) tool. Sets of homogenous particle stacks generated in RELION were imported into cryoSPARC where they were realigned using an inverted postprocessed map to correct for handedness.

For conformational variability analysis on the entire complex, a low pass filtered (15 Å) mask was generated in RELION using the 'MaskCreate' subroutine; this excluded solvent and added a soft edge. The mask was flipped to correct for handedness and was imported to cryoSPARC using the volume import tool. Data was low pass filtered to 5 Å resolution, all other parameters were kept as default. For conformational variability in a subregion of the complex, the same routine was implemented however regions of the mask were removed using the volume eraser tool in Chimera X (v 1.1.1).

## 2.9 Structural modelling and validation

### 2.9.1 Homology-based modelling, rigid body fitting and manual model building

Initially, a homology-based approach was performed using an existing structure of a homologue as a template. Sequence alignments of the eight polypeptide subunits of *cytb<sub>6f</sub>* were carried out using the Clustal Omega web server (v 1.2.4), targeting peptides (including chloroplast transit peptides) were omitted from the alignment. The model was rigid-body docked into the map density using the 'fit in map' function in UCSF Chimera (v 1.13.1) (**Pettersen et al., 2004**). Rigid body docking was followed by manual adjustment and real-space refinement using COOT (v 0.8.9.2) (**Emsley and Cowtan, 2004**). Sequence assignment and fitting of the polypeptide chain was guided by bulky residues such as Arg, Trp, Tyr and Phe. After fitting of the polypeptide chain and any conserved cofactors, additional non-protein molecules were assigned to regions of unassigned density. Prosthetic groups, lipids, detergents, and water molecules were built into the structure using COOT (v 0.8.9.2) followed by iterative cycles of restrained refinement and manual model building. The final model underwent global refinement and minimisation using the real space refinement function in the 'Python-based hierarchical environment for integrated crystallography' software suite (PHENIX) (**Adams et al., 2010**).

### 2.9.2 Comprehensive validation

Refined models were analysed using the 'Comprehensive Validation' tool in PHENIX (**Adams et al., 2010; Afonine et al., 2018; Williams et al., 2018**). Here the overall model quality and fit in the map were assessed while any issues regarding steric clashes and general geometry (e.g. rotamer outliers, Ramachandran outliers, anomalous bond lengths and anomalous bond



angles etc.) were also highlighted. Completed models were uploaded to the PDB (PDB IDs: 6RQF, *S. oleracea* *cytb<sub>6f</sub>*; 7PPW (*Synechocystis* *cytb<sub>6f</sub>*).

Specific details for each model are provided in the relevant results sections.

### 3 Results: The purification of dimeric *cytb<sub>6</sub>f* from the chloroplasts of *Spinacia oleracea*

One of the first observations of active, spectrally pure *cytb<sub>6</sub>f* was as a major contaminant in early ATP synthase preparations from spinach chloroplasts (**Pick and Racker, 1979**). In these early preparations, a combination of octyl-β-D-glucopyranoside (OG) and sodium cholate was used to solubilise ATP synthase from spinach chloroplasts. While the majority of contaminants are removed via ammonium sulphate precipitation and subsequent sucrose gradient fractionation, the resulting ATP synthase was always observed in the presence of a strongly pigmented 'brown' contaminant later revealed to correspond to *cytb<sub>6</sub>f* (initial experiment unpublished but is discussed in **Hauska, 2004**). While alternate methods were sought to remove the persistent co-migratory contaminant, the same original protocol was used as a basis for the purification of *cytb<sub>6</sub>f* (**Hurt and Hauska, 1981**).

To adapt the procedure for exclusive purification of *cytb<sub>6</sub>f*, a wash step was added to the thylakoid preparation using the chaotropic agent NaBr (**Hurt and Hauska, 1981**). Through repetition of this wash step, a number of proteins peripheral to the membrane, including the CF<sub>1</sub> head domain of ATP synthase, could be excluded from the preparation (**Kamienietzky and Nelson, 1975**). Subsequent solubilisation of CF<sub>1</sub>-depleted thylakoids with OG/sodium cholate followed by purification using ammonium sulphate precipitation and sucrose gradient fractionation was found to yield a preparation of spectrally pure *cytb<sub>6</sub>f* in the absence of any contaminating ATP synthase (**Hurt and Hauska, 1981**). The yield and scalability of this preparation was further improved by replacing sucrose density gradient fractionation with hydroxyapatite chromatography (**Hurt and Hauska, 1983**), a form of column chromatography which separates macromolecules based on their differing interactions with hydroxyapatite (Ca<sub>5</sub>(PO<sub>4</sub>)<sub>3</sub>OH)<sub>2</sub>, a form of calcium phosphate. Protein interactions with hydroxyapatite are complex comprising several different interactions including cation exchange (through the negatively charged phosphate groups of the matrix), anion exchange (with the positively charged calcium ions on the matrix) and metal affinity (with the calcium ions). Displacement of these interactions can be achieved using a combination of salts and phosphate in the mobile phase. Given the contributions of these different interactions are distinctive for every

protein, the combination of these different binding mechanisms allows the distinct separation of a range of proteins including the bovine *cytbc<sub>1</sub>* (**Riccio et al., 1977**).

As well as the integration of a hydroxyapatite step, a number of additional changes have been made in recent years to further improve on this original procedure. Of note, studies in *C. reinhardtii* implement the use of 6-O-(N-heptylcarbamoyl)-methyl- $\alpha$ -D-glucopyranoside (HECAMEG) as a substitute to the mixture of OG/sodium cholate found in the original procedure (**Breyton et al., 1997; Pierre et al., 1995, 1997**).

While the use of this mild, non-ionic, glucosidic detergent for selective solubilisation was originally implemented as a more cost effective alternative with similar properties to OG (molecular mass, CMC, aggregation number etc. (**Plusquellec et al., 1989**) (**Table 2.8**), it was also observed to result in fewer solubilised contaminants than the OG/sodium cholate mix. The beneficial effect of HECAMEG use was further enhanced by the replacement of the ammonium sulphate precipitation step with a sucrose density gradient fractionation step. This, in combination with the addition of phospholipids (egg yolk L- $\alpha$ -phosphatidylcholine) to combat monomerisation and subsequent inactivation associated with lipid depletion (**Breyton et al., 1997**), was found to substantially increase the electron transfer activity in preparations of *cytb<sub>6f</sub>* prepared with HECAMEG from *C. reinhardtii* (turnover number  $\sim 250 - 300 \text{ e}^- \text{ s}^{-1}$ ) (**Pierre et al., 1995**) compared to earlier procedures (turnover number  $\sim 14 \text{ e}^- \text{ s}^{-1}$  (**Hurt and Hauska, 1981**) and  $\sim 47 \text{ e}^- \text{ s}^{-1}$  (**Hurt et al., 1983**)).

While this protocol has been further adapted for spinach (*Spinacia oleracea*) by **Dietrich and Kuhlbrandt, 1999**, previous attempts to study the structure of the *cytb<sub>6f</sub>* complex from plants have been unsuccessful. Notably, several issues have been found with the spinach and pea complexes during 3D crystallisation experiments including a strong tendency to irreversibly dissociate into monomers, an apparent susceptibility of these complexes to proteolysis and an inability to form well-ordered crystals (**Baniulis et al., 2011**). Here these issues are circumvented through further optimisation of this protocol. In collaboration with G. E. Mayneord, the protocol has been adapted to enhance both the stability and yield of purified dimeric *cytb<sub>6f</sub>* enabling study by cryo-EM (**Malone et al., 2019**) and methods such as single-molecule atomic force microscopy (AFM) (**Mayneord et al., 2019**).

## 3.1 Selective solubilisation of dimeric *cytb<sub>6</sub>f* from *S. oleracea*

### 3.1.1 Initial small-scale optimisation of solubilisation conditions

It has previously been noted that there is some variability in the effectiveness of HECAMEG between batches and from different sources (**Dietrich and Kuhlbrandt, 1999; Pierre et al., 1995**); for this reason it was necessary to determine the optimal concentration of HECAMEG (Anatrace) for use in selective solubilisation of *cytb<sub>6</sub>f*.

Thylakoids were prepared as described in **section 2.2.2** and solubilised with varying concentrations of HECAMEG (0.7 – 2 % (w/v), 2 mg ml<sup>-1</sup> Chl) for 2 min as described in **section 2.4.1**. The relative enrichment of *cytb<sub>6</sub>f* compared to other photosynthetic components in the solubilised supernatant was assessed by analysing the absorbance signal of the haem Soret band (~ 421 nm) relative to the Chl Soret band (~ 440 nm); as observed in **Dietrich and Kuhlbrandt, 1999**, the haem Soret band should dominate the spectrum in a highly pure *cytb<sub>6</sub>f* sample with the presence of bound Chl indicated by a slight shoulder at ~ 440 nm (Soret band) and a sharp peak corresponding to the Q<sub>y</sub> absorption band at ~ 668 nm. The results of solubilisation trials (**Figure 3.1**) indicate that while the total amount of solubilised material increases with the concentration of HECAMEG used (**Figure 3.1**), the relative purity of the ‘enriched’ supernatant appears to decrease beyond ~ 1.2 % (w/v) (**Figure 3.1**).

Following detergent concentration trials, the experiment was repeated with a fixed concentration of 1 % (w/v) HECAMEG and a varied length of time for solubilisation (1 - 15 min). Subsequent analysis of the solubilised supernatants show there was no significant increase in either the amount of solubilised material or the relative purity with time (**Figure 3.2**) suggesting that solubilisation with HECAMEG is extremely quick. For ease of experimentation, a time of 2 mins was selected for solubilising thylakoids with 1 % (w/v) HECAMEG.

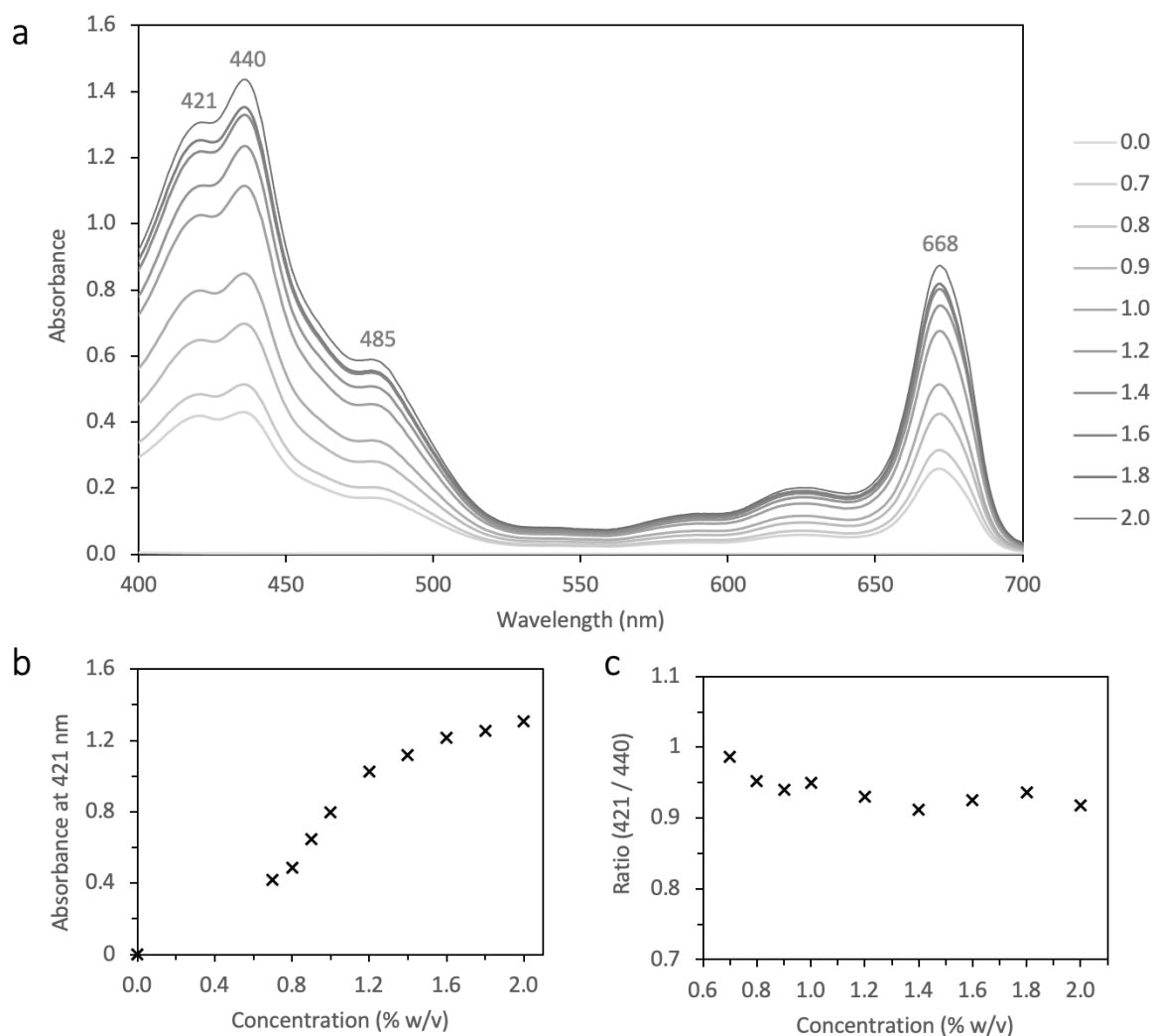


**Figure 3.1 | Optimising the concentration of HECAMEG for selective solubilisation of *cytb<sub>6</sub>f* from spinach thylakoids.** **a**, the absorption spectrum of the solubilised supernatant obtained upon solubilisation of thylakoids ( $2 \text{ mg ml}^{-1}$ ) with varying concentrations of HECAMEG (0.7 – 2 % w/v, 0 % as control) for 2 min. The peak at 421 nm corresponds to the Soret band of haems while the peak at 440 nm corresponds to the Soret band of Chl  $\alpha$ . The shoulder and peak around 455 nm and 485 nm correspond to carotenoid. The peak at 668 nm corresponds to the  $Q_y$  band of Chl  $\alpha$ . **b**, the total amount of material corresponding to *cytb<sub>6</sub>f* in each sample (0.7 – 2 % w/v, 0 % as control) plotted by the absorbance at 421 nm. **c**, the relative enrichment of *cytb<sub>6</sub>f* compared to contaminants in each sample (0.7 – 2 % w/v) plotted as a ratio of the 421 nm signal to 668 nm.

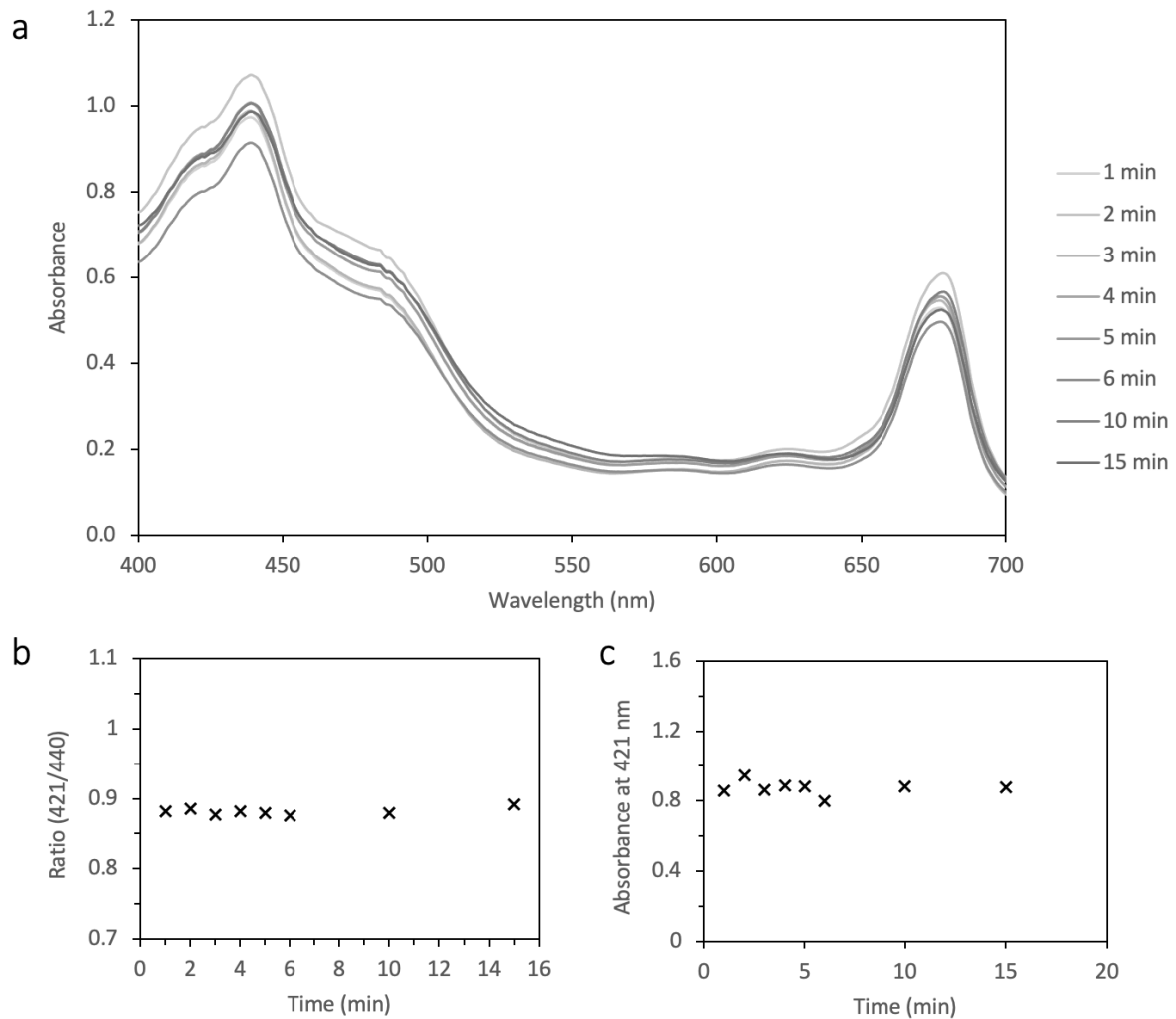


**Figure 3.2| Optimising the length of HECAMEG solubilisation for selective solubilization of *cytb<sub>6</sub>f* from spinach thylakoids.** **a**, the absorption spectrum of the solubilised supernatant obtained upon solubilisation with 1 % (w/v) HECAMEG for varying lengths of time (1 – 15 min). The peak at 421 nm corresponds to the Soret band of haems while the peak at 440 nm corresponds to the Soret band of Chl *a*. The shoulder and peak around 455 nm and 485 nm correspond to carotenoid. The peak at 668 nm corresponds to the Q<sub>y</sub> band of Chl *a*. **b**, the total amount of material corresponding to *cytb<sub>6</sub>f* plotted by the absorbance at 421 nm. **c**, the relative enrichment of *cytb<sub>6</sub>f* compared to contaminants plotted as a ratio of the 421 nm signal to 668 nm.

### 3.1.2 Scaled up selective solubilisation using HECAMEG

A scaled-up version of the optimised solubilisation procedure was carried out (2 mg ml<sup>-1</sup> ChI, 1 % (w/v) HECAMEG). After incubation for 2 mins at room temperature, samples were diluted to 0.7 % (w/v) HECAMEG then ultracentrifuged to remove any unsolubilised material.

### 3.2 Differential Sedimentation using Sucrose Gradient Ultracentrifugation

Following ultracentrifugation, the solubilised supernatant from each tube was pooled and concentrated using a Centriprep 100K centrifugal filter (Merck Millipore Ltd.). The concentrated solution of extracted membrane proteins was then layered on top of 33 ml 10 – 40 % (w/v) continuous sucrose gradients (**Table 2.9**) in 2 ml layers. Gradients were ultracentrifuged in a Beckman SW32 rotor at 174,587 x g (max) for 16 hours, 4 °C.

### 3.3 Hydroxyapatite Column Purification

Following sucrose density ultracentrifugation, two brown coloured bands were observed at the top of the gradients at regions corresponding to ~ 11 and 16 % (w/v) sucrose respectively (**Figure 3.3**).

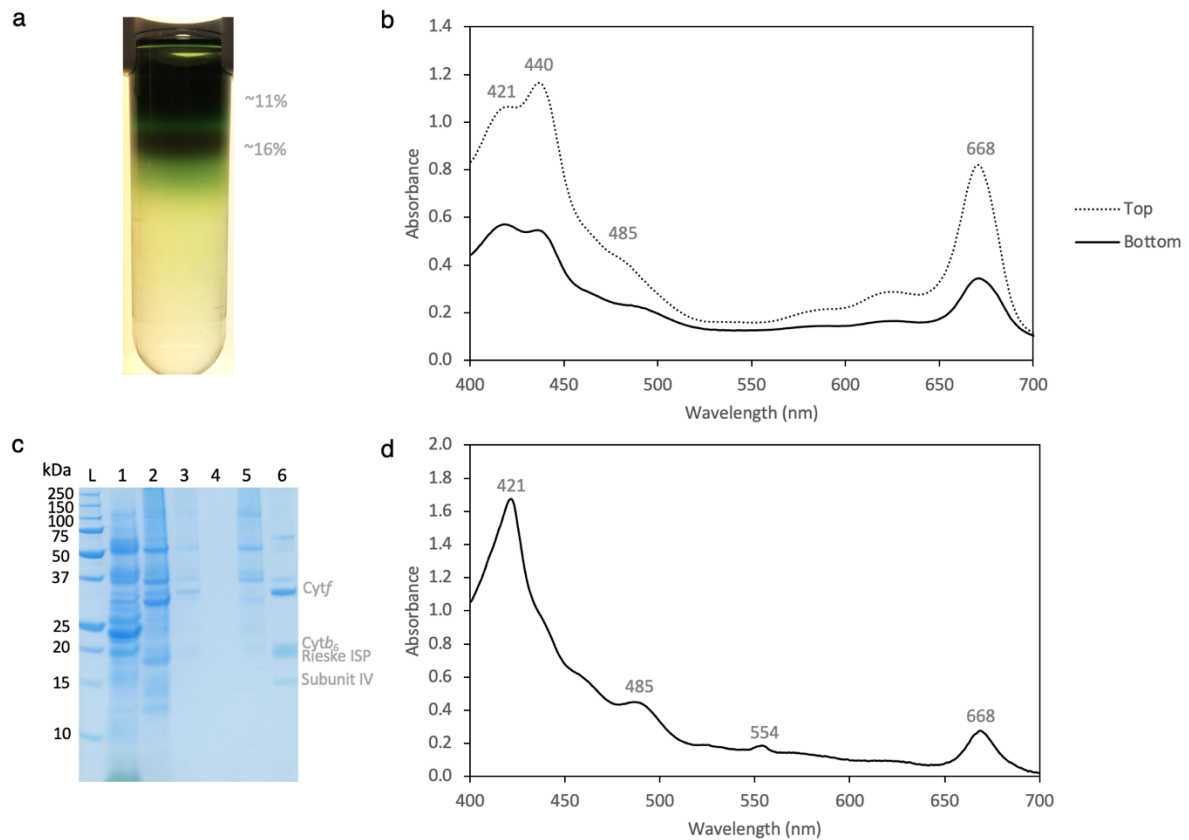


**Figure 3.3| The purification of *cytb<sub>6</sub>f* from spinach thylakoids.** **a**, the sucrose density gradient fractionation of supernatant following solubilisation with 1 % (w/v) HECAMEG. **b**, absorbance spectra of the top (~ 11 % sucrose, dotted line) and bottom (~ 16 % sucrose, solid line) bands of from the sucrose gradient shown in 'a'. **c**, SDS-PAGE of the purification process. Lanes: L) ladder, 1) thylakoids, 2) solubilised thylakoids, 3) bottom band from sucrose gradient shown in 'a', 4) CHT flow through, 5) CHT wash with 100 mM ammonium phosphate, 6) CHT eluate with 400 mM ammonium phosphate. **d**, the absorbance spectrum of the sample eluted from the CHT column. The peak at 421 nm corresponds to the Soret band of haems while the peak at 440 nm corresponds to the Soret band of Chl *a*. The shoulder and peak around 455 nm and 485 nm correspond to carotenoid. The peaks at 554 and 668 nm correspond to *c*-type haems of *cyt<sub>f</sub>* and the Q<sub>y</sub> band of Chl *a*, respectively.



Bands were harvested and analysed by absorbance spectroscopy as shown in **Figure 3.3**. The absorbance spectra reveal the presence of *cytb<sub>6</sub>f* in both bands of the sucrose gradient. The relative height of peaks at ~ 440 and 668 nm in comparison to those observed in the purified sample of *cytb<sub>6</sub>f* spectrum from **Dietrich and Kuhlbrandt, 1999** indicate the presence of Chl containing contaminants. The lower of the two harvested bands (corresponding to ~ 16 % (w/v) sucrose) was selected for further purification.

The majority of remaining contaminating proteins in the sample, were removed by Ceramic Hydroxyapatite (CHT) column chromatography as described in **section 2.4.4**. The eluate was collected and analysed by SDS-PAGE (**Figure 3.3**) and absorbance spectroscopy (**Figure 3.3**) to confirm the removal of most contaminating proteins and the enrichment of *cytb<sub>6</sub>f*.

### 3.4 Detergent Exchange using Sucrose Gradient Ultracentrifugation

While the above procedure appears to result in the effective purification of dimeric *cytb<sub>6</sub>f* from spinach thylakoids (as confirmed by NativePAGE and negative stain EM), it appears that prolonged exposure of *cytb<sub>6</sub>f* to HECAMEG could result in some loss of stability and monomerisation. Indeed, comparison of BN-PAGE gels comprising samples obtained prior to incubation with samples following 48-hour incubation with HECAMEG (0.7 - 1.5 % (w/v), 4 °C) reveals a generalised fading of dimeric bands over time which could correspond to destabilisation of the dimeric complex (**Figure 3.4**). This conclusion is further supported by SDS-PAGE analysis revealing a disproportionate fading of bands corresponding to the *cytf* (31 kDa) and Rieske ISP (17 kDa) subunits after 48-hour HECAMEG incubation (**Figure 3.4**). In both sets of analyses, the presumed loss of stability resulting from HECAMEG exposure appears to become more apparent with increasing HECAMEG concentrations (**Figure 3.4**).

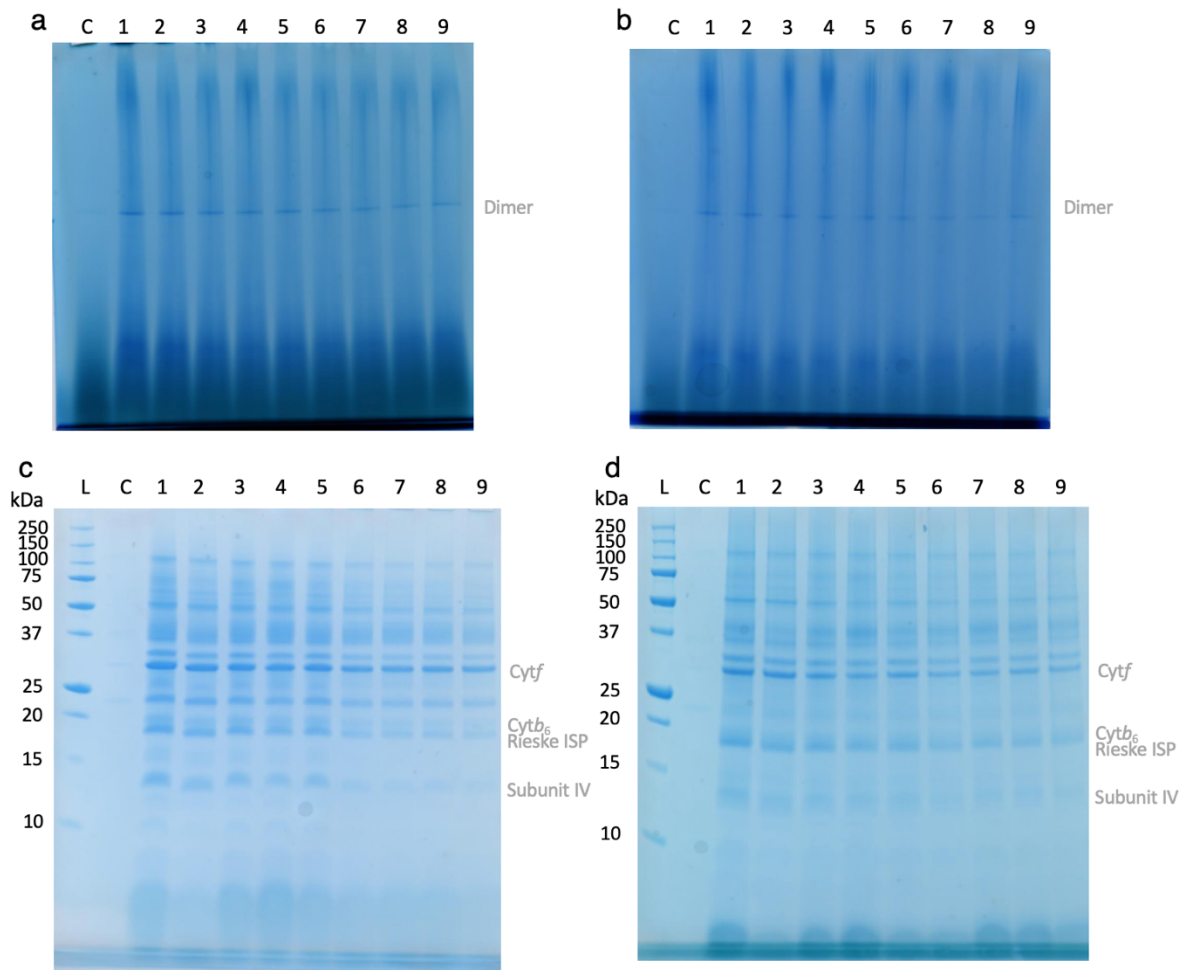


**Figure 3.4| Stability of *cytb<sub>6</sub>f* dimer in changing concentrations of HECAMEG.** **a-b**, BN-PAGE of solubilised supernatant selectively solubilised with differing concentrations of HECAMEG immediately following solubilisation (**a**) and after 48 hours incubation at 4 °C (**b**). Lanes: Ladder C) control with no HECAMEG added 1-9) samples solubilised with 0.7 – 1.5 % (w/v) HECAMEG. The position of the dimeric *cytb<sub>6</sub>f* is indicated. **c-d**, SDS-PAGE of solubilised supernatant selectively solubilised with differing concentrations of HECAMEG immediately following solubilisation (**c**) and after 48 hours incubation at 4 °C (**d**). Lanes: L) Ladder C) control with no HECAMEG added 1 - 9) samples solubilised with 0.7 – 1.5 % (w/v) HECAMEG. The position of the four large subunits of the complex (*cytf*, *cytb<sub>6</sub>*, the Rieske ISP and subunit IV) are indicated running at ~ 31 kDa, ~ 24 kDa, ~ 20 kDa and ~ 17 kDa, respectively. The four small subunits (PetG, PetL, PetM and PetN) running at around 4 kDa are not shown.

To combat destabilisation associated with prolonged HECAMEG exposure we decided to transfer the resultant sample into a second detergent (4-trans-(4-trans-propylcyclohexyl)-cyclohexyl  $\alpha$ -maltoside; tPCC- $\alpha$ -M) (**Table 2.8**) which had previously been shown to be effective in stabilising dimeric, active form of the *cytb<sub>6</sub>f* complex for prolonged periods of time (**Hovers et al., 2011**).

To facilitate detergent exchange, samples were loaded onto 12 ml 10 – 35 % (w/v) sucrose gradients containing 0.3 mM tPCC- $\alpha$ -M (**Table 2.10**) and ultracentrifuged in a Beckman SW41 rotor at 175,117 x g (max) for 16 hours, 4 °C (**Figure 3.5**). To obtain a suitably homogenous sample for cryo-EM studies, a final step of gel filtration was also added to remove any residual monomerised *cytb<sub>6</sub>f* (**Figure 3.5**).

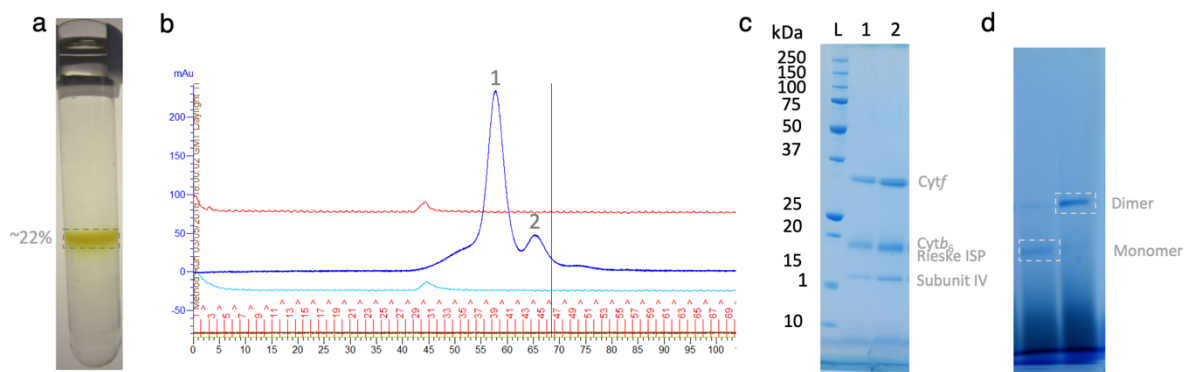


**Figure 3.5| Detergent exchange into tPCC $\alpha$ M.** **a**, Fractionation of CHT eluate on a 10-35 % (w/v) continuous sucrose gradient (50 mM HEPES pH 8, 20 mM NaCl) containing 0.3 mM tPCC $\alpha$ M. Gradients were harvested as indicated by the dotted grey boxes. **b**, a size exclusion elution profile of the band harvested from the 0.3 mM tPCC $\alpha$ M sucrose gradient. **c**, SDS-PAGE analysis of size exclusion peaks from the tPCC $\alpha$ M sample. Lanes: L) Ladder, 1) peak 2, 2) peak 1. The position of the four large subunits of the complex (*cytf*, *cytb<sub>6</sub>*, the Rieske ISP and subunit IV) are indicated running at ~ 31 kDa, ~ 24 kDa, ~ 20 kDa and ~ 17 kDa, respectively. The four small subunits (PetG, PetL, PetM and PetN) running at around 4 kDa are not shown. **d**, BN-PAGE analysis of size exclusion peaks from the tPCC $\alpha$ M sample. Lanes: 1) peak 2, 2) peak 1.

### 3.5 Further improvements to the yield

Following the publication of **Malone et al., 2019**, the purification procedure was further optimised to improve the yield for further study. In this yield-optimised procedure, the initial 16-hour sucrose density gradient containing HECAMEG was removed and the solubilised supernatant was instead filtered through a 0.45  $\mu$ M filter then loaded directly onto a CHT column as described in **section 2.4.4**. Initially, while it was obvious that large amounts of *cytb<sub>6f</sub>* were binding to the CHT column (the column turns from white to brown), subsequent spectroscopic analysis indicated that a large amount of *cytb<sub>6f</sub>* was still present in the flow through. For this reason, a second CHT column was also added to extend the total column volume to 10 ml. The eluate was collected in 1.5 ml fractions and analysed by absorbance spectroscopy to confirm the removal of most contaminating proteins and the enrichment of *cytb<sub>6f</sub>* (**Figure 3.6**).

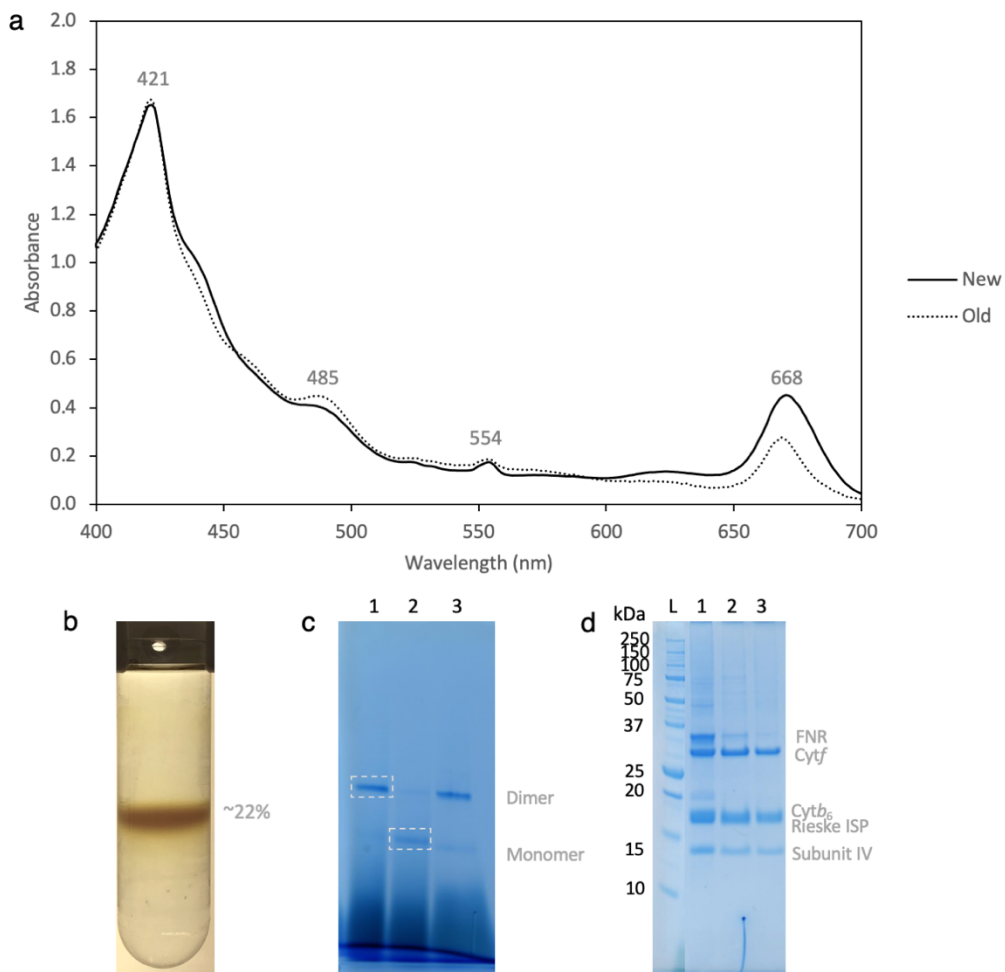


**Figure 3.6| A modified purification of *cytb<sub>6</sub>f* from spinach to optimise yield.** **a**, the absorption spectrum of the CHT eluate from the new and old purification procedures showing the relative purity achieved by both. The peak at 421 nm corresponds to the Soret band of bound haems. The peak at 485 nm corresponds to the bound carotenoid. The peaks at 554 and 668 nm correspond to *c*-type haems of *cytf* and *Chl a* respectively. **b**, The 10 - 35 % (w/v) sucrose density gradient (50 mM HEPES pH 8, 20 mM NaCl, 0.3 mM tPCCaM) following ultracentrifugation. **c**, BN-PAGE of the final sample following gel filtration in comparison with samples from the old purification procedure. Lanes: 1) dimer from old preparation, 2) monomer from old preparation, 3) final sample from new yield-optimised preparation. The position of the dimeric and monomeric *cytb<sub>6</sub>f* is indicated. **d**, SDS-PAGE of the final stages of the new yield-optimised purification procedure. Lanes: L) ladder, 1) CHT eluate, 2) harvested sucrose gradient band, 3) dimeric peak from gel filtration. The position of the four large subunits of the complex (*cytf*, *cytb<sub>6</sub>*, the Rieske ISP and subunit IV) are indicated running at ~ 31 kDa, ~ 24 kDa, ~ 20 kDa and ~ 17 kDa, respectively. The position of the band assumed to correspond to FNR is also indicated. The four small subunits (PetG, PetL, PetM and PetN) running at around 4 kDa are not shown.

As with the first preparation, the pooled fractions from CHT chromatography were concentrated and loaded onto 10 - 35 % (w/v) sucrose gradients (**Table 2.10**) containing 0.3 mM tPCC $\alpha$ M (**Figure 3.6b**) before gel filtration was employed to remove any residual monomer. The final sample was analysed by BN-PAGE (**Figure 3.6c**) and UV/vis spectroscopy (**Figure 3.6a**) to confirm the complex was intact and dimeric as expected; the final stages of the purification procedure were also analysed by SDS-PAGE (**Figure 3.6d**).

As well as a substantially enhanced yield compared to our original preparation (**Malone et al., 2019**), it is interesting to note an additional band in the SDS-PAGE gel at  $\sim$  35 kDa which had not been observed previously (**Figure 3.6d**). This additional band appeared to be present at an approximately 1 : 1 ratio with *cyt<sub>f</sub>* in the CHT eluate however appears to decrease significantly following detergent exchange and subsequent gel filtration. Further investigation into the identity of this band lead to the suggestion that it could correspond to Ferredoxin-NADP<sup>+</sup> reductase (FNR) as observed in a previous study of spinach *cyt<sub>b<sub>6</sub>f</sub>* (**Zhang et al., 2001**).

### 3.6 Quantification of purified dimeric *cyt<sub>b<sub>6</sub>f</sub>* in tPCC- $\alpha$ -M using redox difference spectra

For redox difference spectra (**Figure 3.7**), cytochromes were first fully oxidised with a few grains of potassium ferricyanide followed by reduction with a few grains of sodium ascorbate (*c*-type haem *f*) then sodium dithionite (*c*-type haem *f* and *b*-type haems *b<sub>n</sub>* and *b<sub>p</sub>*). At each stage the sample was mixed thoroughly and incubated for  $\sim$  1 min before recording spectra.

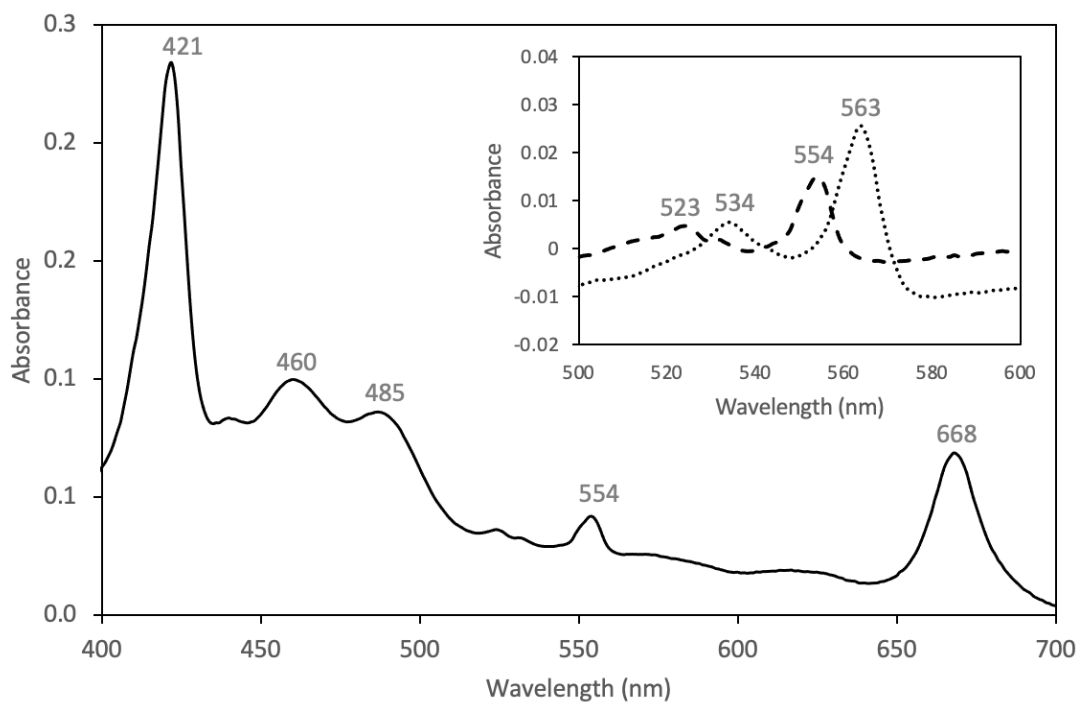


**Figure 3.7 | Purification of *cytb<sub>6</sub>f* from spinach.** Absorption spectrum of ascorbate-reduced purified *cytb<sub>6</sub>f* complex. The peak at 421 nm corresponds to the Soret band of bound haems. The shoulder and peak around 460 nm and 485 nm correspond to carotenoid. The peaks at 554 and 668 nm correspond to *c*-type haems of *cyt<sub>f</sub>* and the *Q<sub>y</sub>* band of Chl *a*, respectively. The inset panel shows redox difference spectra of ascorbate-reduced minus ferricyanide-oxidized *cytb<sub>6</sub>f* (dashed line) and dithionite-reduced minus ascorbate-reduced (dotted line) *cytb<sub>6</sub>f*. Redox difference spectra show haem *f* absorption peaks at 523 and 554 nm as well as absorption peaks at 534 and 563 nm corresponding to the *b*-type haems of *cytb<sub>6</sub>*. The calculated ratio of *cytb<sub>6</sub>* *b*-type haems to the *c*-type haem of *cyt<sub>f</sub>* was  $\sim 2$  using extinction coefficients of  $28 \text{ mM}^{-1} \text{ cm}^{-1}$  (*f*, 554 – 540 nm) and  $24 \text{ mM}^{-1} \text{ cm}^{-1}$  (*b<sub>6</sub>*, 563 - 575) (**Metzger et al., 1997**). The spectra exhibit the absorption properties characteristic of intact *cytb<sub>6</sub>f*. All spectra were recorded at room temperature.

Reduced-oxidised spectra indicated a concentration of  $\sim 13 \mu\text{M}$  purified protein in the sample, additionally the haem *b* : *c* ratio was calculated as  $\sim 2.3$ , a ratio consistent with expectations for an intact dimeric *cytb<sub>6</sub>f* complex. Haem *c<sub>n</sub>* is omitted from this calculation since its  $\alpha$ -band consists of a broad, flat absorption peak with a small extinction coefficient; the Soret band of haem *c<sub>n</sub>* ( $\sim 425 \text{ nm}$ ) is also masked by the absorption peaks of Chl *a* and the other *b*- and *c*-type haems (*b<sub>p</sub>*, *b<sub>n</sub>* and *f*) (**Joliot and Joliot, 1988; Yamashita et al., 2007**).

### 3.7 Activity assays

To confirm the extracted *cytb<sub>6</sub>f* complex retains high levels of activity following purification, the rate of electron transfer from reduced decylplastoquinone (dPQH<sub>2</sub>; Sigma) to purified spinach plastocyanin (PC) was measured *in vitro* using stopped-flow absorbance spectroscopy.

#### 3.7.1 Purification of plastocyanin

For the preparation of plastocyanin, thylakoids were prepared as described in **section 2.2.3** then sonicated as described in **section 2.4.3**. Following ultracentrifugation, the soluble fraction was loaded onto an anionic exchange column and purified as described in **section 2.4.7**. Fractions containing plastocyanin (eluted at ~ 200 mM NaCl) were identified visually through addition of a few grains of potassium ferricyanide to each fraction. In this manner, fractions containing PC exhibit a prominent blue colour when the Cu<sup>+</sup> centre is oxidised ( $E_m = \sim 370$  mV) to Cu<sup>2+</sup>; this can be monitored spectroscopically by the appearance of a broad absorbance band at ~ 597 nm.

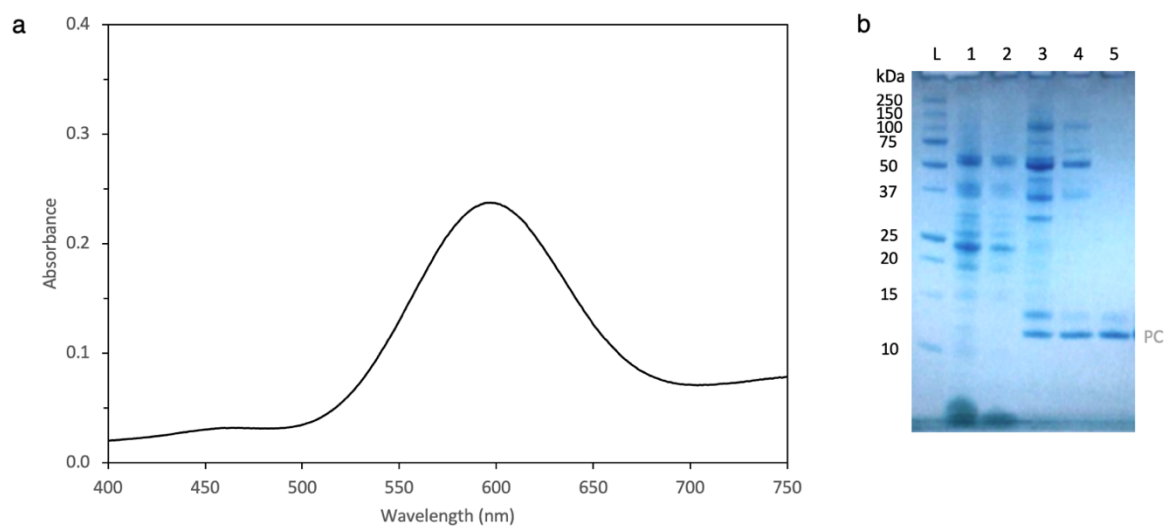


**Figure 3.8| Purification of plastocyanin from spinach.** **a**, Absorption spectrum of ferricyanide-oxidised purified PC. The peak at 597 nm corresponds to the Cu-centre of PC in its 2+ oxidation state. All spectra were recorded at room temperature. **b**, SDS-PAGE of the PC purification procedure. Lanes: L) ladder, 1) thylakoids, 2) insoluble fraction after sonication, 3) soluble fraction after sonication, 4) pooled and concentrated anionic exchange fractions, 5) pooled and concentrated gel filtration fractions.



Fractions containing PC were identified visually through the addition of a few grains of potassium ferricyanide to each fraction. In this manner, fractions containing PC exhibit a prominent blue colour when their  $\text{Cu}^+$  centre is oxidised ( $E_m = \sim 370$  mV) to  $\text{Cu}^{2+}$ ; this can be monitored spectroscopically by the appearance of a broad absorption band at  $\sim 597$  nm. Fractions containing PC were pooled, concentrated and flash frozen in liquid nitrogen for storage at  $-80$  °C. The purity of the PC was assessed spectroscopically (**Figure 3.8**) and using SDS-PAGE (**Figure 3.8**); the concentration of PC was calculated using the absorbance signal at 597 nm and an extinction coefficient of  $4.5 \text{ mM}^{-1} \text{ cm}^{-1}$  (**Tan and Ho, 1989**).

### 3.7.2 Activity assays

The transfer of electrons from  $\text{dPQH}_2$  to PC by *cytb<sub>6</sub>f* (**Figure 3.9**) was monitored by stopped-flow absorbance spectroscopy at  $20$  °C as described in **section 2.5.4**.

The rate of ET by *cytb<sub>6</sub>f* was determined by taking the initial linear region from the enzyme-catalysed reaction and subtracting the background rate measured in the absence of enzyme. The resulting rate of  $200 \text{ e}^- \text{ s}^{-1}$  is in good agreement with previously published figures from studies on *cytb<sub>6</sub>f* from spinach (**Dietrich and Kuhlbrandt, 1999**), *C. reinhardtii* (**Hovers et al., 2011; Pierre et al., 1995**) and native spinach chloroplasts (**Hope, 1993**).

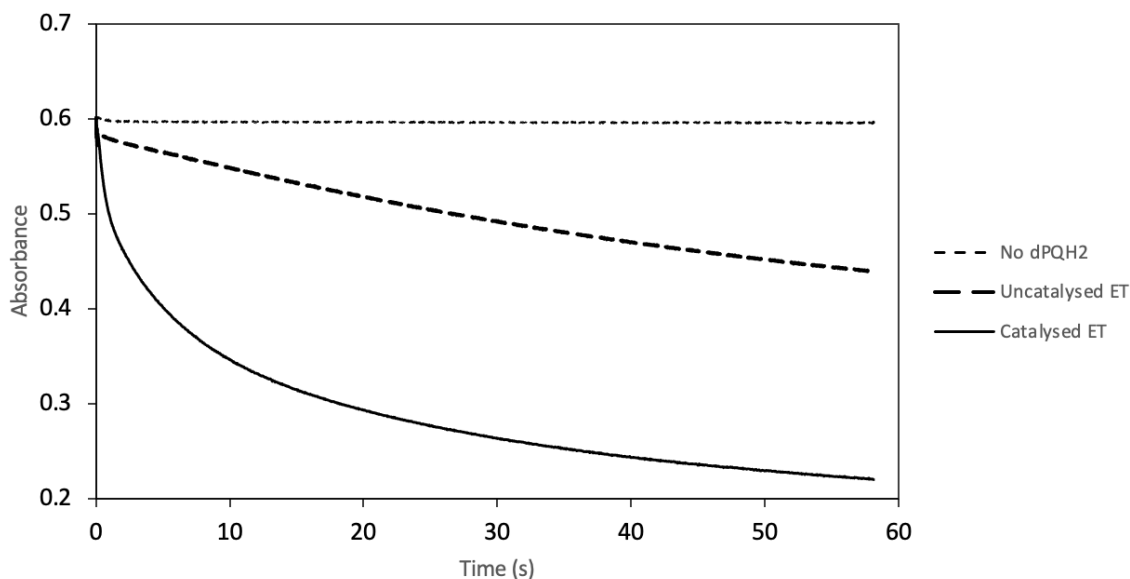


**Figure 3.9 | The catalytic rate of PC reduction by the purified dimeric *cytb<sub>6</sub>f* complex as determined by stopped-flow absorbance spectroscopy.** A rate of  $200 \text{ e}^- \text{ s}^{-1}$  was determined by taking the initial linear region from the enzyme-catalysed reaction (solid line) and subtracting the background rate measured in the absence of enzyme (long-dashed line). Plastocyanin reduction was not observed in the absence of dPQH<sub>2</sub> (short-dashed line). Reactions were initiated upon addition of dPQH<sub>2</sub> to the solution containing PC and *cytb<sub>6</sub>f* while monitoring the loss of absorbance at 597 nm. Final concentrations were 50  $\mu\text{M}$  plastocyanin, 185 nM *cytb<sub>6</sub>f* and 250  $\mu\text{M}$  dPQH<sub>2</sub>. All experiments were performed in triplicate and controls were performed in the absence of *cytb<sub>6</sub>f* or dPQH<sub>2</sub>.

### 3.8 Discussion

Despite studies on the *b<sub>6</sub>f* complex from various species as discussed in **chapter 1**, a number of questions still remain regarding the vital role of this complex in the photosynthetic electron transfer pathway and, in particular, the central role of this complex in the regulatory mechanisms of higher plants.

While a successful and efficient procedure has been established to purify this extraordinary complex from a higher plant source (**Dietrich and Kuhlbrandt, 1999**), previous attempts to study these samples by x-ray crystallography have been largely unsuccessful. Notably, several issues have been found with the spinach and pea complexes during 3D crystallisation experiments including a strong tendency to irreversibly dissociate into monomers, an

apparent susceptibility of these complexes to proteolysis and an inability to form well-ordered crystals (**Baniulis et al., 2011**).

In the present chapter, we attempt to circumvent these issues by further optimising the protocol established by **Dietrich and Kuhlbrandt, 1999** to provide a sample suitable for high resolution structural studies by cryo-EM. In comparison to previous preparations, the optimised protocol presented here allows the purification of a highly active *cytb<sub>6</sub>f* from *S. oleracea* with significantly enhanced stability. The ratios of all spectroscopically identifiable cofactors are as expected; furthermore SDS-PAGE shows the presence of all four of the major subunits. The preparation is indicated to be largely dimeric as indicated by BN-PAGE; the homogeneity of this sample will be further clarified through negative stain EM in **chapter 4**.

## 4 Results: Structural determination of *cytb<sub>6f</sub>* from *S. oleracea*.

### 4.1 Negative stain TEM analysis

Samples (prepared as described in **chapter 3**) were analysed by negative stain TEM (as described in **section 2.6**) to confirm sample homogeneity and to gauge approximately what concentration might be best as a starting point for cryo-EM screening.

Analysis of the recorded images reveals the purified sample is extremely homogenous with particles exhibiting the size and shape expected for dimeric *cytb<sub>6f</sub>* (**Figure 4.1**). Of the various concentrations trialled, optimum particle distribution was achieved with a 40-fold diluted (0.325  $\mu$ M, 31.5  $\mu$ g/ml) sample (**Figure 4.1**).

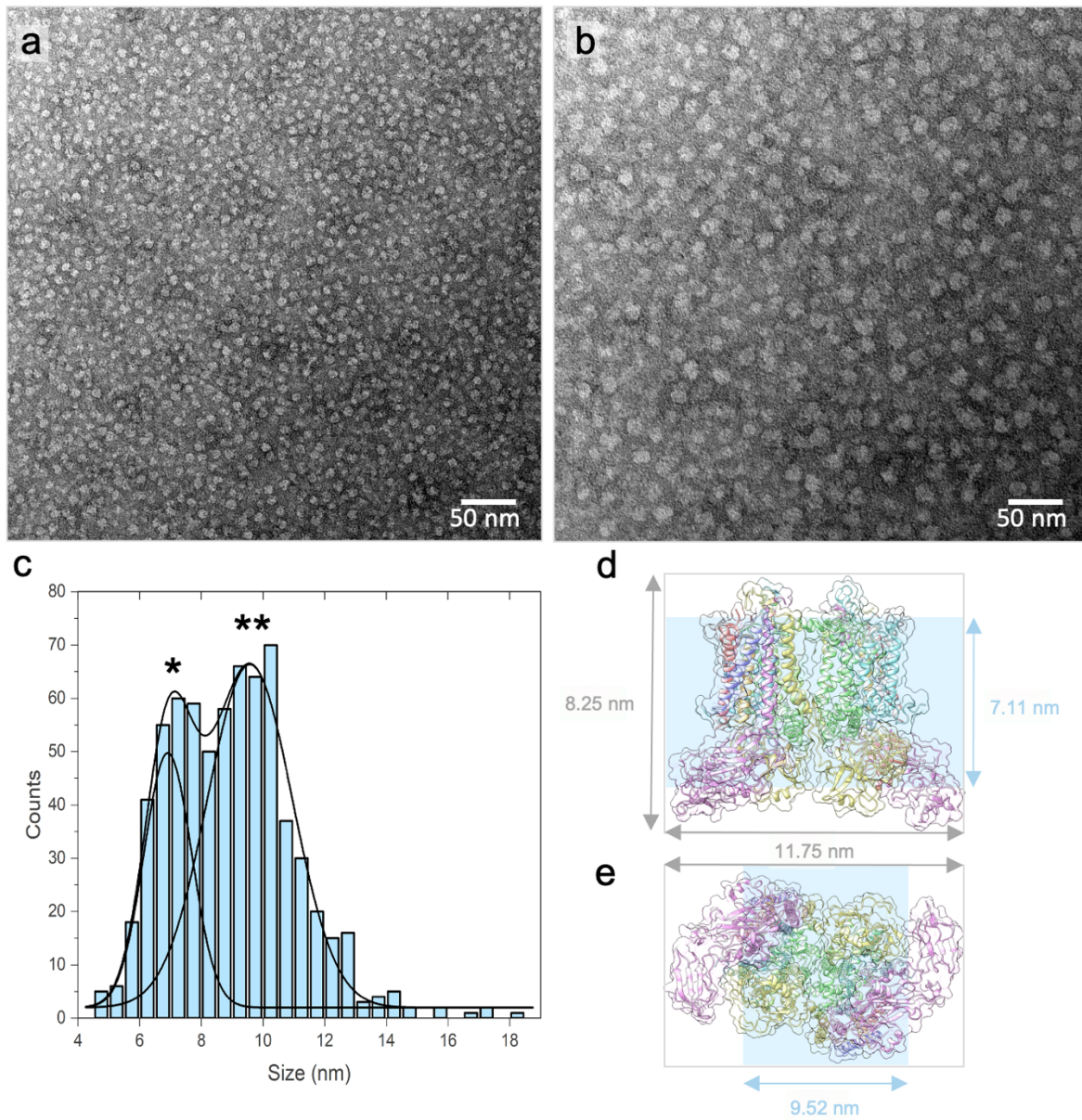


**Figure 4.1 | Negative stain analysis of the cytb<sub>6</sub>f complex purified from *S. oleracea*.** A 40-fold diluted (0.325  $\mu$ M) sample of the purified *S. oleracea* cytb<sub>6</sub>f complex imaged at **a**, 39,000X and **b**, 73,000X magnification. **c**, A histogram showing the measurements of particle in negative stain micrographs (measured in Image J). A Gaussian fit over the histogram indicates peaks at  $\sim 6.9 \pm 0.1$  nm (\*) and  $\sim 9.5 \pm 0.1$  nm (\*\*). **d-e**, the cytb<sub>6</sub>f structure of *C. reinhardtii* showing the full dimensions of the complex (grey) and regions of high density (highlighted in blue) which likely correspond to the peaks observed in 'c'.

## 4.2 Cryo-TEM analysis

### 4.2.1 Sample preparation and screening

While screening revealed the *cytb<sub>6f</sub>* particles had a tendency to stick to the edges of the carbon support, it was observed that an optimal particle distribution could be achieved with an undiluted sample (13  $\mu$ M, 2.86 mg/ml) on Quantifoil R1.2/1/3 400 mesh Cu grids; these were prepared and screened as described in **section 2.7**. On these grids, a large number of monodisperse particles of roughly similar sizes were observed, these appeared to adopt multiple orientations within the ice.

### 4.2.2 Data acquisition

Automated data acquisition was set up using the EPU software (v 1.11.0) on a Titan Krios microscope (Thermo Fisher) operated at 300 kV, equipped with an energy filtered (slit width 20 eV) K2 summit direct electron detector (Gatan) (**Table 2.19**). A total of 6,035 movies were collected in counting mode over a defocus range of - 1.5 to - 2.5  $\mu$ m at a nominal magnification of 130,000 X (pixel size of 1.065 Å). A total dose of 55.2 e<sup>-</sup>/Å<sup>2</sup> was applied over 12 sec with movies dose-fractionated into 48 fractions.

### 4.2.3 Beam-induced motion correction and CTF estimation

All subsequent steps were performed as described in **section 2.8** using RELION 2.1 (**Fernandez-Leiro and Scheres, 2017**) or 3.0 (**Zivanov et al., 2018**) unless otherwise stated.

Movies were motion corrected and dose-fractionated using MotionCor2 before the GCTF subroutine (**Zhang, 2016**) was employed to estimate Contrast Transfer Function (CTF) parameters of the dose-weighted, motion corrected images.

### 4.2.4 Particle picking and 2D classification

Following CTF estimation, 422,600 particles were manually picked and extracted from micrographs using a box size of 220 x 220 pixels; an example micrograph showing picked particles is shown in **Figure 4.2**; this micrograph clearly exhibits a good distribution of single protein particles embedded in a thin and even layer of vitreous ice. Some minor ice and ethane contamination was observed in some of the micrographs, however no significant aggregation of protein was shown and the quality of the protein preparation is clearly reflected in the micrographs.



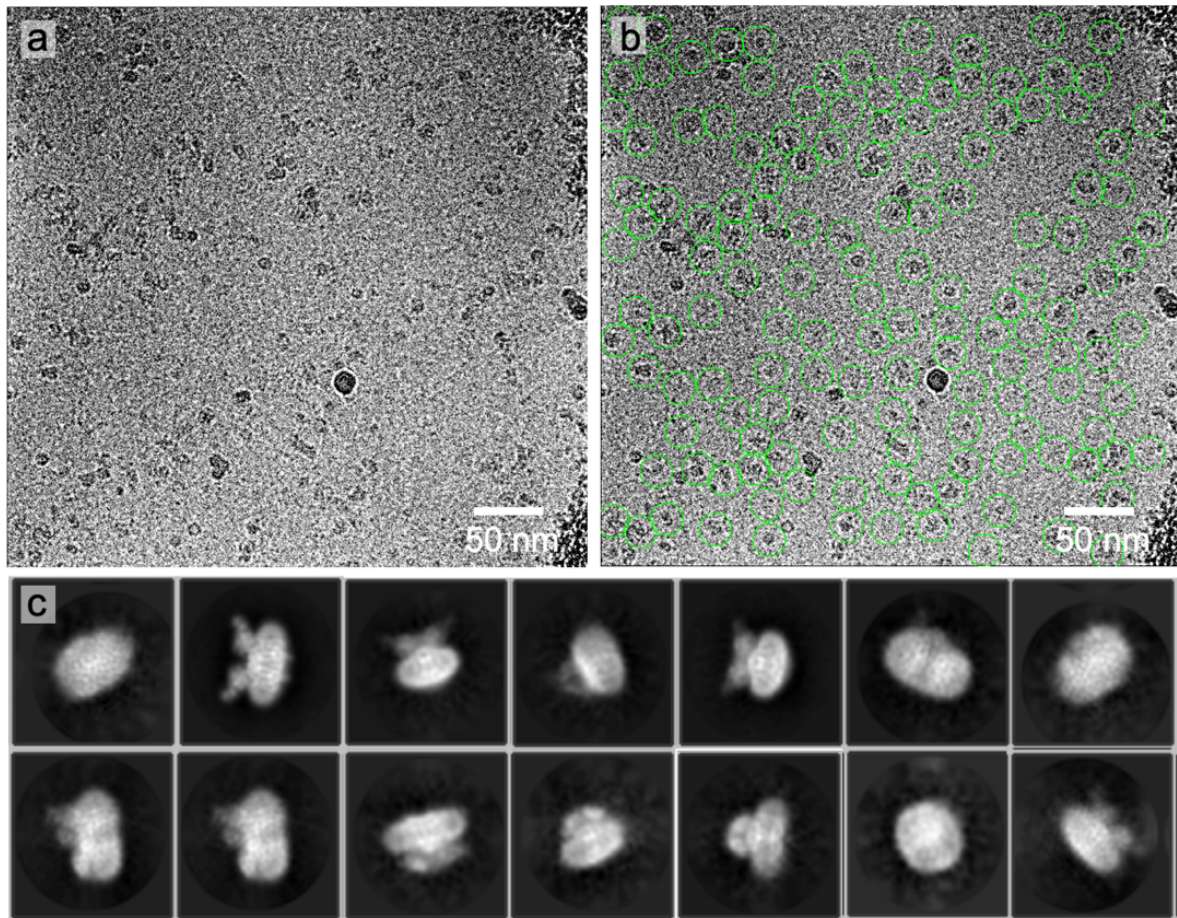


**Figure 4.2 | Cryo-EM micrographs of the spinach *cytb<sub>6f</sub>* complex and calculation of the cryo-EM map resolution.** **a**, Cytochrome *b<sub>6f</sub>* particles covered by a thin layer of vitreous ice on a supported carbon film. **b**, Examples of dimeric cytochrome *b<sub>6f</sub>* particles are circled in green. 6035 cryo-EM movies were recorded, from which 422,660 particles were picked manually for reference-free 2D classification. 108,560 particles were used for calculation of the final density map. **c**, A gallery showing a representative subset of selected 2D classes.

The extracted particles were subjected to reference-free 2D classification to iteratively generate 150 class averages revealing several different views of the complex. A representative subset of 2D classes is shown in (**Figure 4.2**); these display a number of orientations of the complex with the side-on view being most recognisably *cytb<sub>6f</sub>*.

Particles that categorised into poorly defined classes were rejected, while the remaining 292,242 (69.2 %) particles were retained for high resolution reconstruction.

#### 4.2.5 *De novo* 3D model generation

A subset of 30,000 extracted particles were used to generate a low-resolution 3D model using the '3D initial model' subroutine in RELION. Since it was possible that the two halves of the complex may display slightly different structural features, symmetry was not applied (i.e. C1). The model exhibited the general architecture expected for the *cytb<sub>6f</sub>* complex as predicted from analysis of the cyanobacterial (Baniulis et al., 2009; Hasan and Cramer, 2014a; Hasan et al., 2013a, 2013b, 2014; Kurisu et al., 2003; Yamashita et al., 2007; Yan et al., 2006) and algal crystal structures (**Stroebel et al., 2003**).

#### 4.2.6 3D reconstruction to 3.58 Å

To obtain a suitably homogenous set of particles, unsupervised 3D classification ('3D classification') was performed iteratively to generate 10 3D classes using the initial model low pass filtered to 20 Å as a reference map. The 10 low resolution 3D classes (**Figure 4.3**) were analysed in UCSF Chimera (v 1.13.1) before one stable 3D class (class 5, 5.85 Å) of sufficient homogeneity was selected for further refinement. The selected subset of 108,560 particles (25.6 %) was further refined iteratively using the '3D auto-refine' procedure in RELION to produce a higher resolution model (4.58 Å). The resultant model preserved the general architecture observed in the initial model, however the increased resolution revealed further details such as the internal helical architecture of the transmembrane region of *cytb<sub>6f</sub>* as well as an outline of the extrinsic domains of *cyt<sub>f</sub>* and the Rieske ISP. The subset of refined particles underwent re-extraction and re-centring before another round of 3D auto refinement was applied. Per-particle CTF-refinement was then carried out and a soft mask was created from the 3D map low pass filtered to 15 Å with a soft edge of 10 pixels. This mask incorporated the detergent shell surrounding the transmembrane portion of the complex but excluded surrounding solvent.



The masked CTF-refined particles were subjected to a further round of 3D refinement, the resultant density map was then corrected for the modulation transfer function (MTF) of the Gatan K2 summit camera and further sharpened using the post-processing procedure in RELION.

An overview of the data processing procedure is shown in **Figure 4.3**. The final global resolution estimate of 3.58 Å was based on the gold-standard Fourier shell correlation (FSC) cut off of 0.143 (**Figure 4.4**) (**Scheres, 2012; Scheres and Chen, 2012**). Local resolution was determined using one of the two unfiltered half-maps from the final round of 3D refinement as an input, a calibrated pixel size of 1.065 Å and a B-factor of - 103 Å<sup>2</sup>. The output local resolution map is shown in **Figure 4.4**.

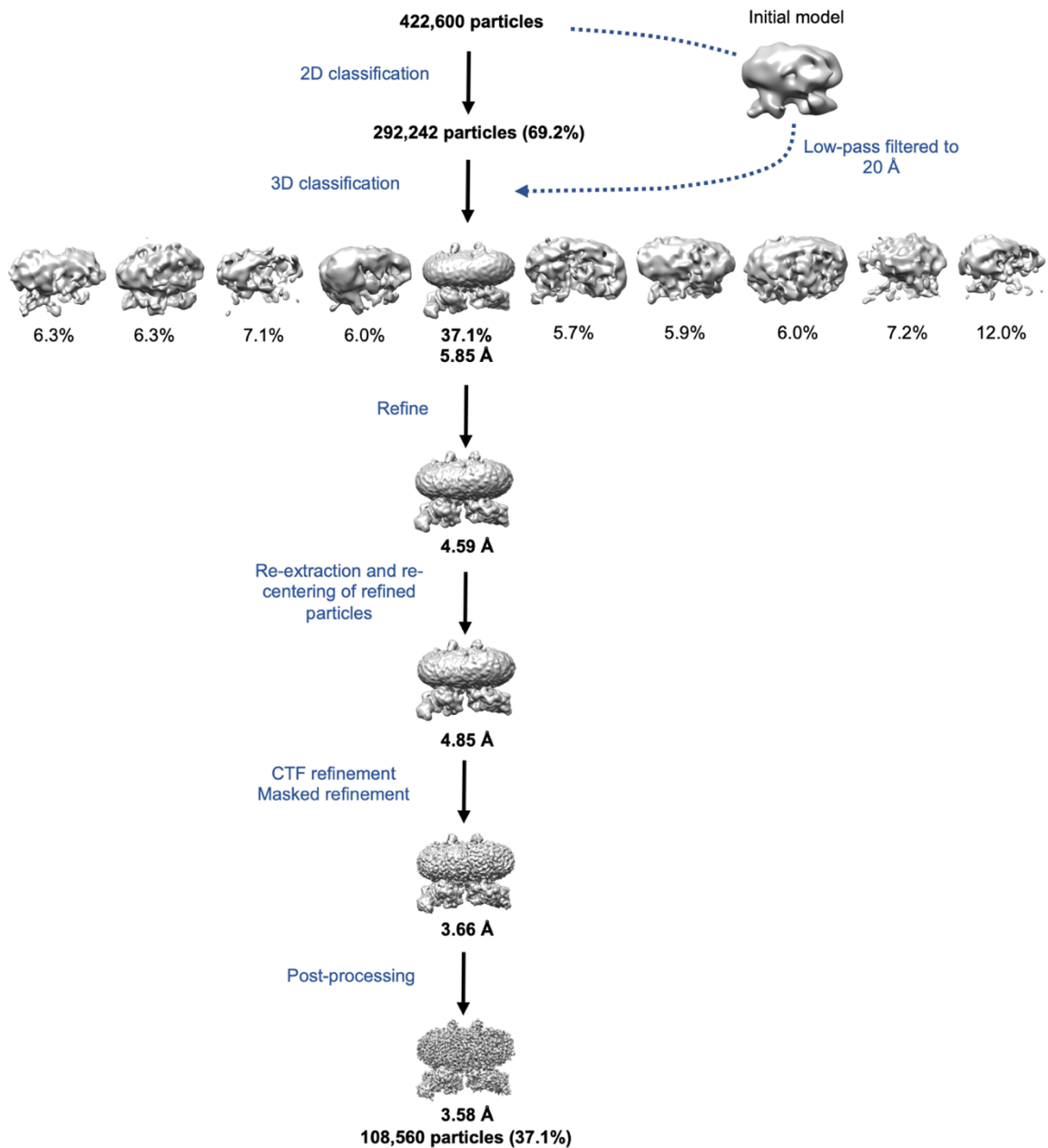


**Figure 4.3 | A flowchart for processing of the *S. oleracea* *cytb<sub>6</sub>f* cryo-EM map outlining the steps for data processing in RELION.** We recorded 6,035 cryo-EM movies, from which 422,660 particles were picked manually for reference-free 2D classification. The final density map was calculated from 108,560 particles. The average resolution in angstroms (Å) and number of particles (%) at each stage is indicated with the final global resolution for the entire *cytb<sub>6</sub>f* complex from *S. oleracea* estimated to be ~ 3.58 Å.

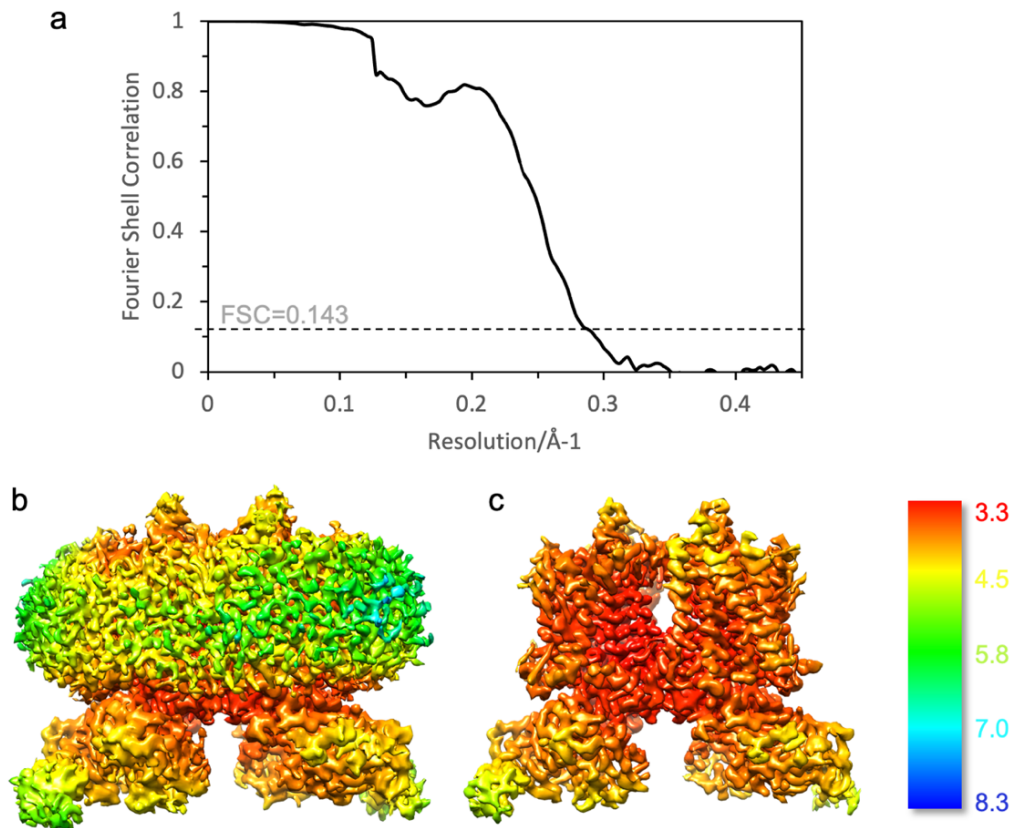


**Figure 4.4 | Calculation of the *S. oleracea* *cytb<sub>6</sub>f* cryo-EM map global and local resolution.** **a**, Gold-standard refinement was used for estimation of the final map resolution (solid black line). The global resolution of 3.58 Å was calculated using a FSC cut-off at 0.143. **b-c**, A C1 density map of the *cytb<sub>6</sub>f* complex both with (**b**) and without (**c**) the detergent shell. The map is coloured according to local resolution estimated by RELION and viewed from within the plane of the membrane. The colour key on the right shows the local structural resolution in angstroms (Å).

### 4.3 Structural modelling

#### 4.3.1 Multiple sequence alignment of the *S. oleracea* *cytb<sub>6</sub>f* with cyanobacterial and algal complexes

The polypeptide sequences of the eight subunits of *S. oleracea* *cytb<sub>6</sub>f* were aligned with their counterparts from cyanobacterial (*M. laminosus*, *Nostoc* sp. PCC 7120) and algal (*C. reinhardtii*) species using Clustal Omega v 1.2.4 (**Figure 4.5** and **Figure 4.6**) (**Goujon et al., 2010; Sievers et al., 2011**). Targetting peptides (including chloroplast transit peptides) were omitted from the alignment.

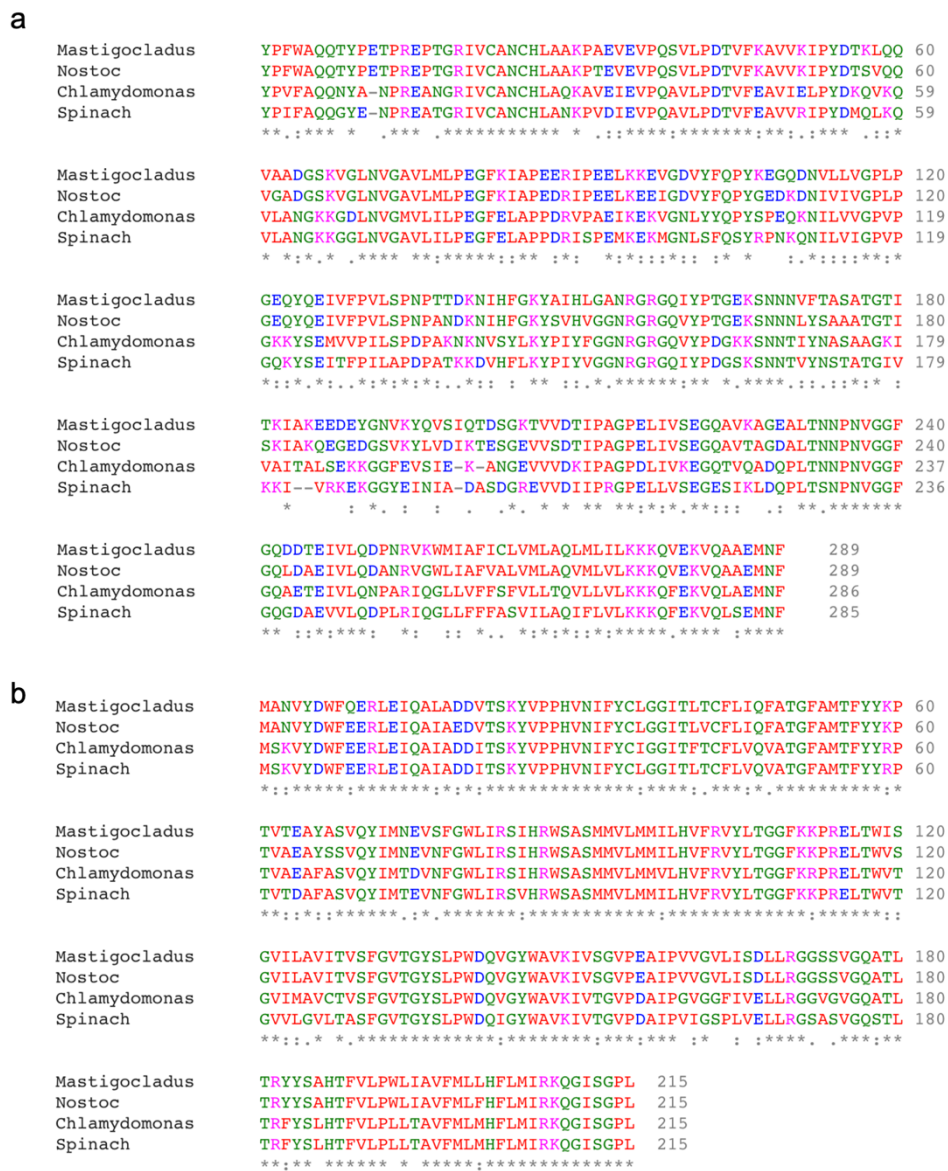


**Figure 4.5 | Multiple sequence alignment of *cytb<sub>6</sub>* subunits *cyt<sub>f</sub>* and *cytb<sub>6</sub>*. a-b, Sequences of *cyt<sub>f</sub>* (a) and *cytb<sub>6</sub>* (b) from cyanobacterial (*Mastigocladus laminosus*, *Nostoc* sp. PCC7120), algal (*Chlamydomonas reinhardtii*) and plant (*Spinacia oleracea*) were aligned in Clustal Omega v 1.2.4. Conserved identities are indicated by asterisks (\*), and similarities by double (:), then single dots (.). Polar residues are coloured in green, positively charged residues are coloured pink, hydrophobic residues are coloured red and negatively charged residues are coloured blue. The sequences omit targeting peptides.**

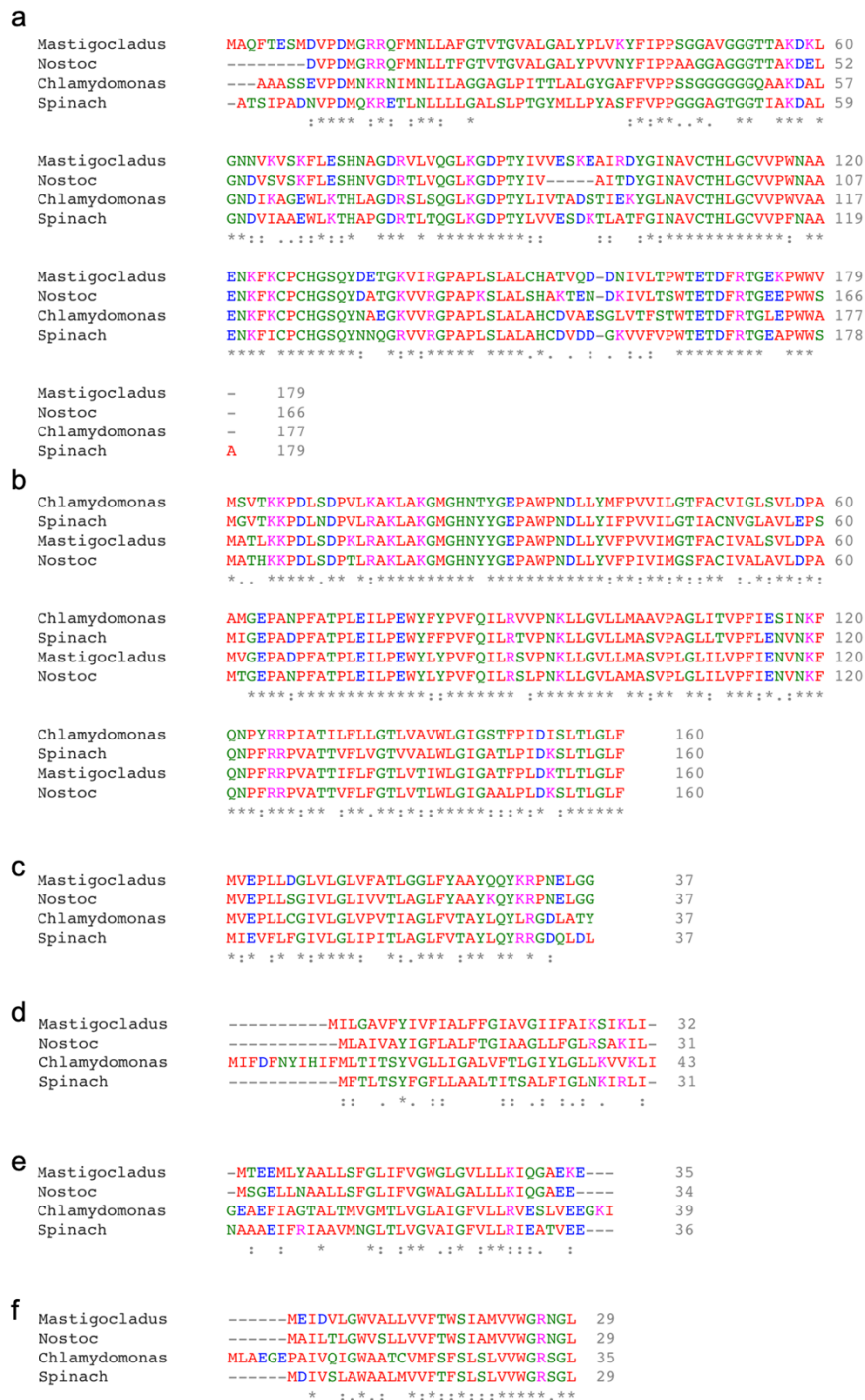


**Figure 4.6 | Multiple sequence alignment of *cytb<sub>6</sub>* subunits Rieske ISP, subunit IV, PetG, PetL, PetM and PetN.** **a-f**, Sequences of the Rieske ISP (**a**), subIV (**b**), PetG (**c**), PetL (**d**), PetM (**e**) and PetN (**f**) from cyanobacterial (*Mastigocladus laminosus*, *Nostoc* sp. PCC7120), algal (*Chlamydomonas reinhardtii*) and plant (*Spinacia oleracea*) were aligned in Clustal Omega v 1.2.4. Conserved identities are indicated by asterisks (\*), and similarities by double (:), then single dots (.). Polar residues are coloured in green, positively charged residues are coloured pink, hydrophobic residues are coloured red and negatively charged residues are coloured blue. The sequences omit targeting peptides.

### 4.3.2 Model Building

Initially, a homology-based approach was performed as described in **section 2.9.1** using the crystallographic structure of *Nostoc* sp. PCC 7120 *cyt<sub>b</sub>cf* (PDB: 4OGQ) (**Hasan and Cramer, 2014b**) as a template and the sequence alignments generated by Clustal Omega as a guide. The model was rigid-body docked into the density using the 'fit in map' function in Chimera (**Pettersen et al., 2004**). This was then followed by manual adjustment and real-space refinement using COOT (v 0.8.9.2) (**Emsley and Cowtan, 2004**) using bulky residues such as Arg, Trp, Tyr and Phe as a guide to aid fitting.

After fitting of the polypeptide chains and cofactors in one half of the dimeric complex, the other half of the complex was then independently modelled into the C1 density map. Once the polypeptide chain was complete for both halves of the complex, additional non-protein molecules (e.g. ligands such as plastoquinone-9 (PQ), lipids and cofactors) were assigned to regions of unassigned density. The model underwent several cycles of iterative global refinement and minimisation using the real space refinement function in PHENIX (**Adams et al., 2010**) followed by validation and manual refinement.

### 4.3.3 Model Validation

Model validation was carried out using the 'Comprehensive Validation' tool in PHENIX as described in **section 2.9.2** (**Adams et al., 2010; Afonine et al., 2018; Williams et al., 2018**) to assess the overall model quality and highlight any issues regarding steric clashes and general geometry such as rotamer outliers, Ramachandran outliers, anomalous bond lengths and anomalous bond angles.

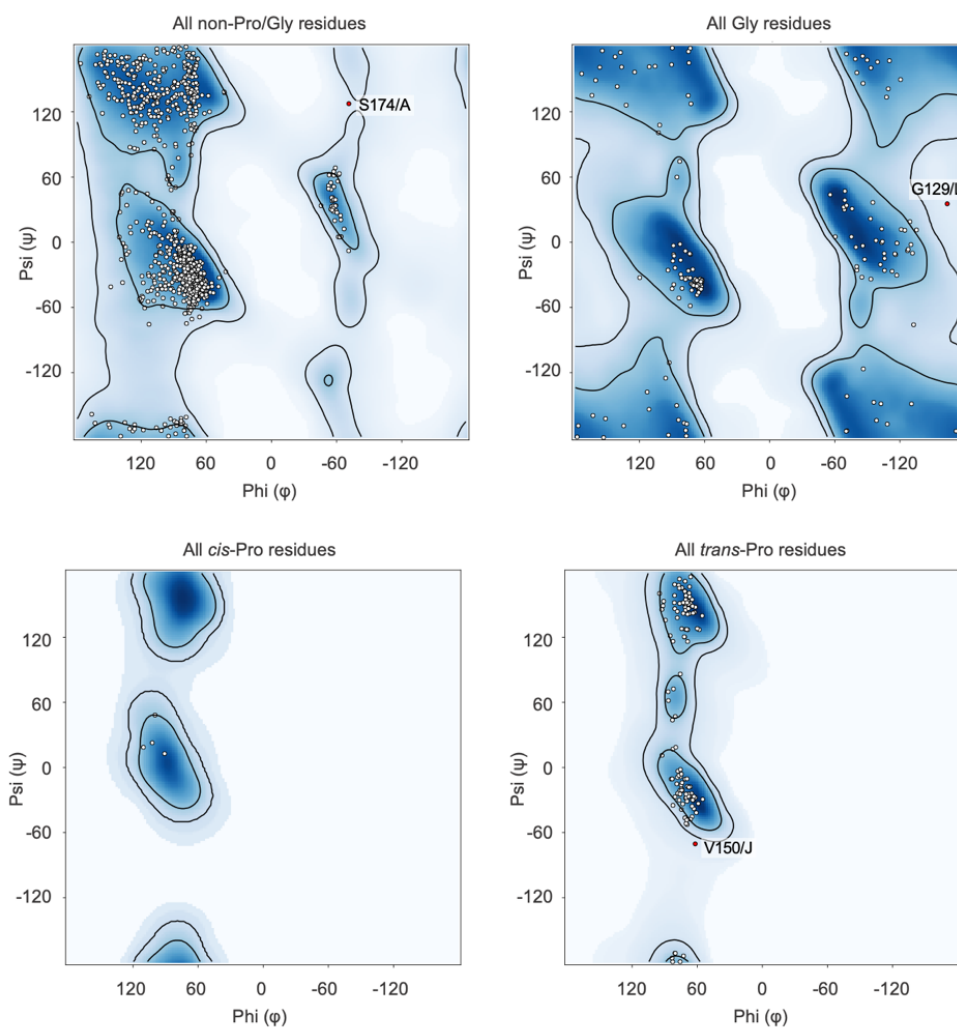
The 'Comprehensive Validation' tool in PHENIX utilises MolProbity (**Chen et al., 2010**) features to quantify model quality; this generates two summarised statistics; both of these are scaled and normalised relative to other structures of a similar resolution (within 0.25 Å) submitted to the PDB.

The first summarised statistic is an all-atom 'clash score' (**Chen et al., 2010**) which accounts for the number of unfavourable steric clashes between non-donor-acceptor atom pairs in the model. Hydrogen atoms are added to the model and the number of 'serious' atom-atom overlaps (i.e., > 0.4 Å overlap for non-H-bonded atoms) per 1000 atoms is quantified. In this

case the clash score (**Table 4.1**) is well within the expected range for a structure at this resolution.

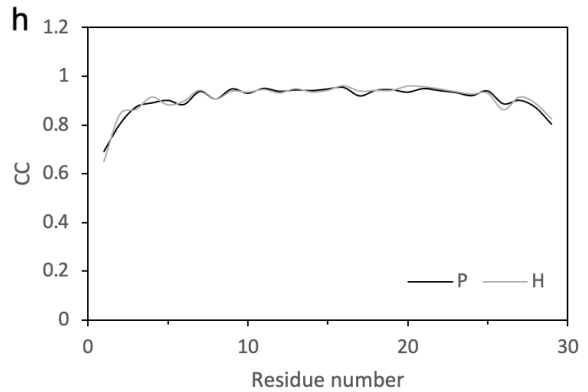
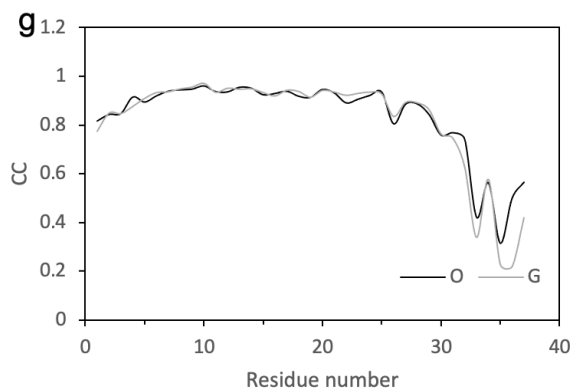
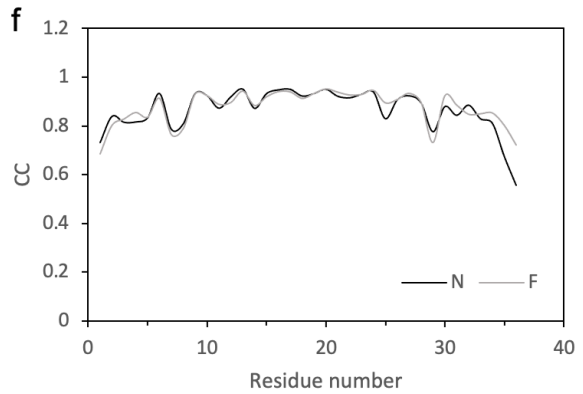
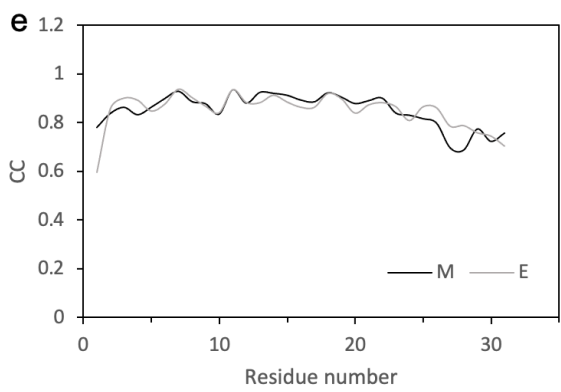
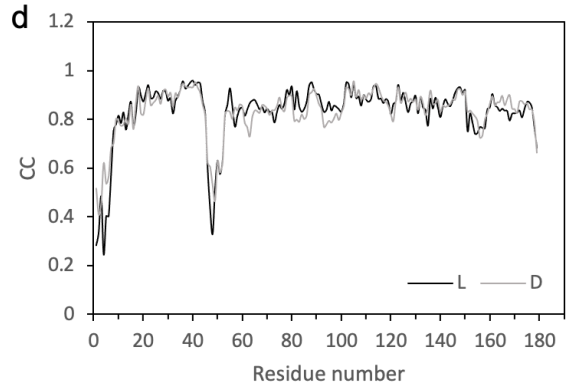
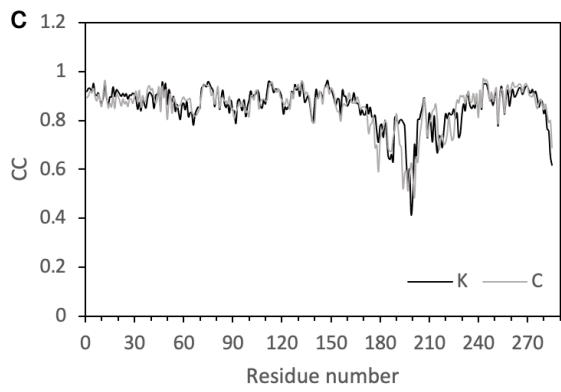
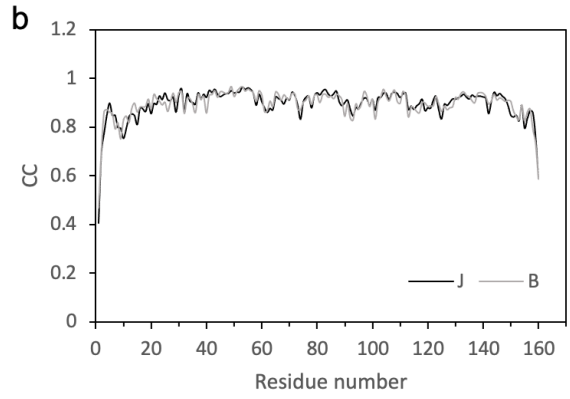
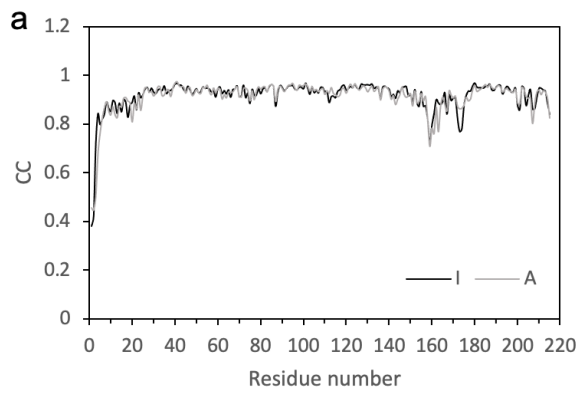
The second summarised statistic is the 'MolProbity score' (**Chen et al., 2010**), this provides an overall assessment of model quality in terms of both sterics and geometry. The score is a log-weighted combination of the clash score, Ramachandran outliers (%) and rotamer outliers (%) in the model; these values are scaled and normalised to provide a single number that reflects the resolution at which those values might be expected. A structure with a Molprobity score numerically lower than its actual global resolution is determined as being better in quality than the average structure on the PDB at that resolution. In this case, the Molprobity score for the *S. oleracea* *cytb<sub>6f</sub>* map is 1.83 (**Table 4.1**) indicating that the model quality is much higher than the average structure on the PDB at  $\sim 3.58 (\pm 0.25)$  Å resolution.

In addition to these two summarised statistics, Molprobity also provides a detailed assessment of Ramachandran ( $\phi$ ,  $\psi$ ) (**Figure 4.7**) (**Ramachandran et al., 1963**) outliers and cis/twisted peptides.



**Figure 4.7 | Ramachandran analysis of the *S. oleracea* *cytb<sub>6f</sub>* model.** Of the 1,944 residues modelled, 95.4 % occupy 'favourable' regions and 4.24 % occupy 'allowed' regions. There are three outliers (S174/A, G129/L and V150/J) built marginally outside of the permitted zones, these are labelled and shown as red dots.





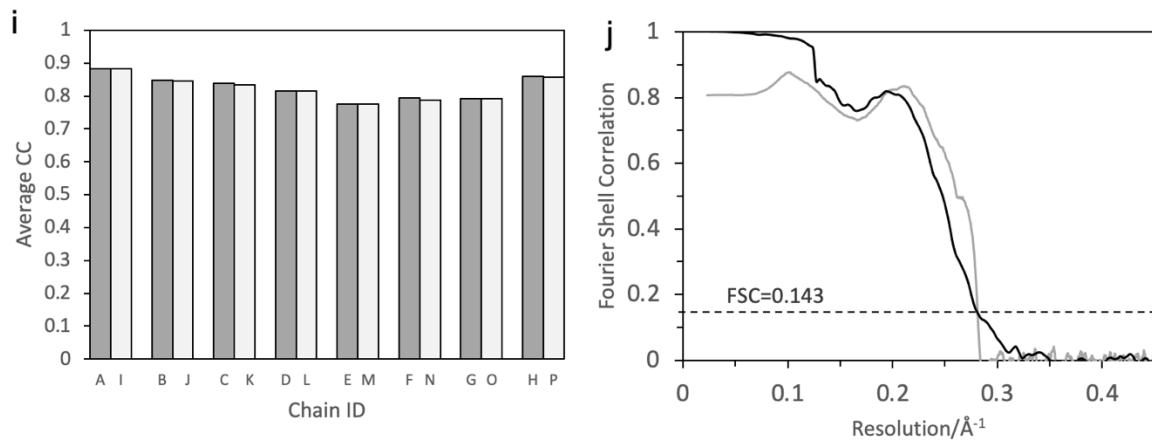


**Figure 4.8| An assessment of the quality of modelled data fit in the cryo-EM map of *S. oleracea* *cytb<sub>6</sub>f*.** Correlation coefficients (CC) for each of the eight subunits in the *S. oleracea* *cytb<sub>6</sub>f* dimer calculated on a per-residue basis for **a**, the *cyt b<sub>6</sub>* subunit (chains A and I), **b**, subIV (chains B and J), **c**, *cyt<sub>f</sub>* (chains C and K), **d**, the Rieske ISP (D and L), **e**, Pet L (chains E and M), **f**, Pet M (chains F and N), **g**, Pet G (chains O and G) and **h**, Pet N (chains H and P). Significant dips in the plotted CC values correspond to regions of the map where the resolution is lower and the fit is more ambiguous such as around the tips of the *cyt<sub>f</sub>* soluble domain (residues 170 - 220), the Rieske ISP hinge region (residues 41 - 56) and the N- and C- terminal regions of subunits. **i**, CC averages for each chain. **j**, Comparison of the FSC curve for experimental data (solid black line) and the calculated model-to-map FSC curve (solid grey line).

**Table 4.1 | Cryo-EM data collection, refinement and validation statistics.**

\*(Rosenthal and Henderson, 2003).

Parameter	<i>S. oleracea cytb<sub>6f</sub></i> (EMB-4981) (PDB 6RQF)
<b>Data collection and processing</b>	
Nominal Magnification	130,000 X
Accelerating Voltage (kV)	300
Electron exposure (e <sup>-</sup> /Å <sup>2</sup> )	1.15 (55.2 e- on 48 frames)
Defocus range (-μm)	-1.5 to -2.5
Pixel size (Å)	1.065
Symmetry imposed	C1
Initial particle images (no.)	422,660
Final particle images (no.)	108,560
Map resolution (Å) (global)	3.58
FSC threshold	0.143
Map resolution range (Å)	~ 3.3 - 8.3
<b>Refinement</b>	
Initial model used	RELION <i>de novo</i> model from 30,000 particles
Model resolution (Å)	3.58
FSC threshold	0.143
Model resolution range (Å)	~ 3.3 – 8.7
Map sharpening <i>B</i> factor (Å <sup>2</sup> )	Estimated automatically using RELION
<b>Model composition</b>	
Non-hydrogen atoms	16,359

Protein residues	1,944
Ligands	29
<b>B factors (Å<sup>2</sup>)</b>	
Protein	RELION auto-estimated
Ligand	RELION auto-estimated
<b>RMS deviations (PHENIX)</b>	
Bond lengths (Å)	0.009
Bond angles (°)	1.182
<b>Validation</b>	
Molprobity score	1.83
Clashscore	9.67
Poor rotamers (%)	0.18
<b>Ramachandran plot</b>	
Favoured (%)	95.40
Allowed (%)	4.24
Disallowed (%)	0.37

## 4.4 Structural analysis

### 4.4.1 Overall architecture and comparison with the cyanobacterial and algal complexes

Initial inspection of the model indicates that the global architecture of the dimeric *S. oleracea* *cyt<sub>b</sub>f* complex is largely similar to crystallographic structures of algal and cyanobacterial complexes from *C. reinhardtii* (PDB ID: 1Q90) (Stroebel et al., 2003), *M. laminosus* (PDB IDs: 1VF5, 2E74, 2D2C, 2E76, 4H13, 4PVI, 2E75, 4H0L, 4I7Z) (Hasan et al., 2013a, 2013b, 2014;

Kurisu et al., 2003; Yamashita et al., 2007; Yan et al., 2006) and *Nostoc* sp. PCC 7120 (PDB ID: 2ZT9, 4H44, 4OGQ) (Baniulis et al., 2009; Hasan and Cramer, 2014a; Hasan et al., 2013b).

The colour-coded map (**Figure 4.9**) shows the density of each of the eight polypeptide subunits in each half of the dimeric complex; the transmembrane portions of these subunits appear to be surrounded by a band of disordered density corresponding to the detergent micelle. Each monomeric unit of the *cytb<sub>6</sub>f* complex is arranged as observed in the algal and cyanobacterial structures, with four large polypeptide subunits (*cytf*, *cytb<sub>6</sub>*, ISP, subIV) containing eight prosthetic groups (haem *f*, 2Fe-2S, Chl *a*, haem *b<sub>p</sub>*, haem *b<sub>n</sub>*, haem *c<sub>n</sub>*, 9-*cis* β-carotene), and four small subunits (PetG, L, M, N).

The organisation of the transmembrane integral subunits can be seen on the stromal side of the complex (**Figure 4.9**) with 13 TM helices visible within each monomeric unit (**Figure 4.9**). The extrinsic domains of *cytf* and the ISP on the luminal (p-) side of the complex are anchored within the transmembrane region, each by a single helix at the periphery of the dimeric complex (**Figure 4.9**). Peripheral to the core of *cytb<sub>6</sub>* (four TMH) and subIV (three TMH) on the long axis of the complex is the single kinked transmembrane helix of the ISP; a flexible polyglycine linker extends from this transmembrane helix to the soluble domain of ISP. As observed previously, this soluble domain contributes to dimer stability through domain swapping, crossing over to the opposite monomeric unit of the complex where it provides the extrinsic ISP domain of the neighbouring monomeric unit. The single TM helix constituting the membrane anchoring portion of *cytf* is sandwiched at the periphery of the complex between the single kinked helix of the ISP and the four single transmembrane helices of the small subunits (PetG, L, M and N). **Figure 4.10** shows the density and structural model for each subunit.

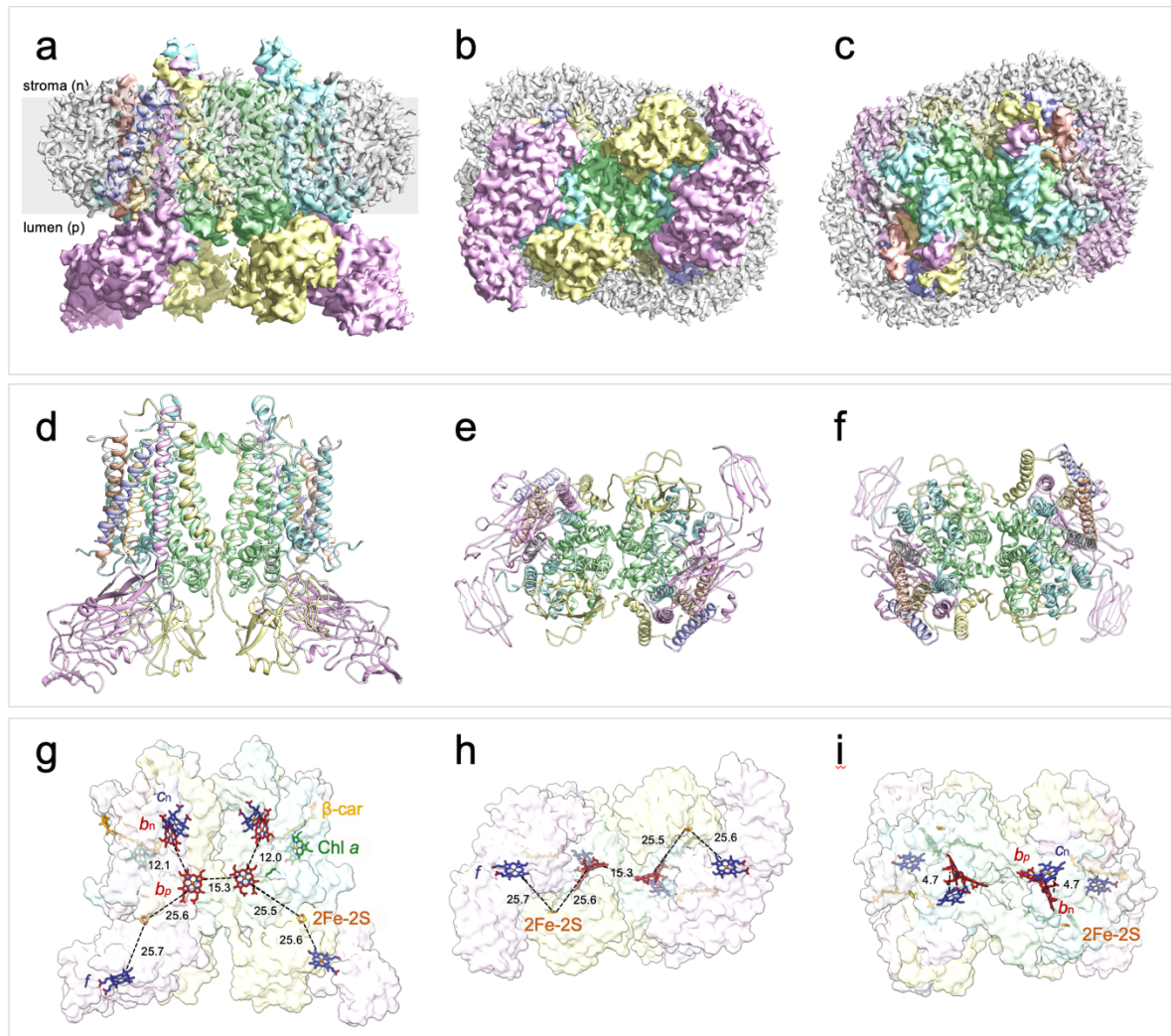


**Figure 4.9 | Cryo-EM structure of the *S. oleracea* cytb<sub>6</sub>f complex.** **a–c**, Views of the colour-coded cytb<sub>6</sub>f density map showing cytb<sub>6</sub> (green), cytf (pink), ISP (yellow), subIV (cyan), PetG (grey), PetM (salmon), PetN (pale orange) and PetL (pale purple). Detergent and other disordered molecules are shown in semi-transparent light grey. **a**, View in the plane of the membrane. The grey stripe indicates the probable position of the thylakoid membrane bilayer. **b**, View perpendicular to the membrane plane from the lumenal (p) side. **c**, View perpendicular to the membrane plane from the stromal (n) side. **d–f**, Modelled subunits of cytb<sub>6</sub>f shown in a cartoon representation and coloured as in a–c. **d**, View in the plane of the membrane. **e**, View perpendicular to the membrane plane from the lumenal side. **f**, View perpendicular to the membrane plane from the stromal side. **g–i**, Modelled cofactors of cytb<sub>6</sub>f showing haem b<sub>n</sub> (firebrick red), haem b<sub>p</sub> (firebrick red), haem c<sub>n</sub> (dark blue), haem f (dark blue), the 2Fe-2S (orange Fe and yellow S), Chl a (green) and β-carotene (orange) in stick representation.

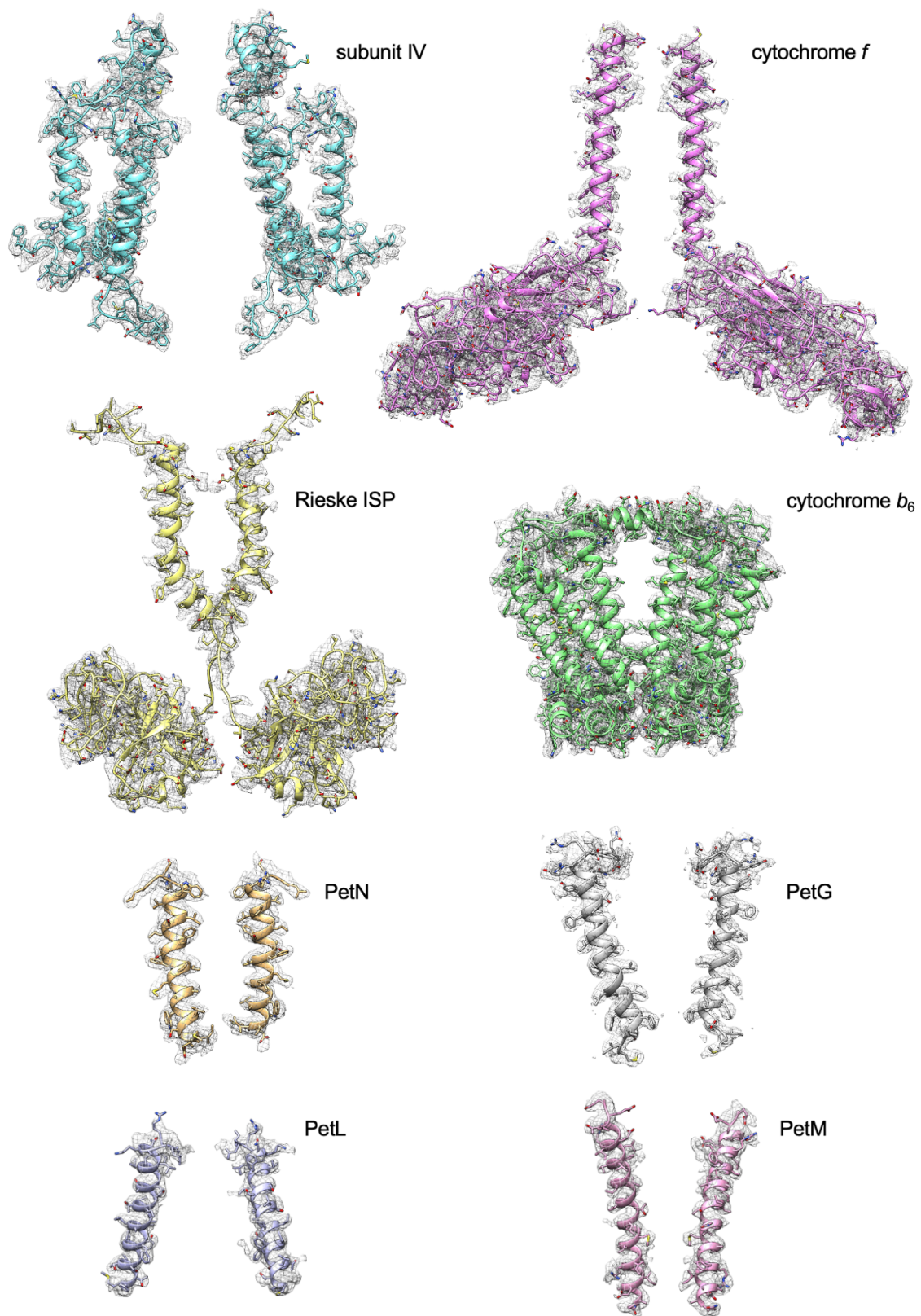


**Figure 4.10|** Cryo-EM densities and structural models of polypeptides in the *cytb<sub>6</sub>f* complex. The colour code is the same as in **Figure 4.9**. The contour levels of the density maps were adjusted to 0.0144.

Each monomeric unit of the complex contains seven prosthetic groups as described previously, these comprise two covalently bound *c*-type haems (haem *f* and haem *c<sub>n</sub>*), two non-covalently bound *b*-type haems (haem *b<sub>p</sub>* and haem *b<sub>n</sub>*), a 2Fe-2S cluster, a 9-*cis*  $\beta$ -carotene molecule and a chlorophyll (Chl) *a* molecule (Baniulis et al., 2009; Hasan and Cramer, 2014a; Hasan et al., 2013a, 2013b, 2014; Kurisu et al., 2003; Stroebel et al., 2003; Yamashita et al., 2007; Yan et al., 2006). In addition to these core prosthetic groups, the 3.58 Å map from *S. oleracea* *cytb<sub>6f</sub>* also resolves three PQ molecules, two monogalactosyl diacylglycerol (MGDG) lipids, four phosphatidylglycerol (PG) lipids, three sulfoquinovosyl diacylglycerol (SQDG) lipids and three phosphatidylcholine (PTC) lipids. **Figure 4.9** shows the organisation of prosthetic groups, PQ molecules and lipids within the *S. oleracea* *b<sub>6f</sub>* dimer, while **Figure 4.11** shows the respective densities and structural model for each molecule.

Comparison with previous structures indicates the edge-to-edge cofactor distances **Figure 4.9** are well conserved among *cytb<sub>6f</sub>* complexes of various species (**Table 4.2**), these are also similar to those observed in the respiratory *cytbc<sub>1</sub>* complex (**Table 4.3**) (**Zhang et al., 1998**). As observed in previous structures, while the cofactor distances along the low-potential pathway appear to be conducive to efficient electron transfer both within (and possibly between neighbouring monomeric units (**Swierczek et al., 2010**)), there appears to be a large gap (~ 26 Å) between cofactors (2Fe-2S cluster and haem *f*) along the high-potential electron transfer pathway which must be bridged to enable electron transfer at meaningful rates, this will be discussed in greater detail in **chapter 6**.



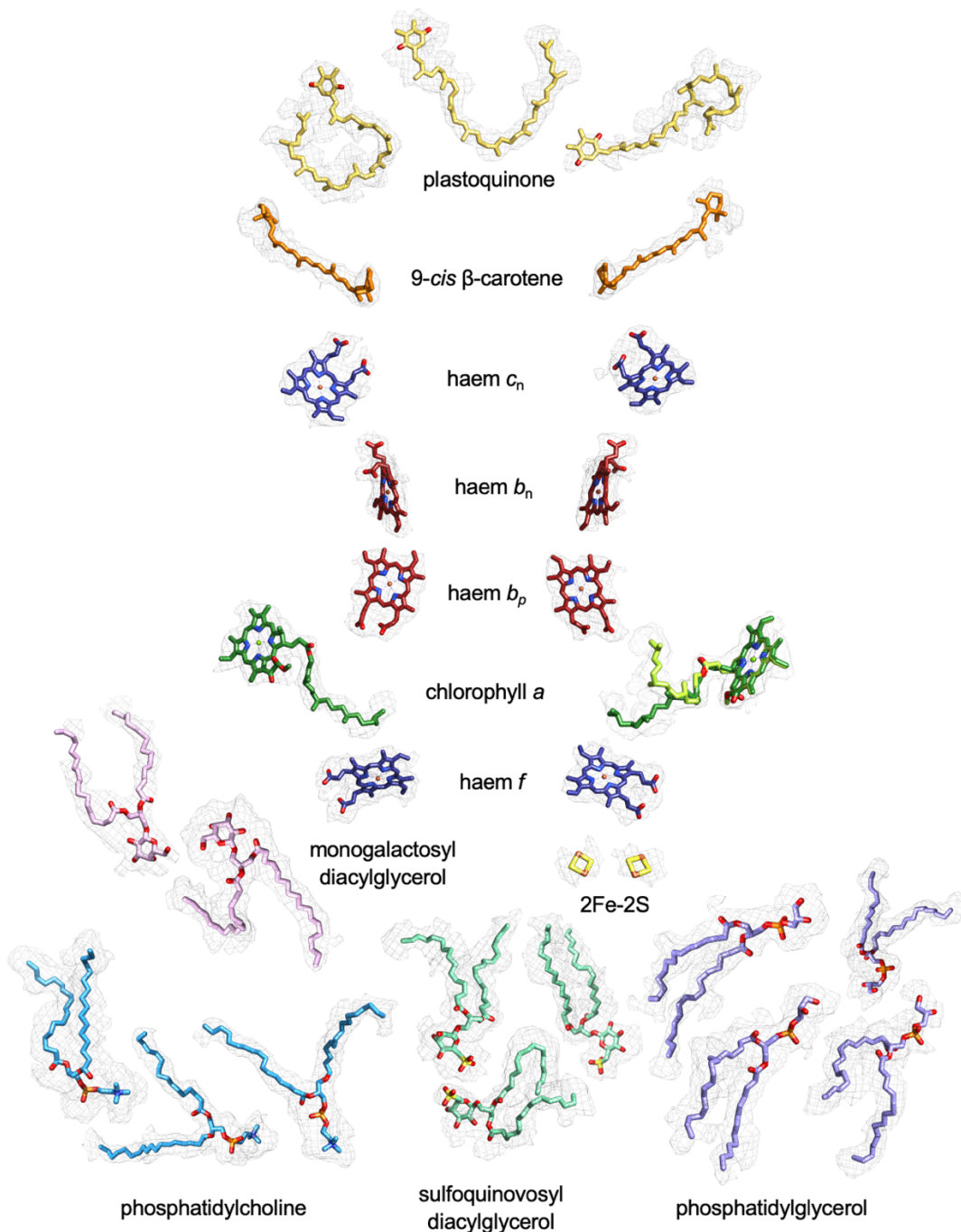


**Figure 4.11 | Cryo-EM densities and structural models of prosthetic groups, lipids and plastoquinone molecules in the *cytb<sub>6</sub>f* complex.** *c*-type haems (*f*,  $c_n$ ; dark blue), *b*-type haems ( $b_p$ ,  $b_n$ ; red), 9-*cis*  $\beta$ -carotene (orange), chlorophyll *a* (major conformation, dark green) (minor conformation, light green), 2Fe-2S (orange/yellow), plastoquinones (yellow), monogalactosyl diacylglycerol (light pink), phosphatidylcholine (light cyan), sulfoquinovosyl diacylglycerol (light green), phosphatidylglycerol (light purple). The contour levels of the density maps were adjusted to 0.0068. Note that the overall arrangement of cofactors depicted here is not necessarily related to their organisation in the modelled protein structure.

**Table 4.2| A comparison of edge-to-edge cofactor distances (Å) in each half of the  $b_6f$  dimer from different species.** Models used include  $b_6f$  from *S. oleracea* (PDB ID: 6RQF (Malone et al., 2019)), *C. reinhardtii* (PDB ID: 1Q90 (Stroebel et al., 2003)), *M. lamosus* (PDB ID: 2E74 (Yamashita et al., 2007)) and *Nostoc* sp. PCC 7120 (PDB ID: 4OGQ (Hasan and Cramer, 2014a)). <sup>a</sup> Inhibitor is indicated by the abbreviation TDS (tridecylstigmatellin).

PDB ID	6RQF	1Q90	2E74	4OGQ
<b>Source</b>	<i>S. oleracea</i>	<i>C. reinhardtii</i>	<i>M. lamosus</i>	<i>Nostoc</i> sp. PCC 7120
<b>Resolution (Å)</b>	3.58 Å	3.1	3.0	2.5
<b>Inhibitors <sup>a</sup></b>	-	TDS (Q <sub>p</sub> )	-	-
<b>Distances:</b>				
$b_n - c_n$ (Å)	4.7, 4.7	4.7, 4.7	4.7, 4.7	4.6, 4.6
$b_n - b_p$ (Å)	12.1, 12.0	12.2, 12.2	12.2, 12.2	12.1, 12.1
$b_p - b_p$ (Å)	15.3	15.1	15.2	15.3
$b_p - [2Fe-2S]$ (Å)	25.6, 25.5	22.9, 22.9	25.5, 25.5	25.3, 25.3
$[2Fe-2S] - f$ (Å)	25.9, 26.1	27.8, 27.8	26.2, 26.2	26.2, 26.2

**Table 4.3| A comparison of edge-to-edge cofactor distances (Å) in each half of  $bc_1$  from *G. gallus*.** Models used include the  $bc_1$  dimer from *G. gallus* with the Rieske ISP in its distal (PDB ID: 1BCC (Zhang et al., 1998)) and proximal (PDB ID: 3BCC (Zhang et al., 1998)) positions.

PDB ID	1BCC (distal)	3BCC (proximal)
<b>Source</b>	<i>G. gallus</i>	<i>G. gallus</i>
<b>Resolution (Å)</b>	3.2	3.7
<b>Inhibitors <sup>a</sup></b>	-	STG (Q <sub>p</sub> ), AMY (Q <sub>n</sub> )
<b>Distances:</b>		
$b_n - b_p$ (Å)	12.4, 12.4	12.3, 12.3

$b_p - b_p$ (Å)	14.4	14.5
$b_p - [2Fe-2S]$ (Å)	30.3, 30.3	23.0, 23.1
$[2Fe-2S] - c_1$ (Å)	16.8, 16.8	27.3, 27.5

#### 4.4.2 The intermonomer cavity and native PQ molecules

As described in **section 1.3.1**, dimerisation of two monomers creates a large, protein-free cavity at the heart of the *cyt<sub>b</sub>6f* complex considered to provide a space to sequester and concentrate substrate near to the active sites (**Baniulis et al., 2009; Hasan and Cramer, 2014a; Hasan et al., 2013a, 2013b, 2014; Kurisu et al., 2003; Stroebel et al., 2003; Yamashita et al., 2007; Yan et al., 2006**) (**Figure 4.12**). In *S. oleracea*, the depth of this cavity is  $\sim 30$  Å, with the roof of the cavity bounded by the N-terminal helices of *cyt b<sub>6</sub>* on the n-side of the complex, while the floor of the cavity on the p-side is delimited by aromatic residues belonging to helices A and D (*cyt b<sub>6</sub>*) and the *b<sub>p</sub>* haems of each monomeric unit (*cyt b<sub>6</sub>*) (**Figure 4.12**). The sides of the cavity are lined by predominantly hydrophobic residues belonging to the A and D helices (*cyt b<sub>6</sub>*), the E helix of subIV and the TM helix of the Rieske ISP (**Figure 4.12**).

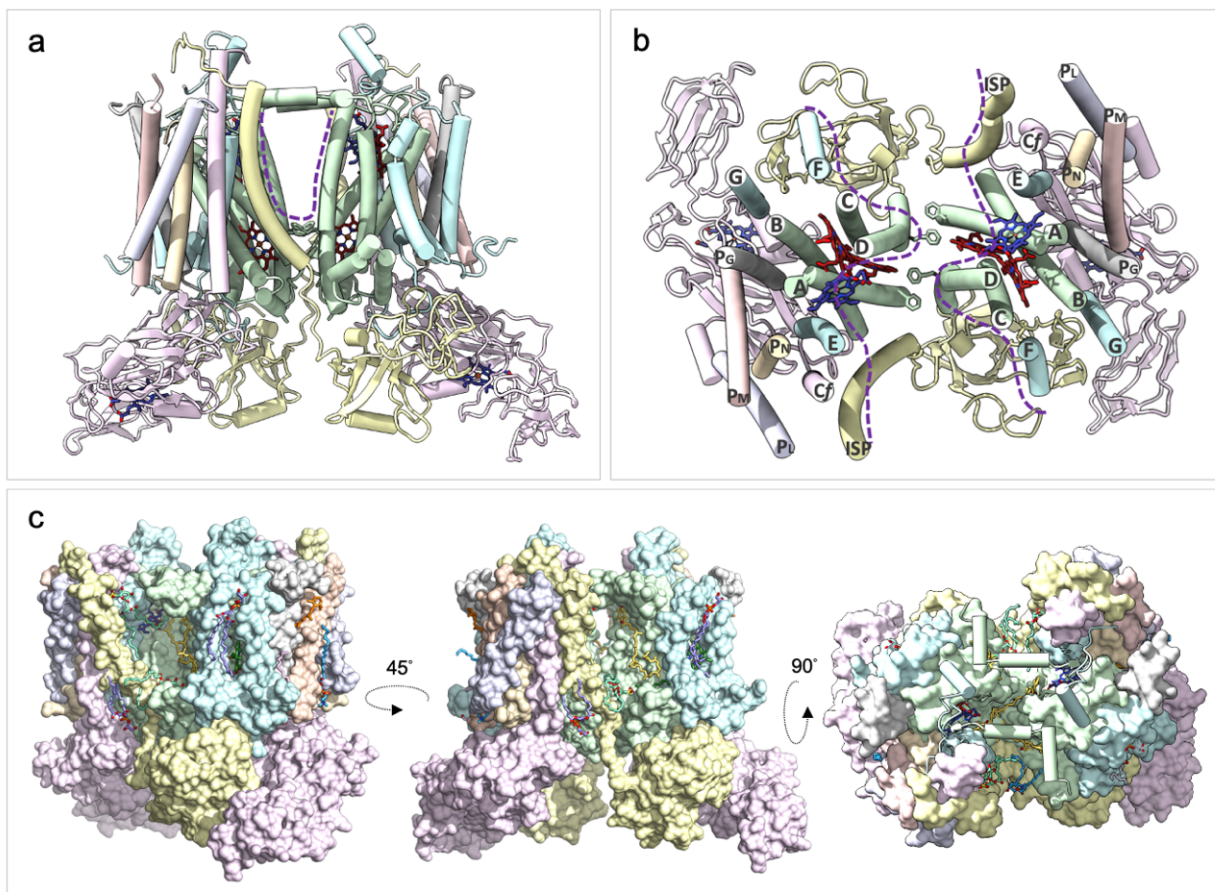


**Figure 4.12|** The intermonomer cavity of the *S. oleracea*  $cytb_6f$  complex. **a-b**, a cartoon representation of the  $cytb_6f$  complex showing the intermonomer cavity (outlined by a purple dashed line) viewed perpendicular (**a**) and normal (**b**) to the plane of the membrane. Aromatic residues that delimit the floor of the cavity and the haems are shown in stick representation. **c**, a surface representation of the  $cytb_6f$  complex showing the intermonomer cavity from various angles. Subunits are coloured as in **Figure 4.9**, and cofactors and lipids coloured as in **Figure 4.11**.

In previous structures, PQ locations have generally been inferred from the locations of tightly bound quinone analogue inhibitors (e.g. tridecyl stigmatellin (TDS), stigmatellin, 2,5-dibromo-3-methyl-6-isopropylbenzoquinone (DBMIB), 2n-nonyl-4-hydroxy-quinoline-N-oxide (NQNO)) included in the crystallographic experiment (Hasan et al., 2013b; Kurisu et al., 2003; Yamashita et al., 2007). Here, the *S. oleracea* cryo-EM structure was obtained with associated endogenous plastoquinone-9 (PQ) molecules present, these were co-purified with the complex from its native plant source (**Figure 4.13**). Three PQ molecules were modelled within the intermonomer cavity, these were clearly defined by their respective densities as shown in **Figure 4.13** with their edge-to-edge distances to the nearest cofactors shown in **Figure 4.13**.

The first natively associated PQ molecule (PQ1) is found on the edge of the Q<sub>p</sub> portal on one side of the dimer (**Figure 4.13**) in a position adjacent to the Chl *a* phytyl tail. In this position, the 1,4-benzoquinone head group of PQ1 is situated ~ 16 Å from haem *b<sub>p</sub>*, ~ 26 Å from the 2Fe-2S cluster (**Figure 4.13**) and distal to the Q<sub>p</sub> quinone oxidising site, defined in the *M. lamosus* *cyt<sub>b</sub><sub>6</sub>f* structure (PDB ID: 4H13) by the bound quinone analogue inhibitor TDS (**Hasan et al., 2013b**). Given the well-defined character of the density corresponding to this PQ, it is possible that this position may indicate a preferred holding place for plastoquinone molecules upon approach to the Q<sub>p</sub> binding niche. It is interesting to note a small patch of positive charge nearby the 1,4-benzoquinone head group. This charged patch conveyed by Arg182 (cyt *b<sub>6</sub>*) could provide a suitably attractive surface for transient interactions with the PQ molecule guiding its approach to the Q<sub>p</sub> site (**Figure 4.13**).

A second PQ molecule (PQ2) is resolved on the opposite monomeric unit to PQ1, in a position proximal to the haem *c<sub>n</sub>/b<sub>n</sub>* pair at the Q<sub>n</sub> reducing site on the stromal side of the complex (**Figure 4.13**). The length of PQ2 adopts a bowed conformation within a narrow conduit which subdivides the intermonomer cavity.

While the head group of PQ2 forms a H-bond with the C6 propionate group of haem *c<sub>n</sub>* in a position which we attribute to the Q<sub>n</sub> site, it is notable that the distal portion of the PQ2 isoprenoid tail appears to partially obstruct the Q<sub>n</sub> plastoquinone reducing site on the opposite half of the complex (these two features will be discussed further in **section 4.4.4**).

A third PQ molecule (PQ3) is observed at a position between the Q<sub>p</sub> site of one monomeric unit and the Q<sub>n</sub> of the other with the 1,4-benzoquinone head group of PQ3 approaching the

narrow channel occupied by PQ2 and the isoprenoid tail of PQ3 appearing adjacent to Chl *a* on the edge of the Q<sub>p</sub> portal (**Figure 4.13**). It is possible that this third PQ may capture a snapshot of the molecule in a preferred resting position during transition between the Q<sub>p</sub> and Q<sub>n</sub> sites in opposite monomers. As with PQ1, a positively charged residue (Lys208, cyt *b*<sub>6</sub>) is located close to the 1,4-benzoquinone head group of PQ3. Interestingly this residue is highly conserved both spatially and sequentially, it is also located next to the catalytic Arg207 and may represent an attractive target for mutagenesis.

Whilst the densities for these three PQ molecules modelled are well defined (**Figure 4.13**), it is worth noting that the long isoprenoid tail of PQ lends itself to forming non-specific interactions with numerous other regions within the hydrophobic intermonomer cavity. Indeed, numerous additional densities within the intermonomer cavity indicate the volume may be tightly packed with lipids, plastoquinone molecules and water molecules however only molecules with clear and strong densities indicating high occupancy could be assigned.

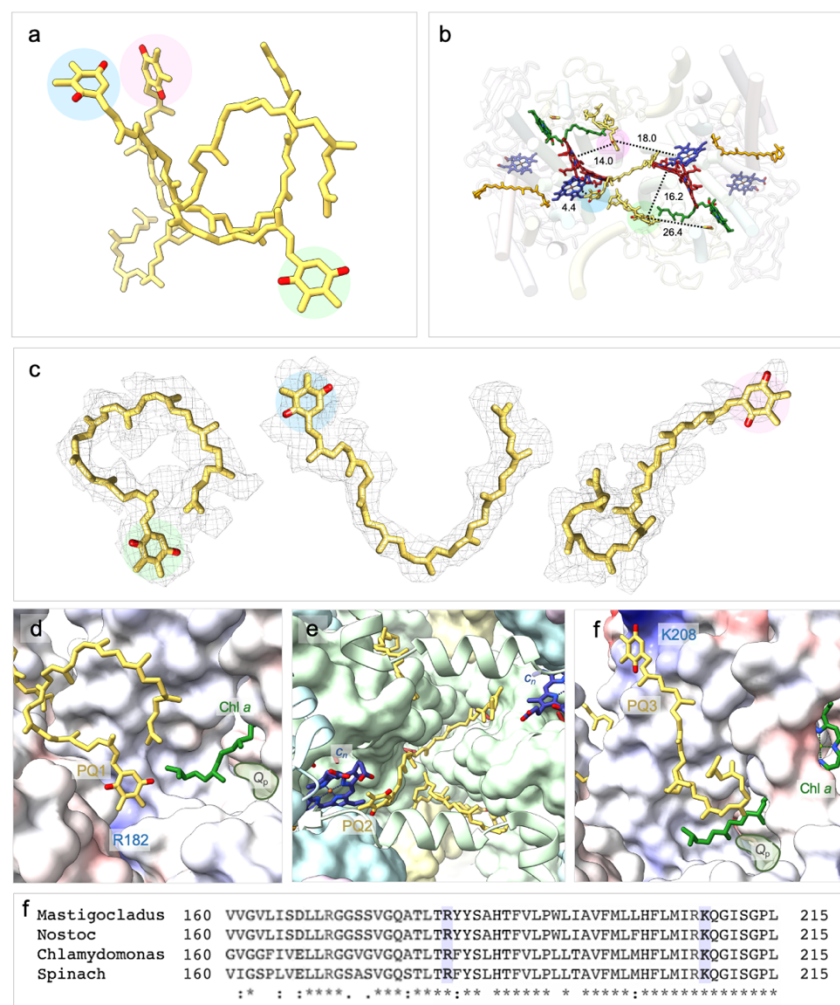




**Figure 4.13** | Three native plastoquinone molecules can be modelled in the *S. oleracea* *cytb<sub>6</sub>f* complex. **a**, a stick representation showing the three native plastoquinone (PQ) molecules resolved within the intermonomer cavity. PQ1 is highlighted in green, PQ2 is highlighted in blue and PQ3 is highlighted in pink. **b**, The arrangement of molecules in the *cytb<sub>6</sub>f* complex viewed perpendicular to the membrane plane from the stromal side. Cofactors and peptide subunits are coloured as in **Figure 4.9** and **Figure 4.11**, edge-to-edge distances (in Å) from each PQ molecule to the nearest cofactors are indicated by black dotted lines. **c**, the densities modelled as PQ1-3 shown as a grey mesh. **d**, Surface view of the complex showing PQ1 (yellow) approaching the plastoquinone oxidation site ( $Q_p$ ). The molecular surface of *cytb<sub>6</sub>f* is coloured by electrostatic potential with hydrophobic regions coloured white, regions with negative potential coloured red and regions with positive potential coloured blue. **e**, Surface view showing PQ2 spanning the intermonomer cavity with the head group bound at the  $Q_n$  site in one half of the dimer and the tail partially obstructing the  $Q_n$  site in the other half of the dimer. Cofactors and peptide subunits are coloured as in **Figure 4.9** and **Figure 4.11**. **f**, Surface view of the complex showing PQ3 (yellow) transitioning between the  $Q_p$  and  $Q_n$  sites in opposite halves of the dimeric complex. The molecular surface of *cytb<sub>6</sub>f* is coloured by electrostatic potential with hydrophobic regions coloured white, regions with negative potential coloured red and regions with positive potential coloured blue. **g**, Multiple sequence alignment of the *cytb<sub>6</sub>* subunit from cyanobacterial (*Mastigocladus laminosus*, *Nostoc* sp. PCC7120), algal (*Chlamydomonas reinhardtii*) and plant (*Spinacia oleracea*) sources were aligned in Clustal Omega v 1.2.4. Conserved identities are indicated by asterisks (\*), and similarities by double (:), then single dots (.). Conserved identities are indicated by asterisks (\*), and similarities by double (:), then single dots (.). R182 and K208 are highlighted in blue.

A third PQ molecule (PQ3) is observed at a position between the  $Q_p$  site of one monomeric unit and the  $Q_n$  of the other with the 1,4-benzoquinone head group of PQ3 approaching the narrow channel occupied by PQ2 and the isoprenoid tail of PQ3 appearing adjacent to Chl *a* on the edge of the  $Q_p$  portal (**Figure 4.13**). It is possible that this third PQ may capture a snapshot of the molecule in a preferred resting position during transition between the  $Q_p$  and  $Q_n$  sites in opposite monomers. As with PQ1, a positively charged residue (Lys208, *cyt b<sub>6</sub>*) is located close to the 1,4-benzoquinone head group of PQ3. Interestingly this residue is highly conserved both spatially and sequentially, it is also located next to the catalytic Arg207 and may represent an attractive target for mutagenesis.

Whilst the densities for these three PQ molecules modelled are well defined (**Figure 4.13**), it is worth noting that the long isoprenoid tail of PQ lends itself to forming non-specific interactions with numerous other regions within the hydrophobic intermonomer cavity. Indeed, numerous additional densities within the intermonomer cavity indicate the volume may be tightly packed with lipids, plastoquinone molecules and water molecules however only molecules with clear and strong densities indicating high occupancy could be assigned.

#### 4.4.3 The $Q_p$ portal and the luminal (p-) side plastoquinol oxidation ( $Q_p$ ) site

Plastoquinol oxidation on the luminal (p-) side of the complex is known to occur at the end of a narrow portal, previously assigned as the ' $Q_p$  portal', which extends from the wall of each intermonomer cavity (**Hasan and Cramer, 2014b**). In the *S. oleracea* complex, this narrow portal is bounded by numerous hydrophobic residues from subIV (Phe81, Val84, Leu88, Val98, Met101) and cyt  $b_6$  (Val126, Ala129, Val133, Val151, Val154) (**Figure 4.14**).

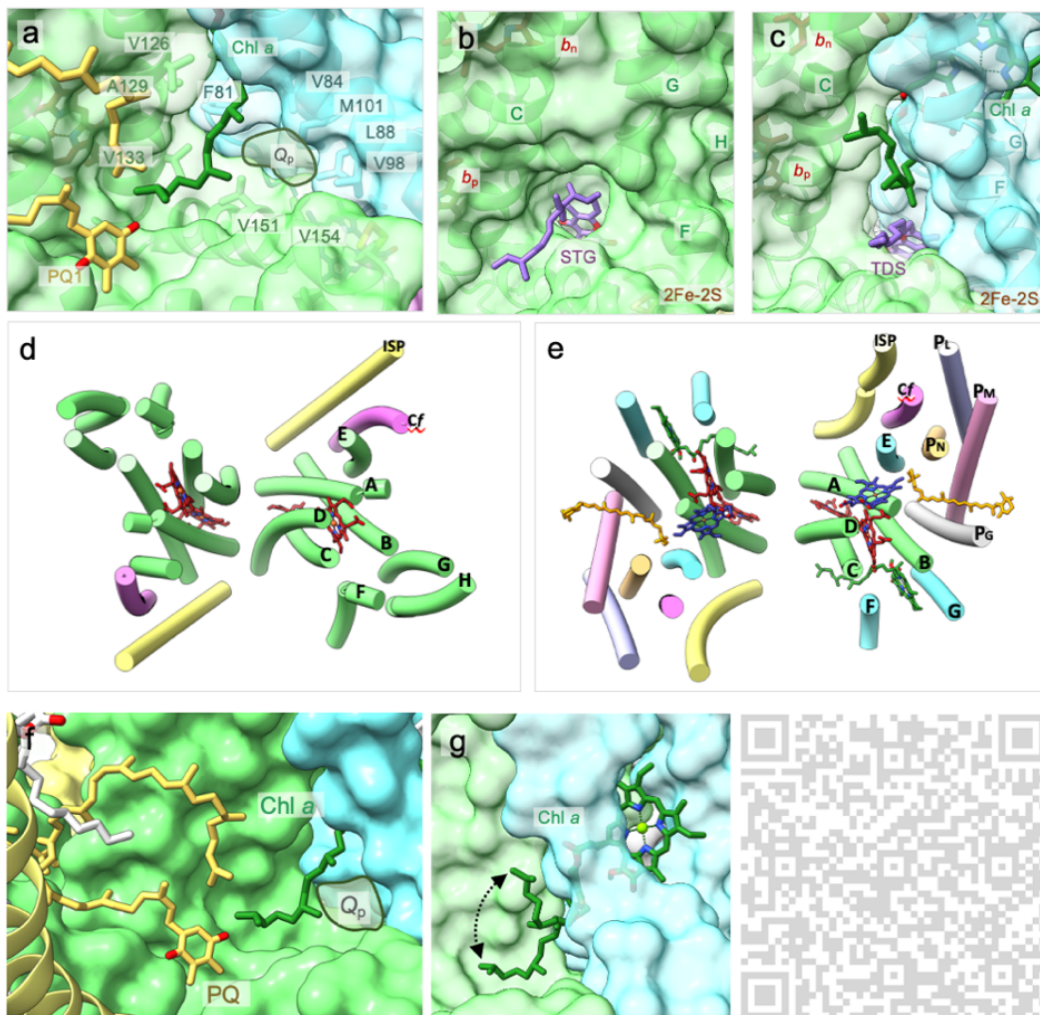




**Figure 4.14 | The Q<sub>p</sub> sites of *cytb<sub>c1</sub>* and *cytb<sub>6f</sub>*.** **a**, A cartoon representation of the Q<sub>p</sub> portal in the *S. oleracea* *cytb<sub>6f</sub>* complex showing residues from subIV (Phe81, Val84, Leu88, Val98, Met101) and *cytb<sub>6</sub>* (Val126, Ala129, Val133, Val151, Val154) which line the portal in stick representation beneath a semi-transparent surface. The entrance to the Q<sub>p</sub> site is outlined by a dark green area shaded in light green. **b-c**, a surface view of the Q<sub>p</sub> site in the *cytb<sub>c1</sub>* complex from *G. gallus* (**a**, PDB ID: 3BCC (**Zhang et al., 1998**)) and the *cytb<sub>6f</sub>* complex from *Mastigocladus laminosus* (**b**, PDB ID: 4H13 (**Hasan et al., 2013b**)). In both complexes, the Q<sub>p</sub> site is defined by TM helices 'C' and 'G' (shown as ribbons); additionally, in both complexes the site is occupied by quinone analogue inhibitors (stigmatellin in *cytb<sub>c1</sub>* and tridecylstigmatellin in *cytb<sub>6f</sub>*). **d-e**, the arrangement of TM helices (shown as cylinders) within complexes shown in panels b-c viewed perpendicular to the membrane plane from the n-side of the membrane (extrinsic domains, loops and additional non-conserved subunits in the *bc* complexes are not shown for clarity). **f**, the PQ molecule resolved adjacent to the Q<sub>p</sub> site in the spinach *cytb<sub>6f</sub>* (PDB ID: 6RQF (**Malone et al., 2019**)) in the context of its surrounding protein environment. The entrance to the Q<sub>p</sub> site is outlined by a dark green outline. **g**, the two conformations of the Chl *a* tail, resolved in the spinach *cytb<sub>6f</sub>* structure (PDB ID: 6RQF (**Malone et al., 2019**)), control access to and from the Q<sub>p</sub> site; an arrow is shown to indicate the direction of movement. A video of the conformational change undergone by the Chl phytyl tail depicted in panel **g** is provided using the QR code in the bottom right panel. Subunits and prosthetic groups are coloured as in **Figure 4.9** and **Figure 4.11**, quinone analogue inhibitors are shown in purple and are labelled 'STG' and 'TDS' respectively.

These residues are mostly conserved both sequentially and spatially except for Phe81 (subIV) which is conserved between algal and plant species however appears to be a Leucine residue in cyanobacterial species. As discussed in **section 1.3.4**, while the architecture of this portal is well conserved between *cytb<sub>c1</sub>* and *cytb<sub>6f</sub>* (**Figure 4.14**), the width of the Q<sub>p</sub> portal in *cytb<sub>6f</sub>* is significantly restricted compared to *cytb<sub>c1</sub>* by the presence of a Chl *a* molecule which appears to guard the entrance to the quinol oxidation site (Q<sub>p</sub>) site (**Figure 4.14**) (**Baniulis et al., 2009; Hasan et al., 2014; Kurisu et al., 2003; Stroebel et al., 2003; Yu et al., 2009; Zhang et al., 2001, 2003**). It is interesting to note that two conformations of the phytyl tail are also resolved in this study: the first appears to permit access to the Q<sub>p</sub> site ('open' conformation) while the second appears to restrict access ('closed' conformation) (**Figure 4.14**). Movement of the phytyl tail between these two conformations, together with some slight movement of surrounding residues, appears to contribute to further narrowing of the Q<sub>p</sub> portal as depicted in **Figure 4.14** and the video provided by the QR code in the bottom right panel of **Figure 4.14**.

The possible functions of this Chl *a* molecule and consequences of these conformational changes will be discussed further in **section 4.5**.

#### 4.4.4 The stromal (n-) side plastoquinone reduction ( $Q_n$ ) site

Following the successive deprotonation and oxidation of  $PQH_2$  at the  $Q_p$ -site, a molecule of fully oxidised PQ can diffuse to the  $Q_n$  site either via exchange with the PQ/ $PQH_2$  pool within the bulk membrane bilayer, or via a route within the complex. Here, the fully oxidised PQ molecule undergoes reduction and protonation to produce reduced  $PQH_2$ .

As discussed in **section 1.3.6**, a major difference between the *cytbc*<sub>1</sub> and *cytb*<sub>6f</sub> complexes is the structure of their respective  $Q_n$  sites (**Figure 4.15**). While in *cytbc*<sub>1</sub>, UQ reduction at the  $Q_n$  site may be achieved by a sequential two-step reduction and protonation by haem *b*<sub>n</sub> and surrounding residues (**Gao et al., 2003**), an equivalent mechanism in *cytb*<sub>6f</sub> is precluded by the presence of haem *c*<sub>n</sub> (**Kurusu et al., 2003; Stroebel et al., 2003; Yamashita et al., 2007**).

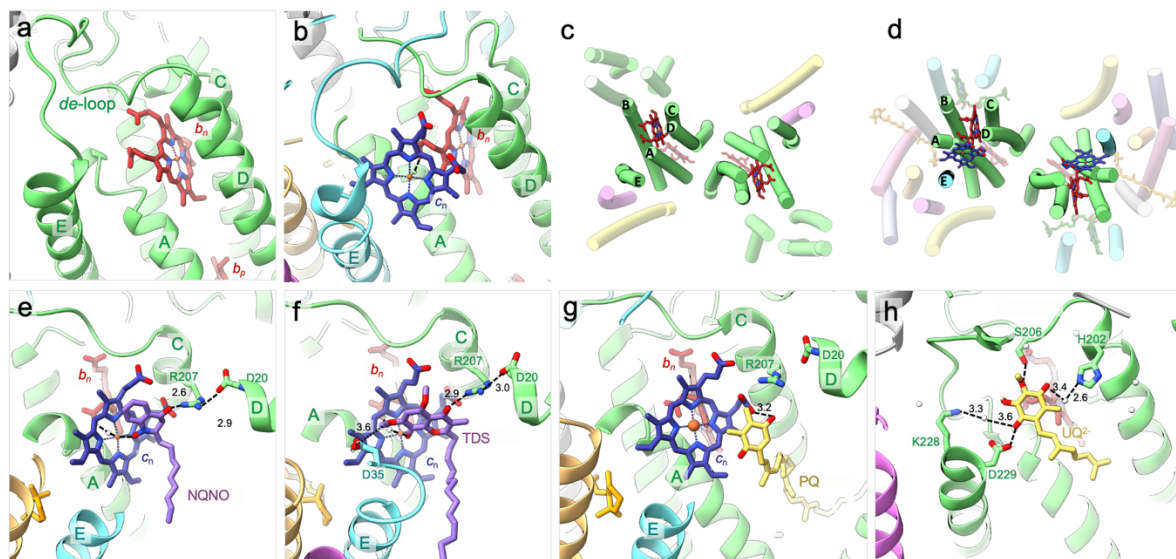


**Figure 4.15 | The  $Q_n$  sites of *cytbc*<sub>1</sub> and *cytb*<sub>6f</sub>.** **a-b**, a ribbon representation of the unoccupied  $Q_n$  site in the *G. gallus* *cytbc*<sub>1</sub> complex (**a**, PDB ID: 2BCC (**Zhang et al., 1998**)) and the *Nostoc* PCC 7120 *cytb*<sub>6f</sub> complex (**b**, PDB ID: 4OGQ (**Hasan and Cramer, 2014a**)). In both complexes, the position of haem *b*<sub>n</sub> between TM helices ‘B’, ‘C’ and ‘D’ is conserved, however in the *cytb*<sub>6f</sub> (**b**) the additional *c*’-type haem (*c*<sub>n</sub>) is present, this is connected to haem *b*<sub>n</sub> via an intervening water molecule and obstructs access to haem *b*<sub>n</sub>. **c-d**, the arrangement of TM helices (shown as cylinders) within complexes shown in panels a-b viewed perpendicular to the membrane plane from the n-side of the membrane (extrinsic domains, loops and additional non-conserved subunits in the *cytbc*<sub>1</sub> complex are not shown for clarity). **e-h**, ribbon representation of the occupied  $Q_n$  site in: **e**, the *cytb*<sub>6f</sub> complex occupied by NQNO

(e, PDB ID: 4H0L (**Hasan et al., 2013b**)); f, the *cytb<sub>6</sub>f* complex occupied by TDS (f, PDB ID: 4H13 (**Hasan et al., 2013b**)); g, the *cytb<sub>6</sub>f* complex occupied by PQ (g, PDB ID: 6RQF (**Malone et al., 2019**)); and h, the *cytbc<sub>1</sub>* complex occupied with UQ (h, PDB ID: 1NTZ (**Gao et al., 2003**)). Prosthetic groups, key interacting residues and quinone analogue inhibitors are shown in stick representation with protein shown as ribbons. Distances between residues are shown by black dashed lines with distances indicated in (Å). Subunits, inhibitors and prosthetic groups are coloured as in **Figure 4.9** and **Figure 4.11**. Key water molecules are shown as white spheres.

Given the observations that the midpoint potential of haem *c<sub>n</sub>* shows a marked pH dependence (– 60 mV/pH unit) (**Alric et al., 2005; de Lavalette et al., 2009**) and a dependence on the occupancy of the Q<sub>n</sub> site ( $E_m = -150$  mV at pH 7 in the presence of the semiquinone analogue NQNO) (**Alric et al., 2005**) it is suggested that haem *c<sub>n</sub>* facilitates the binding of substrate at the Q<sub>n</sub> site. Indeed it has been observed that NQNO (and indeed TDS) can bind directly to haem *c<sub>n</sub>* as an axial ligand (**Yamashita et al., 2007**) (**Figure 4.15**) however it appears that haem *c<sub>n</sub>* retains its penta-coordinate, high-spin character (**Baymann et al., 2007; Zatsman et al., 2006**) despite the presence of these inhibitors indicating binding of NQNO or TDS either displaces the axial H<sub>2</sub>O/OH<sup>-</sup> ligand or that these molecules bind very weakly to haem *c<sub>n</sub>* (**Baymann et al., 2007**). This apparent discrepancy is clarified in the present study where a native PQ molecule is observed bound to the Q<sub>n</sub> site (**Figure 4.15**). Unlike NQNO (**Figure 4.15**), the native PQ molecule does not act as an axial ligand, instead forming a close association with the haem *c<sub>n</sub>* C6 propionate (**Figure 4.15**). Moreover, while the substrate at the Q<sub>n</sub> site in *cytbc<sub>1</sub>* appears to be stabilised by multiple interactions from surrounding residues (His202, Asp229, K228 and Ser206; *G. gallus* *cytbc<sub>1</sub>* numbering) and water molecules (**Gao et al., 2003; Xia et al., 2007; Zhang et al., 1998**) (**Figure 4.15**), the substrate in spinach *cytb<sub>6</sub>f* is apparently only stabilised by a single interaction with the haem *c<sub>n</sub>* C6 propionate (**Figure 4.15**).

Interestingly, while PQ is observed bound to the Q<sub>n</sub> site on one side of the dimeric spinach structure, the other site remains empty. Comparative superimposition of the unoccupied (**Figure 4.16**) and occupied (**Figure 4.16**) halves of the dimer reveal several conformational changes in both the haem *c<sub>n</sub>* propionate group and nearby residues (Arg207 and Asp20; *cytb<sub>6</sub>*) which may underlie PQ binding and subsequent protonation/reduction at the Q<sub>n</sub> site.

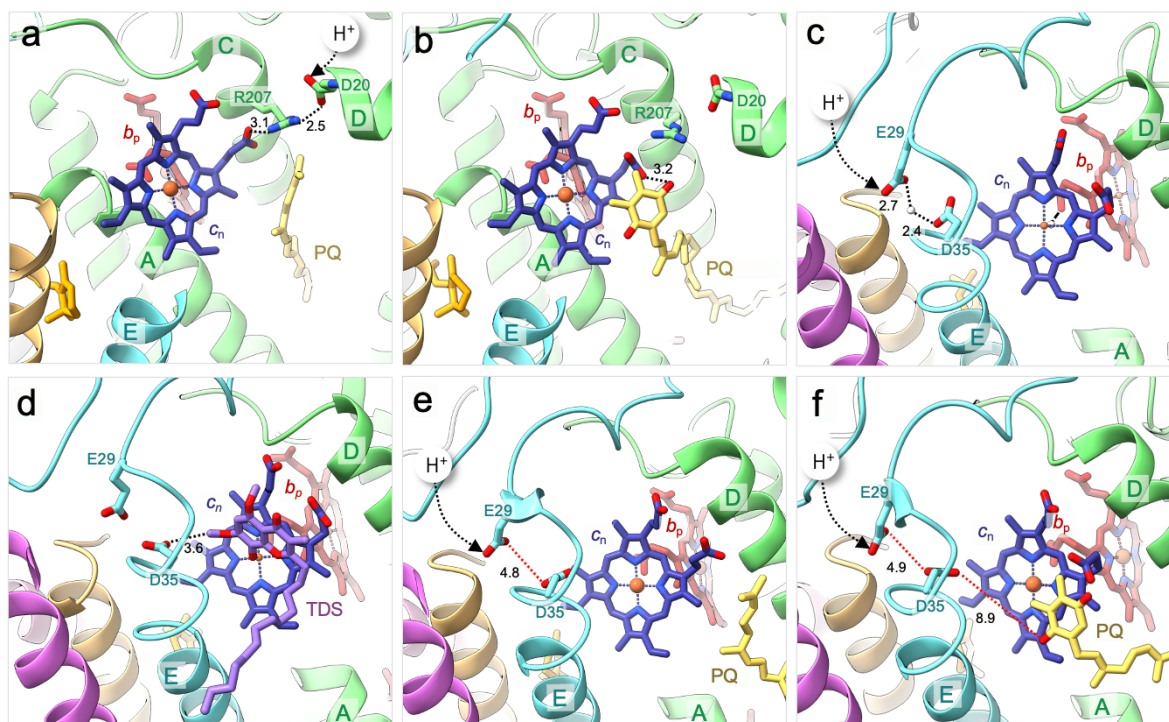


**Figure 4.16 | Conformational changes in the  $Q_n$  site of the  $cytb_6f$  complex may promote catalysis.** **a-b**, a ribbon representation of the unoccupied (**a**) and occupied (**b**)  $Q_n$  sites in opposing halves of the spinach  $cytb_6f$  complex (PDB ID: 6RQF (**Malone et al., 2019**)) showing conformational changes in the surrounding protein environment which may promote catalysis and allow proton uptake to the  $Q_n$  site via the putative D/R pathway. **c-d**, a ribbon representation of the unoccupied (**c**, PDB ID: 4H44 (**Hasan et al., 2013b**)) and occupied (**d**, PDB ID: 4H13 (**Hasan et al., 2013b**))  $Q_n$  sites in *Nostoc* and *M. lamosus* showing putative components and conformational changes of the E/D pathway. **e-f**, a ribbon representation of the unoccupied (**e**) and occupied (**f**)  $Q_n$  sites in opposing halves of the spinach  $cytb_6f$  complex (PDB ID: 6RQF (**Malone et al., 2019**)). Distances that are too far to facilitate proton transfer without the aid of intermediate water molecules are indicated by red dotted lines with the distances indicated below in (Å). Prosthetic groups, key catalytic residues, substrate and quinone analogue inhibitors are shown in stick representation with protein shown as ribbons. Key water molecules are shown as white spheres. Putative proton entry pathways are indicated by black dotted lines and arrows with H-bond distances indicated below in (Å). Subunits, inhibitors and prosthetic groups are coloured as in **Figure 4.9** and **Figure 4.11**.

While in the unoccupied  $Q_n$  site, a short, anhydrous H-bonding network appears to proceed from the stroma to the haem  $c_n$  propionate group via two highly conserved polar residues (Asp20, Arg207; cyt  $b_6$ ) (**Figure 4.16**). This network (previously designated as the D/R putative proton uptake pathway in **section 1.3.6** (Hasan et al., 2013b)) is disrupted in the opposing monomer by the binding of PQ (**Figure 4.16**). In particular, the binding of PQ appears to be accommodated by a rotation ( $\sim 125.5^\circ$ ) of the haem  $c_n$  C6 propionate away from Arg207 and towards the 1,4-benzoquinone head group of the incoming PQ molecule (**Figure 4.16**). In this manner, the carbonyl oxygen atom of the incoming PQ molecule forms an H-bond ( $\sim 3.2 \text{ \AA}$ ) with the C6 propionate group of haem  $c_n$ . These observations, together with the evidence that reduction of haem  $c_n$  is coupled to its protonation (**Alric et al., 2005; Baymann et al., 2007**), suggest a plausible scenario for PQ binding involving the reduction of haem  $c_n$  by haem  $b_n$  and protonation of the haem  $c_n$  propionate by nearby Arg207. In this scenario, protonation of the C6 propionate group of haem  $c_n$  by Arg207 would facilitate rotation of the propionate towards the incoming PQ molecule allowing it to act as an H-bond donor to the carbonyl oxygen on the 1,4-benzoquinone ring of PQ (**Figure 4.16**).

This mode of binding would stabilise the quinone species (rather than the semiquinone as in cyt $b_{c1}$ ), leaving the redox potential of the PQ/PQH $^\bullet$  couple at  $\sim -280 \text{ mV}$  (as in solution). In this scenario, the first endergonic reduction of PQ/PQH $^\bullet$  ( $E_m = \sim -280 \text{ mV}$ ) by haem  $c_n$  ( $E_m = \sim -150 \text{ mV}$ ) would only become likely when a second electron was also available in the low potential chain to allow the subsequent exergonic reduction of the PQH $^\bullet$ /PQH $_2$  couple ( $E_m = \sim +480 \text{ mV}$ ). In this manner, the presence of haem  $c_n$  may provide a redox-gating mechanism, ensuring that the PQH $^\bullet$  species has a very low equilibrium population and that electron transfer can only proceed via a quasi-concerted ‘double-barrelled shotgun’ mechanism when the haem  $b_n^{\text{red}}/c_n^{\text{red}}$  pair is present (**Alric et al., 2005; de Lavalette et al., 2009; Zito and Alric, 2016**). The reduction of PQ would subsequently allow its rapid protonation, with the first proton provided via the haem  $c_n$  propionate upon the oxidation of haem  $c_n$ .

Provision of a second proton to the  $Q_n$  site from the stroma may involve an alternate route as described in **section 1.3.6**. The present study indicates provision of a second proton could be facilitated by the highly conserved Glu29 and Asp35 residues (the E/D pathway) of cyt $b_{cf}$  (Hasan et al., 2013b) (**Figure 4.16**). As the side chain oxygen of Asp35 is too far away from the 1,4-benzoquinone ring oxygen for hydrogen-bond formation ( $\sim 8.9 \text{ \AA}$ ) in the *S. oleracea*

structure, it is possible that an ordered water molecule acts as a bridge to link the E/D pathway to the bound PQ molecule (**Figure 4.16**). Indeed, there are some regions of unassigned density between Asp35 and the PQ molecule which are consistent with bridging water molecules, however a higher resolution structure would be required to confirm this hypothesis.

Another salient feature of the  $Q_n$  site revealed in the spinach *cytb<sub>6</sub>f* structure, is the bowed conformation adopted by the bound PQ molecule with the isoprenoid tail straddling the intermonomer cavity and thereby partially obstructing the  $Q_n$  site on the neighbouring monomer (**Figure 4.17**). This arrangement may have some functional significance in preventing simultaneous binding of two PQ molecules at the  $Q_n$  sites on both sides of the dimeric complex (**Figure 4.17**). In this instance, any electron entering the low potential chain on the monomer bearing an empty  $Q_n$  site could be transferred rapidly to the neighbouring monomer via the 15.3 Å electron-tunnelling distance between the  $b_p$  haems (**Figure 4.17**) (**Świerczek et al., 2017**). If *cytb<sub>6</sub>f* can operate according to this 'electronic bus-bar' principal (**Świerczek et al., 2017**), this could provide a means to avoid competition between the two  $Q_n$  sites for electrons, favouring one turnover of the low potential chain for every two rather than three turnovers of the  $Q_p$  site and thus increasing the efficiency of the Q-cycle.



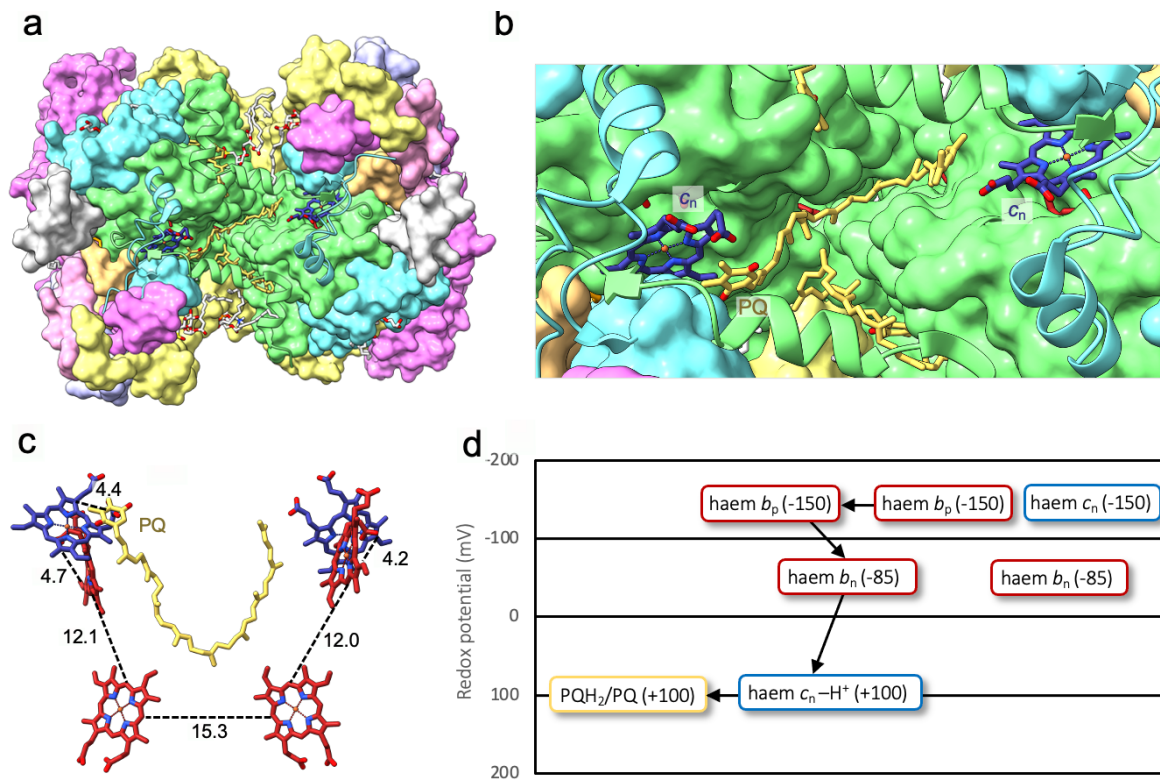


**Figure 4.17** | An electronic bus-bar lies within the core of the cytb<sub>6</sub>f complex allowing electrons to move both within and between monomers via a bridge formed between the two haem b<sub>p</sub> molecules. **a**, A stromal side view of spinach cytb<sub>6</sub>f showing the intermonomer cavity. Peripheral helices of cytb<sub>6</sub> and subIV are shown in cartoon representation for clarity. **b**, A zoomed in view of the intermonomer cavity showing a PQ molecule (PQ<sub>2</sub>) traversing between the two monomeric halves of the dimer between the two-opposing haem c<sub>n</sub> molecules. **c**, Edge-to-edge distances between the components of the low-potential electron transfer pathway in the dimeric cytb<sub>6</sub>f. Distances are indicated by the black dashed lines with distances shown in Å. **d**, the redox-active components of the low potential pathway of cytb<sub>6</sub>f shown on a scale of redox potential. The diagram shows the electronic connection between the two haem b<sub>p</sub> molecules, this is facilitated by the short distance between the molecules (as shown in panel c). The midpoint potentials of the two c<sub>n</sub> haems is proposed to be different, with the protonated c<sub>n</sub> that binds PQ having a more positive potential than that of the c<sub>n</sub> at the empty Q<sub>n</sub> site. Prosthetic groups and PQ molecules are shown in stick representation with protein in surface representation unless otherwise specified. Subunits, prosthetic groups and PQ molecules are coloured as in **Figure 4.9** and **Figure 4.11**.

## 4.5 The role of Chl *a*

As discussed in **sections 1.3.2** and **1.3.4**, the role of Chl *a* in the *cytb<sub>6</sub>f* complex is still unknown and is a subject of great interest.

As mentioned in **section 4.4.3**, it is interesting to note that two conformations of the Chl *a* phytol tail are resolved in the *S. oleracea cytb<sub>6</sub>f* complex (**Figure 4.18**), the first appears to permit access to the Q<sub>p</sub> site ('open' conformation) while the second appears to restrict access ('closed' conformation) (**Figure 4.18**). Movement of the phytol tail between these two conformations, together with some slight movement of surrounding residues, appears to contribute to further narrowing of the Q<sub>p</sub> portal as depicted in **Figure 4.18** (video provided by QR code in the right panel of **Figure 4.18**), this could restrict the portal sufficiently so as to retain substrate within the Q<sub>p</sub> site as suggested by **Hasan et al., 2014**. Given these observations, it is possible that the function of Chl *a* is to prevent semiquinone species from escaping the Q<sub>p</sub> site and disproportionating to form PQ and PQH<sub>2</sub>, which would short circuit the Q-cycle.

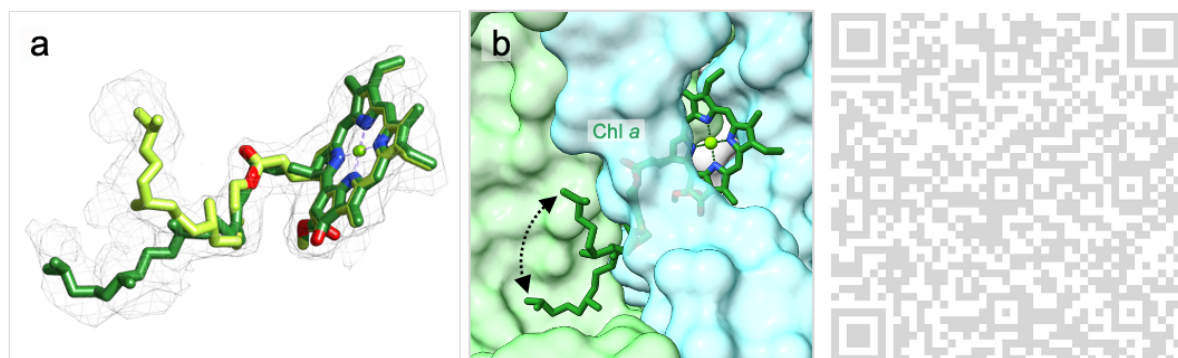


**Figure 4.18 | Conformational alterations in the Chl *a* phytol chain at the plastoquinol oxidation (Q<sub>p</sub>) site may gate access to and from the Q<sub>p</sub> site. a-b**, the two conformations of the Chl *a* tail, resolved in the spinach *cytb<sub>6</sub>f* structure (PDB ID: 6RQF (**Malone et al., 2019**)) showing the density (grey mesh) for the two conformations (represented in dark green and light green) (a) and a surface representation of the protein surrounding the Q<sub>p</sub> site (b). A video of the conformational change undergone by the Chl phytol tail depicted in panel b is provided by scanning the QR code in the right panel. Subunits and prosthetic groups are coloured as in **Figure 4.9** and **Figure 4.11**.



As well as playing a direct role in regulating catalysis, there is also evidence to suggest that this Chl *a* molecule may play a key role in redox sensing and signalling through interactions with STN7, a serine threonine LHCI kinase involved in the regulation of state transitions in higher plants (**Bellafiore et al., 2005**). It has been proposed that the chlorophyll phytyl tail may sense the presence of PQ/PQH<sub>2</sub> bound at the Q<sub>p</sub> site and convey this across the complex to STN7 bound at the n-side of the complex to activate state transitions (**Stroebel et al., 2003**). It is further proposed that such a mechanism could involve displacement of the Chl *a* tail by the isoprenoid tail of the incoming PQH<sub>2</sub> molecule; in this manner interactions between the Chl *a* tail and surrounding residues may be altered; this could serve as a signal to activate the Stt7/STN7 kinase. Such a signal could be conveyed across the membrane either directly through the F and G helices (subIV) which lie adjacent to the Chl *a* macrocyclic ring or via combined mechanism involving these helices and nearby lipids (**Hasan et al., 2013c**).

While, in the *S. oleracea* structure, the 'open' conformation of the Chl *a* tail (also observed in previous structures of the complex with quinone analogue inhibitors bound, PDB ID: 4H13) does appear to coincide with the observation of a PQ molecule approaching the Q<sub>p</sub> portal in one half of the dimer, there are no specific interactions observed between the Chl *a* tail and surrounding residues in either conformation. Furthermore, there do not appear to be any significant conformational changes in either of the adjacent helices of subIV (F and G).

## 4.6 Conclusions

In chapter 3, an optimised purification procedure was presented to purify *cytb<sub>6f</sub>* from *S. oleracea*. The resultant sample was shown to be intact, highly active, and largely dimeric with significantly enhanced stability compared to previous preparations. In the present chapter, this highly homogenous preparation of *S. oleracea cytb<sub>6f</sub>* is further explored by single-particle cryo-EM revealing structural details to a resolution of 3.58 Å.

Subsequent analysis of the modelled structure provides several new and interesting insights into the structural basis for operation of the Q cycle and its redox-sensing function in the higher plant *cytb<sub>6f</sub>*. Of note is the observation of three natively bound substrate molecules (PQ 1-3), these provide insights into the internal mechanics of the complex in the absence of inhibitors.

On the p-side of the complex, PQ1, is captured in a position approaching the PQH<sub>2</sub> oxidation (Q<sub>p</sub>) site in one half of the cytb<sub>6</sub>f dimer while on the n-side of the complex, a second PQ molecule (PQ2) is observed at the Q<sub>n</sub> site. Interestingly, the binding of PQ at the Q<sub>n</sub> site appears to obstruct the Q<sub>n</sub> site in the opposite half of the complex, suggesting a possible mechanism to avoid competition within the dimeric complex. In addition to these findings, comparative superimposition of the two Q<sub>n</sub> sites provides key insights into the catalytic mechanism at the Q<sub>n</sub> site, including conformational changes in both the haem c<sub>n</sub> C6 propionate and surrounding residues. A conformational switch involving the haem c<sub>n</sub> propionate appears to promote a concerted two-electron, two-proton reduction of PQ at the Q<sub>n</sub> site, avoiding the potential for reactive intermediate semiquinone to form. The location of a tentatively assigned third PQ molecule (PQ3) is consistent with a transition between the Q<sub>p</sub> and Q<sub>n</sub> sites in opposite monomeric units suggesting the possibility for intraprotein substrate transfer during the Q-cycle.

The observation of two alternative conformations of the Chl *a* molecule in the *S. oleracea* structure (**Malone et al., 2019**) supports a role for this pigment in gating substrate access to/from the catalytic Q<sub>p</sub> site. Such a gating mechanism has previously been suggested to serve a role in redox sensing and signalling as suggested by **Hasan et al., 2014**. It is also possible that these movements may exert a degree of control over the Q<sub>p</sub> oxidation reactions by preventing the exit of partially oxidised semiquinone species from the Q<sub>p</sub> site; in this manner, the Chl *a* molecule may actively prevent energetically unfavourable short circuits in the Q-cycle and the reduce the likelihood of damaging ROS production.

## 5 Results: The purification and structural determination of *cytb<sub>6f</sub>* from *Synechocystis* sp. PCC 6803

Following the structural determination of the *cytb<sub>6f</sub>* complex from *S. oleracea*, a number of points were outlined which would be of interest to explore further through site-directed mutagenesis. Given the inherent challenges of site-directed mutagenesis studies in a higher plant such as *S. oleracea*, it is of interest to establish a protocol to purify *cytb<sub>6f</sub>* from a prokaryotic cyanobacterial system.

As discussed in **section 1.3.1**, the dimeric *cytb<sub>6f</sub>* complex has previously been purified and studied from several cyanobacterial sources including *M. laminosus* and *Nostoc* sp. PCC 7120 (hereafter *Nostoc*) (Baniulis et al., 2009; Hasan and Cramer, 2014a; Hasan et al., 2013a, 2013b, 2014; Kurisu et al., 2003; Yamashita et al., 2007; Yan et al., 2006). While studies in these organisms have yielded several highly valuable insights into the *cytb<sub>6f</sub>* complex structure and function, unfortunately genetic tools for these organisms are severely limited; for this reason it is desirable to develop a protocol to purify the complex from a model system with better established genetic tools such as the unicellular cyanobacterium *Synechocystis* sp. PCC 6803 (hereafter *Synechocystis*).

In contrast to the filamentous cyanobacterial species (*M. laminosus* and *Nostoc*), *Synechocystis* provides an extremely well-characterised model system for genetic engineering, enabling site-directed mutagenesis of the native *cytb<sub>6f</sub>* complex. Whilst the purification of dimeric *cytb<sub>6f</sub>* from *Synechocystis* has previously been attempted using the same protocols as those used for *M. laminosus* and *Nostoc*, these have been largely unsuccessful due to issues with proteolytic cleavage, monomerisation and subsequent inactivation during purification (**Baniulis et al., 2009**).

The following chapter is a largely collaborative effort between myself, Dr M. Proctor, Dr D. J. K. Swainsbury, Dr A. Hitchcock and Dr D. A. Farmer.

## 5.1 Initial trials to isolate dimeric *cytb<sub>6</sub>f* from *Synechocystis* sp. PCC 6803 using glyco-diosgenin (GDN).

### 5.1.1 Thylakoid preparation

All tagging, growth and harvest of *Synechocystis* strains were carried out using the protocols set out in **sections 2.3.1** and **2.3.2**. Thylakoids were prepared using the protocol set out in **section 2.3.3**, the concentration of the thylakoid suspension was then determined as described in **section 2.2.4**.

### 5.1.2 Solubilisation trials

While the use of HECAMEG was successful for the solubilisation of *cytb<sub>6</sub>f* in *S. oleracea*, initial trials indicated that HECAMEG was detrimental to the structural integrity of the *Synechocystis* *cytb<sub>6</sub>f* complex, for this reason we decided to explore alternative detergents which had previously shown promise for the selective solubilisation of *cytb<sub>6</sub>f* in *S. oleracea*. Among the various detergents trialled was GDN, a synthetic digitonin substitute which had previously shown great promise for the selective solubilisation of *cytb<sub>6</sub>f* and ATP synthase from *S. oleracea* thylakoids (**Figure 5.1**).

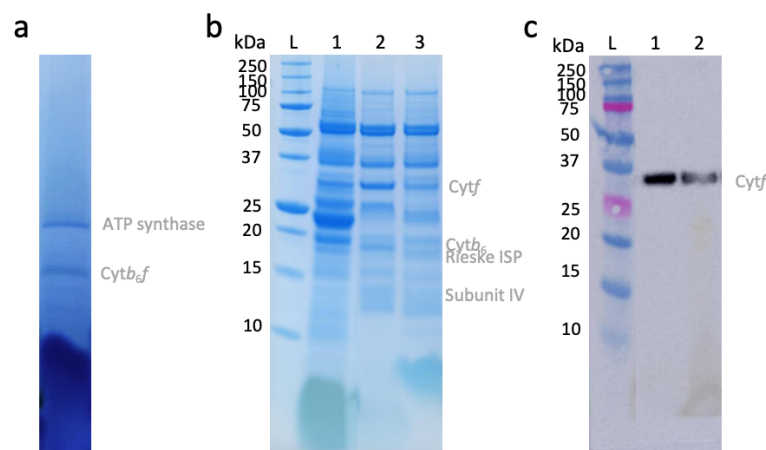


**Figure 5.1| Comparing the efficacy of HECAMEG and GDN for the selective solubilisation of *cytb<sub>6</sub>f* from *S. oleracea*.** **a**, BN-PAGE gel of GDN solubilised *S. oleracea* thylakoids. **b**, SDS-PAGE analysis of *S. oleracea* thylakoids solubilised with 1 % (w/v) HECAMEG (lane 2) and 1 % (w/v) GDN (lane 3). Lanes: L) ladder, 1) *S. oleracea* thylakoids, 2) solubilised supernatant (HECAMEG), 3) solubilised supernatant (GDN). **c**, Western blot analysis of *S. oleracea* thylakoids solubilised with 1 % (w/v) HECAMEG (lane 2) and 1 % (w/v) GDN (lane 3) using an anti-*petA* antibody. Lanes: L) ladder, 1) solubilised supernatant (HECAMEG), 3) solubilised supernatant (GDN).

While in the case of *S. oleracea*, HECAMEG proved to be far more efficacious than GDN for solubilising *cytb<sub>6</sub>f* (**Figure 5.1**), initial solubilisation trials with GDN in *Synechocystis* appeared to result in enhanced structural stability with a larger proportion of purified *cytb<sub>6</sub>f* complex being maintained in an active, dimeric state.

For initial solubilisation trials with GDN, the starting concentration used for solubilisation was 1 % (w/v) as used during the *S. oleracea* detergent trials, however this was later increased to 1.5 % (w/v) to improve the yield. Thylakoids were prepared from an 8000 ml cell culture of the *petA*-Strep *Synechocystis* strain as described in **section 2.3.3**, before solubilisation was carried out using 1 - 1.5 % (w/v) GDN at 2 mg ml<sup>-1</sup> Chl. Samples were mixed thoroughly after addition of detergent and incubated at 4 °C for 60 mins in the dark with mixing.

### 5.1.3 Purification by Strep-Tactin Chromatography

Following incubation, the solubilised thylakoids were ultracentrifuged at 48,500 x *g* (max) for 30 min at 4 °C to remove any unsolubilised material. The solubilised supernatant was diluted 2-fold with *Synechocystis* Thylakoid Buffer 1 (**Table 2.7**) then loaded onto a 5 ml StrepTrap™ column (Merck) pre-equilibrated in StrepTrap Equilibration Buffer (**Table 2.12**). The column was washed with 5 CV of the same buffer before elution with StrepTrap Elution Buffer (**Table 2.12**) at a flow rate of 5 ml min<sup>-1</sup>. 12 x 1ml fractions were collected of the eluate; of these, fractions 4 - 6 were coloured brown. These fractions were analysed by absorbance spectroscopy to assess the relative enrichment of *cytb<sub>6</sub>f* compared to other photosynthetic components in the solubilised supernatant. The purity of fractions was quantified by assessing the ratio between the absorbance signals of the haem Soret band (~ 421 nm) and the Chl *a* Soret band (~ 440nm) (**Figure 5.2**). Fractions 4 - 6 were pooled and concentrated, the purity and oligomeric state of the purified *cytb<sub>6</sub>f* was then further assessed by SDS-PAGE (**Figure 5.2**) and BN-PAGE (**Figure 5.2**). While fractions containing *cytb<sub>6</sub>f* appeared to comprise relatively pure, mostly dimeric *cytb<sub>6</sub>f*, some residual Chl-containing contamination remained.

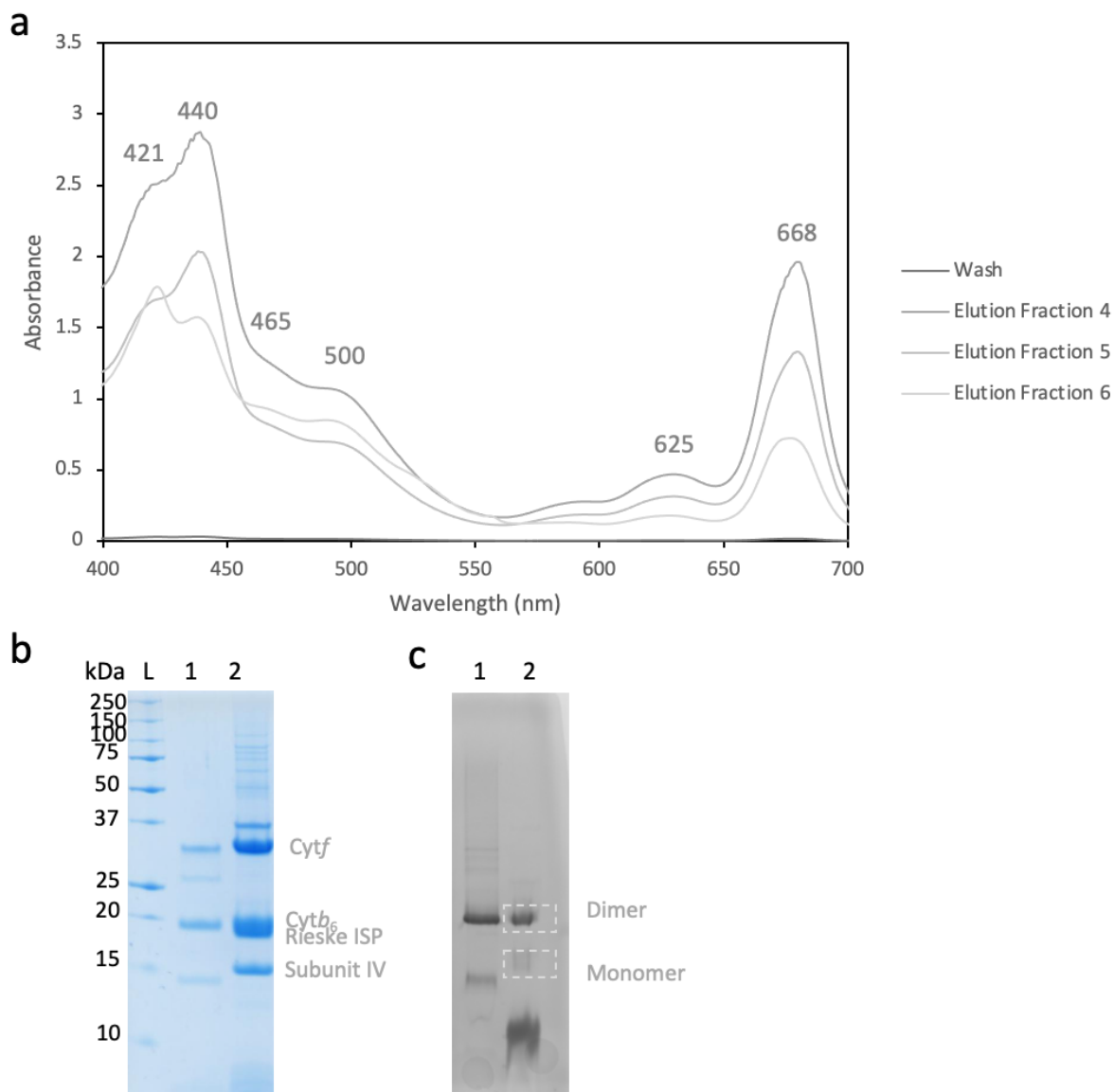


**Figure 5.2 | The purification of *cytb<sub>6</sub>f* (*petA*-strep) from *Synechocystis* sp. PCC 6803 thylakoids using Strep-Tactin affinity chromatography. **a**, Absorbance spectra of neat samples from the Strep-Tactin purification (see key). The peak at 421 nm corresponds to the Soret band of haems while the peak at 440 nm corresponds to the Soret band of Chl *a*. The peak and shoulder around 470 nm and 500 nm correspond to carotenoid. The peaks at 625 and 668 nm correspond to phycocyanin, the peaks at 554 and 668 nm correspond to *c*-type haem of *cyt<sub>f</sub>* and the Q<sub>y</sub> band of Chl *a*, respectively. **b**, SDS-PAGE analysis of size exclusion peaks from the GDN sample. Lanes: L) ladder, 1) peak 2, 2) peak 1. The position of the four large subunits of the complex (*cyt<sub>f</sub>*, *cyt<sub>b</sub><sub>6</sub>*, the Rieske ISP and subunit IV) are indicated running at ~ 31 kDa, ~ 24 kDa, ~ 20 kDa and ~ 17 kDa, respectively. The four small subunits (PetG, PetL, PetM and PetN) running at around 4 kDa are not shown. **c**, BN-PAGE analysis of size exclusion peaks from the GDN sample. Lanes: 1) peak 2, 2) peak 1.**

### 5.1.4 Purification by Gel Filtration

A further round of purification was carried out by size-exclusion chromatography as described in **section 2.4.6**. The elution profile appears to be largely dominated by a tall peak with a slight shoulder spanning from 47.5 – 55 ml (data not shown). Samples of eluate across this peak (elution volumes 47.5 – 55 ml) were analysed by UV/Vis absorbance spectroscopy (**Figure 5.3**) to determine the purity of the purified dimeric complex in each fraction; the results of these analyses reveal the presence of *cytb<sub>6</sub>f* across the peak however the purity of the sample is highest between 52.5 and 55 ml. Fractions comprising highly pure, dimeric *cytb<sub>6</sub>f* were pooled and concentrated using a Centriprep 100K centrifugal filter (Merck Millipore Ltd.).

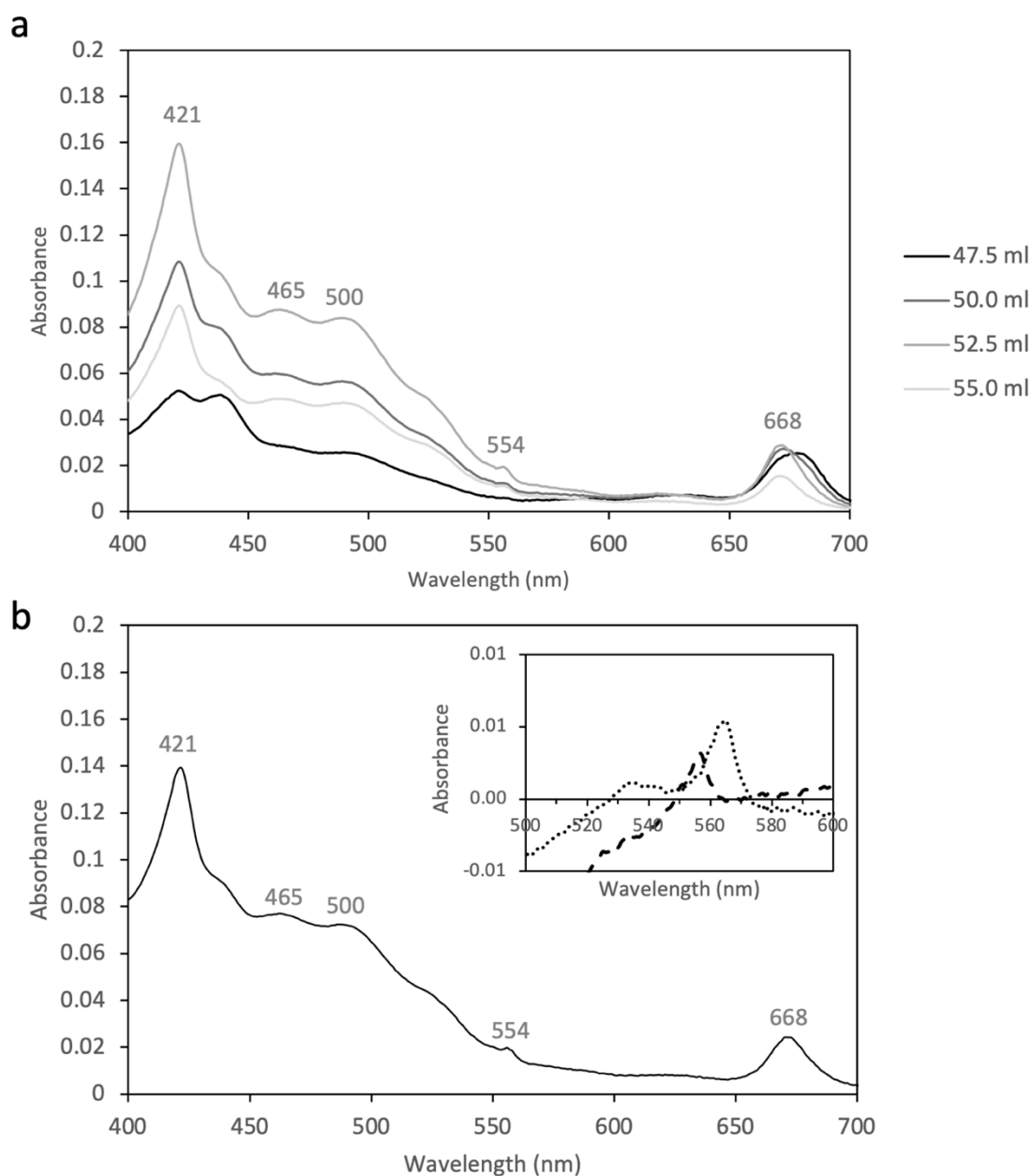


**Figure 5.3 | The purification of *cytb<sub>6</sub>f* (*petA*-strep) from *Synechocystis* sp. PCC 6803 thylakoids using gel filtration.** **a**, Absorbance spectra of samples from gel filtration (see key). The peak at 421 nm corresponds to the Soret band of haems while the peak at 440 nm corresponds to the Soret band of Chl *a*. The peak and shoulder around 470 nm and 500 nm correspond to carotenoid. The peaks at 554 and 668 nm correspond to *c*-type haems of *cytf* and the Q<sub>y</sub> band of Chl *a*, respectively. **b**, Absorbance spectra of pooled and concentrated fractions (52.5 - 55 ml). The inset panel shows redox difference spectra of ascorbate-reduced minus ferricyanide-oxidized *cytb<sub>6</sub>f* (dashed line) and dithionite-reduced minus ascorbate-reduced (dotted line) *cytb<sub>6</sub>f*. Redox difference spectra show haem *f* absorption peaks at 523 and 554 nm as well as absorption peaks at 534 and 563 nm corresponding to the *b*-type haems of *cytb<sub>6</sub>*. The calculated ratio of *cytb<sub>6</sub>* *b*-type haems to the *c*-type haem of *cytf* was ~ 2 using extinction coefficients of 28 mM cm<sup>-1</sup> (*f*, 554 – 540 nm) and 24 mM cm<sup>-1</sup> (*b<sub>6</sub>*, 563 - 575 nm) (Metzger et al., 1997).

## 5.2 Quantification of purified dimeric *cytb<sub>6</sub>f* using redox difference spectra

Reduced-oxidised spectra were carried out as described in **section 2.5.3**; results indicated a concentration of ~ 10 μM purified protein in the sample, additionally the haem *b* : *c* ratio was calculated as 2.02 consistent with expectations for an intact dimeric *cytb<sub>6</sub>f* complex. Haem *c<sub>n</sub>* is omitted from this calculation since its α-band consists of a broad, flat absorption peak with a small extinction coefficient. Additionally, the Soret band of haem *c<sub>n</sub>* (~ 425 nm) is masked by the absorption peaks of Chl *a* and the other *b*- and *c*-type haems (*b<sub>p</sub>*, *b<sub>n</sub>* and *f*) (Joliot and Joliot, 1988; Yamashita et al., 2007).

## 5.3 Activity assays

To confirm the extracted *cytb<sub>6</sub>f* complex retains high levels of activity following purification, the rate of electron transfer from reduced decylplastoquinone (dPQH<sub>2</sub>; Sigma) to plastocyanin (PC) was measured *in vitro* using stopped-flow absorbance spectroscopy.

The rate of ET by *cytb<sub>6</sub>f* was determined by taking the initial linear region from the enzyme-catalysed reaction and subtracting the background rate measured in the absence of enzyme. The resulting rate of ~ 200 e<sup>-</sup> s<sup>-1</sup> is in good agreement with our data from *S. oleracea* (see **section 3.7.2**).



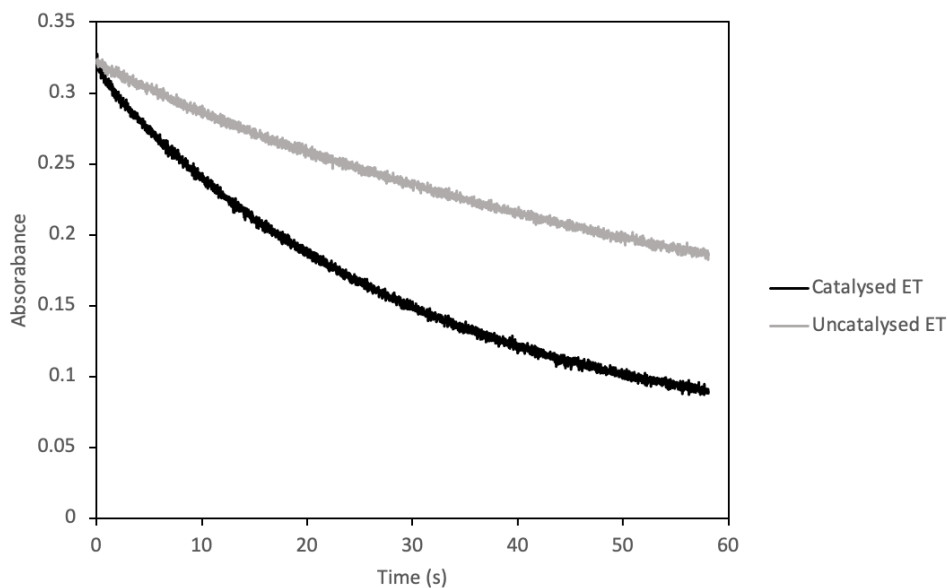


**Figure 5.4 | The catalytic rate of PC reduction by the purified dimeric *cytb<sub>6</sub>f* complex as determined by stopped-flow absorbance spectroscopy.** A rate of  $\sim 200 \text{ e}^- \text{ s}^{-1}$  was determined by taking the initial linear region from the enzyme-catalysed reaction (black line) and subtracting the background rate measured in the absence of *cytb<sub>6</sub>f* (light grey line). Plastocyanin reduction was not observed in the absence of dPQH<sub>2</sub> (grey line). Reactions were initiated upon addition of dPQH<sub>2</sub> to the solution containing PC and *cytb<sub>6</sub>f* while monitoring the loss of absorbance at 597 nm. Final concentrations were 62.5  $\mu\text{M}$  plastocyanin, 170 nM *cytb<sub>6</sub>f* and 250  $\mu\text{M}$  dPQH<sub>2</sub>. All experiments were performed in triplicate and controls were performed in the absence of *cytb<sub>6</sub>f* or dPQH<sub>2</sub>.

#### 5.4 Negative stain TEM analysis

Samples prepared as described in **section 5.1** were analysed by negative stain TEM to confirm sample homogeneity and to gauge approximately what concentration might be best as a starting point for cryo-EM screening.

Analysis of the recorded images reveals the purified *cytb<sub>6</sub>f* sample is extremely homogenous with particles exhibiting the size and shape expected for dimeric *cytb<sub>6</sub>f* (**Figure 5.5**).

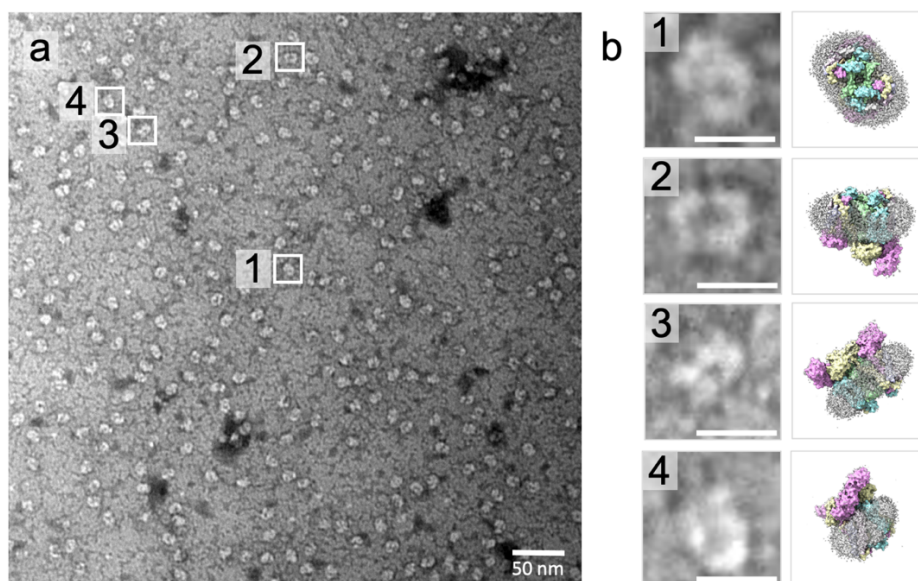


**Figure 5.5 | Negative stain analysis of the *cytb<sub>6</sub>f* complex purified from *Synechocystis sp.* PCC 6803 (*petA-strep*).** **a**, A dilute (0.26  $\mu$ M) sample of the purified *Synechocystis sp.* PCC 6803 (*petA-strep*) *cytb<sub>6</sub>f* complex imaged at 39,000X magnification. **b**, Zoomed images of selected complexes highlighted in panel 'a' and their corresponding surface views from the *S. oleracea* complex. Scale bar is 10 nm.

## 5.5 Single particle cryo-EM

### 5.5.1 Sample preparation and screening

As observed with the *S. oleracea cytb<sub>6</sub>f* sample, screening revealed the particles had a tendency to stick to the edges of the carbon support in most grids trialled; this could be slightly reduced using gold grids however an optimal particle distribution and ice thickness was achieved on a lacey carbon grid prepared using 5  $\mu$ l sample. In this grid, a large number of monodisperse particles of roughly similar sizes were observed, these appeared to adopt multiple orientations within the ice.

### 5.5.2 Sample preparation and screening

Automated data acquisition was set up using the EPU software (v 2.5) on a Titan Krios microscope (Thermo Fisher) operated at 300 kV, equipped with an energy filtered (slit width 20 eV) K3 direct electron detector (Gatan). A total of 18,151 movies were collected in super-resolution mode at a nominal magnification of 81,000 X (pixel size of 0.53 Å) and a dose of

$3.0 \text{ e}^- \text{ \AA}^{-2} \text{ s}^{-1}$ . An exposure time of 3.0 sec was used and the resulting movies were dose-fractionated into 45 fractions. A defocus range of - 1.2 to - 2.5  $\mu\text{m}$  was used.

### 5.5.3 Beam-induced motion correction, particle picking, CTF estimation and 2D classification

Movies were motion corrected and dose-fractionated using MotionCor2 before the GCTF subroutine (**Zhang, 2016**) was employed to estimate Contrast Transfer Function (CTF) parameters of the dose-weighted, motion corrected images.

### 5.5.4 Particle picking and 2D classification

Following CTF estimation, 2,000 particles were manually picked and extracted from micrographs using a box size of 220 x 220 pixels; an example micrograph showing picked particles is shown in **Figure 5.6**; this micrograph clearly exhibits a good distribution of single protein particles embedded in a thin and even layer of vitreous ice. Some minor ice and ethane contamination was observed in some of the micrographs (**Figure 5.6**) however no significant aggregation of protein was shown and the quality of the protein preparation is clearly reflected in the micrographs.

The extracted particles were subjected to reference-free 2D classification to iteratively generate 50 class averages revealing several different views of the complex. A representative subset of 2D classes is shown in (**Figure 5.6**); these display a number of orientations of the complex with the side-on view being most recognisably *cytb<sub>6f</sub>* (see **Figure 4.2** from the *S. oleracea* dataset in **chapter 4**).

Automated particle picking was carried out using the 'Auto-picking' tool in RELION; given the close resemblance of the 2D classes with previous structures of the complex, the cryo-EM map of the *S. oleracea* complex was used as a 3D reference map to guide autopicking, this was low pass filtered to 20  $\text{\AA}$  to eliminate any possible bias.

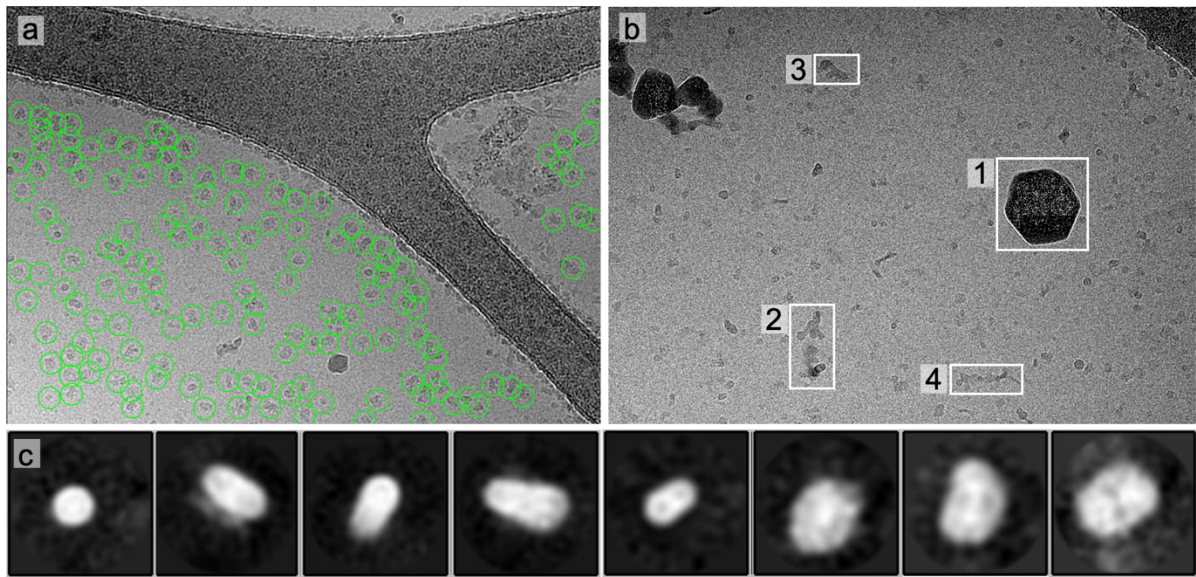


**Figure 5.6 | Initial assessment of cryo-EM micrographs of the *Synechocystis* sp. PCC 6803 (*petA-strep*) *cytb<sub>6</sub>f* complex.** **a**, A representative micrograph showing *cytb<sub>6</sub>f* particles covered by a thin layer of vitreous ice on a supported carbon film. Manually picked coordinates are indicated by the green circles. **b**, examples of contamination observed in some of the micrographs showing ice contamination (1) and some representative examples of possible ethane contamination (2 - 4). **c**, A gallery showing a representative subset of selected 2D classes generated from 2000 manually picked particles.

Autopicked micrographs were manually examined and refined, with particles added where appropriate. Given the use of lacey carbon grids for sample preparation, one of the main issues with autopicking in this dataset was the picking of carbon edges resulting in a large number of ‘junk’ particles; these were subsequently removed through 2D classification using the ‘fast subsets’ option in RELION to enable a relatively quick ‘clean up’ of the picked coordinates. Of the 4,032,212 autopicked coordinates submitted to this initial stage of 2D classification (**Figure 5.7**), 3,546,322 (~ 87.9 %) were selected for further processing. Selected particles were subjected to a further round of 2D classification (**Figure 5.7**) after which 3,396,654 particles (~ 84.2 %) were selected for further processing. A representative subset of 2D classes is shown in (**Figure 5.7**).



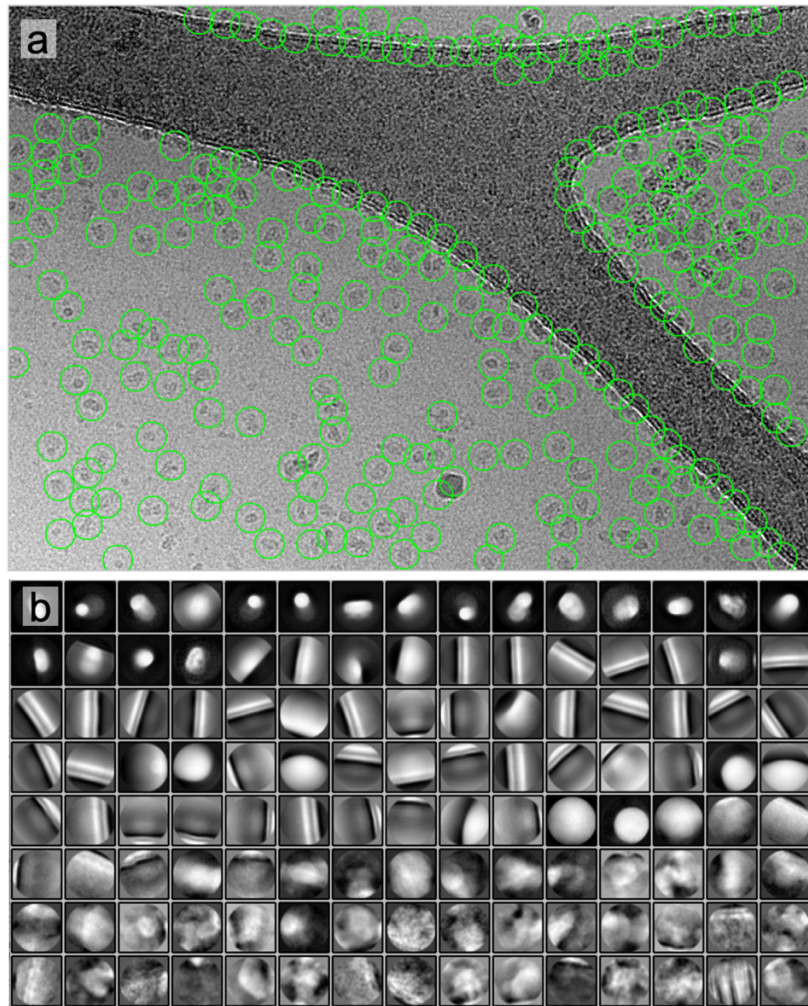


**Figure 5.7 | Automated picking of particles from cryo-EM micrographs of the *Synechocystis* sp. PCC 6803 (*petA-strep*) *cyt<sub>b</sub>f* complex.** **a**, The same representative micrograph as shown in **Figure 5.6** showing autopicked coordinates. **b**, 2D classes following an initial round of 2D classification of 4,032,212 auto-picked coordinates. **c**, A gallery showing a representative subset of selected 2D classes generated from 3,546,322 manually picked particles.

#### 5.5.5 *De novo* 3D model generation

A subset of 460,584 particles (~ 11.4 %) was used to generate a low-resolution 3D model using the ‘3D initial model’ subroutine in RELION. Since it was possible that the two halves of the complex may display slightly different structural features, symmetry was not applied (i.e. C1). The model exhibited the general architecture expected for the *cyt<sub>b</sub>f* complex as predicted from analysis of the cyanobacterial (Baniulis et al., 2009; Hasan and Cramer, 2014a; Hasan et al., 2013a, 2013b, 2014; Kurisu et al., 2003; Yamashita et al., 2007; Yan et al., 2006), algal (Stroebel et al., 2003) and plant (Malone et al., 2019a) structures.

### 5.5.6 3D reconstruction to 2.98 Å

To obtain a suitably homogenous set of particles, unsupervised 3D classification ('3D classification') was performed iteratively to generate four 3D classes using the initial model low pass filtered to 50 Å as a reference map. The four low resolution 3D classes (**Figure 5.8**) were analysed in Chimera X (v 1.1.1) before one 3D class (class 2, 9.32 Å, ~ 24.5 %) was subjected to a further round of 3D classification generating six classes. Of these six 3D classes, one stable 3D class (class 2, 6.85 Å) of sufficient homogeneity was selected for further refinement. The selected subset of 413,442 particles (~ 10.2 %) was further refined iteratively using the '3D auto-refine' procedure in RELION to produce a higher resolution model (4.26 Å). The resultant model preserved the general architecture observed in the initial model, however the increased resolution revealed further details of the polypeptide structure such as the TM helices and an outline of the extrinsic domains of *cyt f* and the Rieske ISP. The subset of refined particles underwent per-particle CTF-refinement and a soft mask was created from the 3D map low pass filtered to 15 Å with a soft edge of 6 pixels. This mask incorporated the detergent shell surrounding the transmembrane portion of the complex but excluded surrounding solvent.

The masked CTF-refined particles were subjected to a further round of 3D refinement, the resultant density map was then corrected for the modulation transfer function (MTF) of the K3 summit camera and further sharpened using the post-processing procedure in RELION resulting in a map of 3.53 Å resolution. Particles were polished using the 'Bayesian polishing' subroutine in RELION, shiny particles then underwent two further rounds of CTF-refinement and post-processing until there was no further improvement in the resolution.

An overview of the data processing procedure is shown in **Figure 5.8**.

The final global resolution estimate of 2.98 Å was based on the gold-standard Fourier shell correlation (FSC) cut off of 0.143 (**Figure 5.9**) (**Scheres, 2012; Scheres and Chen, 2012**). Local resolution was determined using one of the two unfiltered half-maps from the final round of 3D refinement as an input, a calibrated pixel size of 0.53 and a B-factor of  $-78 \text{ \AA}^2$ . The output local resolution map is shown in **Figure 5.9**.

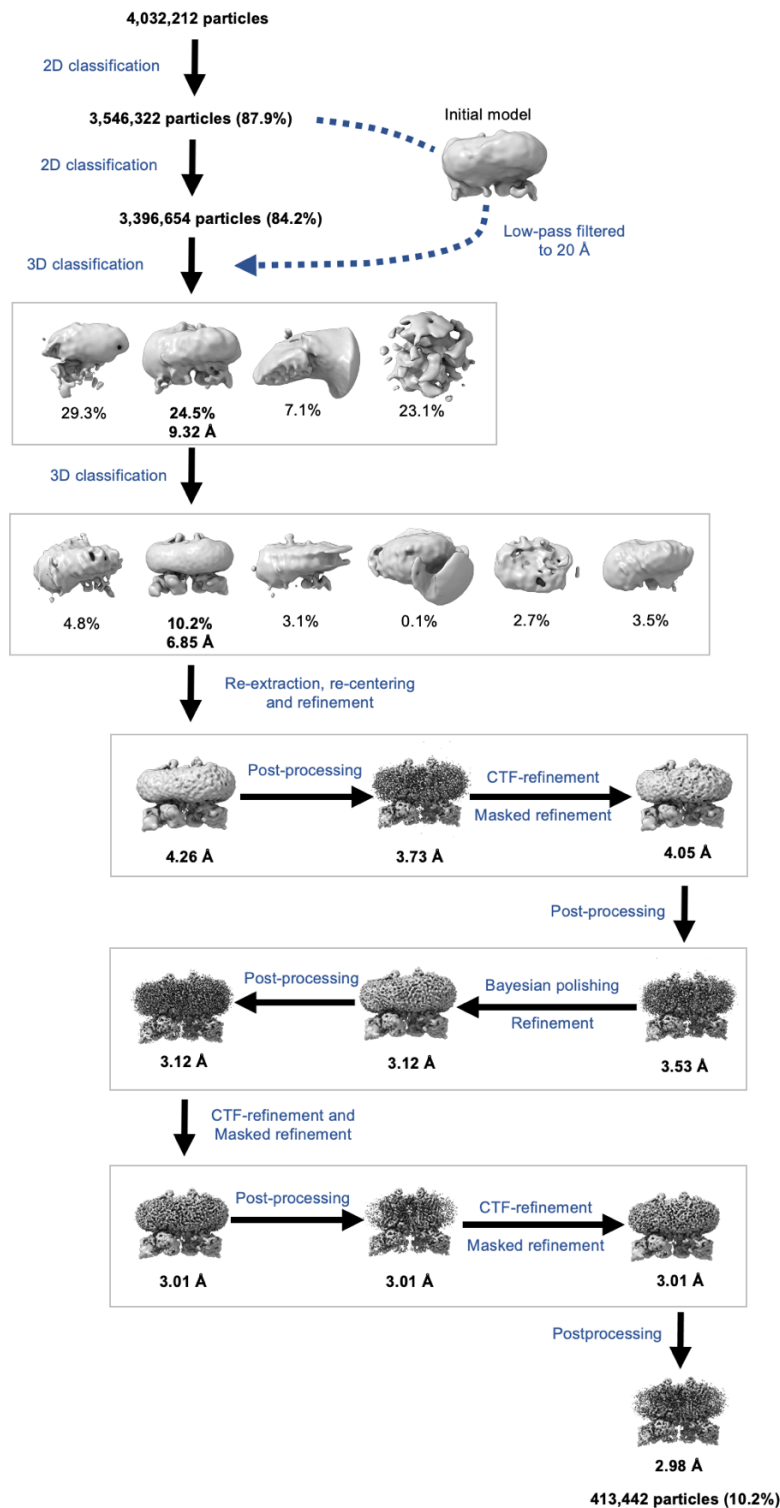


**Figure 5.8 | A flowchart for processing of the *Synechocystis* sp. PCC 6803 (*petA-strep*) *cyt<sub>b</sub>cf* cryo-EM map outlining the steps for data processing in RELION.** We recorded 18,151 cryo-EM movies, from which 4,032,212 particles were auto-picked for reference-free 2D classification. The final density map was calculated from 413,442 particles. The average resolution in angstroms (Å) and number of particles (%) at each stage is indicated with the final global resolution for the entire *cyt<sub>b</sub>cf* complex from *Synechocystis* sp. PCC 6803 estimated to be ~ 2.98 Å.

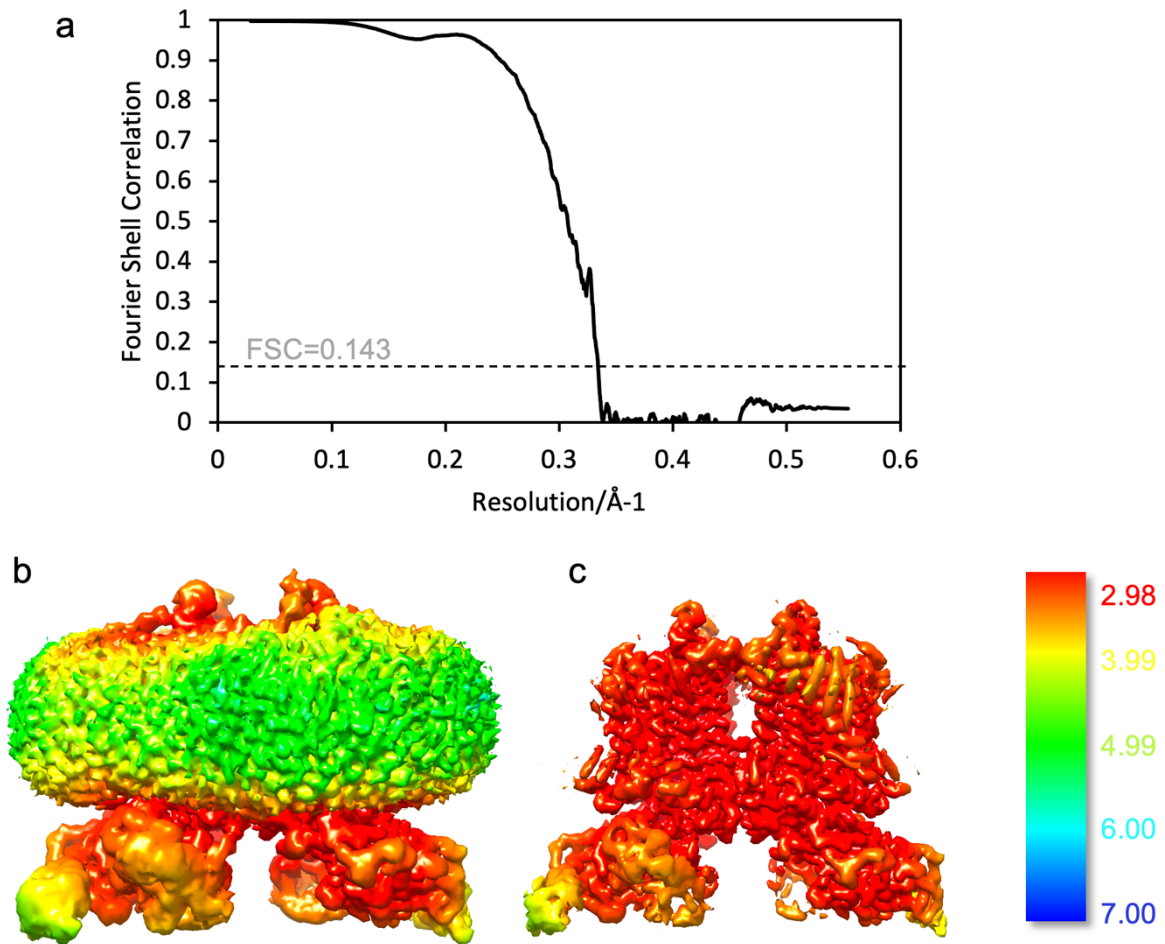


**Figure 5.9 | Cryo-EM micrographs of the *Synechocystis* sp. PCC 6803 (*petA-strep*) *cytb<sub>6</sub>f* complex and calculation of the cryo-EM map global and local resolution. a**, Gold-standard refinement was used for estimation of the final map resolution (solid black line). The global resolution of 2.98  $\text{\AA}$  was calculated using a FSC cut-off at 0.143. **b-c**, A C1 density map of the *cytb<sub>6</sub>f* complex both with (b) and without (c) the detergent shell. The map is coloured according to local resolution estimated by RELION and viewed from within the plane of the membrane. The colour key on the right shows the local structural resolution in angstroms ( $\text{\AA}$ ).



## 5.6 Structural modelling

### 5.6.1 Multiple sequence alignment of the *Synechosystis* sp. PCC 6803 *cytb<sub>6</sub>f* complex with cyanobacterial, algal and plant complexes

The polypeptide sequences of the eight subunits of *cytb<sub>6</sub>f* were aligned with their counterparts from cyanobacterial (*M. laminosus*, *Nostoc* sp. PCC 7120), algal (*C. reinhardtii*) and plant (*S. oleracea*) species using Clustal Omega v 1.2.4 (**Figure 5.10**) (**Goujon et al., 2010; Sievers et al., 2011**). Targeting peptides (including chloroplast transit peptides) were omitted from the alignment.



**c**

```

Synechocystis_petC2      -----MNTQAIAPPSYSRRQLLNFLAGTTVAVTASAGAYAMGKFFVPPAEK 47
Synechocystis_petC1     MLVKILKFRFRFIMTQISGSPDVPDLGRRQFMNLLTFGTITGVAAGALYPAVKYLIPSS- 59
Mastigocladus           -----MAQFTESMDVPDMGRRQFMNLLAFGTVTGVALGALYPLVKYFIPSSG- 47
Nostoc                   -----DVPDMGRRQFMNLLTFGTVTGVALGALYPVVNYFIPPA- 39
Chlamydomonas           -----AAASSEVPDMNKRINMNLILAGGAGLPITTLALGYGAFFVPPSS- 44
Spinacia                 -----ATSIADNVPDMQKRETLNLLLLGALS LPTGYMLLPYASFFVPPGG- 46
                          *: *: *: *:

```

```

Synechocystis_petC2      GGAGGGIIAKDVLGNPIPASQILA-EAPGTRALVAGLAGDPTYLIVKEDGSLDSIGIVDS 106
Synechocystis_petC1     GGSGGVTAKDALGNDVKVTEFLASHNAGDRVLAQGLKGDPTYIVVQGGDDTIANYGINAV 119
Mastigocladus           GAVGGTTAKDKLGNVVKVSKFLESHNAGDRVLVQGLKGDPTYIVVESKEAIRDYGINAV 107
Nostoc                   GGAGGGTTAKDELGNDVSVSKFLESHNVGDRTLVQGLKGDPTYIV-----AITDYGINAV 94
Chlamydomonas           GGGGGGQAAKDALGNDIKAGEWLKTLAGDRSLSQGLKGDPTYLIVTADSTIEKYGLNAV 104
Spinacia                 GAGTGGTIAKDALGNDVIAAEWLKTHAPGDRTLTQGLKGDPTYLVVSDKTLATFGINAV 106
                          *: ** ** ** ** : . : * . * * * * ** *****: : : * :

```

```

Synechocystis_petC2      CTHLGCFFPWNGNDQEFQCPCHGSRYHPDGSVARGPAPLPLKIVQVAVVD-DQIFISPWT 165
Synechocystis_petC1     CTHLGCVVPWNAENKFMCPCHGSQYNAEGKVVRGPAPLSLALAHATVDDDKLVLTWT 179
Mastigocladus           CTHLGCVVPWNAENKFKCPCHGSQYDETKVIRGPAPLSLALCHATVQ-DDNIVLTPWT 166
Nostoc                   CTHLGCVVPWNAENKFKCPCHGSQYDATGKVVRGPAPKSLALSHAKTE-NDKIVLTSWT 153
Chlamydomonas           CTHLGCVVPWNAENKFKCPCHGSQYNAEGKVVRGPAPLSLALAHCDVAESGLVTFSTWT 164
Spinacia                 CTHLGCVVPFNAAENKFIKCPCHGSQYNNQGRVVRGPAPLSLALAHCDVDD-GKVVFLVPT 165
                          *****.:* . : : * *****:*. * * ***** * : : . . : : **

```

```

Synechocystis_petC2      DLDPRTEGEPWV- 178
Synechocystis_petC1     ETDFRTEDEPWVA- 192
Mastigocladus           ETDFRTEGEPWV- 179
Nostoc                   ETDFRTEGEPWWS- 166
Chlamydomonas           ETDFRTEGLEPWVA- 177
Spinacia                 ETDFRTEGAPWWSA 179
                          : * **, ***

```

**d**

```

Synechocystis           MSIIKKPDLSDPDLRAKLAKGMGHNYGEPAPWPNLILYMFPIICILGALGLIAGLAILDPA 60
Chlamydomonas           MSVTKKPDLSDPVLKAKLAKGMGHNTYGEPAWPNLLYMFVVLGTFACVIGLSVLDPA 60
Spinacia                 MGVTKKPDLNDPVLRAKLAKGMGHNYGEPAPWPNLLYIFPVVILGTIACNVGLAVLEPS 60
Mastigocladus           MATLKKPDLSDPKLRAKLAKGMGHNYGEPAPWPNLLYVFPVIMGTAFACIALSVLDPA 60
Nostoc                   MATHKKPDLSDPTLRAKLAKGMGHNYGEPAPWPNLLYVFPVIMGSAFACIALAVLDPA 60
                          *: ******* ****** *****:*****: *::: . .:***:

```

```

Synechocystis           MIGEPADPFATPLEILPEWYLYPTFQILRLIPNKLKLGIAGMAAIPGLMLVPFIESVKNKF 120
Chlamydomonas           AMGEPANPFATPLEILPEWYFYPVFQILRVVFNKLLGVLLMAAVPAGLITVPFIESINKF 120
Spinacia                 MIGEPADPFATPLEILPEWYFFPVFQILRTPNKLKGVLLMASVPAGLLTVPFLENVKNKF 120
Mastigocladus           MVGEPADPFATPLEILPEWYLYPVFQILRSVFNKLLGVLLMASVPLGLILVPFIEVKNKF 120
Nostoc                   MTGEPANPFATPLEILPEWYLYPVFQILRSLPNKLLGVLLMASVPLGLILVPFIEVKNKF 120
                          *****:*****:*.***** :*****: ***:* ** :***:*.***

```

```

Synechocystis           QNPFRRPIAMTVFLFGTAAALWLGAGATFPIDKSLTLGLF 160
Chlamydomonas           QNPYRRPIATILFLLGTLVAVWLGIGSTFPIDISLTLGLF 160
Spinacia                 QNPFRRPVATTVFLVGTVALWLGIGATLPIDKSLTLGLF 160
Mastigocladus           QNPFRRPVATTIFLFGTLVTLWLGIGATFPIDKSLTLGLF 160
Nostoc                   QNPFRRPVATTVFLFGTLVTLWLGIGAAPLIDKSLTLGLF 160
                          ***:***:* :**.*. .:*** *::*: * *****

```

**e**

```

Mastigocladus           MVEPLLDGLVGLVFATLGGFLYAAAYQYKRPNELGG- 37
Nostoc                   MVEPLLSGIVLGLIVVTLAGLFYAAAYKQYKRPNELGG- 37
Chlamydomonas           MVEPLLCGIVLGLVPVTIAGLFVTAYLQYLRGDLATY- 37
Spinacia                 MIEVFLFGIVLGLIPITLAGLFVTAYLQYRRGDQLD- 37
Synechocystis           MIEPLLLGIVLGLIPVTLAGLFVAAYLQYKRGQFNLD 38
                          *: * * * ****: *.*** :** * * :

```

**f**

```

Chlamydomonas           MIFDFNYIHIFMLTITSYVGLLIGALVFTLGIYLGLLKVVKLI 43
Spinacia                 -----MFTLTSYFGFLAALTITSALFIGLNKIRLI- 31
Synechocystis           -----MAAGVGFIFIGYIAVFTGVTGLLGLYLRVFKLI- 32
Mastigocladus           -----MILGAVFYIVFIALFFGIIVGIIFAIKSIIKLI- 32
Nostoc                   -----MLAIVAYIGFLALFTGIAAGLLFGLRSKIL- 31
                          :. : :. : : :

```



**Figure 5.10 | Multiple sequence alignment of *cytb<sub>6</sub>f* subunits *cytf*, *cytb<sub>6</sub>*, Rieske ISP, subunit IV, PetG, PetL, PetM and PetN.** a-h, Sequences of the *cytf* (a), *cytb<sub>6</sub>* (b), Rieske ISP (c), subIV (d), PetG (e), PetL (f), PetM (g) and PetN (h) from cyanobacterial (*Mastigocladus laminosus*, *Nostoc* sp. PCC7120, *Synechocystis* sp. PCC 6803), algal (*Chlamydomonas reinhardtii*) and plant (*Spinacia oleracea*) were aligned in Clustal Omega v 1.2.4. Conserved identities are indicated by asterisks (\*), and similarities by double (:), then single dots (.). Polar residues are coloured in green, positively charged residues are coloured pink, hydrophobic residues are coloured red and negatively charged residues are coloured blue. The sequences omit signal peptides.

## 5.6.2 Model building

Initially, a homology-based approach was performed using the *Nostoc* sp. PCC 7120 *cytb<sub>6</sub>f* (PDB ID: 4OGQ) (**Hasan and Cramer, 2014b**) as a template and the sequence alignments generated by Clustal Omega as a guide. The model was rigid-body docked into the density using the ‘fit in map’ function in Chimera (**Pettersen et al., 2004**).

This was then followed by manual adjustment and real-space refinement using COOT (v 0.8.9.2) (**Emsley and Cowtan, 2004**). Sequence assignment and fitting was guided by bulky residues such as Arg, Trp, Tyr and Phe. After fitting of the polypeptide chains and cofactors in one half of the dimeric complex, the other half of the complex was then independently modelled into the C1 density map. Once the polypeptide chain was complete for both halves of the complex, additional non-protein molecules (e.g. ligands such as plastoquinone-9 (PQ), lipids and cofactors) were assigned to regions of unassigned density.

Interestingly, while existing structures of *cytb<sub>6</sub>f* possess a  $\beta$ -carotene molecule on the periphery of each monomeric unit, in some cyanobacterial species (including *Synechocystis* sp. PCC 6803), this carotenoid is known to be substituted by echinenone (**Figure 5.11**), a

xanthophyll synthesised from  $\beta$ -carotene by a ketolase enzyme known as CrtO (**Boronowsky et al., 2001**). While the core structure of the carotenoid remains the same, the structures differ by the presence of an additional ketone group on one of the head rings of the carotenoid. Modelling of the echinenone molecule was facilitated by comparative superimposition of the *Synechocystis* sp. PCC 6803 cryo-EM map with the map from *S. oleracea*; here we observe an additional area of density in the region of the map corresponding to the membrane exposed carotenoid ring, this was consistent with the presence of a ketone group (**Figure 5.11**).

The model underwent several cycles of iterative global refinement and minimisation using the real space refinement function in PHENIX (**Adams et al., 2010**) followed by validation and manual refinement.

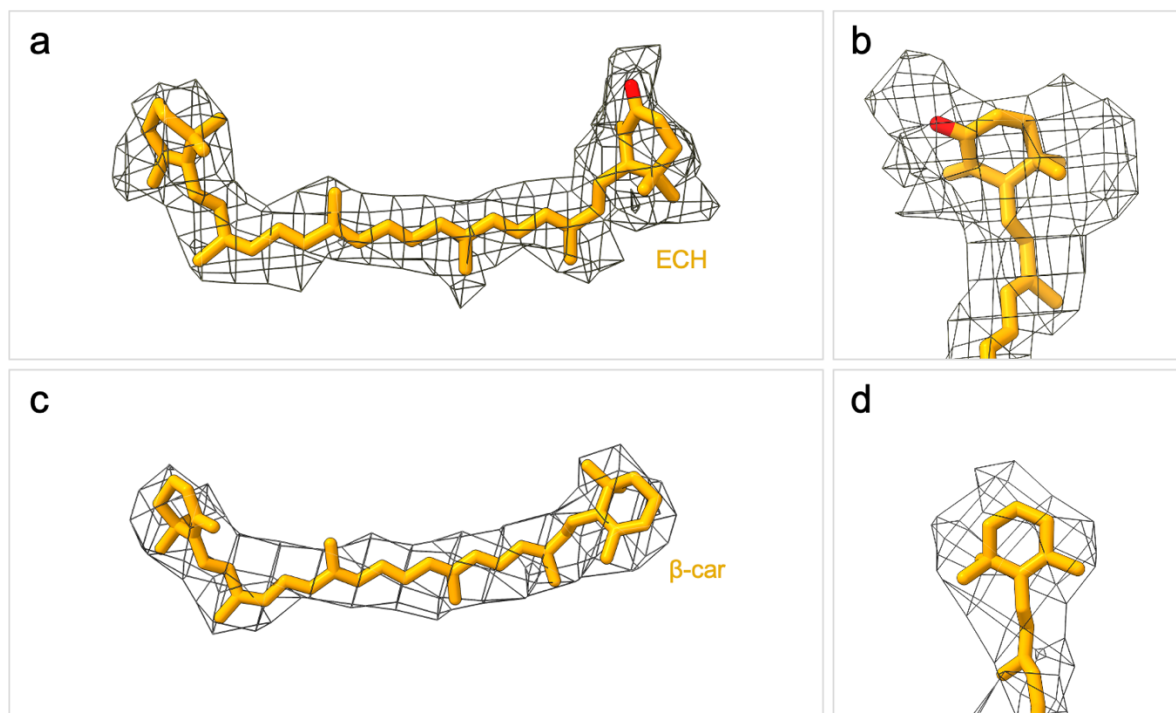


**Figure 5.11 | The modelling of Echinenone in the cryo-EM map of *Synechocystis* sp. PCC 6803 (*petA-strep*) *cytb<sub>6</sub>f*.** a-d, comparison of the cryo-EM densities of the region corresponding to the carotenoid molecule in the in the *Synechocystis* sp. PCC 6803 (*petA-strep*) (a-b) and *S. oleracea* (c-d) *cytb<sub>6</sub>f* complexes. Both echinenone (ECH) and  $\beta$ -carotene ( $\beta$ -car) are coloured orange with the =O of the ketone in echinenone coloured red. The contour levels of the density maps were adjusted to 0.0237 (*Synechocystis*) and 0.0811 (*S. oleracea*) respectively.



### 5.6.3 Model Validation

Model validation was carried out using the ‘Comprehensive Validation’ tool in PHENIX as described in **section 2.9.2 (Adams et al., 2010; Afonine et al., 2018; Williams et al., 2018)** to assess the overall model quality and highlight any issues regarding steric clashes and general geometry such as rotamer outliers, Ramachandran outliers, anomalous bond lengths and anomalous bond angles.

As described previously, the ‘Comprehensive Validation’ tool in PHENIX utilises MolProbity **(Chen et al., 2010)** features to quantify model quality; this generates two summarised statistics; both of these are scaled and normalised relative to other structures of a similar resolution (within 0.25 Å) submitted to the PDB.

The first summarised statistic is an all-atom ‘clash score’ **(Chen et al., 2010)** which accounts for the number of unfavourable steric clashes between non-donor-acceptor atom pairs in the model. Hydrogen atoms are added to the model and the number of ‘serious’ atom-atom overlaps (i.e. > 0.4 Å overlap for non-H-bonded atoms) per 1000 atoms is quantified. In this case the clash score is well within the expected range for a structure at this resolution.

The second summarised statistic is the ‘MolProbity score’ **(Chen et al., 2010)**, this provides an overall assessment of model quality in terms of both sterics and geometry. The score is a log-weighted combination of the clash score, Ramachandran outliers (%) and rotamer outliers (%) in the model; these values are scaled and normalised to provide a single number that reflects the resolution at which those values might be expected. A structure with a Molprobity score numerically lower than its actual global resolution is determined as being better in quality than the average structure on the PDB at that resolution. In this case, the Molprobity score for the *Synechocystis* sp. PCC 6803 (*petA-strep*) *cyt<sub>b</sub>cf* map is 1.97, indicating that the model quality is much higher than the average structure on the PDB at ~ 2.98 (± 0.25) Å resolution.

In addition to these two summarised statistics, Molprobity also provides a detailed assessment of Ramachandran ( $\phi$ ,  $\psi$ ) **(Figure 5.12) (Ramachandran et al., 1963)** outliers and cis/twisted peptides. Analysis indicates that of the 1,916 residues in the structure, 95.16 % occupy ‘favourable’ regions in the Ramachandran plot and 4.79 % occupy ‘allowed’ regions; there is one Ramachandran outlier (I/Thr 7 built marginally outside of the permitted zones). Of note, validation highlighted the presence of two *cis*-peptides in both halves of the model

corresponding to proline residues in *cytb<sub>6</sub>* (Pro120) and in subIV (Pro33). As in the *S. oleracea* structure (**section 4.3.3**), both of these instances appear to correspond to genuine *cis* peptides. While Pro120 (Pro113 in *S. oleracea*) facilitates a sharp turn in a loop between TM helices of the in *cytb<sub>6</sub>* subunit, Pro33 forms part of one of the TM helices of subIV.

An overview of the data collection, processing, refinement and validation statistics is provided in **Table 5.1** while the quality of the modelled data fit can be observed in **Figure 5.13**.

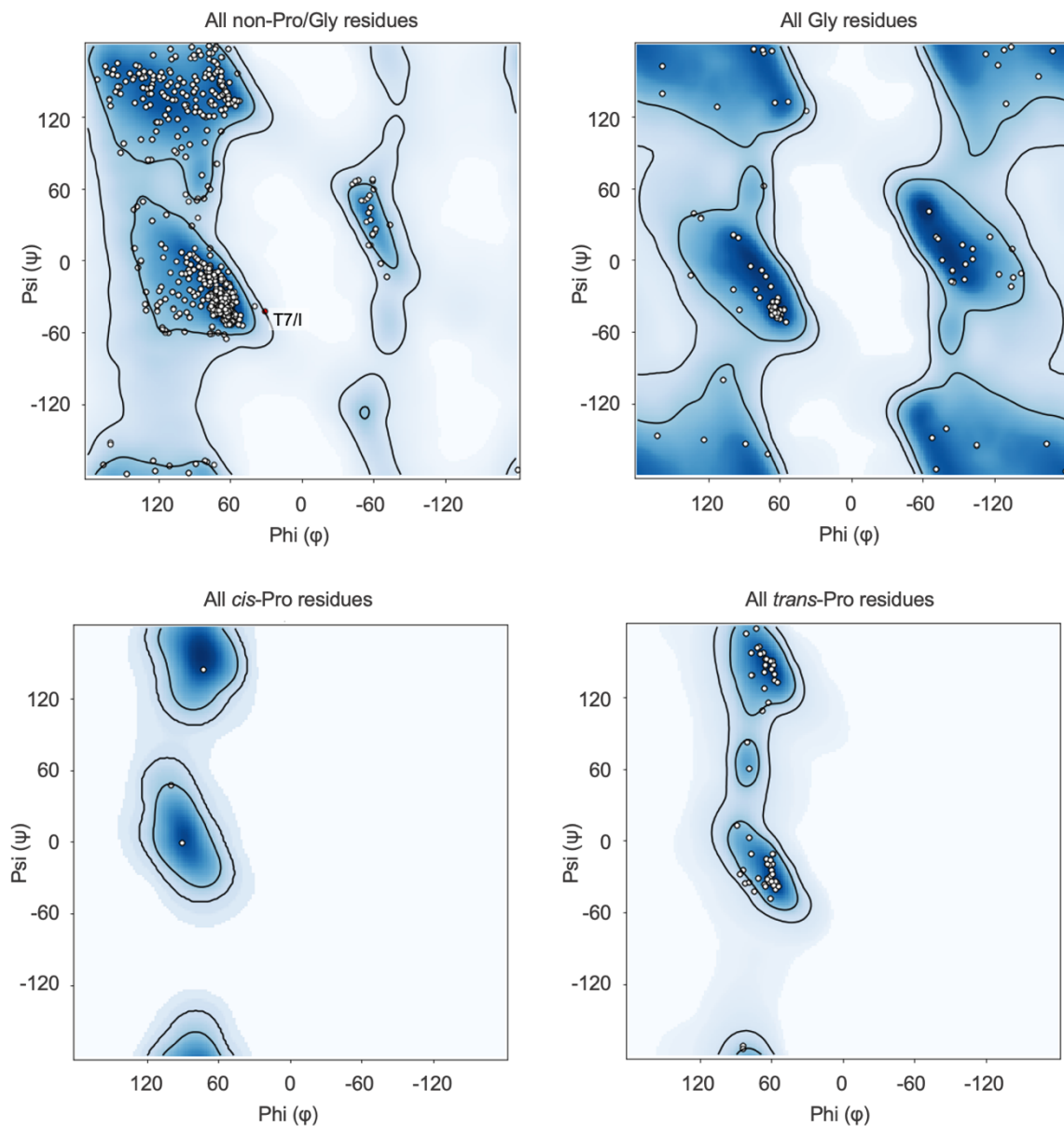


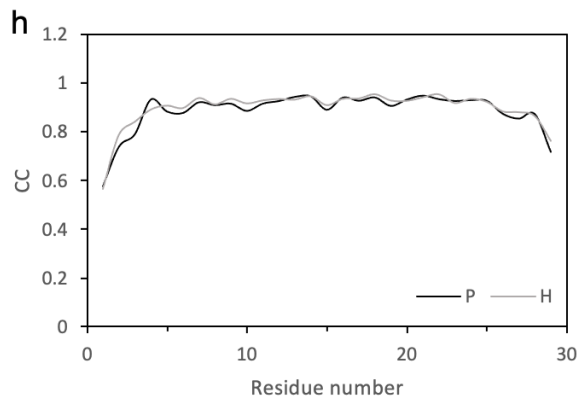
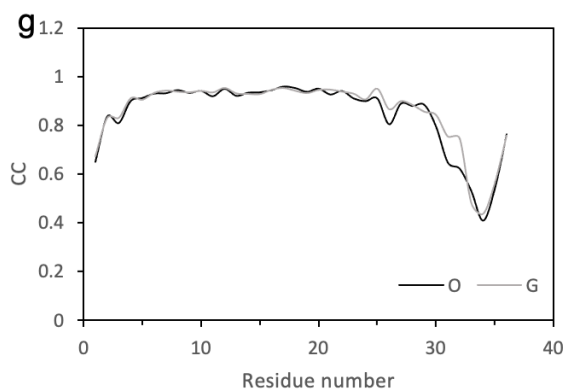
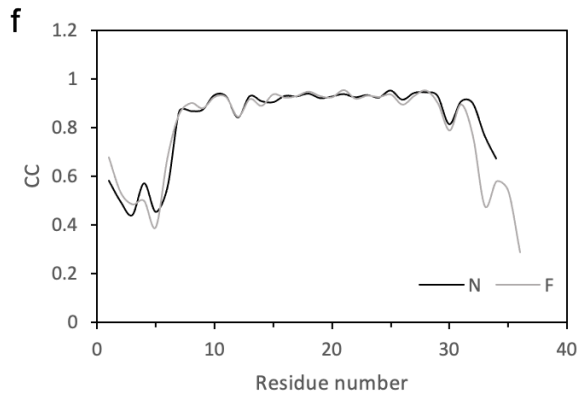
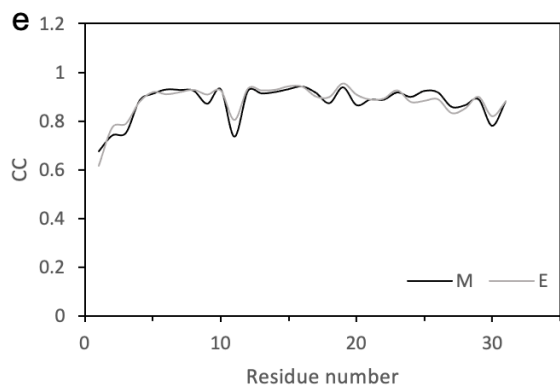
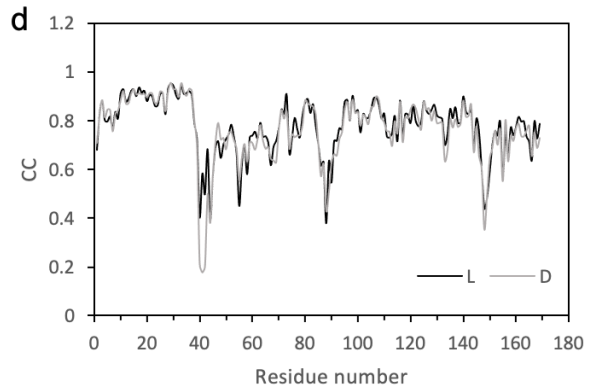
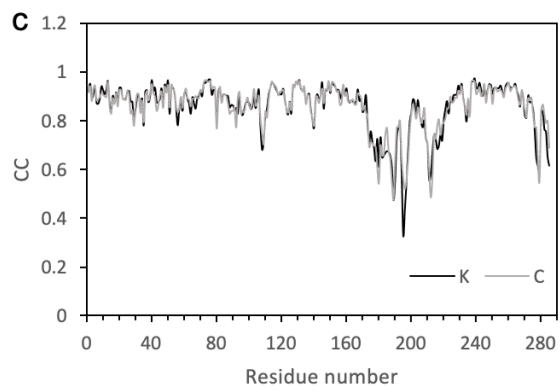
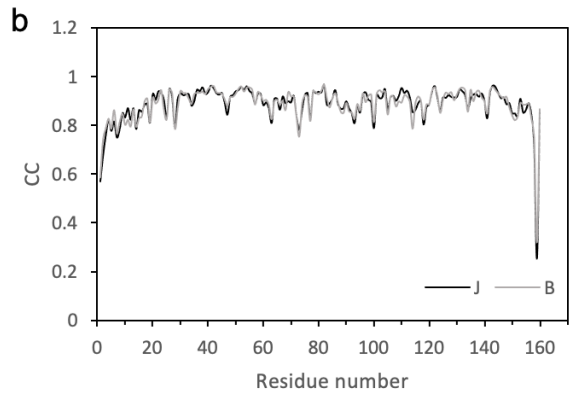
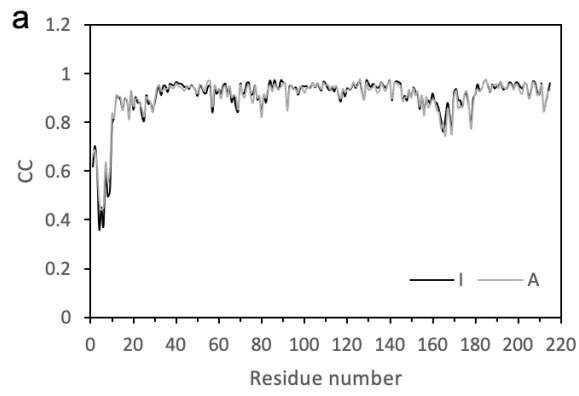
**Figure 5.12 | Ramachandran analysis of the *Synechocystis* sp. PCC 6803 (*petA-strep*) *cytb<sub>6f</sub>* model.** Of the 1,916 residues modelled, 95.15 % occupy ‘favourable’ regions and 4.79 % occupy ‘allowed’ regions. There is one outlier (T7/I) built marginally outside of the permitted zones, this is labelled and shown as a red dot.

**Table 5.1 | Cryo-EM data collection, processing, refinement and validation statistics.**

Parameters	(EMD-13584, PDB 7PPW)
<b>Data collection</b>	
Nominal Magnification	81,000 X
Accelerating Voltage (kV)	300
Electron dose (e <sup>-</sup> /Å <sup>2</sup> /s)	3.0
Exposure time (s)	3.0
Number of fractions	45
Defocus range (-μm)	- 1.2 to - 2.5
Pixel size (Å)	0.53
Symmetry imposed	C1
Initial particle images (no.)	4,032,212
Final particle images (no.)	413,442
Map resolution (Å) (global)	2.98
FSC threshold	0.143
Map resolution range (Å)	~ 2.98 – 7.00
<b>Refinement</b>	
Initial model used	RELION <i>de novo</i> model
Model resolution (Å)	2.98
FSC threshold	0.143
Model resolution range (Å)	~ 2.98 – 7.00
Map sharpening <i>B</i> factor (Å <sup>2</sup> )	Estimated automatically using RELION
<b>Model composition</b>	



Non-hydrogen atoms	15,619
Protein residues	1,916
Waters	2
Ligands	24
<b>B factors (Å<sup>2</sup>)</b>	
Protein	RELION auto-estimated
Ligand	RELION auto-estimated
<b>RMS deviations (PHENIX)</b>	
Bond lengths (Å)	0.011
Bond angles (°)	0.932
<b>Validation</b>	
Molprobit score	1.97
Clashscore	13.47
Poor rotamers (%)	0.64
<b>Ramachandran plot</b>	
Favoured (%)	95.15
Allowed (%)	4.79
Disallowed (%)	0.05



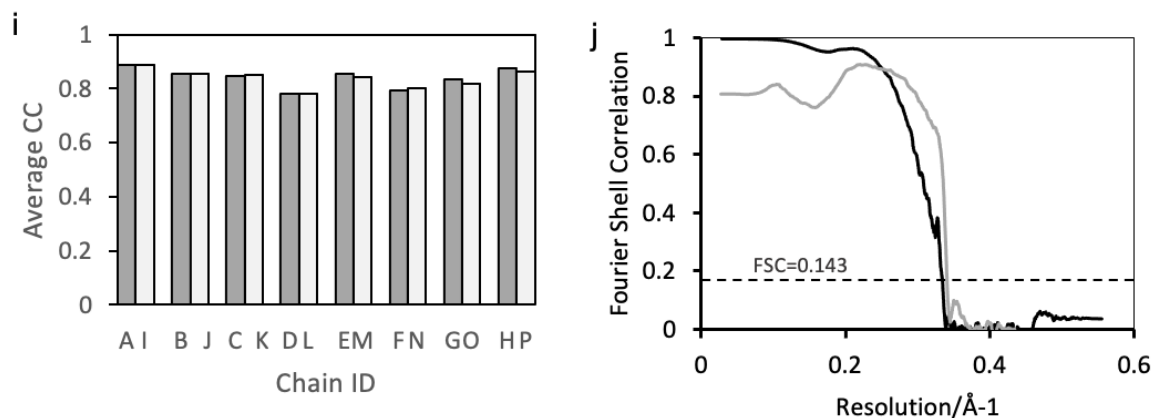


**Figure 5.13 | An assessment of the quality of modelled data fit in the cryo-EM map of *Synechocystis* sp. PCC 6803 (*petA-strep*) *cyt<sub>b</sub><sub>6</sub>f*.** Correlation coefficients (CC) for each of the eight subunits in the *Synechocystis* sp. PCC 6803 (*petA-strep*) *cyt<sub>b</sub><sub>6</sub>f* dimer calculated on a per-residue basis for **a**, the *cyt<sub>b</sub><sub>6</sub>* subunit (chains A and I), **b**, subIV (chains B and J), **c**, *cyt f* (chains C and K), **d**, the Rieske ISP (D and L), **e**, Pet L (chains E and M), **f**, Pet M (chains F and N), **g**, Pet G (chains O and G) and **h**, Pet N (chains H and P). Significant dips in the plotted CC values correspond to regions of the map where the resolution is lower and the fit is more ambiguous such as around the tips of the *cyt f* soluble domain (residues 170 - 220), the Rieske ISP hinge region (residues 41 - 56) and the N- and C- terminal regions of subunits. **i**, CC averages for each chain. **j**, Comparison of the FSC curve for experimental data (solid black line) and the calculated model-to-map FSC curve (solid grey line).

## 5.7 Structural analysis

### 5.7.1 Overall architecture and comparison with the *S. oleracea* complex

The global architecture of the dimeric complex from *Synechocystis* sp. PCC 6803 appears to be largely similar to that observed in the previous structure of the complex from *S. oleracea* (Malone et al., 2019a) as demonstrated by the comparative RMSD values across all chains in both species shown in

#### **Figure 5.14.**

The colour-coded map (**Figure 5.15**) shows the density of each of the eight polypeptide subunits in each half of the dimer, these appear to be encircled by a band of disordered density corresponding to the detergent around the TM portion of the dimer. Each monomeric unit is arranged as observed in the *S. oleracea* complex (**Malone et al., 2019**), with four large polypeptide subunits (*cyt<sub>f</sub>*, *cyt b<sub>6</sub>*, *ISP*, *subIV*) containing the core prosthetic groups (haem *f*, 2Fe-2S, haem *b<sub>p</sub>*, haem *b<sub>n</sub>*, haem *c<sub>n</sub>*), and four small subunits (PetG, L, M, N). **Figure 5.16** shows the density and structural model for each subunit.

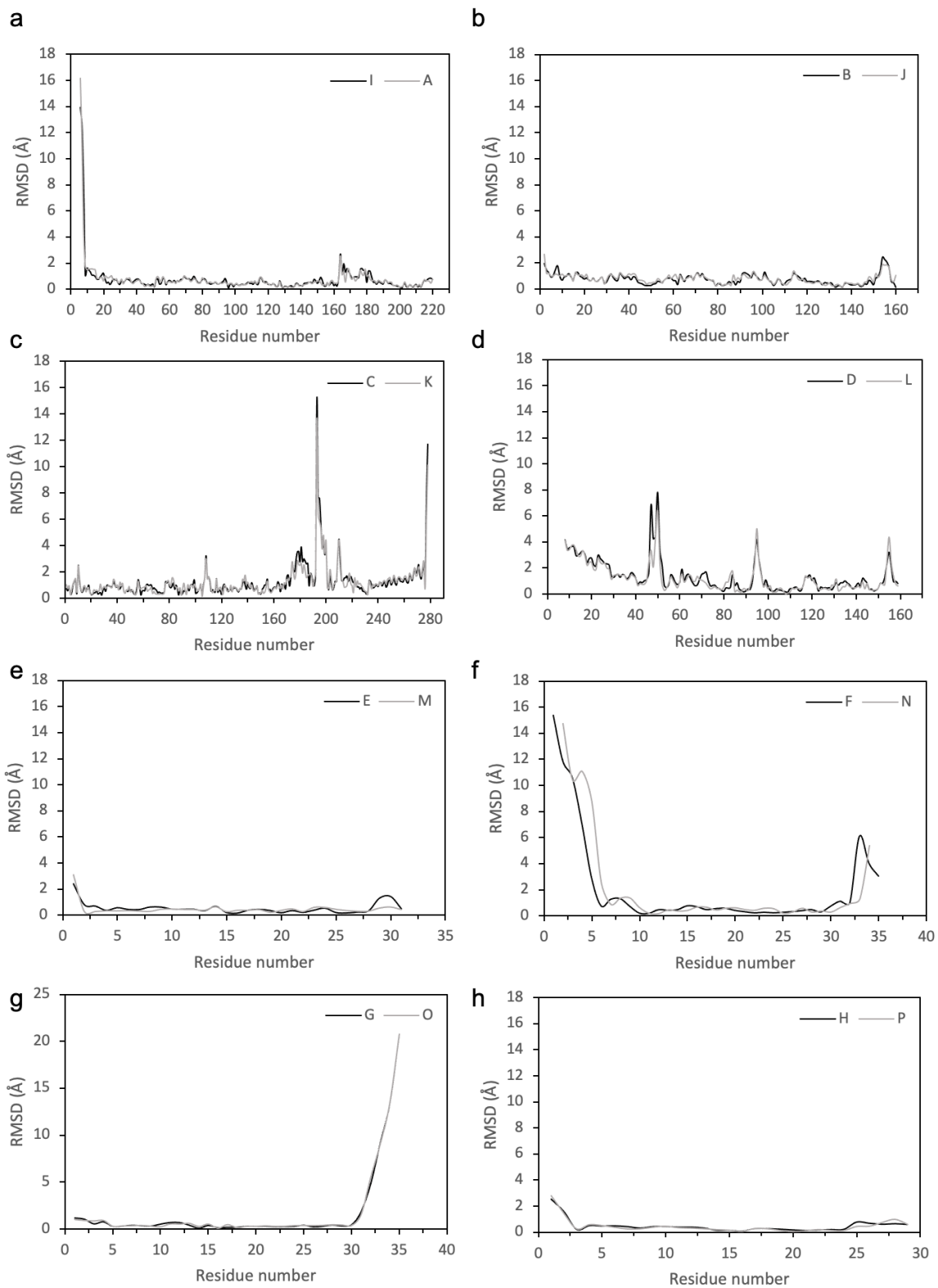


**Figure 5.14 | The root-mean-square-deviation (RMSD) of  $\alpha$  atoms in the *S. oleracea* and *Synechocystis* sp. PCC 6803 (*petA-strep*) *cytb<sub>6</sub>f* structures. a-h, Plots showing RMSD values for each of the eight subunits in the *S. oleracea* and *Synechocystis* sp. PCC 6803 (*petA-strep*) *cytb<sub>6</sub>f* dimers**

showing **a**, the *cyt b<sub>6</sub>* subunit (chains A and I), **b**, subIV (chains B and J), **c**, *cyt f* (chains C and K), **d**, the Rieske ISP (D and L), **e**, Pet L (chains E and M), **f**, Pet M (chains F and N), **g**, Pet G (chains O and G) and **h**, Pet N (chains H and P). Significant dips in the plotted CC values correspond to regions of the map where the resolution is lower and the fit is more ambiguous such as around the tips of the *cyt f* soluble domain (residues 170 - 220), the Rieske ISP hinge region (residues 41 - 56) and the N- and C- terminal regions of subunits.

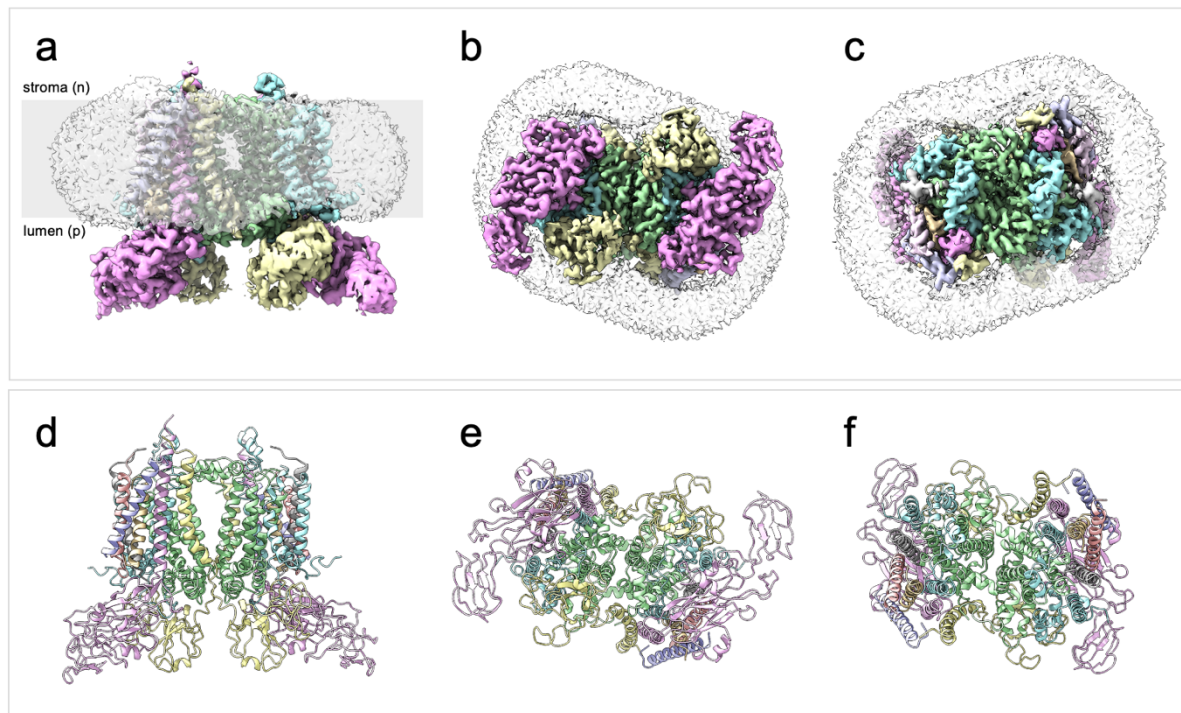


**Figure 5.15 | Cryo-EM structure of the *Synechocystis* sp. PCC 6803 (*petA-strep*) *cytb<sub>6</sub>f* complex.** **a–c**, Views of the colour-coded *cytb<sub>6</sub>f* density map showing *cytb<sub>6</sub>* (green), *cyt f* (pink), ISP (yellow), subIV (cyan), PetG (grey), PetM (salmon), PetN (pale orange) and PetL (pale purple). Detergent and other disordered molecules are shown in semi-transparent light grey. **a**, View in the plane of the membrane. The grey stripe indicates the probable position of the thylakoid membrane bilayer. **b**, View perpendicular to the membrane plane from the lumenal (p) side. **c**, View perpendicular to the membrane plane from the stromal (n) side. **d–f**, Modelled subunits of *cytb<sub>6</sub>f* shown in a cartoon representation and coloured as in a–c. **d**, View in the plane of the membrane. **e**, View perpendicular to the membrane plane from the lumenal side. **f**, View perpendicular to the membrane plane from the stromal side.

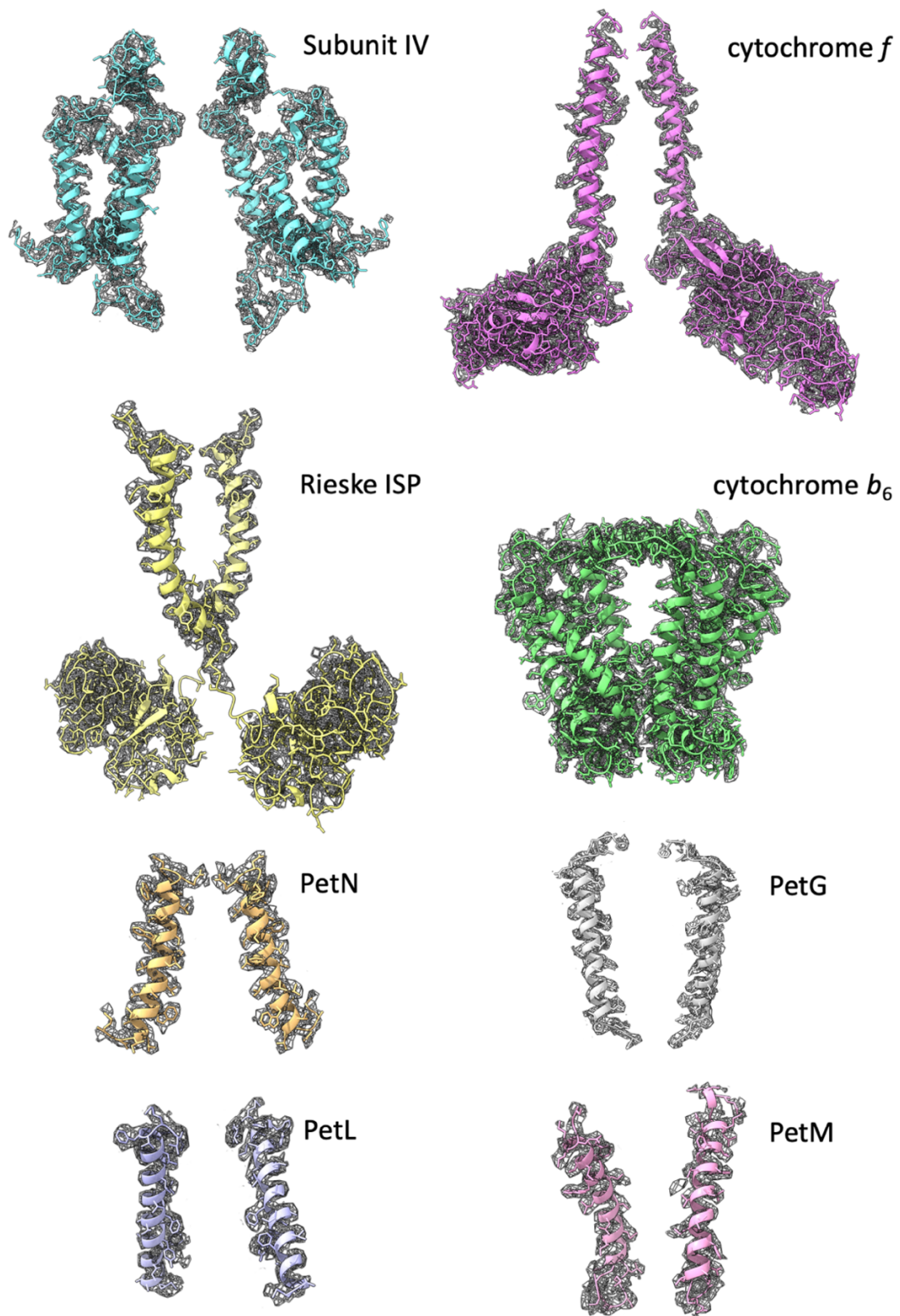
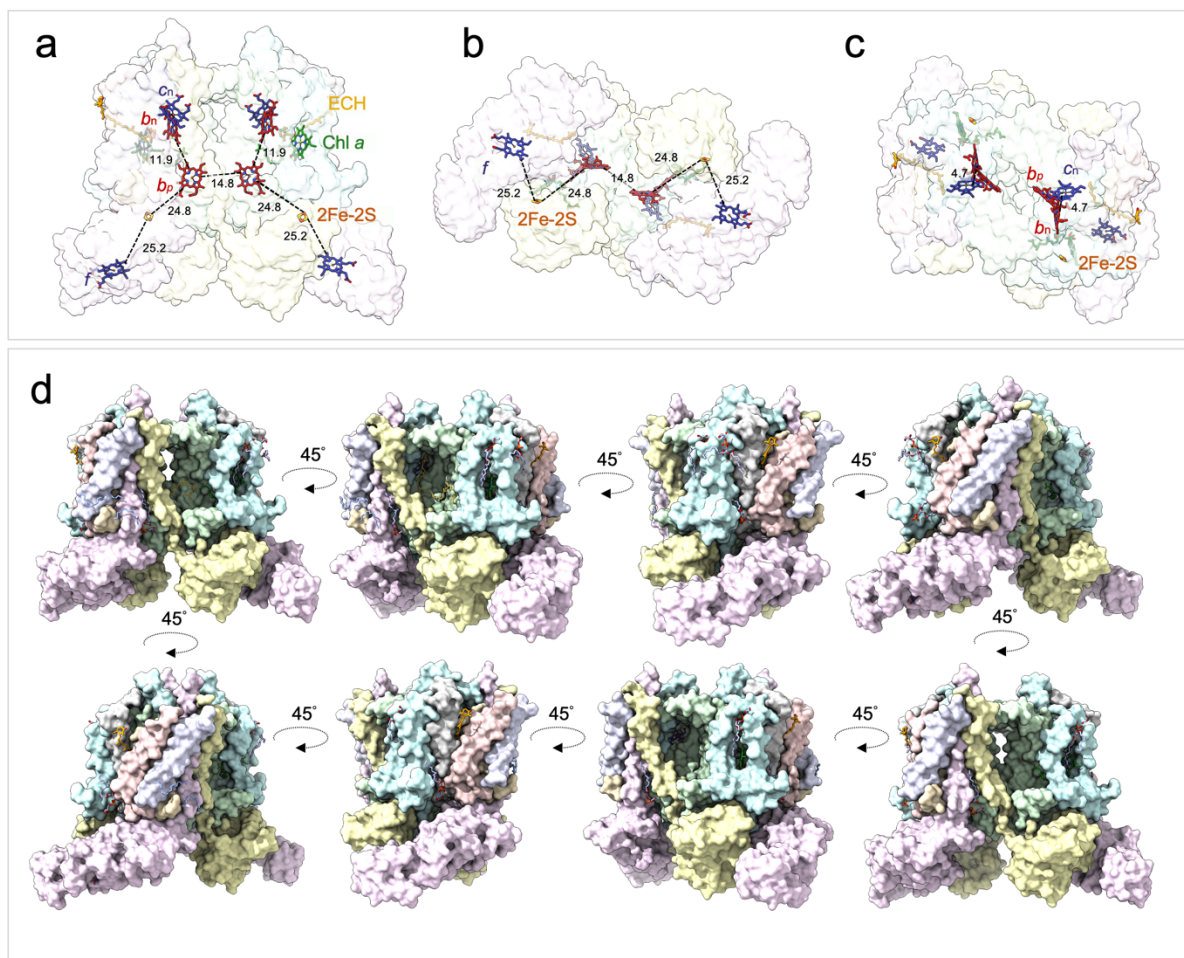


Figure 5.16 | Cryo-EM densities and structural models of polypeptides in the *Synechocystis* sp. PCC 6803 (*petA-strep*) *cytb*<sub>6</sub>*f* complex. The colour code is the same as in Figure 5.15. The contour levels of the density maps were adjusted to 0.043, note ‘dust’ was hidden manually.

At the core of the structure are 7 TM helices belonging to cyt  $b_6$  (helices A-D) and subIV (helices E-G), surrounding these are the single TM helices of PetG, L, M and N and the membrane anchoring helices of *cyt $f$*  and the Rieske ISP. As observed previously, both *cyt $f$*  and the ISP possess extrinsic domains which project from the membrane plane on the p-side of the complex. In the case of the Rieske ISP, this domain extends from one monomer to the neighbouring monomer, forming contacts with the neighbouring *cyt $f$*  subunit and stabilising an interlocked dimeric complex.

Each monomeric unit contains five core prosthetic groups as described previously (**section 4.4.1**), these comprise two covalently bound *c*-type haems (haem *f* and haem  $c_n$ ), two non-covalently bound *b*-type haems (haem  $b_p$  and haem  $b_n$ ) and a 2Fe-2S cluster (**Baniulis et al., 2009; Hasan and Cramer, 2014a; Hasan et al., 2013b, 2013a, 2014; Kurisu et al., 2003; Malone et al., 2019; Stroebel et al., 2003; Yamashita et al., 2007; Yan et al., 2006**). In addition to these core prosthetic groups are two pigment molecules, a Chl *a* molecule and a carotenoid. While the Chl *a* molecule remains highly conserved, it is interesting to note that the position designated as 9-cis- $\beta$ -carotene in other species (including *S. oleracea*) is substituted for an echinenone molecule in *Synechocystis*. As discussed in **section 5.6.2**, this echinenone is modelled with its ketone group protruding from the complex into the lipid phase of the membrane. **Figure 5.17** shows the organisation of prosthetic groups within the *Synechocystis sp.* PCC 6803 *b<sub>6</sub>f* dimer, while **Figure 5.18** shows the respective densities and structural model for each molecule.





**Figure 5.17 | Prosthetic groups, substrate, lipids and hydrocarbons modelled into the *Synechocystis* sp. PCC 6803 (*petA-strep*) *cytb<sub>6</sub>f* complex.** a-c, Modelled cofactors of *cytb<sub>6</sub>f* showing the edge-to-edge distances between the core redox-active cofactors. d, A surface view showing the core cofactors (coloured as in a-c), PQ (yellow), lipids (pale purple) and hydrocarbon chains (pale blue) modelled into the *Synechocystis* sp. PCC 6803 (*petA-strep*) *cytb<sub>6</sub>f* complex. Subunits are coloured with *cytb<sub>6</sub>* (green), *cyt<sub>f</sub>* (pink), ISP (yellow), subIV (cyan), PetG (grey), PetM (salmon), PetN (pale orange) and PetL (pale purple). Cofactors and lipids are coloured with *c*-type haems (*f*, *c<sub>n</sub>*; dark blue), *b*-type haems (*b<sub>p</sub>*, *b<sub>n</sub>*; red), echinenone (orange), chlorophyll *a* (major conformation, dark green) (minor conformation, light green), 2Fe-2S (orange/yellow), phosphatidylglycerol (light purple), plastoquinones (yellow) and hydrocarbon tails (pale blue).

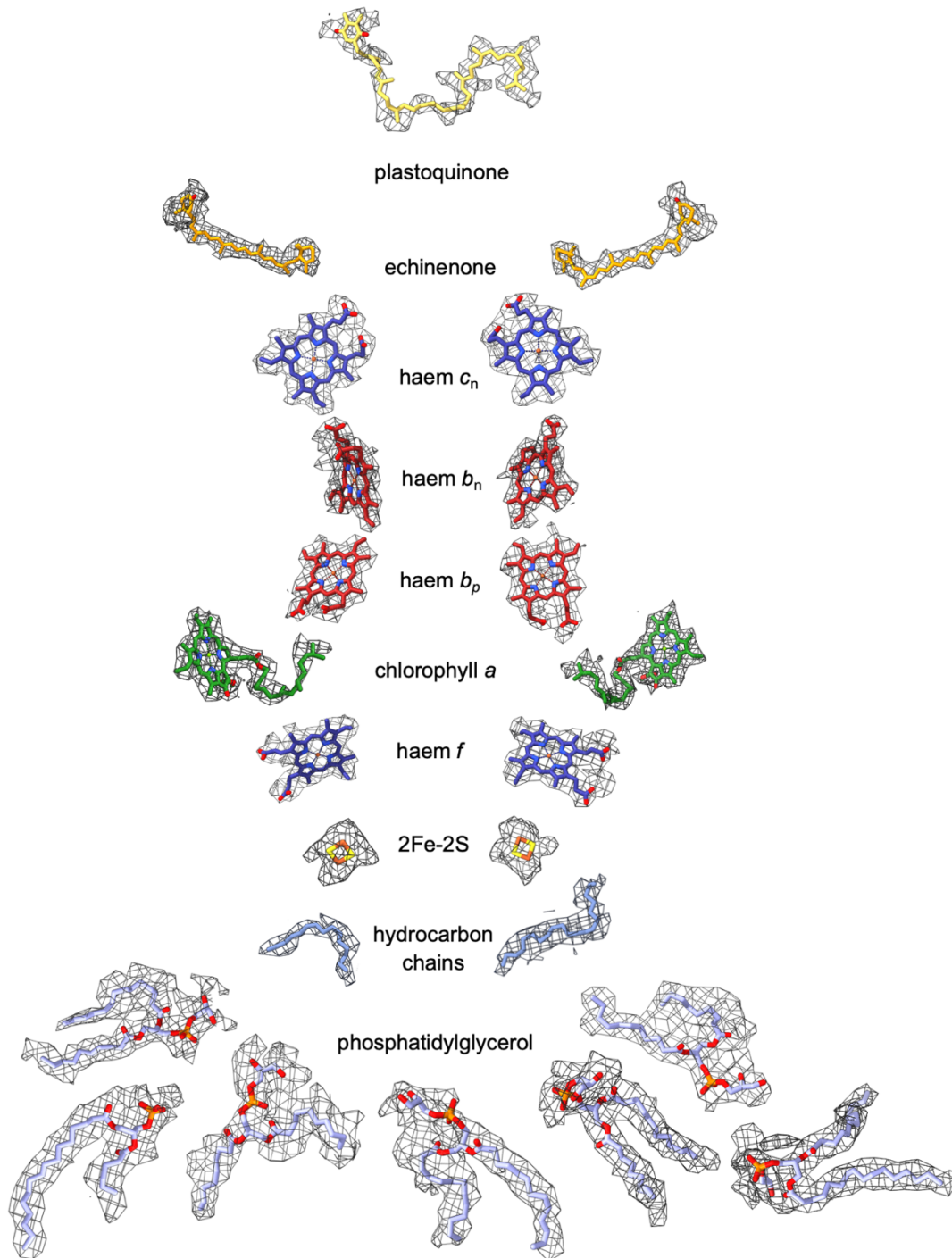


**Figure 5.18 | Cryo-EM densities and structural models of prosthetic groups, lipids and plastoquinone molecules in the *cytb<sub>6</sub>f* complex.** *c*-type haems (*f*, *c<sub>n</sub>*; dark blue), *b*-type haems (*b<sub>p</sub>*, *b<sub>n</sub>*; red), echinenone (orange), Chl *a* (major conformation, dark green) (minor conformation, light green), 2Fe-2S (orange/yellow), phosphatidylglycerol (light purple), plastoquinones (yellow) and hydrocarbon tails (pale blue). The contour levels of the density maps were adjusted to 0.0257. Note that the arrangement of cofactors shown here has little relation to the organisation of cofactors within the 3D structural model.

As observed in the *S. oleracea* structure, the edge-to-edge cofactor distances appear to be well conserved (**Table 5.2**) across all species of *cytb<sub>6</sub>f* however, as noted previously (see **section 4.4.1**), it appears that distances along the high-potential pathway (between the [2Fe-2S] cluster and haem *f*) are not conducive to electron transfer without a conformational change similar to that observed in *cytb<sub>c</sub>1* to bridge this gap (**Zhang et al., 1998**) (this will be discussed further in **chapter 6**).

In addition to these core prosthetic groups, the 2.98 Å map from *Synechocystis sp.* PCC 6803 *cytb<sub>6</sub>f* also resolves a PQ molecule, seven lipids modelled as phosphatidylglycerol (PG) and two hydrocarbon chains which we presume to correspond to the tails of less well-defined lipid moieties (**Figure 5.18**).

**Table 5.2 | A comparison of edge-to-edge cofactor distances (Å) in each half of the *b<sub>6</sub>f* dimer from different species.** Models used include *b<sub>6</sub>f* from *S. oleracea* (PDB ID: 6RQF (**Malone et al., 2019**)), *C. reinhardtii* (PDB ID: 1Q90 (**Stroebel et al., 2003**)), *M. lamosus* (PDB ID: 2E74 (**Yamashita et al., 2007**)) and *Nostoc sp.* PCC 7120 (PDB ID: 4OGQ (**Hasan and Cramer, 2014a**)). <sup>a</sup> Inhibitor is indicated by the abbreviation TDS (tridecylstigmatellin).

PDB ID	7PPW	6RQF	1Q90	2E74	4OGQ
Source	<i>Synechocystis</i>	<i>S. oleracea</i>	<i>C. reinhardtii</i>	<i>M. lamosus</i>	<i>Nostoc</i>
Resolution (Å)	2.98	3.58	3.1	3.0	2.5
Inhibitors <sup>a</sup>	-	-	TDS (Q <sub>p</sub> )	-	-
Distances:					
<i>b<sub>n</sub></i> - <i>c<sub>n</sub></i> (Å)	4.7, 4.7	4.7, 4.7	4.7, 4.7	4.7, 4.7	4.6, 4.6
<i>b<sub>n</sub></i> - <i>b<sub>p</sub></i> (Å)	11.9, 11.9	12.1, 12.0	12.2, 12.2	12.2, 12.2	12.1, 12.1
<i>b<sub>p</sub></i> - <i>b<sub>p</sub></i> (Å)	14.8	15.3	15.1	15.2	15.3
<i>b<sub>p</sub></i> - [2Fe-2S] (Å)	24.8, 24.8	25.6, 25.5	22.9, 22.9	25.5, 25.5	25.3, 25.3
[2Fe-2S] - <i>f</i> (Å)	25.2, 25.2	25.9, 26.1	27.8, 27.8	26.2, 26.2	26.2, 26.2

## 5.7.2 The intermonomer cavity and clues regarding substrate movement in plants

As described in **section 1.3.1**, dimerisation between the two monomeric units creates a large, protein-free intermonomer cavity; this can be further subdivided into two halves connected by a narrow channel. As in the *S. oleracea* structure (**section 4.4.2**), this channel that connects the two halves of the intermonomer cavity is bounded at the top by the N-terminal helix of *cytb<sub>6</sub>* and at the bottom by aromatic residues from the A and D helices of *cytb<sub>6</sub>* (**Figure 5.19**).

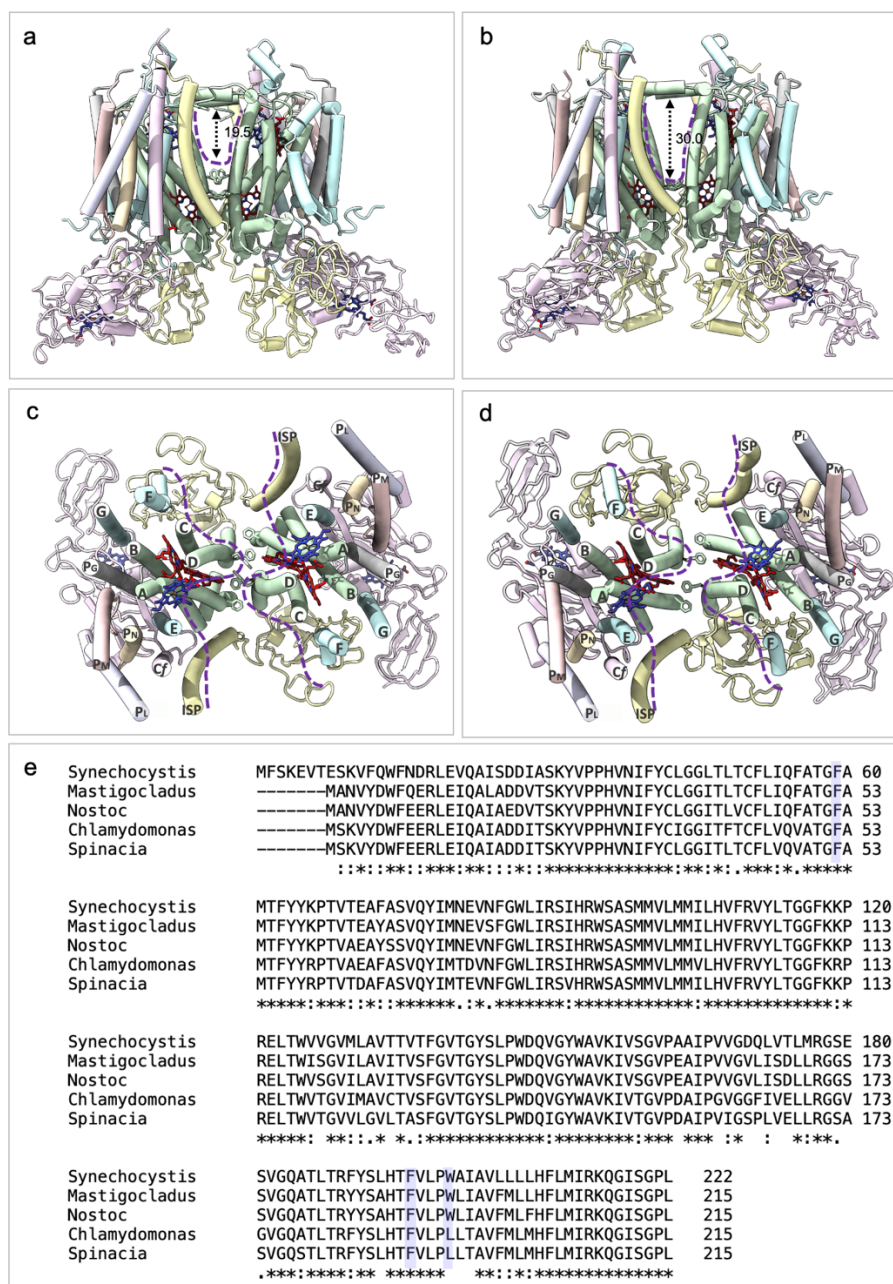




**Figure 5.19| The intermonomer cavity of the *Synechocystis* sp. PCC 6803 (*petA-strep*) *cytb<sub>6</sub>f* complex. a-b**, a cartoon representation of the *cytb<sub>6</sub>f* complex from *Synechocystis* sp. PCC 6803 (*petA-strep*) (**a**) and *S. oleracea* (**b**) showing the intermonomer cavity (outlined by a purple dashed line) viewed perpendicular to the plane of the membrane. Aromatic residues that delimit the floor of the cavity and the haems are shown in stick representation. **c-d**, a cartoon representation of the *cytb<sub>6</sub>f* complex from *Synechocystis* sp. PCC 6803 (*petA-strep*) (**c**) and *S. oleracea* (**d**) showing the intermonomer cavity (outlined by a purple dashed line) viewed normal to the plane of the membrane. Aromatic residues that delimit the floor of the cavity and the haems are shown in stick representation. Subunits are coloured as in **Figure 5.17**, and cofactors and lipids coloured as in **Figure 5.18.e**. Multiple sequence alignment of the *cytb<sub>6</sub>* subunit from cyanobacterial (*Mastigocladus laminosus*, *Nostoc* sp. PCC7120), algal (*Chlamydomonas reinhardtii*) and plant (*Spinacia oleracea*) sources were aligned in Clustal Omega v 1.2.4. Conserved identities are indicated by asterisks (\*), and similarities by double (:), then single dots (.). Conserved identities are indicated by asterisks (\*), and similarities by double (:), then single dots (.). F59, F196 and W200 are highlighted in blue.

While the residues which bound the base of the cavity in *S. oleracea* (Phe52 and 189 in *S. oleracea*; Phe59 and 196 in *Synechocystis*) are highly conserved across all species analysed (**Figure 5.19**), it is interesting to note that the channel in *Synechocystis* is significantly shallower (depth ~ 19.5 Å compared to the 30 Å observed in *S. oleracea*) owing to the presence of two Trp residues (Trp200) which protrude from helix D of *cytb<sub>6</sub>* forming a base to the channel around 10 Å above that observed in *S. oleracea* (**Figure 5.19**). It is extremely interesting to note that while this Trp is highly conserved in the cyanobacterial structures (PDB ID: 1VF5, 2E74, 2D2C, 2E76, 4H13, 4PVI, 2E75, 4H0L, 4I7Z, 2ZT9, 4H44, 4OGQ) (**Baniulis et al., 2009; Hasan and Cramer, 2014a; Hasan et al., 2013a, 2013b, 2014; Kurisu et al., 2003; Yamashita et al., 2007; Yan et al., 2006**), in both the algal (*C. reinhardtii*) (**Stroebel et al., 2003**) and plant (*S. oleracea*) (**Malone et al., 2019**) structures it is substituted for a substantially smaller Leu residue. This structural change opens the channel in *S. oleracea* sufficiently to allow the entry of substrate, facilitating exchange of substrate between the two halves of the intermonomer cavity. As we observe in **section 4.4.4**, the entry of substrate into this channel in *S. oleracea* enables PQ bound at the Q<sub>n</sub> site of one monomer to potentially obstruct the Q<sub>n</sub> site of the opposite monomer (**Figure 5.20**) such that the binding of substrate at the Q<sub>n</sub> site may be a mutually exclusive event.

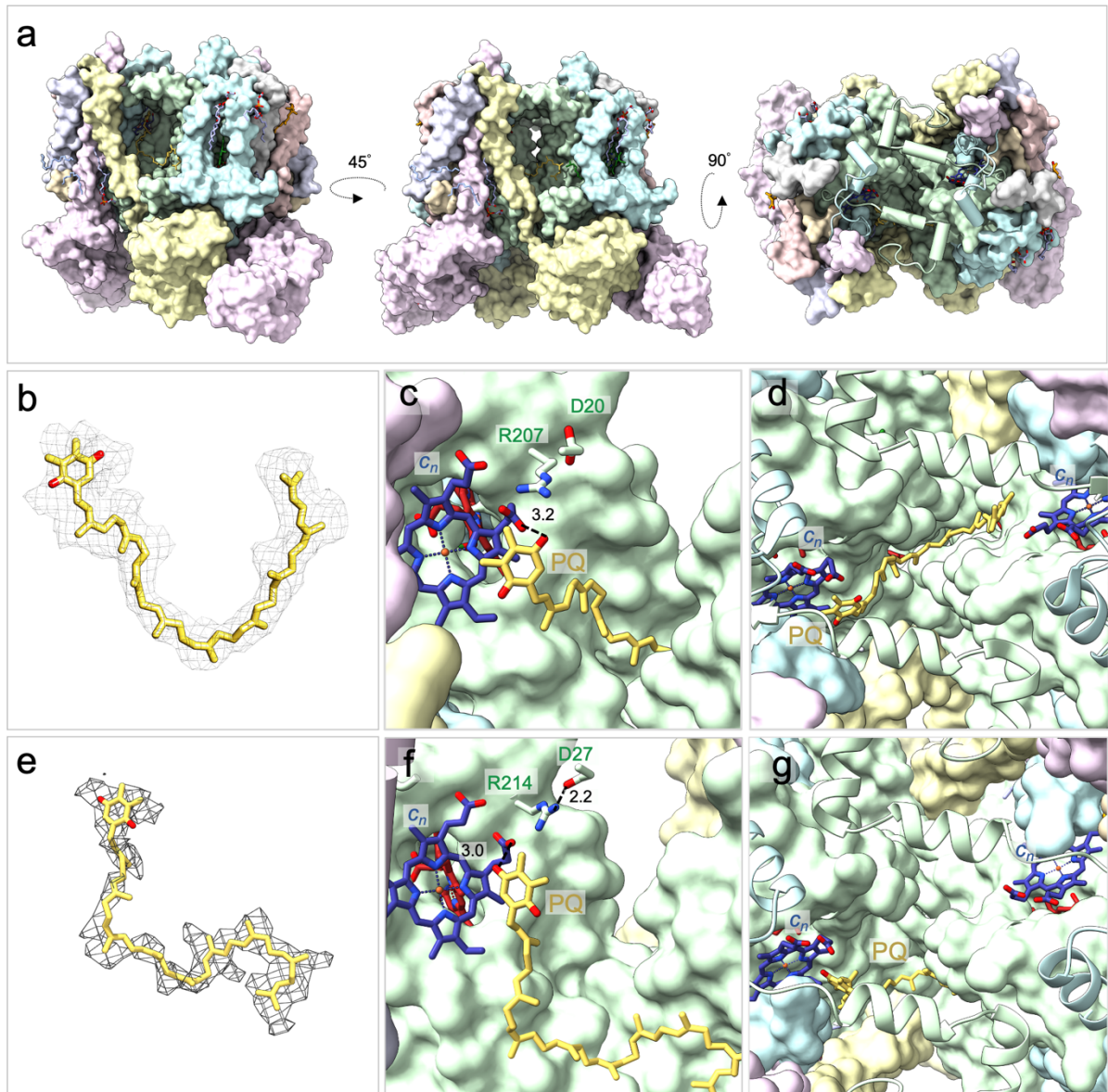


**Figure 5.20** | A native plastoquinone molecule is copurified in the *Synechocystis* sp. PCC 6803 (*petA-strep*) *cytb<sub>6</sub>f* complex. **a**, a surface representation of the *cytb<sub>6</sub>f* complex showing the intermonomer cavity from various angles. **b-d**, the Q<sub>n</sub> bound PQ molecule in *S. oleracea* showing density modelled as PQ shown as a grey mesh (**b**) and the position of the bound PQ in relation to the surrounding environment (**c-d**). **e-g**, the Q<sub>n</sub> bound PQ molecule in *Synechocystis* showing density modelled as PQ shown as a grey mesh (**e**) and the position of the bound PQ in relation to the surrounding environment (**f-g**). Subunits are coloured as in **Figure 5.17**, and cofactors and lipids coloured as in **Figure 5.18**.

In this scenario, competition between the two  $Q_n$  sites is decreased allowing electrons obtained from the  $Q_p$  site on either side of the dimer to be funnelled towards a singular occupied  $Q_n$  site via an electronic ‘bus-bar’ mechanism. In this manner, the rapid two electron reduction of PQ bound at the  $Q_n$  site may be facilitated increasing the overall efficiency of the Q-cycle. Additionally, the lifetime of unpaired electrons, which may give rise to ROS, is also minimised.

Interestingly, while we observe the binding of PQ at the  $Q_n$  site via the C6 propionate of haem  $c_n$  in *Synechocystis* (as in the *S. oleracea* structure), (**Figure 5.20**), the positioning of the tail of this PQ is substantially different to that observed in *S. oleracea* (**Figure 5.20**). While in latter, the tail straddles the channel between the two  $Q_n$  sites, comparative superimposition indicates that the tail in *Synechocystis* appears to be prevented from adopting the same position by the presence of Trp200. It is possible that the blocking mechanism we observe in *S. oleracea* may serve a role in plants and algae that is not necessary in cyanobacterial species. Possibly such a mechanism may have evolved to facilitate the rapid production of PQH<sub>2</sub> under oxidising conditions, e.g. low light. In contrast, cohabitation of *cyt<sub>b</sub>6/f* in cyanobacterial thylakoids with quinone reducing respiratory complexes (such as succinate dehydrogenase and NDH dehydrogenases) could negate the need for such adaptations by keeping the redox poise more reducing even under low light. Alternatively, the presence of PQ between the two  $Q_n$  sites could serve as part of another mechanism exclusive to higher plants and algae. Regardless, it would be interesting to explore this further through site directed mutagenesis in *C. reinhardtii* (i.e. Leu193 → Trp).

### 5.7.3 The plastoquinol oxidation ( $Q_p$ ) site and the high-potential electron transfer pathway.

As observed in the *S. oleracea* structure, the  $Q_p$  site is positioned on the p-side of the intermonomer cavity at the base of a narrow channel termed the ‘ $Q_p$  portal’. The architecture of both the bifurcated  $Q_p$  site and the entrance to the portal is well conserved as noted in the *S. oleracea* structural work, however it is worth noting that while two conformations of the Chl *a* tail were observed in the *S. oleracea* structure (**Malone et al., 2019**), only one is observed here. This single conformation corresponds to the ‘open’ conformation observed in previous cyanobacterial studies of the complex (**Baniulis et al., 2009; Hasan et al., 2014; Kurisu et al., 2003; Yu et al., 2009; Zhang et al., 2001, 2003**) (**Figure 5.21**).

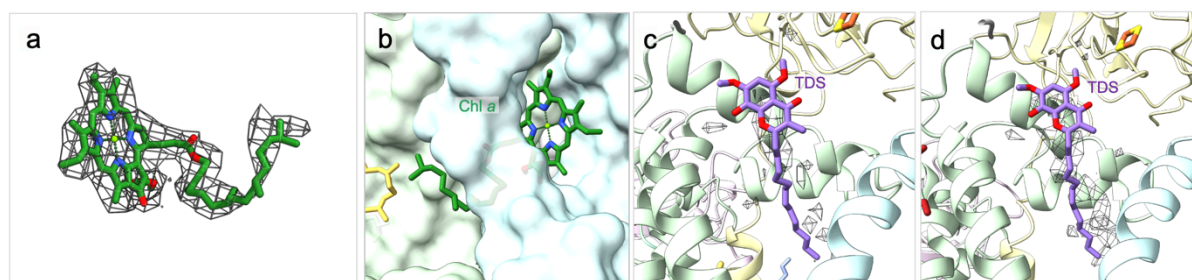


**Figure 5.21 | Conformations of the Chl *a* molecule at the plastoquinol oxidation ( $Q_p$ ) site.** a-b, the ‘open’ conformation of the Chl *a* tail, resolved in the *Synechocystis* sp. PCC 6803 (*petA-strep*) *cytb<sub>6</sub>f* structure showing the density (grey mesh) for the (a) and a surface representation of the protein surrounding the  $Q_p$  site (b). c-d, Weak density at within the  $Q_p$  site overlays well with superimposed TDS (PDB ID: 4H13 (Hasan et al., 2013b)) bound in the [2Fe-2S] proximal position. Figure 5.17, and cofactors and lipids coloured as in Figure 5.18. A protein-free map was created in COOT and using to identify ligand positions. Here the region of the protein-free map corresponding to the  $Q_p$  site is displayed. For clarity, the map is restricted to include only regions within 3 Å of the superimposed TDS molecule. Contour levels of the density maps were adjusted to 0.242. Figure 5.17, and cofactors and lipids coloured as in Figure 5.18.

As observed in previous native structures of *cytb<sub>6</sub>f* (PDB IDs: 4OGQ, 1VF5, 2D2C, 2E74, 2E75, 2ZT9, 4HO1, 4H44, 4PV1, 6RQF) (Baniulis et al., 2009; Hasan and Cramer, 2014a; Hasan et al., 2013b, 2013a, 2014; Kurisu et al., 2003; Malone et al., 2019; Stroebel et al., 2003; Yamashita et al., 2007; Yan et al., 2006), the  $Q_p$  site appears to be largely unoccupied, although there is some weak density within the  $Q_p$  site on either side of the dimer which could correspond to native copurified substrate. In contrast to the clear density assigned to PQ at the  $Q_n$  site, this latter density is much weaker and cannot be unambiguously assigned as PQ however structural superimposition with the *M. lamosus* structure with bound tridecylstigmatellin (TDS) (PDB ID: 4H13) (Hasan et al., 2013b) indicates that it overlays extremely well with the position expected for PQH<sub>2</sub> bound in the 2Fe-2S proximal lobe of the  $Q_p$  site (Figure 5.21).

In line with the  $Q_p$  site being predominantly unoccupied, the Rieske ISP appears to exhibit an ‘intermediate’ conformation relative to the catalytic ‘*b*’ ( $Q_p$  proximal) and ‘*c*’ (proximal to *c*-type haem acceptor) states observed in *cytb<sub>c</sub>1* (Esser et al., 2004; Iwata et al., 1998; Kim et al., 1998; Zhang et al., 1998). In this position, the 2Fe-2S cluster is shifted by ~ 4 Å away from



the 'b' position (approximated by superimposition with the TDS-containing structure, PDB ID 4H13) but is still  $\sim 25.2$  Å from haem *f* (cyt*f*) (**Figure 5.22**). Interestingly, while the position of the [2Fe-2S] cluster appears to be largely unchanged ( $\sim 2$  Å difference) between the *S. oleracea* and *Synechocystis* structures, the position of haem *f* (cyt*f* subunit) appears to exhibit some slight variation. While the extent of this apparent shift is only  $\sim 3.5$  Å between the *S. oleracea* and *Synechocystis* structures, it has been suggested previously that movement in the cyt*f* subunit could, in part, bridge the substantial gap along the high-potential electron transfer chain (**Figure 5.22**). This possibility will be explored further in **chapter 6**.

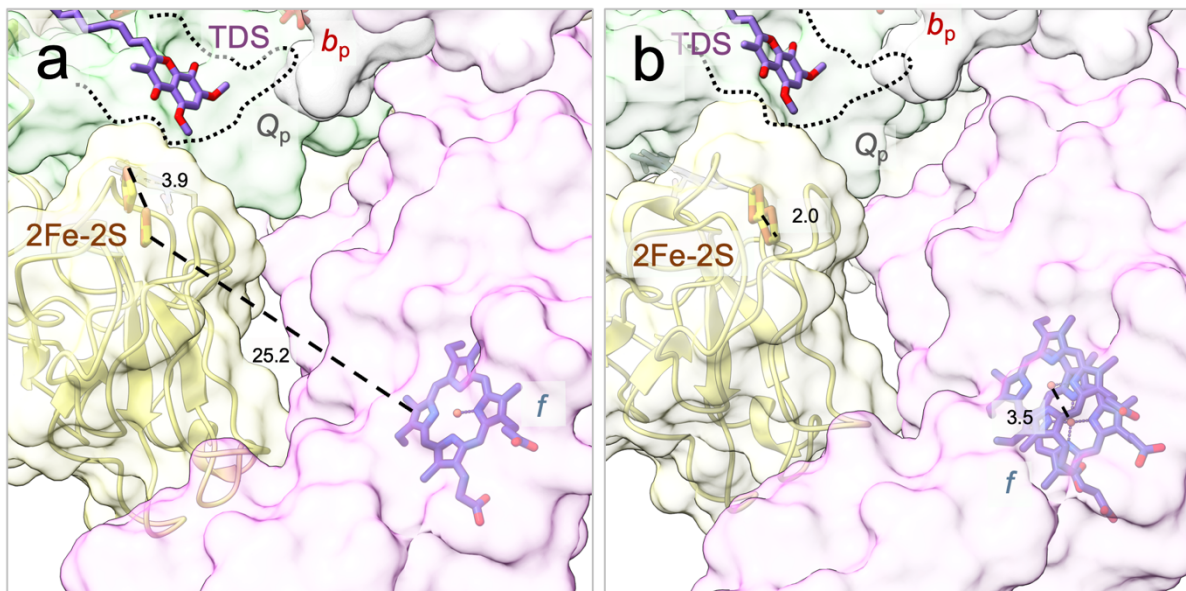


**Figure 5.22 | Conformational differences within the extrinsic domains of the ISP and cyt*f*.** A close up view of the ISP and cyt*f* in cyt<sub>6*f*</sub> showing **a**, the positions of the 2Fe-2S cluster in the structures from *M. laminosus* with TDS bound at the Q<sub>p</sub> site (PDB ID: 4H13 (**Hasan et al., 2013b**)) and *Synechocystis* and **b**, the positions of haem *f* structures from *Synechocystis* and *S. oleracea* (PDB ID: 6RQF (**Malone et al., 2019**)). Distances are indicated by a black dashed line with the distance indicated below in (Å). Prosthetic groups are shown in stick representation beneath a transparent protein surface. An outline of the Q<sub>p</sub> site is also indicated by a grey dotted line with TDS (purple) from 4H13 superimposed. Subunits are coloured as in **Figure 5.17**, and cofactors and lipids coloured as in **Figure 5.18**.

## 5.8 Conclusion

Where the structure of the *cytb<sub>6</sub>f* complex from *S. oleracea* presented in **chapter 4** provides key insights into the internal mechanics of the Q-cycle, the work presented in this chapter provides the means to further explore these findings through mutagenesis.

In addition to providing an excellent platform for mutagenesis studies, the structure of the *Synechocystis cytb<sub>6</sub>f* also provides further insights into the internal mechanics of the complex. Indeed, as in *S. oleracea*, PQ appears to be bound at the Q<sub>n</sub> site via the C6 propionate of haem *c<sub>n</sub>*; while in *S. oleracea*, PQ binding in one half of the complex appears to occlude binding in the opposite Q<sub>n</sub> site, it is interesting to note that the binding in *Synechocystis* does not appear to influence binding in the opposite monomer. Indeed, a conformation of PQ which spans the narrow channel between both dimers (as in *S. oleracea*) appears to be facilitated by a significantly deeper channel than that observed in *Synechocystis*. While other cyanobacterial structures appear to show similarly shallow intermonomer channels uncondusive to PQ access, the *cytb<sub>6</sub>f* complex of *C. reinhardtii* appears to possess a channel of a similar size to that observed in higher plants. It is possible that these differences in the intermonomer channel (and indeed the relationship between the Q<sub>n</sub> sites in either half of the dimeric structure) might represent an evolutionary difference between the prokaryotic and eukaryotic *cytb<sub>6</sub>f* complexes. This hypothesis remains to be further explored through mutagenesis studies.

## 6 Results: Rieske head domain dynamics

### 6.1 Introduction

As discussed in **section 1.3.4**, in both *cytbc<sub>1</sub>* and *cytb<sub>6f</sub>*, access to and from the Q<sub>p</sub> site is provided by a long, narrow, hydrophobic portal. At the base of this portal in both complexes is a bifurcated volume, the two lobes of which extend respectively towards either the [2Fe-2S] cluster or haem *b<sub>p</sub>* (**Figure 6.1**). In *cytbc<sub>1</sub>*, it has been observed that different positions within the bifurcated Q<sub>p</sub> site are preferentially occupied by different classes of quinone analogue inhibitors in a mutually exclusive manner (**Crofts et al., 1999; Esser et al., 2004; Kim et al., 1998; Zhang et al., 1998**). Specifically, molecules that mimic the structural state of ubiquinol (UQH<sub>2</sub>) (class I inhibitors: stigmatellin and 5-*n*-undecyl-6-hydroxy-4,7-dioxobenzothiaole) are observed to occupy the 2Fe-2S-proximal lobe (**Figure 6.1**) while molecules which mimic the structural state of semiquinone (class II inhibitors: myxothiazole and β-methoxyacrylatestilbene; (MOAS)-type inhibitors) occupy the haem *b<sub>p</sub>* proximal lobe (**Figure 6.1**). It is expected that such a conformational shift of the semiquinone species between the 2Fe-2S-proximal and haem *b<sub>p</sub>*-proximal lobes promotes rapid electron transfer from the semiquinone to haem *b<sub>p</sub>*; this reduces the lifetime of the reactive semiquinone and reduces the risk of potentially damaging side reactions with O<sub>2</sub> (**Crofts et al., 1999**).

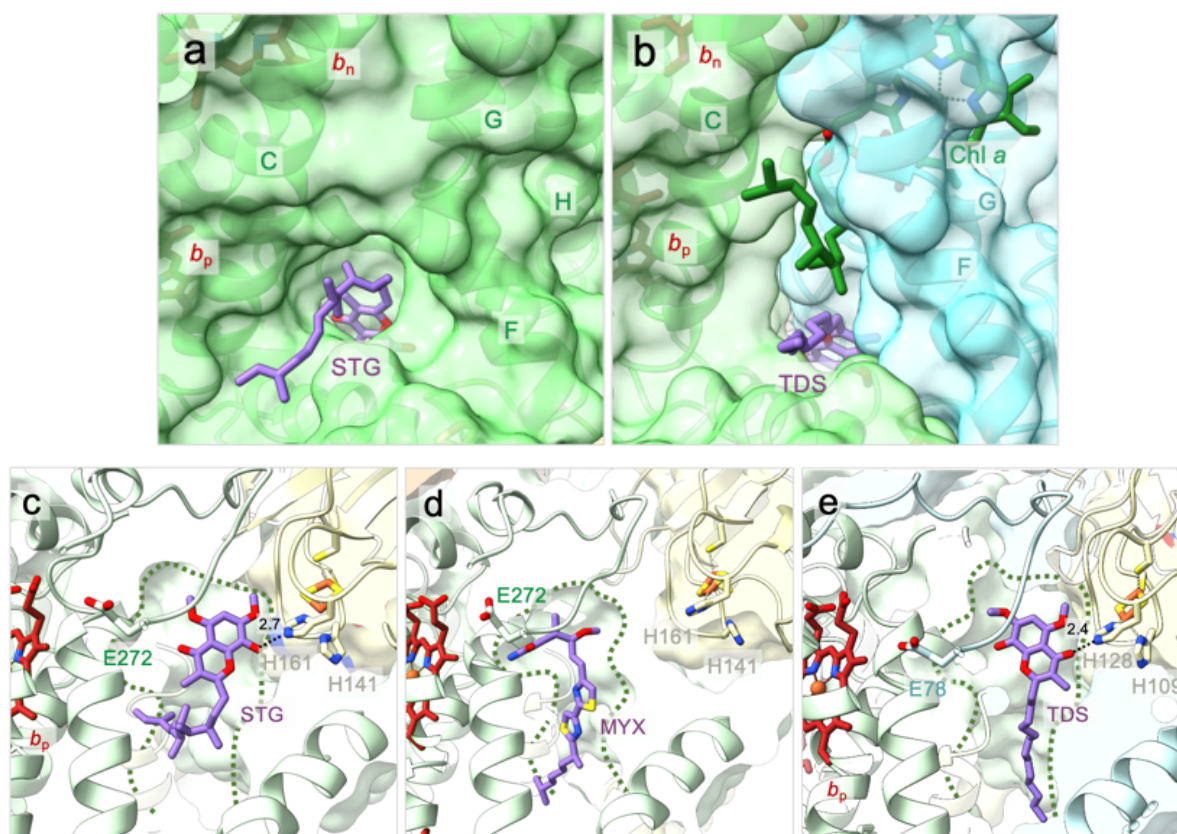


**Figure 6.1 | The Q<sub>p</sub> sites of *cytb<sub>c1</sub>* and *cytb<sub>6f</sub>*.** **a-b**, a surface view of the Q<sub>p</sub> site in the *cytb<sub>c1</sub>* complex from *G. gallus* (**a**, 3BCC (**Zhang et al., 1998**)) and the *cytb<sub>6f</sub>* complex from *Mastigocladus laminosus* (**b**, 4H13 (**Hasan et al., 2013b**)). In both complexes, the Q<sub>p</sub> site is defined by TM helices ‘C’ and ‘G’ (shown as ribbons); additionally, in both complexes the site is occupied by quinone analogue inhibitors (stigmatellin in *cytb<sub>c1</sub>* and tridecylstigmatellin in *cytb<sub>6f</sub>*). **c-e**, A cartoon representation of the bifurcated volume observed in the Q<sub>p</sub> site of *cytb<sub>c1</sub>* (**c**, PDB ID: 3BCC (**Zhang et al., 1998**) and **d**, PDB ID: 1SQP (**Esser et al., 2004**)) and *cytb<sub>6f</sub>* (**e**, PDB ID: 4H13 (**Hasan et al., 2013b**)). Error! Reference source not found., and cofactors and lipids coloured as in Error! Reference source not found., plastoquinone is coloured in yellow and is labelled ‘PQ’, quinone analogue inhibitors are shown in purple and are labelled ‘STG’, ‘MYX’ and ‘TDS’ respectively. An outline of the Q<sub>p</sub> site is also indicated by a green dotted line.

It is further observed that differential binding of quinone analogue inhibitors appears to coincide with different conformational states of the Rieske head domain (**Figure 6.2**) (**Table 6.1**). Specifically, the binding of class I inhibitors in the 2Fe-2S-proximal lobe results in the formation of a hydrogen bond with one of the residues that ligates the [2Fe-2S] cluster (His161) (**Figure 6.2**) stabilising the Rieske head domain in a position proximal to the Q<sub>p</sub> site (‘b’ position) (PDB IDs: 3BCC, 1SQX). This position promotes both deprotonation of the

substrate via His161 and enables rapid electron transfer to the [2Fe-2S] cluster (**Esser et al., 2004; Kim et al., 1998; Zhang et al., 1998**).

Conversely, when class II inhibitors that mimic semiquinone are bound within the haem  $b_p$  proximal lobe of the  $Q_p$  site or the site is empty, the conformation of the Rieske ISP head domain appears to shift to a largely mobile state. This conformational switch disconnects the 2Fe-2S cluster from the  $Q_p$  site (thus reducing the likelihood of unproductive back reactions) and brings the 2Fe-2S cluster closer to the  $c$ -type haem of  $cytc_1$  (**Crofts et al., 1999; Esser et al., 2004; Kim et al., 1998**). While a number of intermediate positions are observed in this mobile state (PDB IDs: 1SQQ, 1SQP) (**Figure 6.2**), it is likely that electron transfer is facilitated by the stabilising of the Rieske ISP head in a position proximal to the haem  $c_1$  (' $c'$ ' position) (PDB IDs: 1BCC, 1BE3) (**Figure 6.2**) (**Iwata et al., 1998; Zhang et al., 1998**).

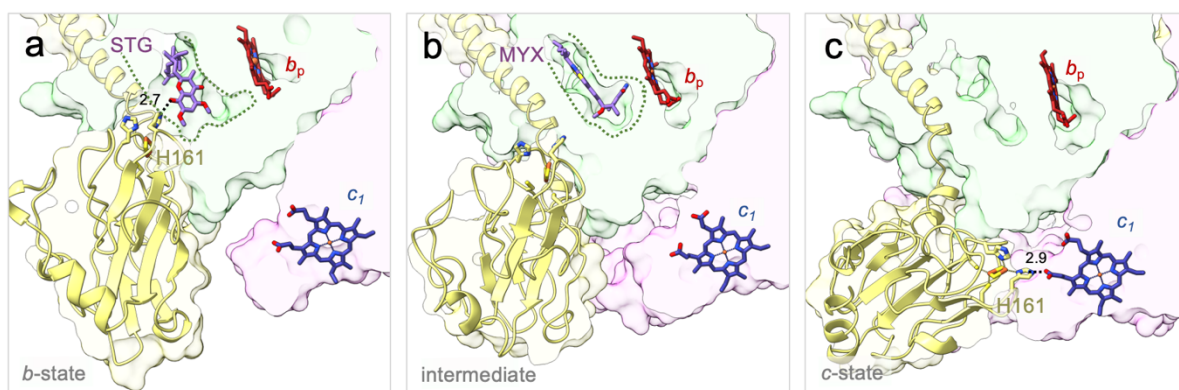


**Figure 6.2 | Conformational changes occurring within the extrinsic domains of the ISP in  $cytb_{c1}$ .** A close up view of the ISP and  $cytc$  in  $cytb_{c1}$  showing the positions of the 2Fe-2S cluster in **a**, the structures from *G. gallus* with STG bound at the  $Q_p$  site (PDB ID: 3BCC (**Zhang et al., 1998**)) **b**, the structures from *B. taurus* with MYX bound at the  $Q_p$  site (PDB ID: 1SQP (**Esser et al., 2004**)) and **c**, the native structures from *B. taurus* (PDB ID: 1BE3 (**Iwata et al., 1998**)). Distances are indicated by a black dashed line with the distance indicated below in (Å). Prosthetic groups are shown in stick representation beneath a transparent protein surface. An outline of the  $Q_p$  site is also indicated by a green dotted line. Subunits are coloured as in Error! Reference source not found., and cofactors and lipids coloured as in Error! Reference source not found..

**Table 6.1| A comparison of edge-to-edge cofactor distances (Å) in each half of  $bc_1$  from various species with and without  $Q_p$  inhibitors.** Models used include native structures (PDB IDs: 1BCC (Zhang et al., 1998) and 1BE3 (Iwata et al., 1998)), structures with class I inhibitors (PDB IDs: 3BCC (Zhang et al., 1998) and 1SQX (Esser et al., 2004)) and structures with class II  $Q_p$  inhibitors bound (PDB IDs: 1SQQ and 1SQP (Esser et al., 2004)). <sup>a</sup> Inhibitors are indicated by the abbreviations STG (stigmatellin), MOAS (Methoxy Acrylate Stilbene) and MYX (myxothiazol).

PDB ID	1BCC	1BE3	3BCC	1SQX	1SQQ	1SQP
<b>Source</b>	<i>G. gallus</i>	<i>B. taurus</i>	<i>G. gallus</i>	<i>B. taurus</i>	<i>B. taurus</i>	<i>B. taurus</i>
<b>Resolution (Å)</b>	3.2	3.0	3.7	2.6	3.0	2.7
<b><math>Q_p</math> Inhibitor<sup>a</sup></b>						
Class I	-	-	STG	STG	-	-
Class II	-	-	-	-	MOAS	MYX
<b>Distances (Å)</b>						
$b_p$ - [2Fe-2S]	30.3, 30.3	30.3, 30.2	23.0, 23.1	22.5, 22.4	24.8, 24.8	24.9, 24.9
Inhibitor- [2Fe-2S]	-	-	7.2, 7.4	8.0, 8.0	12.0, 12.0	13.0, 13.0
[2Fe-2S] - $c_1$	16.8, 16.8	10.9, 10.9	27.2, 27.3	27.3, 27.3	26.9, 26.6	27.1, 27.1
Inhibitor - $b_p$	-	-	12.5, 12.9	12.7, 12.7	7.1, 7.1	6.3, 6.3
$b_p$ - $b_p$	14.4	14.1	14.5	13.8	13.7	13.3
$b_n$ - $b_p$	12.4, 12.4	11.9, 11.9	12.3, 12.3	12.1, 12.1	12.2, 12.2	12.1, 12.1



Based on the structural similarities between the two complexes and the homology between their ISP subunits, it is expected that a conformational change similar to that observed in the  $bc_1$  complex is required to mediate electron transfer along the high potential pathway in  $cytb_6f$ .

A number of lines of evidence support this notion, including:

- 1) Sequence alignments of the  $b_6f$  and  $bc_1$  ISP indicating the highly flexible 'hinge region' is conserved in  $b_6f$  complexes (**Yan and Cramer, 2003**)
- 2) Evidence from EPR studies which suggests the [2Fe-2S] cluster adopts different orientations in the presence of quinol analogue inhibitors (2,5-dibromo-3-methyl-6-isopropylbenzoquinone, DBMIB) (**Schoepp et al., 1999**)
- 3) Flash-induced kinetics experiments showing the inhibitory effect of increased luminal viscosity on the rate of reduction of cytochromes ( $cytf$  and  $cytb_6$ ) in thylakoid membranes (**Heimann et al., 2000**)
- 4) *In vitro* electron transfer experiments between the [2Fe-2S] cluster of the Rieske ISP and the *c*-type haem of  $cytf$  (**Soriano et al., 2002**)
- 5) 2D crystals and negative stain studies that indicate a conformational change in the extrinsic domains of the  $b_6f$  complex occurs upon binding of stigmatellin (**Breyton, 2000**)

Despite these numerous studies, the topic of conformational flexibility in the ISP of the  $b_6f$  complex remains a subject of much debate and structural evidence of ISP movements in the  $b_6f$  complex remains limited. In contrast to  $bc_1$  where absence or addition of class II quinone analogue inhibitors induces an extensive conformational change in the soluble ISP head domain, no such response in the  $cytb_6f$  complex has been observed. Additionally, while mutagenesis of the hinge region in  $bc_1$  has significant detrimental effects on the electron transfer activity, it has been observed that changing the flexibility and/or length of the hinge region in  $b_6f$  has little effect on its electron transfer functions. Indeed, the poly-glycine hinge in  $b_6f$  can be mutated to become more flexible, more rigid or up to 4 residues longer with no significant effect on electron transfer activity (**Yan and Cramer, 2003**). In comparison to the extreme sensitivity of  $bc_1$  to structural changes in this region, this observation implies either that the ISP motion in  $b_6f$  occurs on a much smaller scale than in  $bc_1$  or that a significant difference in the mechanism of electron shuttling exists between the two complexes.

Analysis of the structures of  $b_6f$  from various species with and without inhibitors (**Table 6.2**) (**Figure 6.3**) indicates some conformational flexibility of the ISP head domain; as in  $bc_1$  this appears to be dependent on the state of occupation of the  $Q_p$  site.

**Table 6.2** | A comparison of edge-to-edge cofactor distances (Å) in each half of the  $b_6f$  dimer from different species with and without  $Q_p$  inhibitors. Models used include native structures (PDB IDs: 2E74 (Yamashita et al., 2007) and 4OGQ (Hasan et al., 2013b)) and structures with class I inhibitors bound (PDB IDs: 1Q90 (Stroebel et al., 2003) and 4H13 (Hasan et al., 2013b)).<sup>a</sup> Inhibitor is indicated by the abbreviation TDS (tridecylstigmatellin).

PDB ID	1Q90	4H13	2E74	4OGQ
<b>Source</b>	<i>C. reinhardtii</i>	<i>M. laminosus</i>	<i>M. laminosus</i>	<i>Nostoc</i>
<b>Resolution (Å)</b>	3.1	3.07	3.0	2.5
<b><math>Q_p</math> Inhibitor <sup>a</sup></b>				
Class I	TDS	TDS	-	-
Class II	-	-	-	-
<b>Distances (Å)</b>				
$b_p$ - [2Fe-2S]	22.9, 22.9	22.7, 22.7	25.5, 25.5	25.3, 25.3
Inhibitor- [2Fe-2S]	7.6, 7.6	7.1, 7.1	-	-
[2Fe-2S] - $f$	27.8, 27.8	28.1, 28.1	26.2, 26.2	26.2, 26.2
Inhibitor - $b_p$	12.9, 12.9	13.2, 13.2	-	-
$b_n$ - $c_n$	4.7, 4.7	4.7, 4.7	4.7, 4.7	4.6, 4.6
$b_n$ - $b_p$	12.2, 12.2	12.5, 12.5	12.2, 12.2	12.1, 12.1
$b_p$ - $b_p$	15.1	15.3	15.2	15.3



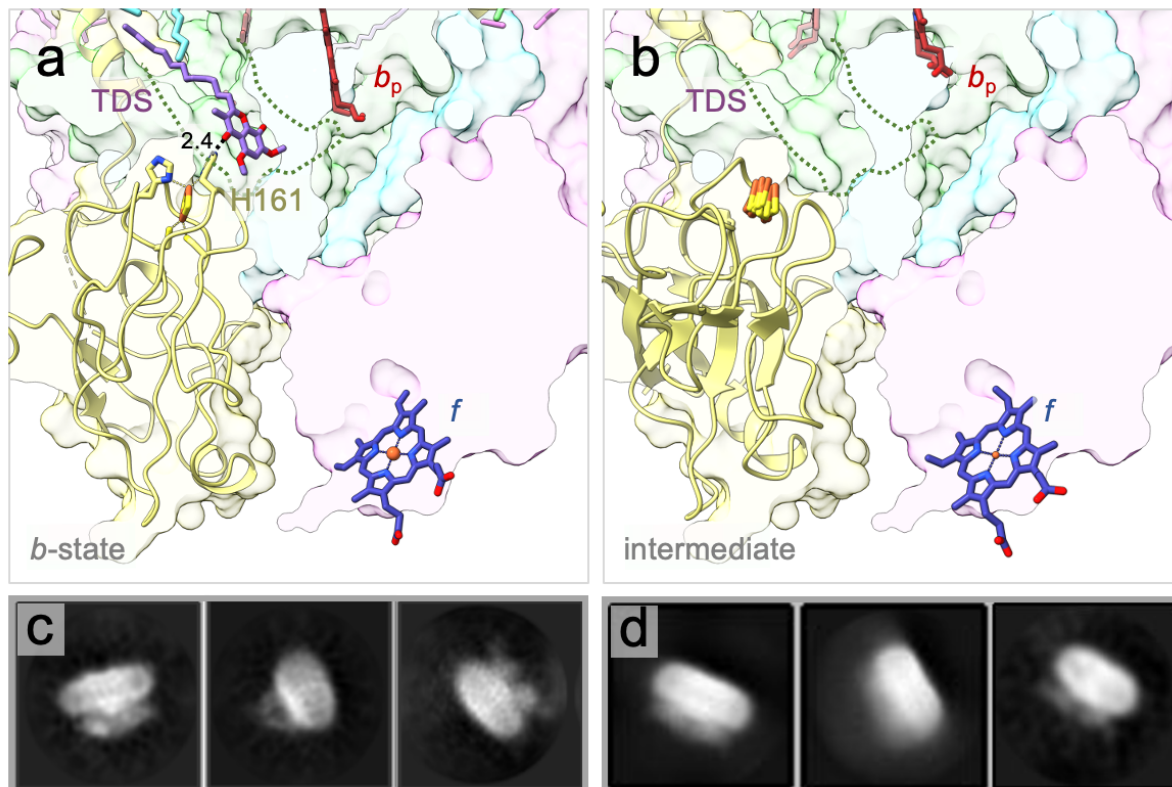


**Figure 6.3 | Evidence for conformational changes occurring within the extrinsic domains of the ISP in *cytb6f*.** **a-b**, A close up view of the ISP and *cytf* in *cytb6f* showing the positions of the 2Fe-2S cluster in **a**, the structure from *M. laminosus* with TDS bound at the  $Q_p$  site (PDB ID: 4H13 (Hasan et al., 2013b)) and **b**, structures of the native complex from various cyanobacterial (PDB ID: 1VF5 (Kurusu et al., 2003), 2E74 (Yamashita et al., 2007), 2D2C (Yan et al., 2006), 4PV1 (Hasan et al., 2014), 2E75 (Yamashita et al., 2007), 4H0L (Hasan et al., 2013b), 4I7Z (Hasan et al., 2013a), 2ZT9 (Baniulis et al., 2009), 4H44 (Hasan et al., 2013b), 4OGQ (Hasan et al., 2013b)) and plant (PDB ID: 6RQF (Malone et al., 2019a)) species. **c-d**, 2D classes which displayed potential conformational flexibility within the luminal domains in the *Synechocystis* (c) and *S. oleracea* (d) datasets. Subunits are coloured as in Error! Reference source not found., and cofactors and lipids coloured as in Error! Reference source not found.. An outline of the  $Q_p$  site is indicated by a green dotted line with the 'TDS' molecule coloured purple.

While structures containing class I inhibitors (tridecylstigmatellin, TDS) appear to exhibit a fixed  $Q_p$  proximal conformation equivalent to the 'b' position observed in *cytb<sub>c1</sub>*, the absence of  $Q_p$  inhibitors appears to expel the ISP head from this position and shift it to a more mobile state. While in *cytb<sub>c1</sub>*, a number of structures capture the broad range of motion exhibited by the ISP head (from the fixed 'b' position to the 'c' position and multiple intermediate positions between), in *cytb<sub>6f</sub>* structural observations appear to be limited to 'intermediate' positions (Table 6.2) (Figure 6.3) (Baniulis et al., 2009; Hasan and Cramer, 2014; Hasan et al., 2013a, 2013b, 2014; Kurisu et al., 2003; Stroebel et al., 2003; Yamashita et al., 2007; Yan et al., 2006).

It is possible that mobility of the ISP head has been limited by crystal contacts in the various crystallographic studies of the *cytb<sub>6f</sub>* complex; alternatively, it has been suggested that the distance between the [2Fe-2S] and the *c*-type haem of *cyt<sub>f</sub>* may be bridged by another means such as a conformational change within the *cyt<sub>f</sub>* subunit (Hasan and Cramer, 2012; Stroebel et al., 2003; Yamashita et al., 2007).

Cryo-EM of the native *cytb<sub>6f</sub>* complex provides a new opportunity to observe the conformational changes of the Rieske ISP head group in the absence of potential factors which may limit mobility.

## 6.2 Indications of motion in the *S. oleracea* and *Synechocystis* datasets

Purification protocols undertaken in this study have been designed to yield intact and active preparations of dimeric *cytb<sub>6f</sub>*. In both *S. oleracea* and *Synechocystis* sp. PCC 6803, purification yields highly active preparations of native complex with turnover rates of  $\sim 200 \text{ e}^- \text{ s}^{-1}$ . Both preparations are found to contain some copurified native PQ/PQH<sub>2</sub> as indicated by structural analysis which could potentially facilitate catalytic turnover under the right conditions. While both cryo-EM structures appear to have PQ/PQH<sub>2</sub> bound on the n-side of the complex at the  $Q_n$  site, neither of the final maps show any strong density within the  $Q_p$  site which could be attributed unequivocally to substrate (the *Synechocystis* map does show some density in the region expected for PQ bound in the [2Fe-2S]-proximal lobe however this density is too weak to be assigned unambiguously as PQ). In both structures, it is further observed that the ISP

head domain appears to be found in an intermediate position between the 'b' and 'c' positions as observed in inhibitor-free structures of *cytb<sub>6f</sub>* from other species (**Table 6.3**).

Analysis of the 2D classes in both data sets indicates some blurring of density on the p-side of the complex which could correspond to motion in the ISP head domain, this is particularly apparent in side-on profiles of the complexes (**Figure 6.3**). In several of the 2D classes from this dataset, there appear to be additional, weaker densities on the p-side of the complex, these could correspond to alternate and substantially less populated conformations of the p-side extrinsic subunits. It is particularly interesting to note that in the various 2D classes analysed, it appears that both the ISP head and *cyt<sub>f</sub>* may exhibit some degree of conformational flexibility. While a continuum of potential conformations may be present in the dataset, it is likely that lesser populated conformational substates may be averaged out during high resolution 3D reconstruction in RELION.

**Table 6.3 | A comparison of edge-to-edge cofactor distances (Å) in each half of the  $b_6f$  dimer from *S. oleracea*, *Synechocystis* sp. PCC 6803 in relation *M. laminosus* with and without  $Q_p$  inhibitors. Models used include native structures from *S. oleracea* (PDB ID: 6RQF (Malone et al., 2019a)), *Synechocystis* sp. PCC 6803 (PDB ID: 7PPW) and *M. laminosus* (PDB ID: 2E74 (Hasan et al., 2013b)) and structures with class I inhibitors bound (PDB ID: 4H13 (Hasan et al., 2013b)). <sup>a</sup> Inhibitor is indicated by the abbreviation TDS (tridecylstigmatellin).**

PDB ID	6RQF	7PPW	2E74	4H13
<b>Source</b>	<i>S. oleracea</i>	<i>Synechocystis</i>	<i>M. laminosus</i>	<i>M. laminosus</i>
<b>Resolution (Å)</b>	3.6	2.98	3.0	3.07
<b><math>Q_p</math> Inhibitor <sup>a</sup></b>				
Class I	-	-	-	TDS
Class II	-	-	-	-
<b>Distances (Å)</b>				
$b_p$ - [2Fe-2S]	25.1, 25.1	24.6, 24.7	25.5, 25.5	22.7, 22.7
Inhibitor- [2Fe-2S]	-	-	-	7.1, 7.1
[2Fe-2S] - $f$	27.1, 26.8	25.2, 25.2	26.2, 26.2	28.1, 28.1
Inhibitor - $b_p$	-	-	-	13.2, 13.2
$b_n$ - $c_n$	4.9, 4.9	4.6, 4.7	4.7, 4.7	4.7, 4.7
$b_n$ - $b_p$	12.1, 12.1	11.9, 11.9	12.2, 12.2	12.5, 12.5
$b_p$ - $b_p$	15.3	14.8	15.2	15.3

Like many existing methods, 3D reconstruction in RELION makes use of the standard cryo-EM image formation model (**Frank, 2007; Scheres, 2012a; Scheres et al., 2007**) (**Equation 8**). Here it is assumed that each 2D particle image ( $X_i$ ) is a projection ( $P$ ) of a single homogenous 3D density ( $V$ ) from a particular observed orientation ( $\phi_i$ ) plus noise ( $\eta$ ). Accordingly, each projection is also ‘corrupted’ by a number of factors which can cumulatively be described by a contrast transfer function ( $C_i$ ).

$$X_i = C_i P_{(\phi_i)} V + \eta \quad (9)$$

For 3D classification to resolve discrete heterogeneity in a sample, this model can be extended (**Scheres, 2012b, 2016; Scheres et al., 2007; Zhang, 2016**) to assume each particle is a projection from one of several distinct and independent 3D densities.

Whilst methods such as these excel at resolving static structures of proteins to a high resolution where large populations of distinct conformational substates are expected (e.g. through use of inhibitors or by other means to capture a substate such as time-resolved plunge freezing), these methods are unable to resolve the full range of continuous flexible motion that underlie the mechanistic function of many protein complexes.

An alternative technique known as ‘3D variability analysis’ (3DVA) (**Punjani and Fleet, 2021a**) has been developed that allows the resolution and visualisation of continuous conformational motion and flexibility that may be present in many single particle cryo-EM samples.

Unlike conventional 3D classification methods, 3DVA utilises Principal Component Analysis (PCA) (**Punjani and Fleet, 2021b; Tipping and Bishop, 1999**) to generate a continuous set of 3D reconstructions which capture all possible conformations within the data set in multi-dimensional space.

### 6.3 3D variability analysis of the *Synechocystis* cytb<sub>6</sub>f dataset

Following the selection of a suitably homogenous 3D class in RELION (described in **section 5.5.6**), the subset of extracted particles corresponding to this class (413,442 particles, ~ 10.2 %) were rescaled to their full resolution and exported to cryoSPARC (v 3.2.0). It is worth noting that for the *Synechocystis* dataset, the final map was inverted following processing in RELION

to correct the handedness for modelling; this was done using the `--invert_hand` command in `relion_image_handler`.

To ensure the correct handedness in subsequent 3DVA analysis, imported particles were realigned in cryoSPARC using the inverted postprocessed map (low pass filtered to 30 Å) as a reference for alignment. Subsequent aligned particles together with various masks were used to compute variability components using the 3DVA subroutine in cryoSPARC.

### 6.3.1 3DVA using a full mask

Initially, a full mask was used for 3DVA; this incorporated the detergent shell surrounding the transmembrane portion of the complex but excluded surrounding solvent. The mask was created in RELION (v 3.1) using an inverted 3D map with an initial binarization threshold set to 0.0141; the map was low pass filtered to 15 Å for mask calculation then a soft edge of 6 pixels was added.

In this first instance of 3DVA, results were low pass filtered to 5 Å (i.e. eigenvectors of 3D covariance are filtered to 5 Å) to reduce the influence of high-resolution noise and the number of principal components to solve was set to 3. As observed during 3DVA analysis of the *cytbc<sub>1</sub>* complex by **Maldonado et al., 2020**, the inclusion of the detergent belt within the mask appeared to result largely in non-specific conformational heterogeneity within this belt (**Figure 6.4a**). In addition to this non-specific heterogeneity, the *cytb<sub>6f</sub>* complex also appeared to exhibit some global variation in the polypeptide regions of the map (**Figure 6.4b-c**).

While the low-pass filter precludes the observation of variability on the level of particular side chains, it does allow us to observe changes at the level of the secondary structure as well as cofactors with strong, well-defined densities such as the macrocycle rings of haems and Chl *a*.

Global motion appears to be anti-parallel across the dimer (i.e. when monomer A is in global conformation 1, the monomer B is in global conformation 2 and vice versa) possibly indicating that the two monomeric units function in an anti-cooperative, alternating manner.

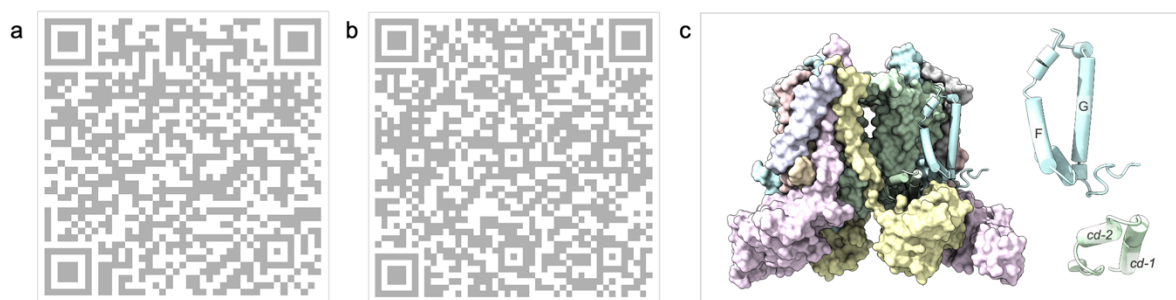


**Figure 6.4** | Videos showing the 3D-variability analysis (3DVA) of the *Synechocystis* sp. PCC 6803 (*petA-strep*) *cytb<sub>6f</sub>* using a full mask. **a-b**, Conformational heterogeneity in the *cytb<sub>6f</sub>* cryo-EM map viewed from the plane of the membrane. The contour level of the map was adjusted to 0.40 (a) and 0.69 (b). **c**, a surface view of the *Synechocystis cytb<sub>6f</sub>* complex with areas of interest shown in cartoon representation for reference.

While there appears to be motion within all of the subunits in the *cytb<sub>6f</sub>* complex, some specific areas are of particular interest. The first area lies within the region of the map corresponding to helices F and G of subIV (**Figure 6.4b-c**). As discussed in **section 4.5**, it is possible that motion within these two helices could be involved in a signalling pathway for the activation of the LHCII kinase (STN7) required for the regulation of state transitions in higher plants (**Hasan et al., 2013c**).

The second area of interest is in the region of the map corresponding to the extrinsic domains of both the ISP and *cyt<sub>f</sub>*; it is interesting to note that movement in the extrinsic domains appears to be accompanied by a prominent flexing motion in the *cd-1* and *cd-2* helices of *cytb<sub>6</sub>* (**Figure 6.4b-c**). Indeed, similar motions within the *cd-1* and *cd-2* helices of the homologous *cytbc<sub>1</sub>* complex have been suggested to either increase or decrease affinity for the ISP in a manner dependent on the occupation of the Q<sub>p</sub> site (**Esser et al., 2006**). While in structures with bound class I inhibitors (e.g. stigmatellin and 5-*n*-undecyl-6-hydroxy-4,7-dioxobenzothiaole), the *cd-1* helix is positioned in a manner exhibiting surface complementarity with the ISP, in structures containing class II inhibitors (e.g. myxothiazole and  $\beta$ -methoxyacrylatestilbene; (MOAS)-type inhibitors), the *cd-1* helix appears to be shifted by  $\sim 1$  Å. In combination with the inhibitor dependent H-bonding pattern discussed in **section 6.1**, it appears that this inhibitor-dependent affinity alteration could form the basis of a control mechanism underlying the conformation switch in the ISP head domain in *cytbc<sub>1</sub>*

(Esser et al., 2006). The observation of similar motions in the *cd-1/cd-2* helices in the *cytb<sub>6f</sub>* complex that we observe here further reinforces the similarity between the catalytic mechanism of *cytb<sub>6f</sub>* and *cytbc<sub>1</sub>*, suggesting that similar mechanisms exist in *cytb<sub>6f</sub>* to control the motion of the ISP.

### 6.3.2 3DVA using a mask focussed on the extrinsic luminal portion of the map

To further analyse the conformational heterogeneity in the p-side extrinsic domains of *cytb<sub>6f</sub>*, a second 3DVA experiment was undertaken using a mask focussed around the p-side extrinsic domains of *cytb<sub>6f</sub>*. The solvent-free mask was created as before in RELION v 3.1 using an inverted 3D map with an initial binarisation threshold set to 0.0141; the map was low pass filtered to 15 Å for mask calculation then a soft edge of 6 pixels was added. Examination of this mask in chimera indicates that the mask bounds are sufficient to encompass motion in the p-side extrinsic domains on the same scale as that observed in *cytbc<sub>1</sub>*.

To focus the mask around just the p-side extrinsic domains of the complex, the regions of the volume corresponding to the TM helices, the detergent micelle and the n-side extrinsic regions were manually erased using the 'map eraser tool' in Chimera X v 1.1.1.

In this second instance of 3DVA, results were again low pass filtered to 5 Å and the number of principal components to solve was set to 3. Upon examination of the results, the largest variability component revealed a distinct 'rocking' motion in the ISP head domain consistent with the large-scale displacement of the [2Fe-2S] cluster from a position proximal to the Q<sub>p</sub> site (*b*-state) to a position much closer to the *cyt<sub>f</sub>* subunit (**Figure 6.5** and **Figure 6.6**).

As observed in *cytbc<sub>1</sub>*, the Rieske ISP head domains in the *Synechocystis cytb<sub>6f</sub>* appear to move independently of one another in an anti-cooperative manner such that when the ISP of monomer A is in a Q<sub>p</sub> proximal position, the ISP of monomer B is in a distal position and vice versa. Interestingly, 3DVA across the whole complex (see **section 6.3.1**) (**Figure 6.4**) appears to suggest that this anti-cooperative movement might be observed across the entire complex such that the binding of substrate may occur in each half alternately.



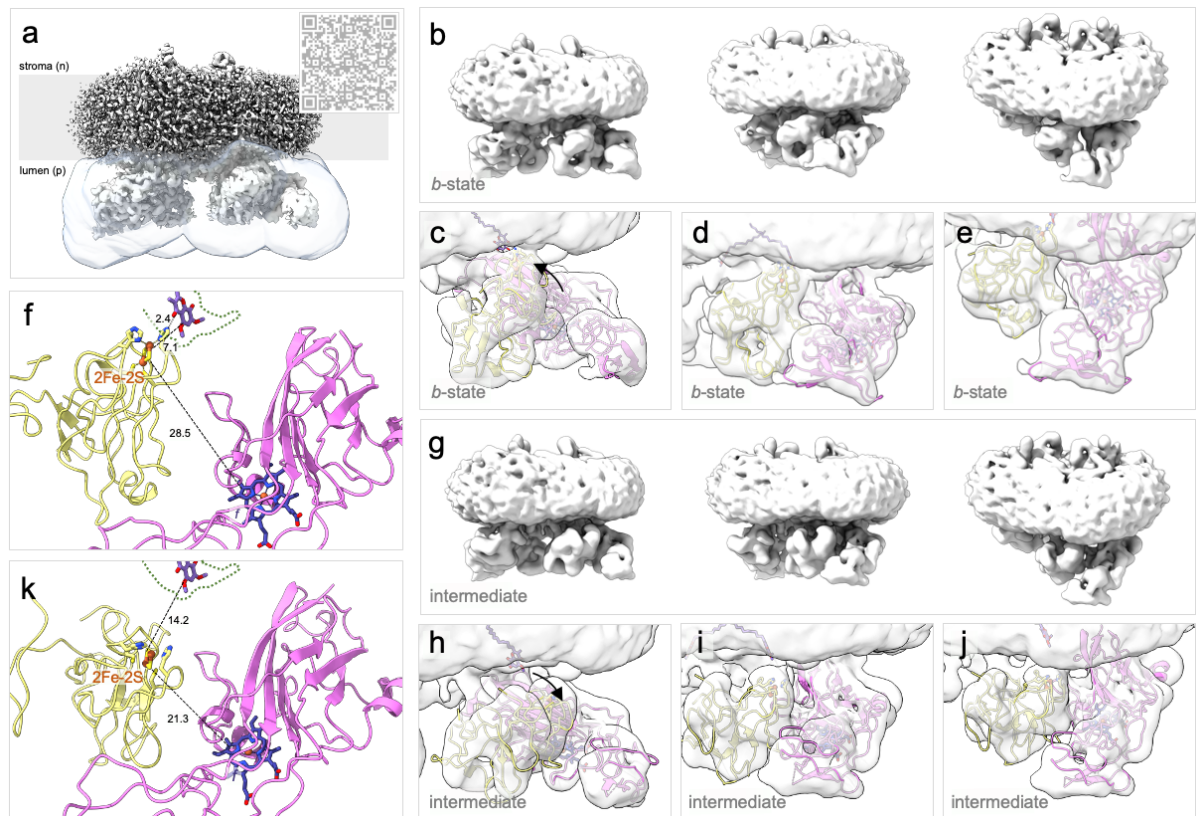


**Figure 6.5 | 3DVA of the *Synechocystis* sp. PCC 6803 (*petA-strep*) *cytb<sub>6</sub>f* using a mask focused around the p-side extrinsic domains.** **a**, a surface representation of the postprocessed *Synechocystis* sp. PCC 6803 (*petA-strep*) *cytb<sub>6</sub>f* cryo EM map showing the soft mask used for 3DVA surrounding the p-side extrinsic domains. The QR code in the top right corner links to a video showing the conformational heterogeneity resolved using this map. **b-f**, the first frame from the 3DVA movie showing the ‘extreme’ conformation corresponding to a Q<sub>p</sub> proximal location for the Rieske ISP viewed from different angles. **b** shows a full surface view of the map viewed from different angles, **c-e** shows zoomed in views of these representations with the ISP (PDB ID: 4H13 (**Hasan et al., 2013b**)) and *cyt<sub>f</sub>* (PDB ID: 1Q90 (**Stroebel et al., 2003**)) rigid body fitted in. **f** shows a cartoon representation of the rigid body fitted model with distances (based on the rigid body model) displayed in Å. **g-k**, the final frame from the 3DVA movie showing the ‘extreme’ conformation nearest to haem *f* for the Rieske ISP viewed from different angles. **g** shows a full surface view of the map viewed from different angles, **h-j** shows zoomed in views of these representations with the ISP (PDB ID: 2D2C) and *cyt<sub>f</sub>* (PDB ID: 4OGQ (**Hasan et al., 2013b**)) rigid body fitted in. **k** shows a cartoon representation of the rigid body fitted model with distances (based on the rigid body model) displayed in Å. Distances are indicated by a black dashed line with the distance indicated below in (Å). Prosthetic groups are shown in stick representation beneath a transparent protein surface. An outline of the Q<sub>p</sub> site is also indicated by a grey dotted line with TDS (purple) from 4H13 superimposed. Subunits are coloured as in Error!

Reference source not found., and cofactors and lipids coloured as in Error! Reference source not found..



**Figure 6.6 | 3D-variability analysis (3DVA) of the *Synechocystis* sp. PCC 6803 (*petA-strep*) *cytb<sub>6f</sub>* using a mask focused only on the extrinsic luminal domains.** Conformational heterogeneity in the extrinsic luminal domains of the *cytb<sub>6f</sub>* cryo-EM map viewed from the plane of the membrane. The contour level of the map was adjusted to 0.40.

## 6.4 3DVA using a ‘lumen-only’ mask

### 6.4.1 Analysis of the two ‘extremes’ revealed by the lumen-only 3DVA

Structural superimposition of the two extreme conformations observed reveals that the density attributed to the ISP in the ‘Q<sub>p</sub>-proximal conformation’ overlays extremely well with structures of the ISP from TDS-containing *cytb<sub>6f</sub>* (PDB ID: 4H13, 1Q90). In this position the [2Fe-2S] cluster is ~ 7.1 Å from the Q<sub>p</sub> site (approximated by the position of superimposed TDS from PDB ID 4H13) (**Figure 6.5**) and ~ 28.5 Å from haem *f* (**Table 6.4**) (**Figure 6.5**). It appears that this position corresponds to the ‘*b*’-state observed in *cytb<sub>c1</sub>*, with the ISP likely fixed via a combination of H-bonding (between His129 and the substrate within the Q<sub>p</sub> site (~ 2.4 Å in 4H13)) and surface complementarity with the *cd-1* helix of the *cytb<sub>6</sub>* subunit as discussed in **section 6.3.1**.

Conversely, the alternate ‘extreme’ appears to equate to an ‘intermediate’ position between the ‘*b*’ and ‘*c*’-states observed in *cytb<sub>c1</sub>* (PDB IDs: 3BCC, 1BE3). Rigid body fitting of this state indicates that from this position, the distance between the [2Fe-2S] cofactor and haem *f* would be ~ 21.3 Å (**Figure 6.5**). Although this is a significant reduction from the 28.5 Å observed between the [2Fe-2S] and haem *f* in the Q<sub>p</sub> proximal ‘*b*’-state, the rate of electron

transfer according to the Moser-Dutton ruler would only be  $\sim 1.95 \text{ e}^- \text{ s}^{-1}$ , giving a half time of  $\sim 354 \text{ ms}$ , which is too slow to account for the  $\sim 250 \text{ e}^- \text{ s}^{-1}$  turnover rate (**Chapter 5**) and 2 - 5 ms half-time observed *in vivo* (**Tikhonov, 2014**).

**Table 6.4** | A comparison of edge-to-edge cofactor distances (Å) in the two ‘extreme’ conformations revealed by 3DVA on the *Synechocystis* sp. PCC 6803 *cytb<sub>6</sub>f* cryo-EM map. Rigid body fitting (using PDB IDs: 2D2C (Yan et al., 2006), 4H13 (Hasan et al., 2013b), 1Q90 (Stroebel et al., 2003) and 4OGQ (Hasan et al., 2013b)) was carried out to approximate the positions of cofactors in each of the two ‘extreme’ conformations. TDS from 4H13 was superimposed to approximate the position of the Q<sub>p</sub> site.

Conformation	Before 3DVA	Q <sub>p</sub> proximal	Q <sub>p</sub> distal
Source	<i>Synechocystis</i>	<i>Synechocystis</i>	<i>Synechocystis</i>
Equivalent ‘state’ in <i>cytb<sub>6</sub>c<sub>1</sub></i>	intermediate	<i>b</i> -state	intermediate
Resolution (Å)	2.98	2.98	2.98
Low pass filter (Å)	-	5	5
<b>Distances (Å)</b>			
<i>b<sub>p</sub></i> - [2Fe-2S]	24.6, 24.7	22.8	29.4
TDS- [2Fe-2S]	9.7, 9.7	7.1	14.2
[2Fe-2S] - <i>f</i>	25.2, 25.2	28.5	21.3

#### 6.4.2 The 70 : 30 model- bridging the gap through the movement of *cyt<sub>f</sub>*

While it appears the scale of motion we observe here for the ISP head is on a smaller scale to that observed for a full ‘*b*’ to ‘*c*’ transition in *cytb<sub>6</sub>c<sub>1</sub>*, it is interesting to note that there appears to be some concurrent motion in the *cyt<sub>f</sub>* domain which could in-part bridge the remaining distance to facilitate electron transfer.

Interestingly, the shift in haem *f* need only be  $\sim 3 - 4 \text{ Å}$  to achieve electron transfer on a scale equivalent to that observed *in vivo* (e.g. at  $17.3 \text{ Å}$  the rate would be  $\sim 490 \text{ e}^- \text{ s}^{-1}$ ). In this model,

the ISP may only need to move 70 % of the distance required to facilitate electron transfer while the remaining 30 % could be made up through movement of the *cyt<sub>f</sub>* subunit. While it is difficult to model the exact position of haem *f* during 3DVA owing to the  $\beta$ -sheet rich structure of *cyt<sub>f</sub>* coupled with the low-resolution afforded by the low pass filter, it is possible to envisage that the degree of motion of the *cyt<sub>f</sub>* subunit overall could encapsulate such small movement of the cofactor. Indeed, there have been previous suggestions that *cyt<sub>f</sub>* could in-part bridge the gap between the [2Fe-2S] cluster and haem *f* (**Hasan and Cramer, 2012**), these suggestions were based on the observation that haem *f* undergoes an  $\sim 2 - 3 \text{ \AA}$  shift between TDS-containing structures (PDB ID: 4H13, 1Q90) and native structures (e.g. PDB ID 4OGQ) (**Figure 6.7**). The possibility of haem *f* being further displaced by another  $2 - 3 \text{ \AA}$  to facilitate electron transfer is not unlikely and indeed the degree of conformational variability we observe in *cyt<sub>f</sub>* could potentially facilitate such a movement.

Indeed it is suggested by **Hasan and Cramer, 2012** that haem *f* is capable of adopting different conformations within the *cyt<sub>f</sub>* subunit ; this suggestion follows EPR evidence from several different sources (**Bergström, 1985; Crowder et al., 1982; Schoepp et al., 2000**) lending further support to this proposal. Additionally, the observation that motion in the ISP in *cyt<sub>b<sub>6</sub>f</sub>* occurs on a smaller scale than that observed in *cyt<sub>b<sub>c</sub>1</sub>* is further supported by results from mutagenesis studies as discussed in **section 6.1**. While in *cyt<sub>b<sub>c</sub>1</sub>*, mutagenesis of the ISP polyglycine hinge is extremely detrimental to electron transfer activity, the same experiment has little effect on the electron transfer functions of *cyt<sub>b<sub>6</sub>f</sub>* (**Yan and Cramer, 2003**). Indeed, the poly-glycine hinge in *b<sub>6</sub>f* can be mutated to become more flexible, more rigid or up to 4 residues longer with no significant effect on electron transfer activity (**Yan and Cramer, 2003**).

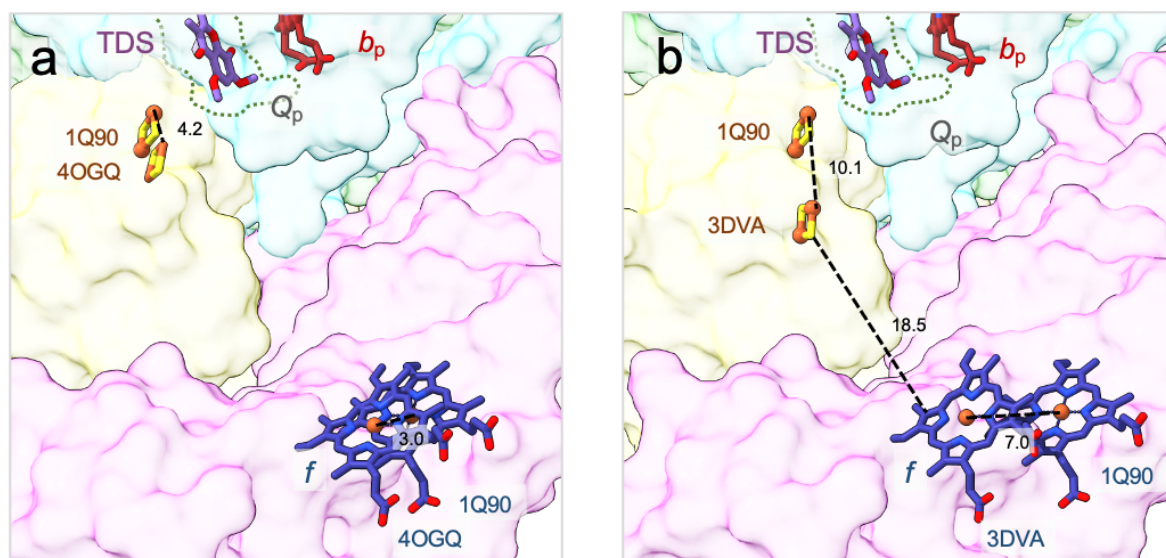


**Figure 6.7 | Conformational changes occurring within the extrinsic domains of the ISP and cytf.** A close up view of the ISP and cytf in *cytb<sub>6</sub>f* showing **a**, the positions of the 2Fe-2S cluster and haem *f* in the structures from *C. reinhardtii* with TDS bound at the Q<sub>p</sub> site (PDB ID: 1Q90 (Stroebel et al., 2003)) and the native structure from *Nostoc* sp. PCC 7120 (PDB ID: 4OGQ (Hasan et al., 2013b)) **b**, the positions of the 2Fe-2S cluster and haem *f* in the structures from *C. reinhardtii* with TDS bound at the Q<sub>p</sub> site (PDB ID: 1Q90 (Stroebel et al., 2003)) and the potential positions which could facilitate electron transfer in the suggested 70:30 model (3DVA). Distances are indicated by a black dashed line with the distance indicated below in (Å). Prosthetic groups are shown in stick representation beneath a transparent protein surface. An outline of the Q<sub>p</sub> site is also indicated by a grey dotted line with TDS (purple) from 4H13 superimposed. Subunits are coloured as in Error! Reference source not found., and cofactors and lipids coloured as in Error! Reference source not found..

#### 6.4.3 Alternatives: a third conformational state?

While it is possible that efficient electron transfer from the [2Fe-2S] cluster to haem *f* could be facilitated through a combined mechanism such as the 70 : 30 model discussed above, it is also possible that ET could proceed via a mechanism encompassing a third conformational state of the ISP which may be extremely transient. As suggested by (Kim et al., 1998) in a study of the mitochondrial *cytbc<sub>1</sub>* complex from *B. taurus*, such an extreme state may be very poorly populated compared to the fixed '*b*'-state or the range of 'intermediate' states; this might suggest that the population of particles in our dataset exhibiting a transient

conformation of the ISP equivalent to the 'c'-state at the moment of freezing could be very small and thus not observable here.

## 6.5 Conclusions

As discussed in **section 1.3.4**, spacing between cofactors (2Fe-2S and *cytf*) along the high-potential chain in *cytb<sub>6f</sub>* observed in existing high-resolution structures of *cytb<sub>6f</sub>* appears to preclude electron transfer at biologically meaningful rates (**Baniulis et al., 2009; Hasan and Cramer, 2014; Hasan et al., 2013b, 2013a, 2014; Kurisu et al., 2003; Malone et al., 2019; Stroebel et al., 2003; Yamashita et al., 2007; Yan et al., 2006**). While it has been suggested that this significant hurdle may be bridged through a large-scale conformational change in the ISP head domain (as observed in the analogous *cytbc<sub>1</sub>* complex), to date no direct high-resolution structural evidence exists to support such a mechanism in *cytb<sub>6f</sub>* (**Breyton, 2000; Esser et al., 2004; Heimann et al., 2000; Kim et al., 1998; Schoepp et al., 1999; Zhang et al., 1998**). It is possible that such conformational motions, if they did indeed exist in *cytb<sub>6f</sub>*, may be limited in crystallography experiments by the confines of the crystal matrix. In this chapter, we attempt to address this using cryo-EM to observe the native *cytb<sub>6f</sub>* complex in the absence of potential factors which may hinder flexibility.

Since many current 3D reconstruction methods are unable to resolve the full range of conformational heterogeneity in a dataset, we have employed a method known as '3D variability analysis' (3DVA) (**Punjani and Fleet, 2021a**) to resolve and visualise continuous conformational variation in the *Synechocystis cytb<sub>6f</sub>* dataset. The results of these analyses provide the first direct evidence of motion in the ISP of *cytb<sub>6f</sub>*, they also demonstrate motion within the extrinsic domain of *cytf* indicating the possibility for a bridging mechanism of electron transfer involving both of these subunits as suggested by **Hasan and Cramer, 2012**.

## 7 Concluding remarks and further work

As discussed in **chapter 1**, oxygenic photosynthesis plays a pivotal role at the very heart of global ecosystems, providing the food, fuel and oxygen that sustains virtually all life on Earth (**Hohmann-Marriott and Blankenship, 2011**). Despite the essential and highly intricate role that photosynthesis plays on Earth, the actual process of photosynthesis appears to be remarkably inefficient with only ~ 9 - 12 % of useable solar energy (wavelengths between 400 – 700 nm) being converted to biomass (**Zhu et al., 2010**).

Given the rising demands on the global food chain associated with climate change and a rising population, it is widely recognised that improvements in the efficiency of this vital process will be required to ensure food security for an ever-increasing population over the coming decades (**Long et al., 2015; Zhu et al., 2010**).

Among the multiple targets which have been identified for potential improvement is *cyt<sub>b</sub><sub>6</sub>f*, a dimeric complex which facilitates the rate limiting step in the light-dependent reactions of photosynthesis in a mechanism analogous to mitochondrial and bacterial *cyt<sub>b</sub><sub>c</sub><sub>1</sub>* complexes (**Berry et al., 2000; Cramer and Kallas, 2016**). As well as facilitating the rate-limiting step in electron and proton transfer, the *cyt<sub>b</sub><sub>6</sub>f* complex also plays a key role as a redox-sensing hub involved in the regulation of light-harvesting, electron transfer, photosynthetic gene expression and adaptation to environmental stress. Together, these characteristics make *cyt<sub>b</sub><sub>6</sub>f* a judicious target for genetic manipulation to enhance photosynthetic yield and promote stress tolerance in crop plants. While a number of studies show great promise in this regard (**Simkin et al., 2017**), further progress is hindered by the lack of a detailed understanding of the structure and function of the *cyt<sub>b</sub><sub>6</sub>f* complex from higher plants.

Whilst previous attempts to study the *cyt<sub>b</sub><sub>6</sub>f* complex from a higher plant source have been unsuccessful (**Baniulis et al., 2011**), a number of clues regarding the structure and function of this extraordinary complex have been provided by high-resolution structural studies from the eukaryotic green alga *C. reinhardtii* (**Stroebel et al., 2003**), and the prokaryotic, filamentous cyanobacteria *Nostoc* (**Baniulis et al., 2009; Hasan and Cramer, 2014; Hasan et al., 2013a**) and *M. laminosus* (**Hasan et al., 2013b, 2013a, 2014; Kurisu et al., 2003; Yamashita et al., 2007; Yan et al., 2006**). These studies provide a number of insights into the internal mechanics of the *cyt<sub>b</sub><sub>6</sub>f* complex and further clarify the structural/functional relationship with *cyt<sub>b</sub><sub>c</sub><sub>1</sub>*



(Berry et al., 2000; Cramer, 2019; Cramer and Kallas, 2016) however a number of questions still remain as discussed in **section 1.3.7**.

## 7.1 Insights into the photosynthetic Q-cycle

While the overall mechanism governing catalysis in *cytb<sub>6</sub>f* is assumed to be largely similar to the Q-cycle occurring in *cytbc<sub>1</sub>* complex, a number of key differences between these complexes add further complexity to this assumption.

### 7.1.1 The role of the enigmatic Chl *a* molecule in the *cytb<sub>6</sub>f* complex

Of particular interest is the role of two pigment molecules unique to the photosynthetic *cytb<sub>6</sub>f* complex which are absent in the respiratory *cytbc<sub>1</sub>*; these include the enigmatic Chl *a* molecule and a carotenoid (9-*cis* β-carotene in *S. oleracea*; echinenone in *Synechocystis*). While the additional carotenoid has been suggested to provide a function in supercomplex formation in a manner akin to the cardiolipin molecule in *cytbc<sub>1</sub>* (Wenz et al., 2009), the observation of two alternative conformations of the Chl *a* molecule in the *S. oleracea* structure (Malone et al., 2019) supports a role for this pigment in controlling access of substrate to/from the catalytic Q<sub>p</sub> site, an adaptation which may be essential for the function of *cytb<sub>6</sub>f* in the highly oxidative environment of the photosynthetic thylakoid as suggested by Hasan et al., 2014.

Indeed, while the first conformation observed in *S. oleracea* appears to permit access to the Q<sub>p</sub> site ('open' conformation), the second appears to restrict access ('closed' conformation) (Figures 4.14 and 4.18). Together, these movements may exert a degree of control over the Q<sub>p</sub> oxidation reactions by preventing the exit of partially oxidised semiquinone species from the Q<sub>p</sub> site; in this manner, the Chl *a* molecule may actively prevent energetically unfavourable short circuits in the Q-cycle and the reduce the likelihood of damaging ROS production.

In addition to serving a role in catalysis, it is further suggested that the motions observed in the Chl *a* phytol tail could provide a means to communicate the redox state of the membrane to external signalling pathways by 'sensing' the occupation state of the Q<sub>p</sub> site. Indeed, such a mechanism has been previously discussed by (Hasan et al., 2013c), however until now a lack of detailed structural evidence for such movements has precluded further study.



Where the structure of *cytb<sub>6f</sub>* from *S. oleracea* provides new insights into these putative mechanisms, the structure of *Synechocystis cytb<sub>6f</sub>* provides new opportunities to further expand and explore these possibilities through mutagenesis. Indeed, we are currently in the process of designing a number of mutants in *Synechocystis* to further examine how the presence of Chl *a* might impact the rate of turnover and also how the motion in the phytyl tail might affect growth and signalling.

### 7.1.2 Bridging cofactor distances in the high-potential ET pathway

Despite the demonstration of rapid electron transfer *in vivo* (2 - 5 ms), the spacing between cofactors (2Fe-2S and *cytf*) along the high-potential chain in *cytb<sub>6f</sub>* observed in existing high-resolution structures of the complex appears to preclude rapid electron transfer (**Baniulis et al., 2009; Hasan and Cramer, 2014; Hasan et al., 2013b, 2013a, 2014; Kurisu et al., 2003; Malone et al., 2019; Stroebel et al., 2003; Yamashita et al., 2007; Yan et al., 2006**). Previously, this has been rationalised by the suggestion that the ISP subunit may undergo a large-scale conformational change to ferry electrons down the high potential pathway as observed in the analogous *cytbc<sub>1</sub>* complex (**Esser et al., 2004; Kim et al., 1998; Zhang et al., 1998**). Despite the close similarities between the ISP in both *cytbc<sub>1</sub>* and *cytb<sub>6f</sub>*, this analogy is precluded by the differences between *cytf* and *cytc<sub>1</sub>*, the structure of the former creating a larger steric barrier to ISP movement (**Hasan et al., 2013b**). Consistent with this, mutation of the ISP hinge region in *cytb<sub>6f</sub>* has little effect on the rate of *cytf* reduction (**Yan and Cramer, 2003**). Thus, while a range of indirect evidence supports movement of the ISP in *cytb<sub>6f</sub>* (**Breyton, 2000; Heimann et al., 2000; Schoepp et al., 1999**), to date no direct high-resolution structural evidence exists. In this study, we suggest an alternative mechanism whereby the significant gap between cofactors may be bridged instead through a concerted movement of both the ISP and *cytf*. Unfortunately, due to limitations in resolution, it is difficult to model the precise conformational change exhibited by these subunits in the 3DVA results; this issue is further compounded by the potential scarcity of such extreme conformations within the dataset. While the findings discussed here may be further clarified by molecular dynamics-based modelling and subsequent simulations, future studies may benefit from methods which may perturb the population of particles in a dataset towards these lesser-seen conformations (e.g. inhibitor binding studies and time-resolved cryoEM experiments). While there is much that remains to be explored, the results presented here provide a key insight into potential

mechanisms which underly the rate-limiting steps in the Q-cycle mechanism, they also provide unique opportunities for mutagenesis studies and more detailed structural study.

### 7.1.3 The role of haem $c_n$ in the *cytb<sub>6</sub>f* complex

In addition to the unique pigment molecules discussed in **section 7.1.1**, the presence of the unique  $c'$ -type haem (haem  $c_n$ ) at the  $Q_n$  site provokes a number of questions regarding the Q-cycle mechanics on the n-side of the complex in *cytb<sub>6</sub>f* which cannot be explained through comparison with the respiratory *cytb<sub>6</sub>c<sub>1</sub>* (**Kurisu et al., 2003; Stroebel et al., 2003**).

Since the discovery of haem  $c_n$ , (discussed in **section 1.3.2**) a number of groups have theorised the possible role of this unique, high-spin haem in both the Q-cycle itself and within the broader expanse of the photosynthetic electron transfer and regulation (**Berry and Trumpower, 1987; Hurt and Hauska, 1981; Joliot and Joliot, 1988; Kurisu et al., 2003; Lavalette et al., 2008; Lavergne, 1983; Stroebel et al., 2003; Whitelegge et al., 2002**).

The present study goes some way towards discerning the role of haem  $c_n$  in the Q-cycle, suggesting a direct role in the binding, reduction and protonation of substrate as well as a possible redox-gating mechanism to mitigate the formation of ROS within the oxygen-rich photosynthetic membrane. In addition to these findings, comparison of the higher plant structure with algal and cyanobacterial structures (both past and present) suggests further adaptations within the Q-cycle which may enable the *cytb<sub>6</sub>f* complex to function optimally within the complex and compartmentalised environment of the eukaryotic cell.

### 7.1.4 Native substrate

In previous structures, catalytic mechanisms have generally been explored through co-crystallisation of the *cytb<sub>6</sub>f* complex with various quinone analogue inhibitors (e.g. tridecyl stigmatellin (TDS), stigmatellin, 2,5-dibromo-3-methyl-6-isopropylbenzoquinone (DBMIB), 2n-nonyl-4-hydroxy-quinoline-N-oxide (NQNO)) (**Hasan et al., 2013a; Kurisu et al., 2003; Yamashita et al., 2007**). Whilst these studies have provided a number of essential insights into the catalytic mechanisms underlying the photosynthetic Q-cycle, it is observed that results from artificial inhibitors can occasionally be misleading and sometimes result in artefacts. Indeed, it is possible that the use of NQNO and TDS to explore the role of haem  $c_n$  in substrate binding may be one such instance of this. Furthermore, the use of crystallisation may directly preclude the observation of conformational flexibility in a sample such that

conformational substates within a sample may only be observable provided that they conform to the confines of the crystal lattice. Cryo-EM of a complex purified directly from its native source coupled with new and innovative techniques to resolve conformational flexibility in a dataset provides unique opportunities to observe catalysis in action without the need for artificial inhibitors. Indeed, in both of the cryo-EM structures we have discussed in this study we observe both native substrate within the *cytb<sub>6</sub>f* complex and catalytically essential conformational changes which further our understanding of how this extraordinary complex fulfils its essential role.

## 7.2 Concluding remarks

Overall, the work presented here significantly enhances our understanding of this extraordinary complex, shedding light on the internal mechanics of the Q-cycle and providing new clues as to how it fulfils its various roles in both higher plants and cyanobacteria. This work not only completes the electron transfer scheme for the light-dependent electron transfer reactions in higher plants, it also provides a number of key mechanistic insights into the *cytb<sub>6</sub>f* complex, many of which may now be further explored through structure-based mutagenesis of the *Synechocystis* complex and molecular dynamics simulations to elucidate the remaining mysteries of this essential complex.

## 8 Bibliography

Adams, P.D., Afonine, P. V., Bunkóczi, G., Chen, V.B., Davis, I.W., Echols, N., Headd, J.J., Hung, L.W., Kapral, G.J., Grosse-Kunstleve, R.W., et al. (2010). PHENIX: A comprehensive Python-based system for macromolecular structure solution. *Acta Crystallographica Section D: Biological Crystallography* 66, 213–221.

Adrian, M., Dubochet, J., Lepault, J., and McDowell, A.W. (1984). Cryo-electron microscopy of viruses. *Nature* 308, 32–36.

Afonine, P. V., Klaholz, B.P., Moriarty, N.W., Poon, B.K., Sobolev, O. V., Terwilliger, T.C., Adams, P.D., and Urzhumtsev, A. (2018). New tools for the analysis and validation of cryo-EM maps and atomic models. *Acta Crystallographica Section D: Structural Biology* 74, 814–840.

Alric, J., Pierre, Y., Picot, D., Lavergne, J., and Rappaport, F. (2005). Spectral and redox characterization of the heme Ci of the cytochrome b6f complex. *Proceedings of the National Academy of Sciences of the United States of America* 102, 15860–15865.

Baniulis, D., Hasan, S.S., Stofleth, J.T., and Cramer, W.A. (2013). Mechanism of Enhanced Superoxide Production in the Cytochrome b6f Complex of Oxygenic Photosynthesis. *Biochemistry* 52, 8975–8983.

Baniulis, D., Yamashita, E., Whitelegge, J.P., Zatsman, A.I., Hendrich, M.P., Hasan, S.S., Ryan, C.M., and Cramer, W.A. (2009). Structure-function, stability, and chemical modification of the cyanobacterial cytochrome b6f complex from *Nostoc* sp. PCC 7120. *Journal of Biological Chemistry* 284, 9861–9869.

Baniulis, D., Yamashita, E., Zhang, H., Hasan, S.S., and Cramer, W.A. (2008). Structure-function of the cytochrome b6f complex. *Photochemistry and Photobiology* 84, 1349–1358.

Baniulis, D., Zhang, H., Zakharova, T., Hasan, S.S., and Cramer, W.A. (2011). Purification and crystallization of the cyanobacterial cytochrome b6f complex. In *Methods in Molecular Biology: Photosynthesis Research Protocols* (2nd Ed.), pp. 65–77.

- Bassham, J.A., Benson, A.A., and Calvin, M. (1950). The path of carbon in photosynthesis. *The Journal of Biological Chemistry* *185*, 781–787.
- Baymann, F., Giusti, F., Picot, D., and Nitschke, W. (2007). The ci/bH moiety in the b6f complex studied by EPR: A pair of strongly interacting hemes. *Proceedings of the National Academy of Sciences of the United States of America* *104*, 519–524.
- Bellafiore, S., Barneche, F., Peltler, G., Rochalx, J.D., Bellaflore, S., Barneche, F., Peltler, G., and Rochalx, J.D. (2005). State transitions and light adaptation require chloroplast thylakoid protein kinase STN7. *Nature* *433*, 892–895.
- Berg, J.M., Tymoczko, J.L., Gregory J. Gatto, J., and Stryer, L. (2015). *Biochemistry*.
- Bergström, J. (1985). The EPR spectrum and orientation of cytochrome b-563 in the chloroplast thylakoid membrane. *FEBS Letters* *183*, 87–90.
- Berry, E.A., and Trumpower, B.L. (1987). Simultaneous determination of hemes a, b, and c from pyridine hemochrome spectra. *Analytical Biochemistry* *161*, 1–15.
- Berry, E.A., Guergova-Kuras, M., Huang, L.S., and Crofts, A.R. (2000). Structure and Function of Cytochrome bc Complexes. *Annual Review of Biochemistry* *69*, 1005–1075.
- Bonaventura, C., and Myers, J. (1969). Fluorescence and oxygen evolution from *Chlorella pyrenoidosa*. *BBA - Bioenergetics* *189*, 366–383.
- Boronowsky, U., Wenk, S.O., Schneider, D., Jäger, C., and Rögner, M. (2001). Isolation of membrane protein subunits in their native state: Evidence for selective binding of chlorophyll and carotenoid to the b6 subunit of the cytochrome b6f complex. *Biochimica et Biophysica Acta - Bioenergetics* *1506*, 55–66.
- Brandt, U., and Trumpower, B. (1994). The protonmotive Q cycle in mitochondria and bacteria. *Critical Reviews in Biochemistry and Molecular Biology* *29*, 165–197.
- Brenner, S., and Horne, R.W. (1959). A negative staining method for high resolution electron microscopy of viruses. *BBA - Biochimica et Biophysica Acta* *34*, 103–110.

Breyton, C. (2000). Conformational changes in the cytochrome b6f complex induced by inhibitor binding. *Journal of Biological Chemistry* 275, 13195–13201.

Breyton, C., Tribet, C., Olive, J., Dubacq, J.-P., and Popot, J.-L. (1997). Dimer to Monomer Conversion of the Cytochrome b6f Complex. *Journal of Biological Chemistry* 272, 21892–21900.

Brugna, M., Rodgers, S., Schricker, A., Montoya, G., Katzmeier, M., Nitschke, W., and Sinning, I. (1999). The Qo -site inhibitor DBMIB favours the proximal position of the chloroplast Rieske protein and induces a pK-shift of the redox-linked proton. *FEBS Letters* 450, 245–250.

Brugna, M., Rodgers, S., Schricker, A., Montoya, G., Kazmeier, M., Nitschke, W., and Sinning, I. (2000). A spectroscopic method for observing the domain movement of the Rieske iron-sulfur protein. *Proceedings of the National Academy of Sciences of the United States of America* 97, 2069–2074.

Buchert, F., Mosebach, L., Gäbelein, P., and Hippler, M. (2020). PGR5 is required for efficient Q cycle in the cytochrome b6f complex during cyclic electron flow. *Biochemical Journal*.

Cape, J.L., Bowman, M.K., and Kramer, D.M. (2006). Understanding the cytochrome bc complexes by what they don't do. The Q-cycle at 30. *Trends in Plant Science* 11, 46–55.

Chen, V.B., Arendall, W.B., Headd, J.J., Keedy, D.A., Immormino, R.M., Kapral, G.J., Murray, L.W., Richardson, J.S., and Richardson, D.C. (2010). MolProbity: All-atom structure validation for macromolecular crystallography. *Acta Crystallographica Section D: Biological Crystallography* 66, 12–21.

Chen, V.B., Arendall, W.B., Headd, J.J., Keedy, D.A., Immormino, R.M., Kapral, G.J., Murray, L.W., Richardson, J.S., and Richardson, D.C. (2010). MolProbity: All-atom structure validation for macromolecular crystallography. *Acta Crystallographica Section D: Biological Crystallography* 66, 12–21.

Corrado, M.E., Aliverti, A., Zanetti, G., and Mayhew, S.G. (1996). Analysis of the oxidation-reduction potentials of recombinant ferredoxin-NADP<sup>+</sup> reductase from spinach chloroplasts. *European Journal of Biochemistry* 239, 662–667.

Cramer, W.A. (2019). Structure–function of the cytochrome b6f lipoprotein complex: a scientific odyssey and personal perspective. *Photosynthesis Research* 139, 53–65.

Cramer, W.A., and Kallas, T. (2016). Cytochrome Complexes: Evolution, Structures, Energy Transduction, and Signaling.

Cramer, W.A., and Zhang, H. (2006). Consequences of the structure of the cytochrome b6f complex for its charge transfer pathways. *Biochimica et Biophysica Acta - Bioenergetics* 1757, 339–345.

Cramer, W.A., Hasan, S.S., and Yamashita, E. (2011). The Q cycle of cytochrome bc complexes: a structure perspective. *Biochimica et Biophysica Acta* 1807, 788–802.

Cramer, W.A., Zhang, H., Yan, J., Kurisu, G., and Smith, J.L. (2006). Transmembrane Traffic in the Cytochrome b6f Complex. *Annual Review of Biochemistry* 75, 769–790.

Crofts, A.R. (2004). The Cytochrome bc 1 Complex: Function in the Context of Structure . *Annual Review of Physiology* 66, 689–733.

Crofts, A.R., and Meinhardt, S.W. (1982). A Q-cycle mechanism for the cyclic electron-transfer chain of *Rhodospseudomonas sphaeroides*. *Biochemical Society Transactions* 10, 201–203.

Crofts, A.R., Barquera, B., Gennis, R.B., Kuras, R., Guergova-Kuras, M., and Berry, E.A. (1999). Mechanism of ubiquinol oxidation by the bc 1 complex: Different domains of the quinol binding pocket and their role in the mechanism and binding of inhibitors. *Biochemistry* 38, 15807–15826.

Crofts, A.R., Berden, J., Crofts, T., Dutton, L., Garland, P., Mitchell, P., Slater, B., Trumpower, B., and Wikström, M. (2004). The Q-cycle – a personal perspective. *Photosynthesis Research* 80, 223–243.

Crofts, A.R., Guergova-Kuras, M., Huang, L.S., Kuras, R., Zhang, Z., and Berry, E.A. (1999b). Mechanism of ubiquinol oxidation by the bc1 complex: Role of the iron sulfur protein and its mobility. *Biochemistry* *38*, 15791–15806.

Crofts, A.R., Hong, S., Ugulava, N., Barquera, B., Gennis, R., Guergova-Kuras, M., and Berry, E.A. (1999d). Pathways for proton release during ubihydroquinone oxidation by the bc1 complex. *Proceedings of the National Academy of Sciences of the United States of America* *96*, 10021–10026.

Crofts, A.R., Hong, S., Zhang, Z., and Berry, E.A. (1999c). Physicochemical aspects of the movement of the rieske iron sulfur protein during quinol oxidation by the bc1 complex from mitochondria and photosynthetic bacteria. *Biochemistry* *38*, 15827–15839.

Crofts, A.R., Meinhardt, S.W., Jones, K.R., and Snozzi, M. (1983a). The role of the quinone pool in the cyclic electron-transfer chain of *Rhodospseudomonas sphaeroides* A modified Q-cycle mechanism. *BBA - Bioenergetics* *723*, 202–218.

Crowder, M.S., Prince, R.C., and Bearden, A. (1982). Orientation of membrane-bound cytochromes in chloroplasts, detected by low-temperature EPR spectroscopy. *FEBS Letters* *144*, 204–208.

de Lavalette, A. de L., Barucq, L., Alric, J., Rappaport, F., and Zito, F. (2009). Is the Redox State of the ci Heme of the cytochrome b6f complex dependent on the occupation and structure of the Qi site and vice versa? *Journal of Biological Chemistry* *284*, 20822–20829.

Dietrich, J., and Kuhlbrandt, W. (1999). Purification and two-dimensional crystallization of highly active cytochrome b6f complex from spinach. *Federation of European Biochemical Societies - Letters* *463*, 97–102.

Dubochet, J., Adrian, M., Chang, J.J., Homo, J.C., Lepault, J., McDowell, A.W., and Schultz, P. (1988). Cryo-electron microscopy of vitrified specimens. *Quarterly Reviews of Biophysics* *21*, 129–228.

Emsley, P., and Cowtan, K. (2004). Coot: Model-building tools for molecular graphics. *Acta Crystallographica Section D: Biological Crystallography* *60*, 2126–2132.



- Esser, L., Elberry, M., Zhou, F., Yu, C.A., Yu, L., and Xia, D. (2008). Inhibitor-complexed structures of the cytochrome bc1 from the photosynthetic bacterium *Rhodobacter sphaeroides*. *Journal of Biological Chemistry* *283*, 2846–2857.
- Esser, L., Gong, X., Yang, S., Yu, L., Yu, C.A., and Xia, D. (2006). Surface-modulated motion switch: Capture and release of iron-sulfur protein in the cytochrome bc1 complex. *Proceedings of the National Academy of Sciences of the United States of America* *103*, 13045–13050.
- Esser, L., Quinn, B., Li, Y.F., Zhang, M., Elberry, M., Yu, L., Yu, C.A., and Xia, D. (2004). Crystallographic studies of quinol oxidation site inhibitors: A modified classification of inhibitors for the cytochrome bc1 complex. *Journal of Molecular Biology* *341*, 281–302.
- Fan, X., Zhao, L., Liu, C., Zhang, J.C., Fan, K., Yan, X., Peng, H.L., Lei, J., and Wang, H.W. (2017). Near-Atomic Resolution Structure Determination in Over-Focus with Volta Phase Plate by Cs-Corrected Cryo-EM. *Structure* *25*, 1623-1630.e3.
- Fernandez-Leiro, R., and Scheres, S.H.W. (2017). A pipeline approach to single-particle processing in RELION. *Acta Crystallographica Section D: Structural Biology* *73*, 496–502.
- Foyer, C., Furbank, R., Harbinson, J., and Horton, P. (1990). The mechanisms contributing to photosynthetic control of electron transport by carbon assimilation in leaves. *Photosynthesis Research* *25*, 83–100.
- Frank, J. (2007). *Three-Dimensional Electron Microscopy of Macromolecular Assemblies : Visualization of Biological Molecules in Their Native State* (Oxford University Press).
- Gao, X., Wen, X., Esser, L., Quinn, B., Yu, L., Yu, C.A., and Xia, D. (2003). Structural basis for the quinone reduction in the bc 1 complex: A comparative analysis of crystal structures of mitochondrial cytochrome bc 1 with bound substrate and inhibitors at the Qi site. *Biochemistry* *42*, 9067–9080.
- Goujon, M., McWilliam, H., Li, W., Valentin, F., Squizzato, S., Paern, J., and Lopez, R. (2010). A new bioinformatics analysis tools framework at EMBL-EBI. *Nucleic Acids Research* *38*, 695–699.

- Gray, H.B., and Winkler, J.R. (1996). Electron Transfer in Proteins. *Annual Review of Biochemistry* 65, 537–561.
- Hahn, A., Vonck, J., Mills, D.J., Meier, T., Kuhlbrandt, W., and Kühlbrandt, W. (2018). Structure, mechanism, and regulation of the chloroplast ATP synthase. *Science* 360, 1–8.
- Hamel, P., Olive, J., Pierre, Y., Wollman, F.A., and De Vitry, C. (2000). A new subunit of cytochrome b6f complex undergoes reversible phosphorylation upon state transition. *Journal of Biological Chemistry* 275, 17072–17079.
- Hasan, S., and Cramer, W.A. (2012). On rate limitations of electron transfer in the photosynthetic cytochrome b6f complex. *Physical Chemistry Chemical Physics* 14, 13853–13860.
- Hasan, S.S. (2013). Structure-Function studies of the cytochrome b6f complex of oxygenic photosynthesis.
- Hasan, S.S., and Cramer, W.A. (2014). Internal lipid architecture of the hetero-oligomeric cytochrome b6f complex. *Structure* 22, 1008–
- Hasan, S.S., Proctor, E.A., Yamashita, E., Dokholyan, N. V., and Cramer, W.A. (2014). Traffic within the cytochrome b6f lipoprotein complex: Gating of the quinone portal. *Biophysical Journal* 107, 1620–1628.
- Hasan, S.S., Stofleth, J.T., Yamashita, E., Cramer, W.A., and S. Saif Hasan, Jason T. Stofleth, Eiki Yamashita, and W.A.C. (2013a). Lipid-Induced Conformational Changes within the Cytochrome b6f Complex of Oxygenic Photosynthesis. *Biochemistry* 52, 2649–2654.
- Hasan, S.S., Yamashita, E., and Cramer, W.A. (2013c). Transmembrane signaling and assembly of the cytochrome b6f-lipidic charge transfer complex.
- Hasan, S.S., Yamashita, E., Baniulis, D., and Cramer, W.A. (2013b). Quinone-dependent proton transfer pathways in the photosynthetic cytochrome b6f complex. *Proceedings of the National Academy of Sciences* 110, 4297–4302.

- Hasan, S.S., Yamashita, E., Ryan, C.M., Whitelegge, J.P., and Cramer, W.A. (2011). Conservation of Lipid Functions in Cytochrome bc Complexes. *Journal of Molecular Biology* 414, 145–162.
- Hauska, G. (2004). The isolation of a functional cytochrome b6f complex: From lucky encounter to rewarding experiences. *Photosynthesis Research* 80, 277–291.
- Heimann, S., Ponamarev, M. V., and Cramer, W.A. (2000). Movement of the Rieske iron-sulfur protein in the p-side bulk aqueous phase: Effect of luminal viscosity on redox reactions of the cytochrome b6f complex. *Biochemistry* 39, 2692–2699.
- Henderson, R. (1992). Image contrast in high-resolution electron microscopy of biological macromolecules: TMV in ice. *Ultramicroscopy* 46, 1–18.
- Hohmann-Marriott, M.F., and Blankenship, R.E. (2011). Evolution of photosynthesis. *Annual Review of Plant Biology* 62, 515–548.
- Hope, A.B. (1993). The chloroplast cytochrome b6 complex A critical focus on function. *BBA - Bioenergetics* 1143, 1–22.
- Hope, A.B., and Valente, P. (1996). Inhibitor binding to isolated chloroplast cytochrome b6f complex. *Photosynthesis Research* 49, 37–48.
- Horton, P. (1985). Interactions between electron transfer and carbon assimilation. In *Photosynthetic Mechanisms and the Environment* (Barber, J. Baker, N.R.), (Elsevier, Amsterdam, NY), pp. 135–187.
- Hovers, J., Potschies, M., Polidori, A., Pucci, B., Raynal, S., Bonneté, F., Serrano-Vega, M.J., Tate, C.G., Picot, D., Pierre, Y., et al. (2011). A class of mild surfactants that keep integral membrane proteins water-soluble for functional studies and crystallization. *Molecular Membrane Biology* 28, 171–181.
- Huang, D., Everly, R.M., Cheng, R.H., Heymann, J.B., Baker, T.S., Cramer, W.A., Schagger, H., Sled, V., Ohnishi, T., Baker, T.S., et al. (1994). Characterization of the Chloroplast Cytochrome b6f Complex as a Structural and Functional Dimer. *Biochemistry* 33, 4401–4409.

Huang, L., Cobessi, D., Tung, E.Y., and Berry, E.A. (2009). Binding of the respiratory chain inhibitor antimycin to the mitochondrial bc1 complex: a new crystal structure reveals an altered hydrogen-bonding pattern. *Journal of Molecular Biology* 49, 1841–1850.

Hunte, C., Koepke, J., Lange, C., Roßmanith, T., and Michel, H. (2000). Structure at 2.3 Å resolution of the cytochrome bc1 complex from the yeast *Saccharomyces cerevisiae* co-crystallized with an antibody Fv fragment. *Structure* 8, 669–684.

Hunte, C., Palsdottir, H., and Trumpower, B.L. (2003). Protonmotive pathways and mechanisms in the cytochrome bc1 complex. *FEBS Letters* 545, 39–46.

Hurt, E., and Hauska, G. (1981). A Cytochrome f/b6 Complex of Five Polypeptides with Plastoquinol-Plastocyanin-Oxidoreductase Activity from Spinach Chloroplasts. *European Journal of Biochemistry* 117, 591–599.

Hurt, E.C., and Hauska, G. (1983). Cytochrome bg from isolated cytochrome b6f complexes: Evidence for two spectral forms with different midpoint potentials. *FEBS Letters* 153, 413–419.

Hurt, E.C., Gabellini, N., Shahak, Y., Lockau, W., and Hauska, G. (1983). Extra proton translocation and membrane potential generation-Universal properties of cytochrome bc1 b6f complexes reconstituted into liposomes. *Archives of Biochemistry and Biophysics* 225, 879–885.

Iwai, M., Takizawa, K., Tokutsu, R., Okamuro, A., Takahashi, Y., and Minagawa, J. (2010). Isolation of the elusive supercomplex that drives cyclic electron flow in photosynthesis. *Nature Letters* 464, 1210–1213.

Iwata, S., Lee, J.W., Okada, K., Lee, J.K., Iwata, M., Rasmussen, B., Link, T.A., Ramaswamy, S., and Jap, B.K. (1998). Complete structure of the 11-subunit bovine mitochondrial cytochrome bc1 complex. *Science* 281, 64–71.

Izrailev, S., Crofts, A.R., Berry, E.A., and Schulten, K. (1999). Steered molecular dynamics simulation of the Rieske subunit motion in the cytochrome bc 1 complex. *Biophysical Journal* 77, 1753–1768.

Johnson, G.N. (2011). Physiology of PSI cyclic electron transport in higher plants. *Biochimica et Biophysica Acta- Bioenergetics* 1807, 384–389.

Johnson, M.P. (2016). Photosynthesis. *Essays In Biochemistry* 60, 255–273.

Joliot, P., and Johnson, G.N. (2011). Regulation of cyclic and linear electron flow in higher plants. *Proceedings of the National Academy of Sciences of the United States of America* 108, 13317–13322.

Joliot, P., and Joliot, A. (1988). The low-potential electron-transfer chain in the cytochrome b/f complex. *BBA - Bioenergetics* 933, 319–333.

Kamienietzky, A., and Nelson, N. (1975). Preparation and Properties of Chloroplasts Depleted of Chloroplast Coupling Factor 1 by Sodium Bromide Treatment. *Plant Physiology* 55, 282–287.

Kim, H., Xia, D., Yu, C.A., Xia, J.Z., Kachurin, A.M., Zhang, L., Yu, L., and Deisenhofer, J. (1998). Inhibitor binding changes domain mobility in the iron-sulfur protein of the mitochondrial bc1 complex from bovine heart. *Proceedings of the National Academy of Sciences of the United States of America* 95, 8026–8033.

Kirchhoff, H., Schöttler, M.A., Maurer, J., and Weis, E. (2004). Plastocyanin redox kinetics in spinach chloroplasts: Evidence for disequilibrium in the high potential chain. *Biochimica et Biophysica Acta - Bioenergetics* 1659, 63–72.

Kramer, D.M., and Evans, J.R. (2011). The importance of energy balance in improving photosynthetic productivity. *Plant Physiology* 155, 70–78.

Kramer, D.M., Avenson, T.J., and Edwards, G.E. (2004). Dynamic flexibility in the light reactions of photosynthesis governed by both electron and proton transfer reactions. *Trends in Plant Science* 9, 349–357.

Kuhlbrandt, W. (2014). Continuing the resolution revolution. *Science* 343, 1443–1444.

Kurusu, G., Zhang, H., Smith, J.L., and Cramer, W.A. (2003). Structure of the Cytochrome b6/f Complex of Oxygenic Photosynthesis : Tuning the Cavity. *Science* 302, 1009–1014.

Lange, C., Nett, J.H., Trumpower, B.L., and Hunte, C. (2001). Specific roles of protein-phospholipid interactions in the yeast cytochrome bc<sub>1</sub> complex structure. *EMBO Journal* 20, 6591–6600.

Lavalette, A. de L. de, Finazzi, G., Francesca, Z., De Lavalette, A.D.L., Finazzi, G., and Zito, F. (2008). b<sub>6</sub>f-associated chlorophyll: Structural and dynamic contribution to the different cytochrome functions. *Biochemistry* 47, 5259–5265.

Lavergne, J. (1983). Membrane potential-dependent reduction of cytochrome b-6 in an algal mutant lacking Photosystem I centers. *BBA - Bioenergetics* 725, 25–33.

Long, S.P., Marshall-Colon, A., and Zhu, X.G. (2015). Meeting the global food demand of the future by engineering crop photosynthesis and yield potential. *Cell* 161, 56–66.

Maldonado, M., Guo, F., and Letts, J.A. (2020). Atomic structures of respiratory complex III 2, complex IV and supercomplex III 2-IV from vascular plants. *BioRxiv* 2020.08.30.274431.

Malkin, R. (1992). Cytochrome and b<sub>6</sub>f complexes of photosynthetic membranes. *Photosynthesis Research* 121–136.

Malone, L.A., Qian, P., Mayneord, G.E., Hitchcock, A., Farmer, D.A., Thompson, R.F., Swainsbury, D.J.K., Ranson, N.A., Hunter, C.N., and Johnson, M.P. (2019a). Cryo-EM structure of the spinach cytochrome b<sub>6</sub>f complex at 3.6 Å resolution. *Nature* 575, 535–539.

Marcus, R.A., and Sutin, N. (1985). Electron transfers in chemistry and biology. *Biochimica et Biophysica Acta* 811, 265–322.

Martinez, S.E., Huang, D., Szczepaniak, A., Cramer, W.A., and Smith, J.L. (1994). Crystal structure of chloroplast cytochrome f reveals a novel cytochrome fold and unexpected heme ligation. *Structure* 2, 95–105.

Mayneord, G.E., Vasilev, C., Malone, L.A., Swainsbury, D.J.K., Hunter, C.N., and Johnson, M.P. (2019). Single-molecule study of redox control involved in establishing the spinach plastocyanin-cytochrome b<sub>6</sub>f electron transfer complex. *Biochimica et Biophysica Acta - Bioenergetics* 1860, 591–599.

Metzger, S.U., Cramer, W.A., and Whitmarsh, J. (1997). Critical analysis of the extinction coefficient of chloroplast cytochrome f. *Biochimica et Biophysica Acta - Bioenergetics* 1319, 233–241.

Mitchell, P. (1975a). Protonmotive redox mechanism of the cytochrome b-c1 complex in the respiratory chain: Protonmotive ubiquinone cycle. *FEBS Letters* 56, 1–6.

Mitchell, P. (1975b). The protonmotive Q cycle: A general formulation. *FEBS Letters* 59, 137–139.

Mitchell, P. (1976). Possible molecular mechanisms of the protonmotive function of cytochrome systems. *Journal of Theoretical Biology* 62, 327–367.

Moser, C.C., Keske, J.M., Warncke, K., Farid, R.S., and Dutton, P.L. (1992). Nature of biological electron transfer. *Nature* 355, 796–802.

Moser, C.C., Page, C.C., Chen, X., and Dutton, P.L. (2000). Electron transfer in natural proteins theory and design. *Sub-Cellular Biochemistry* 35, 1–28.

Moss, D.A., and Bendall, D.S. (1984). Cyclic electron transport in chloroplasts. The Q-cycle and the site of action of antimycin. *BBA - Bioenergetics* 767, 389–395.

Moss, G.P. (1988). Nomenclature of tetrapyrroles. *Eur. J. Biochem.* 328, 277–328.

Mulkidjanian, A.Y. (2005). Ubiquinol oxidation in the cytochrome bc1 complex: Reaction mechanism and prevention of short-circuiting. *Biochimica et Biophysica Acta (BBA) - Bioenergetics* 1709, 5–34.

Munekage, Y., Hashimoto, M., Miyake, C., Tomizawa, K.I., Endo, T., Tasaka, M., and Shikanai, T. (2004). Cyclic electron flow around photosystem I is essential for photosynthesis. *Nature Letters* 429, 579–582.

Murata, K., and Wolf, M. (2018). Cryo-electron microscopy for structural analysis of dynamic biological macromolecules. *Biochimica et Biophysica Acta - General Subjects* 1862, 324–334.

- Murata, N., and Sugahara, K. (1969). Control of excitation transfer in photosynthesis III. Light-induced decrease of chlorophyll a fluorescence related to photophosphorylation system in spinach chloroplasts. *Biochimica et Biophysica Acta* 189, 182–192.
- Nandha, B., Finazzi, G., Joliot, P., Hald, S., and Johnson, G.N. (2007). The role of PGR5 in the redox poisoning of photosynthetic electron transport. *Biochimica et Biophysica Acta - Bioenergetics* 1767, 1252–1259.
- Nelson, M.E., Finazzi, G., Qing, J.W., Middleton-Zarka, K.A., Whitmarsh, J., and Kallas, T. (2005). Cytochrome b6 arginine 214 of *Synechococcus* sp. PCC 7002, a key residue for quinone-reductase site function and turnover of the cytochrome b6 complex. *Journal of Biological Chemistry* 280, 10395–10402.
- Ort, D., and Izawa, S. (1974). Studies on the Energy-coupling Sites of Photophosphorylation. *Plant Physiology* 53, 370–376.
- Osyczka, A., Moser, C.C., and Dutton, P.L. (2005). Fixing the Q cycle. *Trends in Biochemical Sciences* 30, 176–182.
- Page, C.C., Moser, C.C., Chen, X., and Dutton, P.L. (1999). Natural engineering principles of electron tunnelling in biological oxidation-reduction. *Nature* 402, 47–52.
- Petlicki, J., and Van De Ven, T.G.M. (1998). The equilibrium between the oxidation of hydrogen peroxide by oxygen and the dismutation of peroxy or superoxide radicals in aqueous solutions in contact with oxygen. *Journal of the Chemical Society - Faraday Transactions* 94, 2763–2767.
- Pettersen, E.F., Goddard, T.D., Huang, C.C., Couch, G.S., Greenblatt, D.M., Meng, E.C., and Ferrin, T.E. (2004). UCSF Chimera - A visualization system for exploratory research and analysis. *Journal of Computational Chemistry* 25, 1605–1612.
- Pfeffer, S., and Mahamid, J. (2018). Unravelling molecular complexity in structural cell biology. *Current Opinion in Structural Biology* 52, 111–118.



- Pick, U., and Racker, E. (1979). Purification and Reconstitution of the NJV-Dicyclohexylcarbodiimide-sensitive ATPase Complex from Spinach Chloroplasts \*. *Journal of Biological Chemistry* 254, 2793–2799.
- Pierre, Y., Breyton, C., Kramer, D., and Popot, J.-L.L. (1995). Purification and Characterization of the Cytochrome b6 f Complex from *Chlamydomonas reinhardtii*. *Journal of Biological Chemistry* 270, 29342–2934.
- Pierre, Y., Lemoine, Y., Robert, B., Vernotte, C., Popot, J., Yvette, F.-G.S., Upr, C., and Yvette, F.-G.S. (1997). On the Presence and Role of a Molecule of Chlorophyll a in the Cytochrome b6f Complex. *Journal of Biological Chemistry* 272, 21901–21908.
- Plusquellec, D., Chevalier, G., Talibert, R., and Wroblewski, H. (1989). Synthesis and characterization of 6-O-(N-heptylcarbamoyl)-methyl- $\alpha$ -D-glucopyranoside, a new surfactant for membrane studies. *Analytical Biochemistry* 179, 145–153.
- Porra, R.J., Thompson, W.A., and Kriedemann, P.E. (1989). Determination of accurate extinction coefficients and simultaneous equations for assaying chlorophylls a and b extracted with four different solvents: verification of the concentration of chlorophyll standards by atomic absorption spectroscopy. *Biochimica et Biophysica Acta- Bioenergetics* 975, 384–394.
- Punjani, A., and Fleet, D.J. (2021). 3D Variability Analysis: Resolving continuous flexibility and discrete heterogeneity from single particle cryo-EM. *Journal of Structural Biology* 213, 1–25.
- Punjani, A., Rubinstein, J.L., Fleet, D.J., and Brubaker, M.A. (2017). CryoSPARC: Algorithms for rapid unsupervised cryo-EM structure determination. *Nature Methods* 14, 290–296.
- Ramachandran, G.N., Ramakrishnan, C., and Sasisekharan, V. (1963). Stereochemistry of polypeptide chain configurations. *Journal of Molecular Biology* 7, 95–99.
- Rebeiz, C.A., Benning, C., Bohnert, H.J., Daniell, H., Hooper, J.K., Lichtenthaler, H.K., Portis, A.R., and Tripathy, B.C. (2010). The chloroplast.

Riccio, P., Schägger, H., Engel, W.D., and Von Jagow, G. (1977). bc<sub>1</sub>-complex from beef heart, one-step purification by hydroxyapatite chromatography in triton X-100, polypeptide pattern and respiratory chain characteristics. *BBA - Bioenergetics* 459, 250–262.

Rich, P.R. (2004). The quinone chemistry of bc complexes. *Biochimica et Biophysica Acta - Bioenergetics*.

Rohou, A., and Grigorieff, N. (2015). CTFFIND4: Fast and accurate defocus estimation from electron micrographs. *Journal of Structural Biology* 192, 216–221.

Rosenthal, P.B., and Henderson, R. (2003). Optimal determination of particle orientation, absolute hand, and contrast loss in single-particle electron cryomicroscopy. *Journal of Molecular Biology* 333, 721–745.

Sarewicz, M., Bujinowicz, L., Bhaduri, S., Singh, S., Cramer, W.A., and Osyczka, A. (2017). Metastable radical state, nonreactive with oxygen, is inherent to catalysis by respiratory and photosynthetic cytochromes bc<sub>1</sub>/b<sub>6</sub>f. *Proceedings of the National Academy of Sciences of the United States of America* 114, 1323–1328.

Scheres, S.H.W. (2012). RELION: Implementation of a Bayesian approach to cryo-EM structure determination. *Journal of Structural Biology* 180, 519–530.

Scheres, S.H.W. (2012a). A Bayesian view on cryo-EM structure determination. *Journal of Molecular Biology* 415, 406–418.

Scheres, S.H.W. (2015). Semi-automated selection of cryo-EM particles in RELION-1.3. *Journal of Structural Biology* 189, 114–122.

Scheres, S.H.W. (2016). *Processing of Structurally Heterogeneous Cryo-EM Data in RELION* (Elsevier Inc.).

Scheres, S.H.W., and Chen, S. (2012). Prevention of overfitting in cryo-EM structure determination. *Nature Methods* 9, 853–854.

Scheres, S.H.W., Gao, H., Valle, M., Herman, G.T., Eggermont, P.P.B., Frank, J., and Carazo, J.M. (2007). Disentangling conformational states of macromolecules in 3D-EM through likelihood optimization. *Nature Methods* 4, 27–29.

Schoepp, B., Brugna, M., Riedel, A., Nitschke, W., and Kramer, D.M. (1999). The Q(o)-site inhibitor DBMIB favours the proximal position of the chloroplast Rieske protein and induces a pK-shift of the redox-linked proton. *FEBS Letters* 450, 245–250.

Schoepp, B., Chabaud, E., Breyton, C., Verméglio, A., and Popot, J.L. (2000). On the spatial organization of hemes and chlorophyll in cytochrome b6f. A linear and circular dichroism study. *Journal of Biological Chemistry* 275, 5275–5283.

Schünemann, V., Trautwein, A.X., Illerhaus, J., and Haehnel, W. (1999). Mossbauer and electron paramagnetic resonance studies of the cytochrome b<sub>6</sub>f complex. *Biochemistry* 38, 8981–8991.

Seelert, H., Poetsch, A., Dencher, N.A., Engel, A., Stahlberg, H., and Müller, D.J. (2000). Proton-powered turbine of a plant motor. *Nature* 405, 418–419.

Shaikh, T.R., Gao, H., Baxter, W.T., Asturias, F.J., Boisset, N., Leith, A., and Frank, J. (2008). SPIDER image processing for single-particle reconstruction of biological macromolecules from electron micrographs. *Nature Protocols* 3, 1941–1974.

Sievers, F., Wilm, A., Dineen, D., Gibson, T.J., Karplus, K., Li, W., Lopez, R., McWilliam, H., Remmert, M., Söding, J., et al. (2011). Fast, scalable generation of high-quality protein multiple sequence alignments using Clustal Omega. *Molecular Systems Biology* 7.

Simkin, A.J., McAusland, L., Lawson, T., and Raines, C.A. (2017). Overexpression of the rieskeFeS protein increases electron transport rates and biomass yield. *Plant Physiology* 175, 134–145.

Slater, E.C. (1973). The mechanism of action of the respiratory inhibitor, antimycin. *Biochemica et Biophysica Acta* 301, 129–154.

Solmaz, S.R.N.N., and Hunte, C. (2008). Structure of complex III with bound cytochrome C in reduced state and definition of a minimal core interface for electron transfer. *Journal of Biological Chemistry* 283, 17542–17549.

Soriano, G.M., Guo, L.W., De Vitry, C., Kallas, T., and Cramer, W.A. (2002). Electron transfer from the Rieske iron-sulfur protein (ISP) to cytochrome f in vitro: Is a guided trajectory of the ISP necessary for competent docking? *Journal of Biological Chemistry* 277, 41865–41871.

Stroebel, D., Choquet, Y., Popot, J.L., and Picot, D. (2003). An atypical haem in the cytochrome b6f complex. *Nature* 426, 413–418.

Swierczek, M., Cieluch, E., Sarewicz, M., Borek, A., Moser, C.C., Dutton, P.L., and Oszycka, A. (2010). An Electronic Bus Bar Lies in the Core of Cytochrome bc1. *Science* 329, 451–454.

Świerczek, M., Cieluch, E., Sarewicz, M., Borek, A., Moser, C.C., Dutton, P.L., and Osyczka, A. (2017). An Electronic Bus Bar Lies in the Core of Cytochrome bc1 Monika. *PLoS ONE* 32, 736–740.

Tan, S., and Ho, K.-K. (1989). Purification of an acidic plastocyanin from *Microcystis aeruginosa*. *Biochemica et Biophysica Acta* 973, 111–117.

Tang, G., Peng, L., Baldwin, P.R., Mann, D.S., Jiang, W., Rees, I., and Ludtke, S.J. (2007). EMAN2: An extensible image processing suite for electron microscopy. *Journal of Structural Biology* 157, 38–46.

Tikhonov, A.N. (2013). The cytochrome b6f complex at the crossroad of photosynthetic electron transport pathways. *Plant Physiology and Biochemistry* 81, 1–20.

Tipping, M.E., and Bishop, C.M. (1999). Probabilistic principal component analysis. *Journal of the Royal Statistical Society* 61, 611–622.

Trumpower, B. (1990). The protonmotive Q cycle. *Journal of Biological Chemistry* 265, 11409–11412.

Volkmer, T., Schneider, D., Bernát, G., Kirchhoff, H., Wenk, S.O., and Rögner, M. (2007). Ssr2998 of *Synechocystis* sp. PCC 6803 is involved in regulation of cyanobacterial electron transport and associated with the cytochrome b<sub>6</sub>f complex. *Journal of Biological Chemistry* 282, 3730–3737.

Wagner, T., Merino, F., Stabrin, M., Moriya, T., Antoni, C., Apelbaum, A., Hagel, P., Sitsel, O., Raisch, T., Prumbaum, D., et al. (2019). SPHIRE-crYOLO is a fast and accurate fully automated particle picker for cryo-EM. *Communications Biology* 2, 1–13.

Wenz, T., Hielscher, R., Hellwig, P., Schägger, H., Richers, S., and Hunte, C. (2009). Role of phospholipids in respiratory cytochrome bc<sub>1</sub> complex catalysis and supercomplex formation. *Biochimica et Biophysica Acta - Bioenergetics* 1787, 609–616.

Whitelegge, J.P., Zhang, H., Aguilera, R., Taylor, R.M., and Cramer, W.A. (2002). Full subunit coverage liquid chromatography electrospray ionization mass spectrometry (LCMS+) of an oligomeric membrane protein: cytochrome b<sub>6</sub>f complex from spinach and the cyanobacterium *Mastigocladus laminosus*. *Molecular & Cellular Proteomics : MCP* 1, 816–827.

Williams, C.J., Headd, J.J., Moriarty, N.W., Prisant, M.G., Videau, L.L., Deis, L.N., Verma, V., Keedy, D.A., Hintze, B.J., Chen, V.B., et al. (2018). MolProbity: More and better reference data for improved all-atom structure validation. *Protein Science* 27, 293–315.

Xia, D., Esser, L., Yu, L., and Yu, C.A. (2007). Structural basis for the mechanism of electron bifurcation at the quinol oxidation site of the cytochrome bc<sub>1</sub> complex. *Photosynthesis Research* 92, 17–34.

Xia, D., Yu, C.A., Kim, H., Xia, J.Z., Kachurin, A.M., Zhang, L., Yu, L., and Deisenhofer, J. (1997). Crystal structure of the cytochrome bc<sub>1</sub> complex from bovine heart mitochondria. *Science* 277, 60–66.

Yamashita, E., Zhang, H., and Cramer, W.A. (2007). Structure of the Cytochrome b<sub>6</sub>f Complex: Quinone Analogue Inhibitors as Ligands of Heme cn. *Journal of Molecular Biology* 370, 39–52.

- Yamori, W., and Shikanai, T. (2016). Physiological Functions of Cyclic Electron Transport Around Photosystem I in Sustaining Photosynthesis and Plant Growth. *Annual Review of Plant Biology* 67, 81–106.
- Yan, J., and Cramer, W.A. (2003). Functional insensitivity of the cytochrome b6f complex to structure changes in the hinge region of the Rieske iron-sulfur protein. *Journal of Biological Chemistry* 278, 20925–20933.
- Yan, J., Kurisu, G., and Cramer, W.A. (2006). Intraprotein transfer of the quinone analogue inhibitor 2,5-dibromo-3-methyl-6-isopropyl-p-benzoquinone in the cytochrome b6f complex. *Proceedings of the National Academy of Sciences of the United States of America* 103, 69–74.
- Yu, L., Yang, S., Yin, Y., Cen, X., Zhou, F., Xia, D., Yu, C.A., and Chang-An Yu (2009). Analysis of Electron Transfer and Superoxide Generation in the Cytochrome bc1 Complex. *Methods in Enzymology* 456, 459–473.
- Zatsman, A.I., Zhang, H., Gunderson, W.A., Cramer, W.A., and Hendrich, M.P. (2006). Heme-heme interactions in the cytochrome b6f complex: EPR spectroscopy and correlation with structure. *Journal of the American Chemical Society* 128, 14246–14247.
- Zhang, H., Huang, D., and Cramer, W.A. (1999). Stoichiometrically Bound  $\beta$ -Carotene in the Cytochrome b6f Complex of Oxygenic Photosynthesis Protects against Oxygen Damage. *Journal of Biological Chemistry* 274, 1581–1587.
- Zhang, H., Kurisu, G., Smith, J.L., and Cramer, W.A. (2003). A defined protein-detergent-lipid complex for crystallization of integral membrane proteins: The cytochrome b6f complex of oxygenic photosynthesis. *Proceedings of the National Academy of Sciences* 100, 5160–5163.
- Zhang, H., Whitelegge, J.P., and Cramer, W.A. (2001). Ferredoxin:NADP<sup>+</sup> Oxidoreductase Is a Subunit of the Chloroplast Cytochrome b6f Complex. *Journal of Biological Chemistry* 276, 38159–38165.
- Zhang, K. (2016). Gctf: Real-time CTF determination and correction. *Journal of Structural Biology* 193, 1–12.

Zhang, Z.L., Huang, L.S., Shulmeister, V.M., Chi, Y.I., Kim, K.K., Hung, L.W., Crofts, A.R., Berry, E.A., and Kim, S.H. (1998). Electron transfer by domain movement in cytochrome bc<sub>1</sub>. *Nature* 392, 677–684.

Zheng, S.Q., Palovcak, E., Armache, J.-P., Verba, K.A., Cheng, Y., and Agard, D.A. (2017). MotionCor2 - anisotropic correction of beam-induced motion for improved cryo-electron microscopy. *Nature Methods* 14, 331–332.

Zhu, X.-G., Long, S.P., and Ort, D.R. (2010). Improving Photosynthetic Efficiency for Greater Yield. *Annual Review of Plant Biology* 61, 235–261.

Zito, F., and Alric, J. (2016). Heme c<sub>i</sub> or c<sub>n</sub> of the Cytochrome b<sub>6</sub> f Complex, A Short Retrospective. p.

Zito, F., Finazzi, G., Joliot, P., and Wollman, F.-A. (1998). Glu78, from the Conserved PEWY Sequence of Subunit IV, Has a Key Function in Cytochrome b<sub>6</sub>f Turnover. *Biochemistry* 37, 10395–10403.

Zivanov, J., Nakane, T., and Scheres, S.H.W. (2019). A Bayesian approach to beam-induced motion correction in cryo-EM single-particle analysis. *IUCr* 6, 5–17.

Zivanov, J., Nakane, T., and Scheres, S.H.W. (2020). Estimation of high-order aberrations and anisotropic magnification from cryo-EM data sets in RELION-3.1. *IUCr* 7, 253–267.

Zivanov, J., Nakane, T., Forsberg, B., Kimanius, D., Hagen, W., Lindahl, E., and Scheres, S. (2018). RELION-3: new tools for automated high-resolution cryo-EM structure determination. *BioRxiv* 421123.

...

“YOU'LL GET MIXED UP, OF COURSE,  
AS YOU ALREADY KNOW.  
YOU'LL GET MIXED UP  
WITH MANY STRANGE BIRDS AS YOU GO.

SO BE SURE WHEN YOU STEP.  
STEP WITH CARE AND GREAT TACT  
AND REMEMBER THAT LIFE'S  
A GREAT BALANCING ACT.  
JUST NEVER FORGET TO BE DEXTEROUS AND DEFT.  
AND NEVER MIX UP YOUR RIGHT FOOT WITH YOUR LEFT.

...



...

AND WILL YOU SUCCEED?  
YES! YOU WILL, INDEED!  
(98 AND 3/4 PERCENT GUARANTEED.)

KID, YOU'LL MOVE MOUNTAINS!

SO... BE YOUR NAME BUXBAUM OR BIXBY OR BRAY  
OR MORDECAI ALI VAN ALLEN O'SHEA,  
YOU'RE OFF TO GREAT PLACES!  
TODAY IS YOUR DAY!

YOUR MOUNTAIN IS WAITING.  
SO... GET ON YOUR WAY!"

- DR. SEUSS. OH, THE PLACES YOU'LL GO!

